Collisional and structural properties of water ice in planet-forming regions

Thesis

The Open University

Collisional and structural properties of water ice in planet-forming regions

Submitted for the degree of Doctor of Philosophy

in Astronomy

Catherine R. Hill MChem (Oxon.)

The Open University

Date of submission: 11th September 2015

Abstract

With the number of detected exoplanets standing at close to 2000, it seems that planets are ubiquitous throughout the universe. However, the processes leading to their formation are not well understood. It is widely accepted that planets form by dust aggregation from the material of protoplanetary disks, with micron-sized particles sticking together by van der Waals forces and kilometre-sized particles sticking together due to gravity. The process of growth between millimetre and kilometre sizes is yet to be explained, despite decades of research studying the collisions of silicate dust particles which form the main component of protoplanetary dust. However, the water ice that is present in the outer regions of protoplanetary disks has so far received less consideration.

In this thesis, the collisional and structural properties of ices analogous to those in planet-forming regions were studied experimentally. Low velocity collisions of millimetre and centimetre-sized crystalline ice particles (both pure water and ice composed of pure water and water containing 5% methanol or formic acid) were investigated using a dedicated experimental set up for use on board parabolic flights. The porosity and pore collapse of amorphous solid water (ASW) grown at a variety of temperatures was investigated using neutron scattering.

The results presented in this thesis show that crystalline water ice particles do not stick at relevant collision velocities, casting doubt on their ability to enhance planet formation by particle adhesion. However, the results of the neutron scattering experiments suggest that ASW is likely to remain porous at temperatures below 121 K, which may increase the likelihood of particle sticking. Sticking may also be enhanced by ice restructuring during pore collapse. The results of the experiments growing ASW at temperatures below 77 K show that these ices have different porosities, but further work is needed to fully characterise this.

Acknowledgements

Firstly, thank you to my supervisors Helen Fraser and Nigel Mason for all of their help and support during the course of the PhD. Thanks must also go to other academics in the department, in particular Jim Hague, Stephen Serjeant, Silvia Bergamini and Sally Jordan, for supporting me at crucial points during my PhD. Jürgen and Daniel, thank you for letting me pay a visit to Braunschweig and for teaching me all about ice collisions, it was a pleasure to work with you! Tristan, Daniel and Chris, thank you for your tireless support before and during our ISIS experiments. Thomas, thank you for the many interesting discussions and helpful suggestions regarding the ISIS work. To all the astrochemistry students, past and present (Aleksi, Pavel, Ewelina, Binu, Natalia, Olivier, George and Lawrence), thank you for your friendship and humour which has definitely helped to keep me sane! To the others I've got to know at the OU, through the department or through PGSS, there are too many of you to mention but it's been so great to spend time with you. Special mentions to Ele for welcoming me on my very first day which made settling in so much easier, Beca and Phillipa for all the long chats, Phil for sorting all my IT emergencies and Liam for making me laugh. To everyone at Christ the King Community Church, particularly Lou, Peter, Pauline, Rachael and Dan, thank you for the support you've given me during the last three years, it has been invaluable. Jack, Sarah and Michael - we may no longer all be living in the same city but I know I can always count on your friendship and support. Mum, Dad and Alison, thank you for always being there for me and believing in me. Last but not least, thank you to Richard. It's something of a cliche to say "I couldn't have done it without you" but in this case it is true. Your support throughout, especially when I felt like giving up, has been a constant source of strength. Thank you.

I see Your power in the moonlit night

Where planets are in motion and galaxies are bright

We are amazed in the light of the stars

It's all proclaiming who You are

-Phil Wickham, You're Beautiful

Contents

List of Figures

List of Tables

Non book component: List of figures

The following figures appear in the PDF file on the CD at the back of this thesis. Page numbers for the supplementary material are also given.

Chapter 1

Introduction

Since the first confirmed discovery of an exoplanet in 1995 (Mayor & Queloz, 1995), nearly two thousand have been discovered. Exoplanets are mainly found orbiting main sequence stars but have also been observed orbiting binary systems (Zhou et al., 2012) and pulsars (Wolszczan & Frail, 1992), and there is some evidence to suggest that planets could also form around dying stars (Wang et al., 2006). As planets are clearly widespread, the question of their formation is of great scientific importance. Proto-planetary disks (where planet formation takes place) contain both dust and ice; and while dust has been studied extensively in the context of planet formation, the same cannot be said for ice, on which far less work has been done. The first big question of this thesis is this:

How do ice particles collide in planet-forming regions, and can they help planet formation?

Understanding the structure of the ice is also vital for understanding the collisional properties, and in the case of amorphous solid water, which has been detected in relevant regions (Schegerer & Wolf, 2010), the structure, porosity and porosity changes with temperature are not well understood. The second big question of this thesis is therefore:

What is the structure and porosity of amorphous solid water in planet-forming regions, and how do these properties change with time and temperature?

The current models of planet formation, the problem of growth between millimetre and kilometre sizes and possible solutions, including the role of ice, are presented in this chapter. Additionally, the current understanding of amorphous solid water and previous research on its porosity is discussed.

1.1 Planet formation

1.1.1 Protoplanetary disks

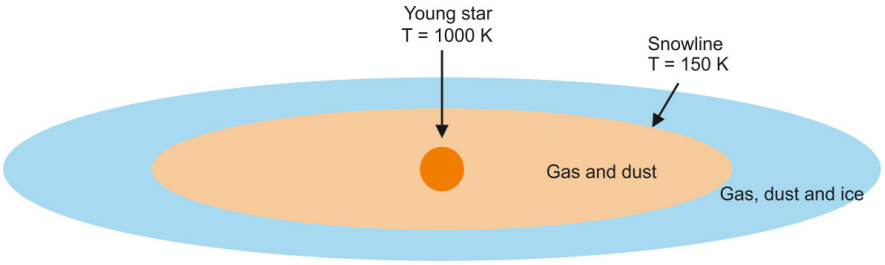

Figure 1.1: Diagram of a protoplanetary disk composed of gas, dust and ice surrounding the central star. The temperature decreases with increasing distance from the star. When the temperature has reached 150 K, water ice can condense onto dust grains.

Gravitational collapse in molecular clouds leads to star formation. The young star is surrounded by a disk composed of gas and dust in which planets can form - a protoplanetary disk. Protoplanetary disks are mainly composed of gas (which is dominated by molecular hydrogen), although a small fraction of their mass is silicate or carbonaceous dust grains (around 1 %) (Ollivier et al., 2009, pg. 155). The initial temperatures towards the centre of such disks are around 1000 K (Papaloizou & Terquem, 1999); further out the temperatures are cooler and dust grains can form. There comes a point, around 150 K, where ice can form on the surface of dust grains, this is known as the snowline (Lauretta & McSween, 2006, pg. 311). Snowlines are specific to particular molecules; in the remainder of this chapter, "snowline" refers to the water snowline. These features are illustrated in the diagram in Fig. 1.1. Pressures in protoplanetary disks are around 10^{-2}-10^{-3} mbar (Weidenschilling et al., 1993). The dust grains in protoplanetary disks are greater than 1 μm in size, much larger than interstellar dust,

suggesting that dust aggregation is common (Ollivier et al., 2009, pg. 155). It is from the material of these disks that planets form.

1.1.2 Current model of planet formation

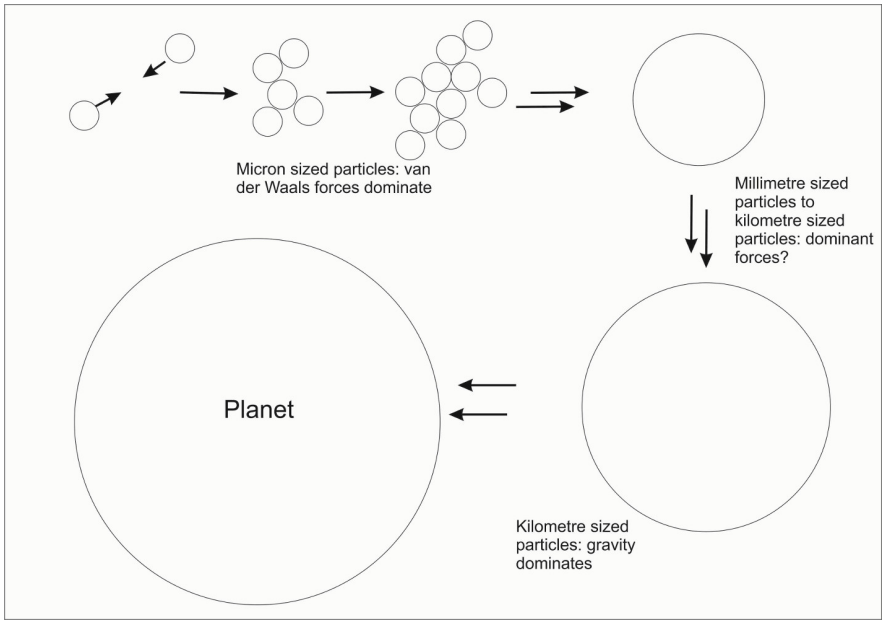

Figure 1.2: Dust aggregation leading to planet formation. Micron-sized particles will stick together by van der Waals forces and kilometre-sized bodies will stick together by gravitational attraction but it is unclear how the intermediate sized particles can stick.

Initial models of planetary formation invoked gravitational instability in protoplanetary disks, but it became apparent that this mechanism would be inhibited by turbulence in the disk (Weidenschilling & Cuzzi, 1993). The theory of planet formation by dust aggregation was first suggested by Weidenschilling (1977, 1980). This theory has now become widely accepted and has been investigated experimentally and theoretically ever since. This model is illustrated in Fig. 1.2. In this model, small, micron-sized dust particles collide and stick together, forming larger and larger particles and eventually forming a planet. Collisions between dust particles occur due to the relative velocities they possess, resulting from Brownian motion (for smaller, micron-sized particles) and gas turbulence (for larger, millimetre and centimetre-sized particles). If the collision velocities are low enough (below 1 m s^{-1} (Güttler et al., 2010; Kothe et al., 2013)), small, micron-sized particles will stick together by van der

Waals forces. It has been demonstrated that such aggregates can grow to centimetre sizes due to these interactions (Blum & Wurm, 2008; Güttler et al., 2010; Weidling et al., 2012; Kothe et al., 2013). For planetisimals (kilometre sized bodies that are the precursors of planets), gravity comes into play as the bodies are massive enough to achieve runaway growth. However, it is unclear how the centimetre-sized aggregates can grow to kilometre sizes, as van der Waals forces can no longer lead to sticking (Zsom et al., 2010).

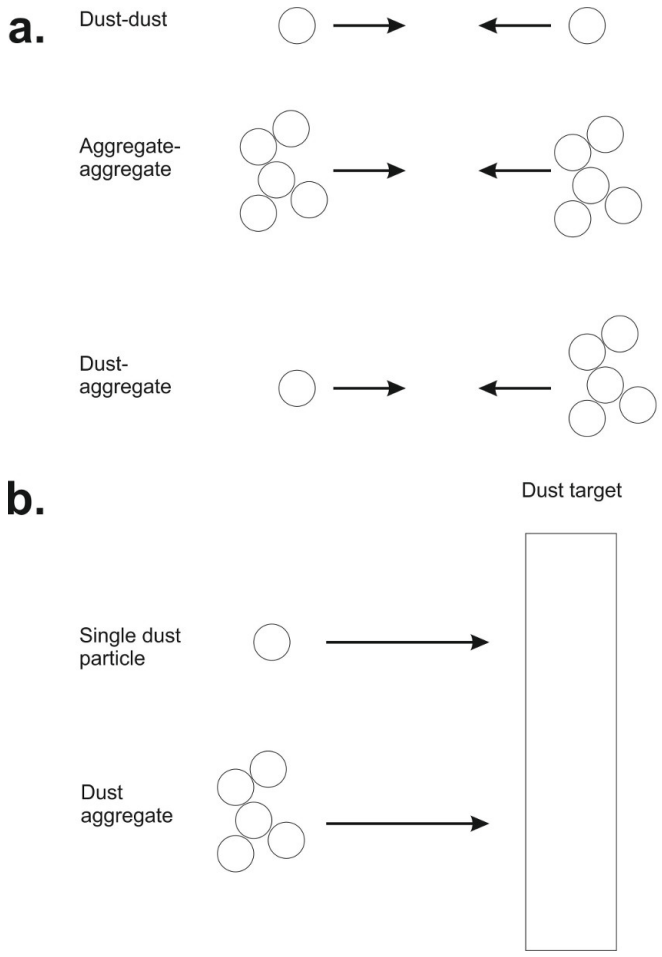

Figure 1.3: **a.** Collisions of dust particles and dust aggregates with each other. **b.** Collisions of dust particles and dust aggregates with a dust target.

Studying the collisions of silicate dust particles has been the subject of much experimental research. Collisions of both dust particles and dust aggregates have been carried out, colliding the particle or aggregate either with another particle or aggregate, or with a dust target. The collision variants are shown in Fig. 1.3. Fig. 1.3**a.** shows

collisions between two individual dust particles, two dust aggregates (created from individual dust particles) and an individual dust particle with a dust aggregate. All three collision processes simulate different types of dust aggregation between similar sized particles. Fig. 1.3**b.** shows collisions between a dust particle and a dust target, and a dust aggregate and a dust target. These collisions simulate the effect of colliding a smaller body with a much larger one. Dust collisions are achieved using a variety of techniques, but are usually conducted using free-falling particles to reproduce the low collision velocities in protoplanetary disks without gravity induced sedimentation affecting the results (see Section 2.1 of Chapter 2). It is possible to carry out some collisions in the laboratory (for example by carrying out collisions in the vertical plane, firing one particle upwards and releasing the other to fall downwards (Blum & Munch, 1993), or by dropping a particle onto a target (Blum & Wurm, 2000), or even by directing a jet of dust towards a target using a piston and rotating cog wheel (Poppe & Blum, 1997; Poppe et al., 2000b)), but most are carried out in microgravity environments, either by observing collisions occurring in a free floating dust sample (e.g. Blum & Wurm (2000); Blum et al. (2000)) or by colliding dust particles towards each other or a target using pistons (Salter et al., 2009). A full description of the need for microgravity and ways of accessing microgravity is given in Sections 2.1 and 2.2 of Chapter 2.

In a collision between dust aggregates, there are three possible outcomes: sticking, bouncing and fragmentation. The outcome partly depends on the relative particle velocities. Sticking tends to occur at low collision velocities, with increasing collision velocities leading to bouncing and then fragmentation (Güttler et al., 2010). The critical velocity for the onset of bouncing decreases with increasing particle size (Güttler et al., 2010; Kothe et al., 2013), and this is known as the "bouncing barrier". At the same time, relative particle velocities increase with particle size (Weidenschilling, 1977), making sticking less likely as particle sizes increase. Millimetre and centimetre-sized particles in protoplanetary disks have relative collision velocities on the order of 0.1 m s^{-1} (Weidenschilling et al., 1993) and it is in this size and velocity regime that bouncing tends to dominate. There has also been research carried out investigating

the effects of the material composition of micron-sized dust grain on sticking probabilities. It was found that the dust material (comparing silica, diamond, enstatite and silicon carbide) was much less important than the grain size and surface roughness, with increased surface roughness leading to increased sticking (Poppe et al., 2000a). Shape was also important, with irregularly shaped dust grains having less of a decrease in sticking probability with increasing impact velocity (Blum, 2000). However, all research to date suggests that dust particles cannot grow to kilometre sizes by a simple hit-and-stick mechanism (Blum, 2010).

1.1.3 Overcoming the "bouncing barrier"

There have been multiple investigations into effects that could overcome the "bouncing barrier" and allow the growth of larger bodies, including collisional grain charging, re-growth after fragmentation and mass transfer in collisions.

Work by Poppe et al. (2000a,b) on dust collisions showed rebounding particles returning to the target; this was thought to be caused by electrostatic forces due to collisional induced grain charging. Growth due to electrostatic forces has also been demonstrated in microgravity experiments on the International Space Station (Love et al., 2014), although these experiments were extremely basic, making these results somewhat controversial. However, electrostatic forces are only strong enough to cause growth for smaller particles and so it is unlikely that this mechanism could lead to growth of larger particles (Blum, 2010).

Some work has shown that re-growth of dust aggregates after fragmentation can occur (Wurm et al., 2001; Teiser & Wurm, 2009b), particularly when the collisions took place in the presence of a rarefied gas flow, which allowed the fragments to return to the collision target and re-accrete (Blum & Wurm, 2001). Fragmentation had previously been thought to be detrimental to particle sticking but this research shows that this is not necessarily the case, as small (submillimetre) fragments can easily stick to larger particles. However, it is not clear whether this process could lead to growth

from centimetre to kilometre sizes because of dust aggregate erosion (Schräpler & Blum, 2011; Seizinger et al., 2013).

Growth of dust aggregates has also been observed through mass transfer, where part of an aggregate breaks off and sticks to another particle (Wurm et al., 2005; Paraskov et al., 2007; Langkowski et al., 2008; Teiser & Wurm, 2009a,b; Kothe et al., 2010; Teiser et al., 2011; Windmark et al., 2012a,b; Garaud et al., 2013; Meisner et al., 2013). Growth in this way has been demonstrated at collision velocities up to 25 m s^{-1} (Wurm et al., 2005) for millimetre-sized particles which is well beyond the "bouncing barrier" (which is less than 1 m s^{-1} for particles of this size (Güttler et al., 2010; Kothe et al., 2013)). It has been suggested that the "bouncing barrier" might actually be beneficial to growth as it leaves more millimetre-sized particles to be "swept-up" by larger ones (Windmark et al., 2012a). Mass transfer can occur from a smaller particle to a larger particle (Wurm et al., 2005) or vice versa (Paraskov et al., 2007; Langkowski et al., 2008). However, as larger particles have increasing relative velocities, it is unclear whether this mechanism could lead to growth beyond centimetre sizes. Erosion of dust aggregates is also a factor that may prevent this process from producing significant growth (Schräpler & Blum, 2011; Seizinger et al., 2013).

So far, none of these effects have been able to overcome the "bouncing barrier". However, the research discussed so far has focussed on silicate dust particles, but it is known that beyond the snowline, water ice will be present. Therefore, its presence must be taken into account when considering planetisimal formation.

Another method of planet formation that has been proposed in recent years is formation via streaming instabilities (Youdin & Goodman, 2005). Streaming instabilities result from the decoupling of larger particles (millimetre-sized and upwards) from the gas of the protoplanetary disk. These particles are slowed down by friction from the gas, leading to particle "pile-ups", which have recently been observed by ALMA (Yen et al., 2014). If the particle concentrations become large enough, it has been suggested that planets could form due to gravitational instability (Johansen et al., 2007; Nagel-Vega, 2010; Johansen & Klahr, 2011; Youdin, 2011). This thesis will first investigate

whether ice particles can overcome the "bouncing barrier" by enabling particle sticking. However, if particles lose energy in collision but do not stick, this loss of energy could also contribute to increased particle concentrations, and hence planet formation via streaming and gravitational instabilities.

1.1.4 Ice in planet forming regions

Water ice is abundant in many regions in space, including the interstellar medium, cloud cores, dense clouds, protostellar regions and protoplanetary disks (Oberg et al., 2011a). The study of deuterium-to-hydrogen enrichments in recent research has demonstrated that water was present in the early solar nebula (Cleeves et al., 2014). Water ice has been observed around young stellar objects (which are the precursors of planet forming systems) in both crystalline and amorphous phases (Schegerer & Wolf, 2010). Cold water vapour has been detected in outer disk regions with Herschel and it is likely that this was produced by desorption from the surface of dust grains (van Dishoeck et al., 2011; Podio et al., 2013). Therefore, it is vital to study the collisional properties of water ice as it is possible that its presence on protoplanetary dust grains may help to overcome the "bouncing barrier".

As early as 1993, it was suggested that dust coagulation in dense clouds requires the dust grains to be coated with an ice mantle to proceed efficiently (Chokshi et al., 1993) and it is possible that the same may be true in protoplanetary disks. Ice particles have been found to have a larger rolling friction force (Gundlach et al., 2011) and reduced elasticity (Hertzsch, 2002) compared to silicate dust particles, which would make sticking in collisions more likely by increasing the threshold velocity for sticking. If the icy particles are composed of amorphous solid water (see later) instead of crystalline ice, electrostatic effects may come into play which would also increase the chances of particle sticking, as amorphous solid water can form permanent dipoles (Wang et al., 2005). In addition, recent model simulations have demonstrated that ice condensation onto dust grains could allow growth to decimetre sizes around the snow-

line (Ros & Johansen, 2013) and even to icy planetisimals if the original grains were submicrometre-sized (Kataoka et al., 2013).

It is also possible that the presence of ice could promote planet formation at the snowline indirectly. There will be a high concentration of small silicate particles along the snow line due to break up of ice aggregates drifting inwards towards the central star (Saito & Sirono, 2011). It has been proposed that this concentration of small particles would boost the formation of planetisimals at the snowline, either by these particles being swept up by larger bodies or by inducing gravitational instability (Aumatell & Wurm, 2011). Studies of micron-sized water ice particles have shown them stick at much higher collision velocities than dust particles (Gundlach & Blum, 2015). The next step is therefore to study collisions of millimetre and centimetre-sized ice particles to see if they can overcome the "bouncing barrier". Previous research on ice particle collisions is described in Section 4.1 of Chapter 4.

1.1.5 Ice in planetary ring systems

While the main focus of this thesis is ice in the context of planet formation, ice collisions are also relevant in planetary ring systems. The most well known planet with a ring system is Saturn, where the rings consist of small icy bodies (Cuzzi & Pollack, 1978; Cuzzi et al., 1980, 2010) between 1 cm and 10 m in size (Zebker et al., 1985). Rings are also present around Jupiter, Uranus and Neptune, but the recent detection of two small, dense rings around the Centaur (10199) Chariklo (Braga-Ribas et al., 2014; Duffard et al., 2014), shows that ring systems are not only present around giant planets. The rings of Saturn have complex dynamics; resonances between ring particles and nearby moons are counteracted by low velocity collisions between the ring particles themselves. The particles have typical relative collision velocities of well below 1 cm s^{-1} (Esposito, 2002; Colwell et al., 2009) when the rings are unperturbed, but gravitational perturbations may considerably raise the particle velocities. The kinetic energy dissipated in these collisions determines the ring stability (Salo et al., 2001;

Schmidt et al., 2001). Knowledge of collisional properties is therefore vital for modelling ring structure, wakes and instabilities, as well as the well confined ring heights (Colwell et al., 2006, 2007; Hedman et al., 2007; Thomson et al., 2007).

1.2 Amorphous solid water

1.2.1 Water ice structures

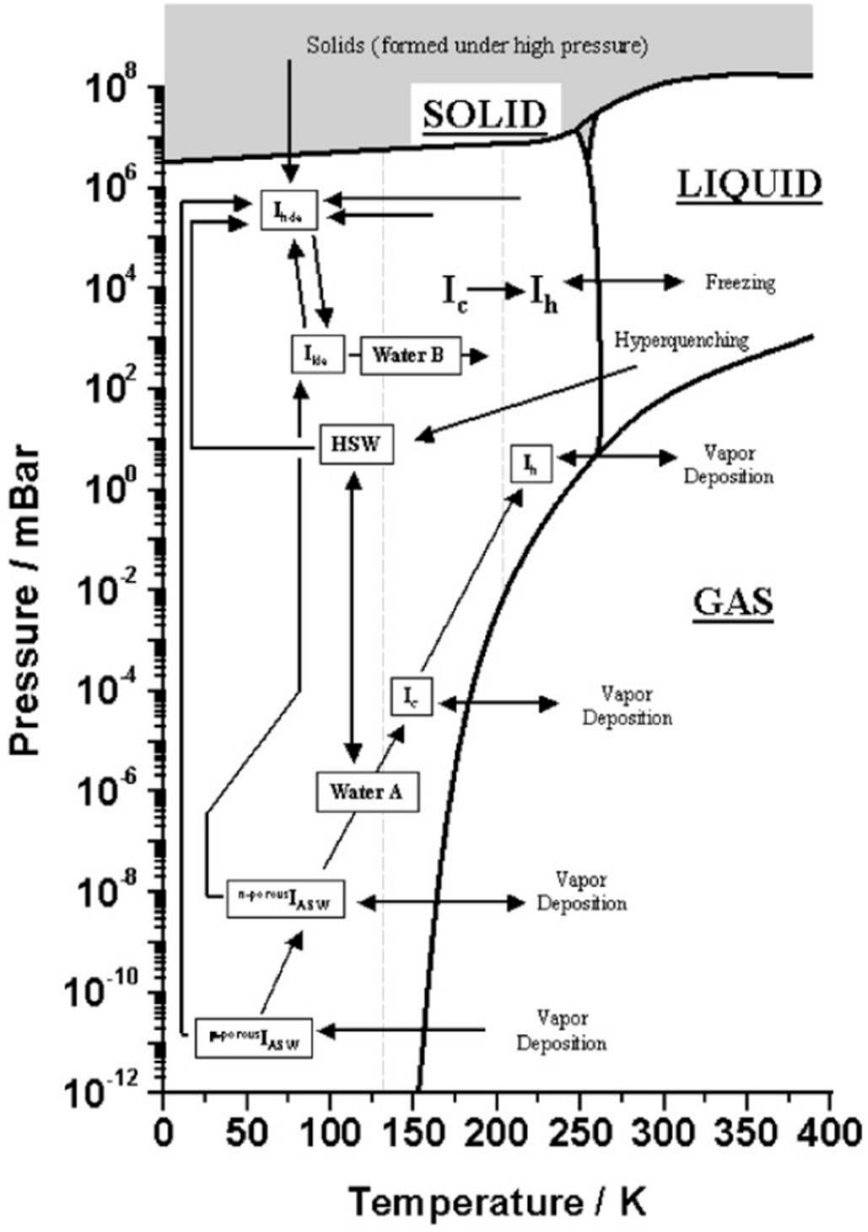

Figure 1.4: The low temperature phase diagram of water. Figure taken from Ehrenfreund et al. (2003).

Studies of water ice have identified at least 15 different structures (Salzmann et al., 2006). Hexagonal crystalline ice (I_h) is the most common form of ice found on Earth and is formed by freezing liquid water and by vapour deposition at temperatures above 150 K and pressures around 1 mbar. Water ice can also have a cubic structure (I_c) when formed by vapour deposition at temperatures between 130 K and 150 K and pressures around 10^{-4} mbar, or on warming some amorphous forms of ice. Other crystalline structures of water ice can be formed at higher pressures. Water ice can also exist in multiple amorphous forms. Rapid freezing of liquid water droplets (less than 3 μm in size) produces hyper-quenched glassy water (HGW). The droplet size must be small enough to freeze water molecules in their "liquid" positions before they can rearrange into the more thermodynamically stable crystalline structure; for this reason, rapid freezing of water droplets of greater sizes will not produce HGW (Mayer & Brüggeller, 1982; Hallbrucker et al., 1989b; Angell, 2004). High density amorphous ice (HDA) is formed under pressures of around 10^6 mbar from hexagonal or cubic ice or HGW at 77 K.

These forms of water ice are shown on the low temperature phase diagram of water in Fig. 1.4. Of particular interest is the "Water A" phase through which ASW passes to form I_c. This transition is known as the glass transition and it has been suggested that this transition involves a viscous liquid (Smith & Kay, 1999). The nature of the glass transition is controversial (see Section 8.1 of Chapter 8 for a more detailed discussion), but if a liquid-like state is involved, sticking of ice particles may be more likely to occur during this transition as sintering could occur, binding ice particles together.

1.2.2 Importance of amorphous solid water in space

Amorphous solid water has been observed in a wide variety of environments in space. It has been detected on interstellar dust grains (Leger et al., 1979), on comets (Patashni et al., 1974; Klinger, 1981; Smoluchowski, 1981; Delsemme, 1983) and planetary satellites (Smoluchowski, 1978), in star-forming regions (Smith & Wright, 2011) and

around young stellar objects (Schegerer & Wolf, 2010). On interstellar dust grains, it provides a surface on which a rich chemistry can take place (Takahashi, 1999; Manico et al., 2001; Raunier et al., 2003; Vidali et al., 2006; Fillion et al., 2011). It can also trap gases within its pores, allowing these gases to be retained on the dust grain well above their desorption temperatures (Collings et al., 2003b). It has been suggested that amorphous solid water may play a role in planet formation (Ehrenfreund et al., 2003), a suggestion that warrants further investigation given its ability to increase sticking by electrostatic forces (Wang et al., 2005).

1.2.3 Formation of amorphous solid water

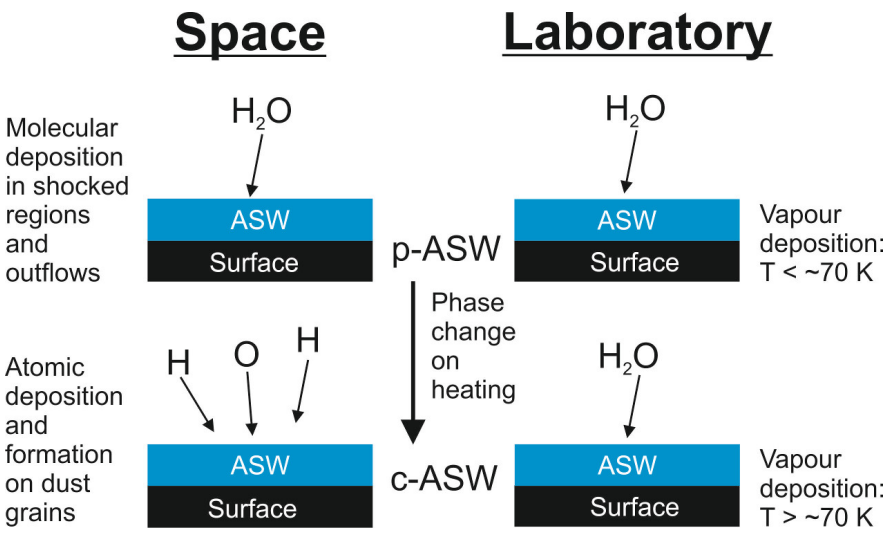

Figure 1.5: Formation of amorphous solid water in space (by formation on dust grains and vapour deposition from shocks and outflows) and in the laboratory (by vapour deposition). The mode of formation/deposition affects the porosity of the ice, with compact amorphous solid water (c-ASW) being formed by chemical reactions on the grain surface or by depositing at temperatures above ∼70 K and porous amorphous solid water (p-ASW) being formed by vapour deposition at temperatures below ∼70 K.

The different forms and formation routes of ASW are shown in Fig. 1.5. In space, ASW can form by grain surface reactions (Ioppolo et al., 2008; Oba et al., 2009; Cuppen et al., 2010); it is also possible that it can form by vapour deposition through sputtering of water from shocks and outflows or in dark clouds (Williams et al., 1992; Papoular, 2005). In the laboratory, it is can be formed by vapour deposition; at low

temperatures (around 10 K) this produces a very porous ASW (p-ASW) (Stevenson et al., 1999; Kimmel et al., 2001) which undergoes a phase change to a more compact ASW (c-ASW) between ∼30 and ∼70 K (Jenniskens & Blake, 1994; Horimoto et al., 2002; Collings et al., 2003b). Vapour deposition at higher temperatures also produces c-ASW. The more compact form of ASW still displays significant microporosity (Horimoto et al., 2002; Collings et al., 2003b; Isokoski et al., 2014).

The extent of porosity in ASW could have far reaching effects. A more porous ice would have a greater surface area available for surface chemistry and would be capable of trapping a higher volume of gas. Previous research has shown increased porous dust aggregates are more likely to stick than non-porous ones (Langkowski et al., 2008) and that increased porosity translates to increased sticking for centimetre-sized ice particles (Shimaki & Arakawa, 2012), so it is possible that the porosity of ASW could affect the sticking of icy particles in planet-forming regions. It is therefore vital to investigate the porosity of ASW.

1.2.4 Porosity and pore collapse of amorphous solid water

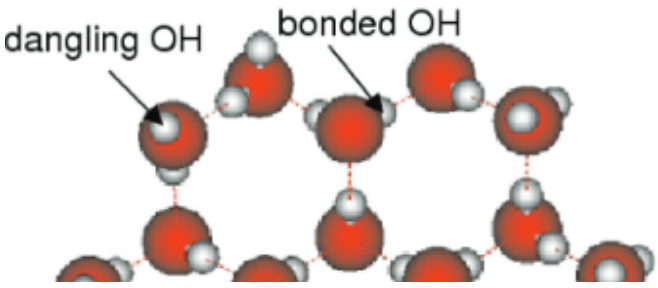

Figure 1.6: Dangling and bonded OH bonds in hexagonal ice. These dangling bonds can also be present in amorphous solid water. Figure adapted from Al-Halabi et al. (2004).

The porosity of amorphous solid water has been studied using a wide variety of experimental techniques, all of which have demonstrated pore collapse when the ice is heated. One of the most well known techniques is to study dangling OH bonds using infra-red spectroscopy (Buch & Devlin, 1991; Zondlo et al., 1997; Schriver-Mazzuoli et al., 2000). Dangling OH bonds occur at the surface of water ice where OH bonds

do not participate in hydrogen bonding with the bulk ice (see Fig. 1.6). The presence of these dangling bonds has been used to infer porosity, and their disappearance when the ice is heated has been used to infer collapse of the pores (Zondlo et al., 1997). In addition, the fact that dangling OH bonds are not observed in interstellar regions has been used to suggest that ices in these regions are non-porous (e.g. Palumbo (2006)). However, recent work has shown that a lack of dangling OH bonds does not necessarily imply a lack of porosity (Isokoski et al., 2014), casting doubt on this method of studying the porosity.

The adsorption of molecules such as CO, N_2 and CH_4 into the pores (Raut et al., 2007) and the trapping of such molecules within the pores (Ayotte et al., 2001; Horimoto et al., 2002; Collings et al., 2003b; Gálvez et al., 2008) has also been used to investigate porosity. However, non-adsorption into the pores of the ASW does not necessarily imply a lack of porosity, as the ice could contain pores that are closed to the vacuum interface, such that no gas can enter. Support for this is given by Collings et al. (2003b), where some CO remained trapped within the ice until it crystallised at 140 K, well above its expected desorption temperature at 20-60 K. This indicates that the pores closed during this temperature range, thus preventing the CO from desorbing. A similar phenomenon was observed by Horimoto et al. (2002), where the ice was no longer able to trap molecules when the ice was annealed above 60 K. Desorption of D_2 from both compact and porous ices has also been studied, with desorption from porous ices happening more slowly due to the ability of D_2 to diffuse into the pores. Once again, this method can only observe open pores. Therefore, studying ASW porosity through gas adsorption, trapping and desorption is somewhat limited.

Positron annihilation spectroscopy is a novel technique for investigating ASW porosity. The basic premise is that positrons (the antiparticles of electrons) will annihilate on encounter with electrons, producing gamma rays that can be detected. If pores are present within a material, the positrons will travel for longer before encountering an electron and annihilating. This technique has the huge advantage of not only being able to observe closed pores as well as open ones but to distinguish between

them and give information about pore clustering, pore collapse and crystallisation (Wu et al., 2010, 2011; Townrow & Coleman, 2015). However, this technique cannot give information such as pore size or shape.

Porosity has also been studied by studying thickness changes in ASW films with temperature (Bossa et al., 2012), also demonstrating pore collapse on heating. Once again, this technique cannot give information on pore sizes and shapes.

More recently, neutron scattering has been used to study pore collapse in amorphous solid water (Mitterdorfer et al., 2014). This technique is able to give information on pore size, shape, spacing and surface roughness, as well as the specific surface area of the ice. Mitterdorfer et al. (2014) found that the pores are cylindrical in shape, with radii of 10-12 Å. When heated, they collapse suddenly from cylinders to platelets between temperatures of 120-140 K, depending on the method of ice deposition. As neutron scattering is able to provide such a wealth of information on ice porosity, it is this technique that has been chosen for studying the porosity and pore collapse of ASW in this thesis, building on the work of Mitterdorfer et al. (2014). Neutron scattering is described in more detail in Chapter 6.

1.3 This thesis

This thesis investigates both the collisional properties of water ice in planet-forming regions and the structural properties of such ice, specifically the porosity and pore collapse. This chapter has provided a background of the current understanding on these subjects. The rest of the thesis is structured in two parts, with the first part (Chapters 2, 3, 4 & 5) dealing with ice collisions and the second part (Chapters 6, 7, 8 & 9) dealing with ice porosity.

Chapter 2 describes the experimental apparatus used for conducting ice collisions on board parabolic flights. The parabolic flight environment allows the collisions to be carried out under microgravity; the reasons for the use of microgravity and the choice of this particular microgravity platform are also presented in this chapter. The analysis

of the resulting video images of the ice collisions is complex. Chapter 3 presents the methods for tracking the particles and extracting collisional information, which were developed by the current author from methodology used by other researchers working with the same apparatus. A worked example for extracting collisional information is given in Appendix A.

Chapters 4 and 5 are results chapters. Chapter 4 describes the results of experiments colliding millimetre-sized ice particles composed of pure water ice with each other (i.e. particle-particle collisions). Chapter 5 describes the results of colliding centimetre-sized ice particles composed of either pure water or water with 5% methanol or formic acid, either with a pure ice target or with each other (i.e. both particle-target and particle-particle collisions). All ice particles were crystalline. The aim of these experiments was to see if the collisions would result in particle sticking (thereby providing a way to overcome the "bouncing barrier"), how the energy was dissipated in collision, and whether the impact velocity, impact parameter (describing how head-on/glancing the collision is, see Chapter 3), temperature or particle composition affected the collisional properties.

In the second part of the thesis, Chapter 6 describes the technique of neutron scattering and its suitability for studying the porosity of amorphous solid water. The ISIS neutron source, the NIMROD instrument on which the experiments were conducted and the experimental apparatus used are also presented here. Chapter 7 explains the parameters that can be extracted from the neutron scattering data and explains the methods of extraction. The Python and IDL code used to extract these parameters is given in Appendix B.

Chapters 8 and 9 are results chapters. Chapter 8 describes the results of an experiment investigating the pore collapse of ASW grown at 77 K, shedding light on both the process of pore collapse and the glass transition of ASW. Chapter 9 investigates the growth and pore collapse of ices grown in situ on the beam line at temperatures of $\sim$50 K and $\sim$17 K, to see what effect, if any, the different growth temperatures have on the porosity and the pore collapse. This study also functions as a proof-of-concept

experiment for the in situ growth apparatus.

Finally, Chapter 10 summarises the results of this thesis, drawing conclusions and commenting on their relevance to planet formation. Suggestions for future work are also presented.

Chapter 2

Experimental methods I: low velocity ice particle collisions

Understanding low velocity collisions of millimetre and centimetre-sized ice particles is of great astronomical interest, both in the context of planetesimal formation and planetary ring systems. A key question for planetesimal formation is whether the ice collisions result in sticking; however, if the collisions result in bouncing, the focus is on how the energy is dissipated. The latter scenario is also the focus for understanding planetary rings. The results of collisional experiments are used to inform attempts to model planetesimal formation and collisional processes in planetary ring systems. To access the low collision velocities of interest without gravity induced sedimentation affecting the results, collisions must be conducted under microgravity conditions. This chapter discusses different ways of accessing microgravity and why parabolic flights were chosen as a platform for these experiments. The experimental set up and how it was designed and adapted for use in this environment is also presented. The collision experiments using this set up (the results of which are detailed in Chapters 4 and 5) were carried out prior to the start of this PhD but the data was reduced and analysed by the current author.

2.1 Introduction

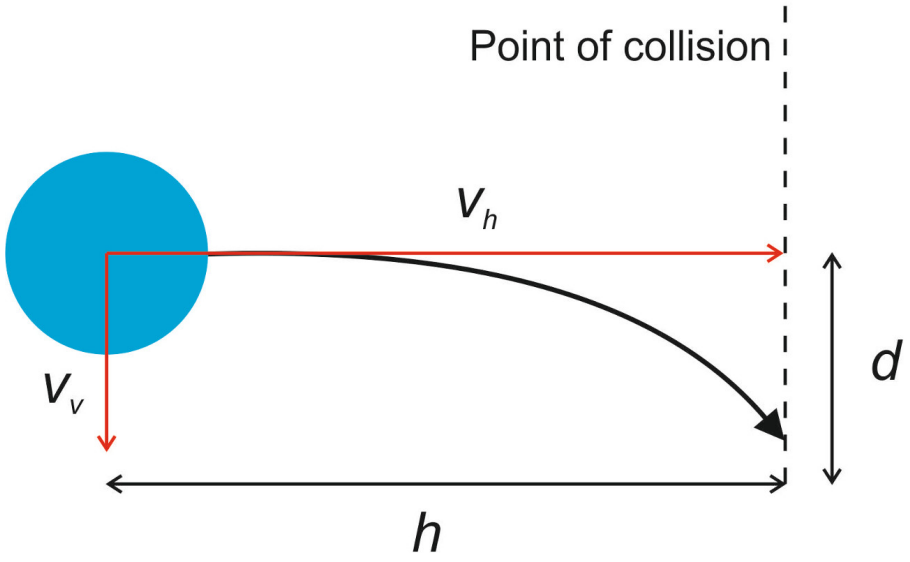

Figure 2.1: A particle fired from a piston has a velocity with horizontal (v_h) and vertical (v_v) components that cause it to follow a curved trajectory. The vertical distance the particle travels through (d) depends on the acceleration due to gravity (G) and the horizontal velocity component.

Particle collisions at relative velocities $\ll 1$ m s^{-1} cannot be realised in a laboratory environment without gravity having a significant effect on the collisional outcomes (Salter et al., 2009). However, as discussed in Chapter 1, the collision velocities relevant in protoplanetary disks are on the order of 0.1 m s^{-1} (Weidenschilling et al., 1993; Weidenschilling, 1997). When attempting to perform collisions at these lower collision velocities, the time spent in transit before collision is longer, allowing the particles to fall a greater distance vertically before collision (see Fig. 2.1).

The time, t, for the particle to travel a horizontal distance, h, is given by:

$$t = \frac{h}{v_h} \tag{2.1}$$

where v_h is the horizontal component of the velocity. The vertical component of the velocity, v_v, increases by $G\,\mathrm{m\,s^2}$ where G is the acceleration due to gravity (equal to g under normal Earth gravity conditions). Therefore the vertical component of the

velocity is given by:

$$v_v = Gt \tag{2.2}$$

Substituting Equation 2.1 gives:

$$v_v = \frac{Gh}{v_h} \tag{2.3}$$

v_v can also be expressed in terms of the acceleration due to gravity and the vertical distance traveled by the particle (d):

$$v_v = \sqrt{2Gd} \tag{2.4}$$

Combining Equations 2.3 and 2.4, d is given by:

$$d = \frac{Gh^2}{2v_h^2} \tag{2.5}$$

Therefore, reducing the horizontal velocity will increase this distance and decreasing the acceleration due to gravity will reduce it.

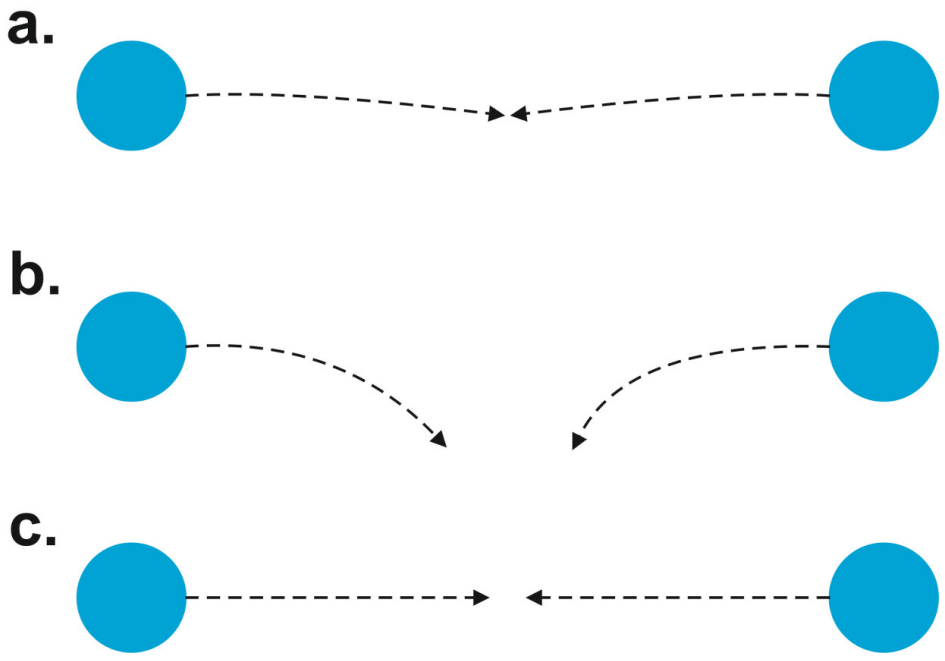

Figure 2.2: **a.** Collision of particles at high velocity under normal Earth gravity conditions. **b.** Attempted collision of particles at low velocity under normal Earth gravity conditions. **c.** Collision of particles at low velocity under microgravity conditions.

If the velocities are too low under normal gravity conditions, the particles will fall to the bottom of the collision volume before they are able to collide. This is known as gravity induced sedimentation (see Fig. 2.2**a.** and **b.**). Gravity has also been shown to cause compaction of dust aggregates (Blum & Wurm, 2000). Therefore, to access the lower collision velocities and reduce gravity induced compaction, it is necessary to perform collisions under microgravity conditions. A microgravity environment is one within which the pull of gravity is very weak. There are several different ways of creating a microgravity environment on or close to the Earth which all involve a system in free-fall. Different ways of accessing microgravity are described, compared and contrasted in Section 2.2, where it is also explained why parabolic flights were chosen for these experiments. Within these environments, objects experience very low g forces, between $10^{-2}g$ to $10^{-6}g$ where $1\,g$ is the force of gravity experienced on Earth. This significantly reduces the vertical distance traveled by the particles before collision and makes low velocity collisions possible (see Fig. 2.2**c.**).

Ice particle collisions take place in protoplanetary disks (and in planetary ring systems) beyond the snowline, where temperatures are below 150 K and pressures are around $10^{-2} - 10^{-3}$ mbar (Weidenschilling et al., 1993). It is necessary to replicate these temperatures and pressures as far as possible in the experimental collisions of ice particles. Achieving these temperatures requires cryogenic cooling which presents a significant experimental challenge as cryogens are not permitted on board the aircraft. Achieving the correct pressures is relatively straightforward with appropriate pumps. However, the experimental set up described in this chapter is operated at lower pressures, around 10^{-5} mbar, to reduce water condensation on the particle surfaces. The experimental set up, its adaptations to parabolic flight and its operation are discussed in Section 2.3.

2.2 Accessing microgravity

Table 2.1: Comparison of different microgravity platforms in terms of g levels, duration of microgravity and whether the experiment can be manned.

Platform	Microgravity levels	Duration	Manned/Unmanned
Drop tower	$10^{-3}g$ - $10^{-6}g$	4-10 s	Unmanned
Sounding rockets	$10^{-4}g$	6-13 mins	Unmanned
International Space Station	$10^{-4}g$ - $10^{-6}g$	Continuous	Manned
Parabolic flight	10^{-2} - $10^{-3}g$	22 s	Manned

The requirement of the ice collision set up is that it must be able to facilitate low velocity (on the order of 0.10 m s^{-1}) ice collisions at temperatures below 150 K. A microgravity environment is required to access these low collision velocities. Microgravity environments available to researchers include drop towers, sounding rockets, the International Space Station and parabolic flights. These are compared in Table 2.1 and described in more detail in the following sections. Drop towers and the International Space Station have the highest levels of microgravity (lowest g forces) whereas parabolic flights have the lowest. Particle collisions have been carried out in drop tower experiments (e.g. Blum & Wurm (2000, 2001); Langkowski et al. (2008); Heißelmann et al. (2010)) and in sounding rocket experiments (e.g. Blum et al. (2000)), but as such experiments must be unmanned, these experiments focussed on collisions of ensembles of particles. It is difficult to obtain an unobstructed view of individual particle collisions in such experiments (particularly in drop tower experiments where the duration of microgravity is short, so the ensemble must incorporate a large number of particles in a small volume to ensure a useful number of collisions takes place within the experimental timescale (Salter et al., 2009)), so, to complement these studies, the experimental set up described in this chapter was built to study individual ice collisions. As studying individual collisions complicates the experiment, it requires researchers to operate it and so parabolic flights were chosen as the microgravity platform. The different microgravity platforms are described in greater detail in the following sections.

2.2.1 Drop tower

A drop tower is a vertical shaft within which a capsule can be dropped, providing microgravity conditions within the capsule. The levels of microgravity provided can range from $10^{-3}g$ to $10^{-6}g$ depending on the conditions within the tower, e.g. higher levels of microgravity (lower g forces) can be accessed if the tower is evacuated to reduce air drag. The duration of microgravity varies depending on the height of the tower but is usually the order of a few seconds. As an example, the ZARM drop tower situated in Bremen (Germany) is 146 m tall and can provide 4.74 s of microgravity if the capsule is dropped from the top of the tower. A newer feature of this tower is the catapult feature, where the capsule is fired upwards from a chamber below the bottom of the tower and allowed to fall; this method provides up to 9.3 s of microgravity. Both timescales are a little short as far as ice collisions are concerned, but more importantly, it is not possible for researchers to be present within the capsule to operate the experiment and so all experiments carried out in this way must be fully automated and require no intervention during the drop. This reduces the complexity of experiment it is possible to carry out and hence this platform is not suitable for conducting individual ice collisions.

2.2.2 Sounding rockets

Sounding rockets are sub-orbital rockets (i.e. they do not enter orbit around the Earth) that create a microgravity environment by following a parabolic flight path. The sounding rockets used by ESA give between 6 and 13 minutes of microgravity with g levels around $10^{-4}g$. While the microgravity duration is far longer than can be achieved in a drop tower, the quality of microgravity is somewhat poorer. As with a drop tower, researchers may not fly on the rocket, so experiments have to be unmanned, again reducing the complexity of experiments that can be carried out in this manner. Once again, this means that this platform is not suitable for conducting individual ice collisions.

2.2.3 International Space Station

The first component of the International Space Station (ISS) was launched in 1998 and it has remained in a low Earth orbit of between 300 and 400 km above sea level ever since. Microgravity levels are between $10^{-4}g$ and $10^{-6}g$. The huge advantages to carrying out experiments on the ISS are that experiments can be manned by the station crew, and the duration of microgravity is very long indeed, removing many of the time restrictions of other methods of accessing microgravity. However, due to the training needed and restrictions on becoming an astronaut, often researchers cannot operate their own experiments. Demand for experiment time on the ISS is very high, meaning that despite the advantages, this platform is inaccessible to many researchers.

2.2.4 Parabolic flight

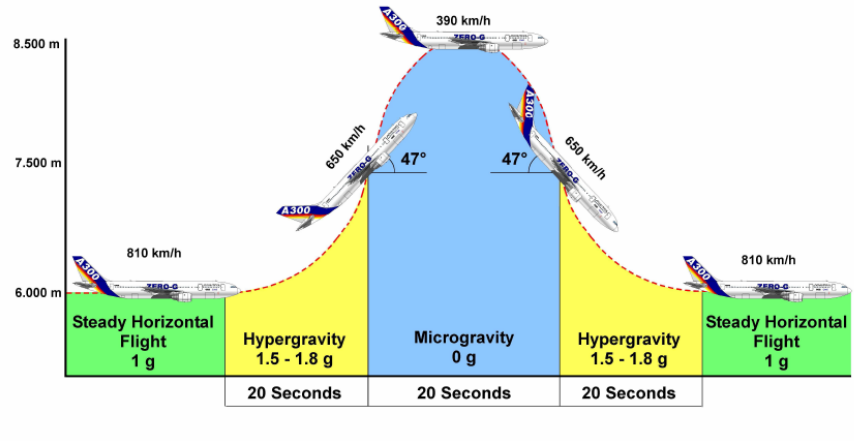

Figure 2.3: Parabolic flight manoeuvre. Each parabola includes two periods of hypergravity either side of a 22 s period of microgravity as the plane goes over the top of the parabola. *Image credit: Novespace*

Parabolic flight makes use of specially adapted aeroplanes following a parabolic flight path (Fig. 2.3). The aircraft flies horizontally and then climbs for around 20 seconds. When an angle of around 47° is reached, the engine level is reduced to the minimum required to compensate for air drag and the plane follows a free fall parabolic trajectory, giving rise to approximately 22 seconds of microgravity. When the plane reaches 47° again, it "pulls out" to horizontal flight. This procedure is repeated 30

times in one flight. Microgravity levels achieved by this method are typically between $10^{-2}g$ and $10^{-3}g$. While the quality of microgravity is the poorest of all the platforms discussed, parabolic flights offer a huge advantage in that researchers may fly with and operate their own experiments - the only requirement is that a person is generally fit and healthy. The microgravity duration of 22 s is long enough to perform at least one ice collision with the experimental set up described later in the chapter (and in some cases more). There are 31 parabolas available per flight, and three flights available to an experiment per campaign. With at least 93 collision attempts possible, this allows a significant amount of data to be collected. Hence this platform was selected for performing individual ice collisions.

Performing ice collisions during a parabolic flight presents significant experimental challenges. The experimental set up and how it is adapted to parabolic flight restrictions is detailed in the next section.

2.3 Experimental set up for ice collisions onboard parabolic flights

The experimental set up was purpose-built for conducting and observing individual, head-on collisions on parabolic flights and is described in detail by Salter et al. (2009). The following description focuses on the collisions of ice particles at cryogenic temperatures, although the set up has also been used to study dust collisions at higher temperatures. Fig. 2.4 shows schematics of the experimental set up in two different configurations. In brief, the set up consists of a rotating particle storage system (or colosseum) that is kept cold (between 77 and 160 K), enclosed within a vacuum chamber. Collisions are initiated by firing two diametrically opposed pistons. Collisions can be particle-particle collisions (configuration 1 in Fig. 2.4**a**) or particle-target collisions (configuration 2 in Fig. 2.4**b**). The components of the system are discussed in detail in the following sections.

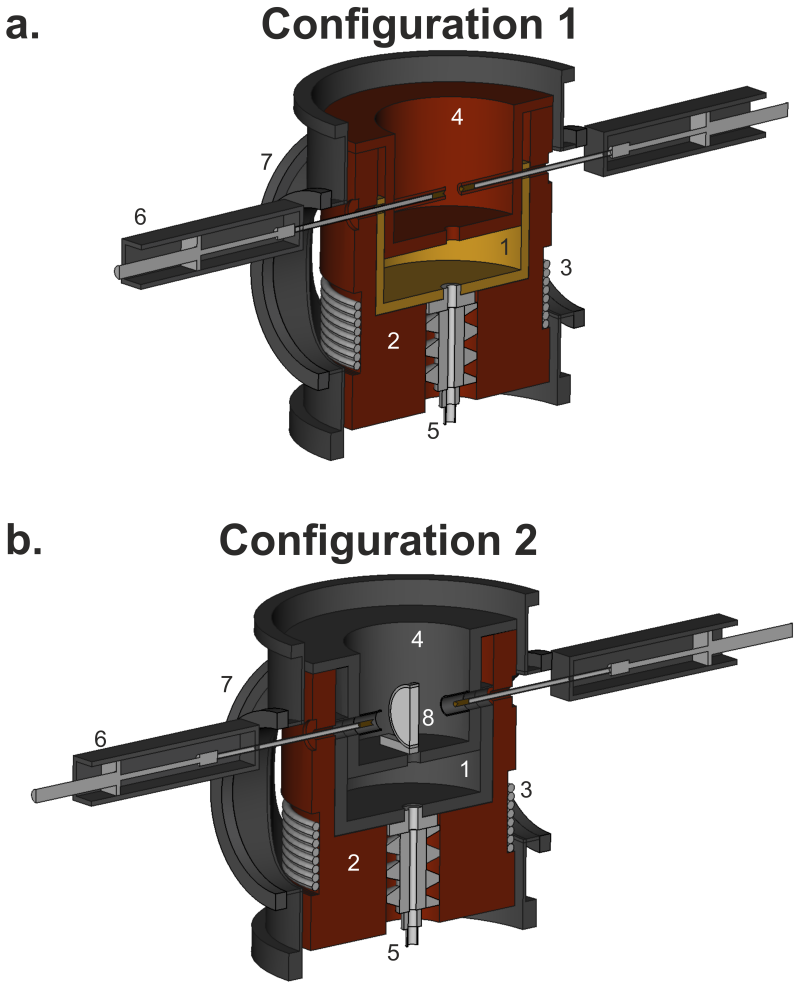

Figure 2.4: Computer aided design (CAD) schematic of the experimental set up in the two configurations relevant to this thesis: **a.** configuration 1 for millimetre-sized ice collisions and **b.** configuration 2 for centimetre-sized ice collisions with an ice target. The ice particles are stored in a rotating particle storage device or colosseum (1) made from copper (configuration 1) or aluminium (configuration 2). This sits on top of a 45 kg copper block (2) which acts as a heat sink, keeping the system cool during flight. The system is cooled by passing liquid nitrogen through a cooling ring (3) prior to take-off. The particles are contained within the colosseum with a U-shaped copper (configuration 1) or aluminium (configuration 2) cryo shield (4). The colosseum is rotated (5) to line up two particles with diametrically opposed pistons (6) and a collision is initiated. The set up is enclosed within a vacuum chamber (7). In configuration 2, a removable ice target (8) can be attached in the centre of the collision volume to allow particle-target collisions to take place. This figure is adapted from those appearing in Hill et al. (2015a) and Hill et al. (2015b).

2.3.1 Particle storage

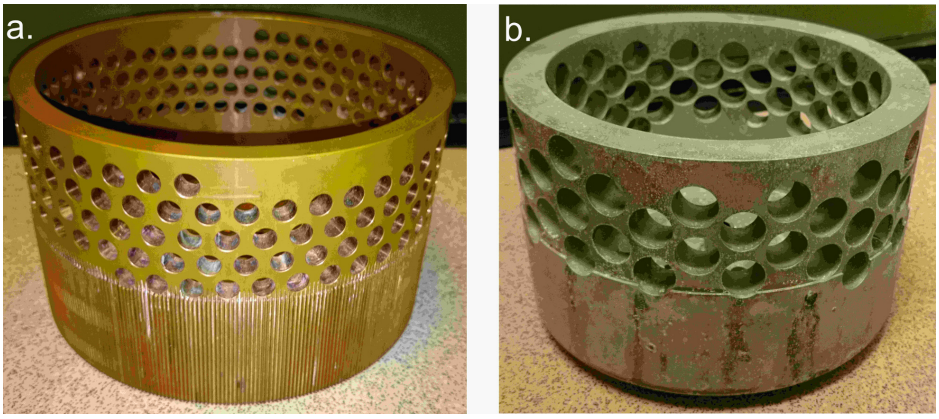

Figure 2.5: **a.** Copper colosseum for storage of millimetre-sized particles in configuration 1. **b.** Aluminium colosseum for storage of centimetre-sized particles in configuration 2.

The ice particles are stored in a cylindrical storage device, or colosseum. The colosseum has holes drilled in it in a double-helix pattern, creating particle storage compartments such that each compartment is directly opposite another. This allows two opposing particles to be fired towards one another (see Section 2.3.4). In configuration 1 is is possible to collide millimetre-sized ice particles and in this case, a copper colosseum with 180 holes of 8 mm in diameter is used (Fig. 2.5**a.**). Configuration 2 makes use of an aluminium colosseum to store 64 ice particles in compartments of 16 mm in diameter (Fig. 2.5**b.**). A U-shaped cryo shield made of copper (configuration 1) or aluminium (configuration 2) is placed over the colosseum. This protects the particles from radiative heating and keeps them inside their storage compartments.

In both cases, the colosseum can be manually rotated via a connection to a brass cork-screw system which is in turn connected to a hand wheel situated outside the vacuum chamber. Prior to each collision, the colosseum is rotated using this hand wheel until two particle storage compartments are aligned with two guiding tubes attached to the U-shaped cryo shield leading into the collision volume through which the pistons pass. This is achieved by aligning a third particle storage compartment by eye with an additional hole drilled into the copper block within which the colosseum sits (by looking through a viewing window into the vacuum chamber). This hole is positioned such

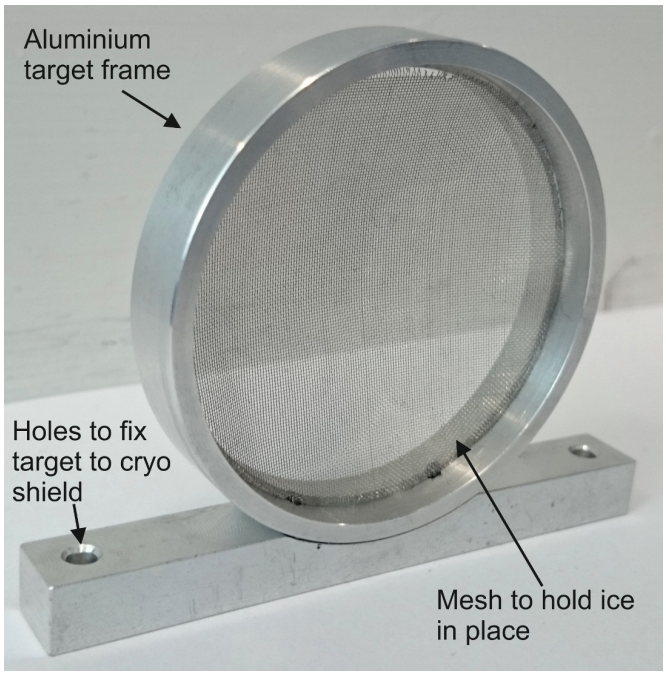

Figure 2.6: .
Aluminium target frame for ice target. The mesh within the frame helps to keep the ice in place. The target is fixed to the bottom of the cryo shield with screws.

that when a particle storage compartment is aligned with it, two other particle storage compartments are aligned with the pistons and the guiding tubes into the collision volume.

In configuration 2, it is possible to attach a removable target to the base of the cryo shield (Fig. 2.6). Colliding particles with a target simulates collisions between a small particle and a much larger one. The target frame is made of aluminium and is 52 mm in diameter and 10 mm thick. The target is composed of pure water ice which is held within the target frame by a circular mesh within the centre of the frame. The target can be fixed in multiple different orientations to vary the impact angle of the collision. This is illustrated in Section 3.3.1.

2.3.2 Cooling and cryogenic operation

To operate the experiment at cryogenic temperatures requires cooling with liquid nitrogen. However, liquid nitrogen is not permitted on board the aircraft for safety reasons. To maintain cryogenic temperatures throughout the course of a flight, the set up incor-

porates a 45 kg copper block (that acts as a thermal reservoir) on which the colosseum sits. Copper has a high heat capacity per unit volume and acts as a heat sink, slowing down the warm up of the system. Before each flight, the system is passively cooled to temperatures of around 77 K by passing liquid nitrogen through a copper cooling tube that winds around the thermal reservoir. This conductively cools the copper block, colosseum, U-shaped cryo shield and the pistons. After the particles are loaded (see Section 2.3.3), the chamber is evacuated to a base pressure of around 10^{-5} mbar using a turbomolecular pump backed by a membrane pump. While this is lower than the pressures expected in protoplanetary disks (see Section 1.1.1 of Chapter 1), it is necessary to prevent water condensation within the chamber as water would dominate the vacuum at higher pressures. The vacuum in planet-forming regions is likely to be dominated by hydrogen gas (e.g. Carmona et al. (2008)), and so this compromise has been taken to remove the effect of water condensation on the experiments.

Just before the flight, the flow of liquid nitrogen is stopped and the experiment is loaded onto the aircraft. Eight K-type thermocouples positioned at different locations within the chamber are used to measure the temperature rise over the course of the flight. Fig. 4.16 (Section 4.4.4 in Chapter 4) shows the typical temperature rise over the course of a flight.

2.3.3 Particle loading

A surface of condensed water vapour (sometimes described as frost) on the surface of an ice particle can make the collision significantly more inelastic (Hatzes et al., 1988). Such condensation is unlikely to occur in protoplanetary regions and so it is necessary to prevent it as far as possible during the course of the experiments, so as to obtain the most relevant results. During flight, water condensation is prevented by the low pressures and temperatures within the chamber. When the chamber is evacuated to a pressure of 10^{-5} mbar and the copper thermal reservoir is cooled to 77 K, the copper acts as a cryopump for any remaining water vapour. This leaves the actual vacuum

in the chamber dominated by H_2, CO and N_2 gas (Fraser et al., 2002). However, it is also important to reduce the possibility of water condensation during the loading of the particles into the colosseum.

Particles are created by freezing water with liquid nitrogen or freezing water in spherical moulds in a standard kitchen freezer (see Chapters 4 and 5 for more details on particle creation). After creation, the particles are placed one by one into a container of liquid nitrogen. The liquid nitrogen is allowed to quiesce until the liquid and icy particle are in thermal equilibrium before the next particle is added. Once all the particles have reached liquid nitrogen temperatures, the container is placed within the centre of the colosseum, which has been pre-cooled to liquid nitrogen temperatures as described in Section 2.3.2. The particles are placed into their storage compartments using tweezers that have been cooled in liquid nitrogen. Once all the particles have been loaded, the U-shaped cryo shield is fixed in place and the chamber is closed and evacuated. This occurs while the ice particles are still outgassing liquid nitrogen and this effectively prevents water condensation onto the surfaces of the particles. The results of Chapters 4 and 5 show this procedure to be robust (see discussion in Section 4.4.4).

2.3.4 Particle acceleration

Once the colosseum is aligned as described in Section 2.3.1, a collision is initiated using the piston assembly. In configuration 1, the pistons are hydraulically driven; for configuration 2, this system was replaced by a master-and-slave dc motor combination. The only practical difference between the two systems is that the latter provides better velocity control, giving access to lower collision velocities. The pistons are composed of a hollow, stainless steel rod with piston tips made of gold coated copper. The gold coated copper provides a large thermal conductivity and heat capacity. The piston tips are retracted into the outer edge of the copper block between experiments and are passively cooled by being in this cold environment (see Fig. 2.7). This prevents the piston tips from inducing particle heating (and hence surface melting) during their

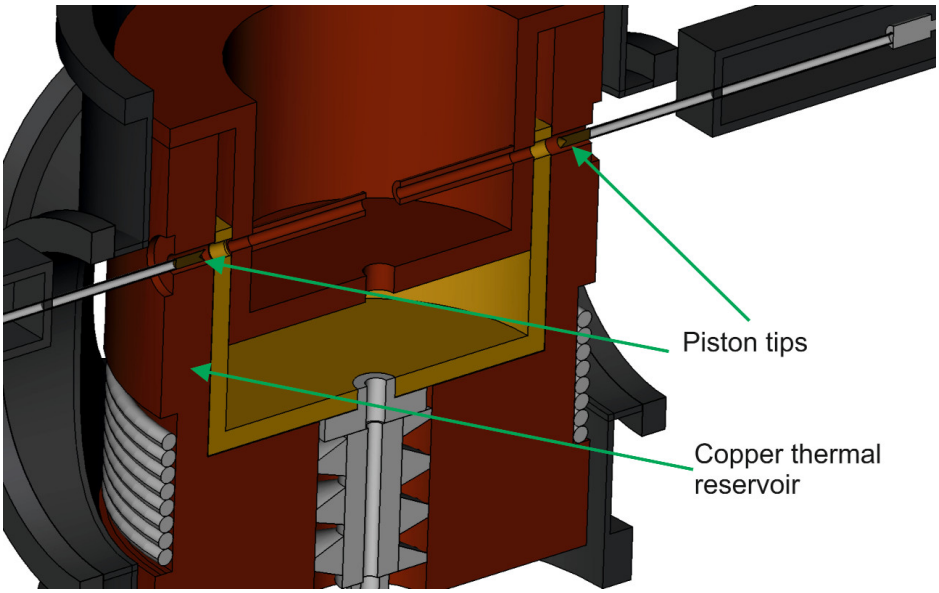

Figure 2.7: Computer aided design schematic of the experimental set up between collisions. The pistons are retracted such that the gold coated copper piston tips are within the outer edge of the copper thermal reservoir.

brief contact with the particles. In contrast, the stainless steel rod provides low thermal conductivity. This is necessary because part of the rod is situated outside of the vacuum chamber and hence is at ambient temperature.

The pistons enter the vacuum chamber through differentially pumped feedthroughs. To initiate a collision, both pistons are constantly accelerated to the same velocity (controlled with LabView software and associated electronic systems) and then stop abruptly before immediately retracting back to their starting positions. This accelerates the ice particles through the guide tubes to the centre of the collision volume where the collision takes place.

2.3.5 Imaging

Video footage of the collision is recorded using a high-speed, high resolution digital camera, placed above a viewing window on the top of the vacuum chamber. The camera has a frame rate of 107 frames per second and continuous recording capability. The collision volume is lit by two Xenon flash lamps which are mounted on the top flange of the vacuum chamber and are time synchronised with the camera. To re-

construct the 3 dimensional information, it is necessary to have video footage of the collision from two different views; this is achieved with a single camera by the use of beam splitter optics. This allows the camera to capture light from two vantage points either 60° (configuration 1) or 48.8° (configuration 2) apart. The horizontal field of view of the camera is approximately 2.4 cm $\times$ 2.0 cm. The vertical range is limited to 0.5 cm by the focal depth of the beam splitter optics. The reconstruction of three dimensional information from the two views of the collision is discussed in Section 3.3 of Chapter 3.

2.3.6 Experimental procedure

Ice collision experiments are carried out as follows. The set up is cooled with liquid nitrogen until the colosseum reaches 77 K and then the particles are loaded into their individual storage compartments as described in Section 2.3.3. The chamber is then evacuated to a base pressure of 10^{-5} mbar, the flow of liquid nitrogen is stopped, and the experiment is placed onto the aircraft. The aircraft takes off and travels to a suitable airspace to perform the parabolas. At the onset of microgravity, the camera and strobe lights are started and the pistons are fired. When the pistons are retracted, the colosseum is rotated to allow access to the next set of particles and the collision process can start again.

2.4 Conclusions

To access low collision velocities in free space, ice particle collisions must be carried out in a microgravity environment. Of all the available microgravity platforms, parabolic flight is most suited to these experiments as it allows individual ice particle collisions to be studied. Carrying out ice collisions in this environment presents a significant experimental challenge, requiring a dedicated experimental set up such as the one presented in this chapter. The experiment stores multiple pairs of ice particles and collides them either with each other or with an ice target. The particles are kept at

cryogenic temperatures during the flight by passively cooling the copper environment surrounding the particles with liquid nitrogen before take-off and relying on the copper acting as a thermal reservoir to keep the particles cold. The collisions are recorded using a high-speed camera.

After the experiments have taken place, the next step is to analyse the resulting video images and extract collisional information from them. The methods of analysing the video images are presented in Chapter 3.

Chapter 3

Data reduction and analysis for low velocity ice collisions

Chapter 2 described the experimental set up for carrying out ice particle collisions on parabolic flights. In this chapter, the methods used to reduce and analyse the data are presented. The main parameters used to describe ice particle collisions are the coefficient of restitution, which gives a measure of the translational kinetic energy lost in the collision, and the normalised impact parameter, which indicates how head-on or glancing the collision is. These parameters can be extracted from particle trajectories before and after the collision. These trajectories are obtained by manually tracking the particles. Particle rotation is measured by manually tracking a certain point on a particle as it rotates. Uncertainties on the relative velocities and coefficients of restitution are calculated using standard methods for the propagation of uncertainties. The calculations were performed using IDL programs that were written and developed by the author of this thesis.

3.1 Introduction

Ice collisions can have three possible outcomes: sticking, bouncing and fragmentation (see Chapter 1). For bouncing collisions, a key parameter is the coefficient of restitu-

tion (ε). This is the ratio of the relative velocities of the colliding particles after ($v_{rel,a}$) and before ($v_{rel,b}$):

$$\varepsilon = \frac{v_{rel,a}}{v_{rel,b}} \tag{3.1}$$

The coefficient of restitution is a measure of how elastic the collision is: a value of 1 means that the collision is elastic (i.e. no translational kinetic energy has been lost in the collision) and a value of 0 means that the particles did not move apart after the collision. It is related to the fraction of kinetic energy lost in the collision ($E_{KE\,lost}$) by the following equation:

$$E_{KE\,lost} = 1 - \varepsilon^2 \tag{3.2}$$

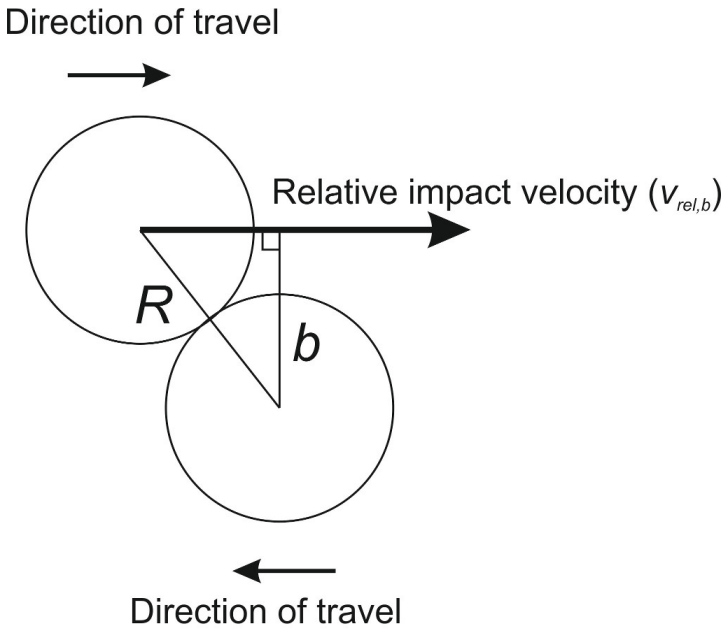

Figure 3.1: Diagram showing the impact parameter (b) for two colliding particles (direction of travel is indicated by arrows). The distance between the centres of masses of the particles at the point of collision (R) is also shown.

The other parameter of interest is the normalised impact parameter, b/R. The normalised impact parameter is the distance of closest approach of the two particles perpendicular to their relative velocity vector b, normalised to R, the distance between the centre of masses of the two particles at the point of collision. This is illustrated in Fig. 3.1.

To extract the coefficient of restitution and normalised impact parameter from the

video images, the particle positions must be tracked. The methods for doing this are discussed in Section 3.2. Once the particle positions within the images (given in pixels) have been extracted, IDL programs are used to derive relative velocities before and after the collision and hence the coefficient of restitution and normalised impact parameter. The extraction of these properties from the particle positions in pixels is discussed in Section 3.3. A worked example is given in Appendix A.

3.2 Particle tracking

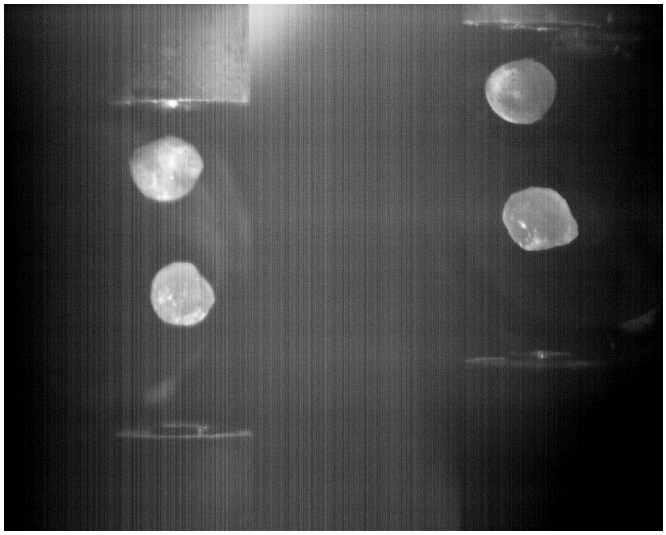

Figure 3.2: Example image from a particle collision video. Two views of the particles are shown with the view on the left separated from the view on the right by 60°. The two views are slightly offset due to the set up of the beam splitter optics.

Fig. 3.2 shows an example image from a particle collision video. Two views of the collision are shown in the image with the view on the left separated from the view on the right by 60°. This was achieved using beam splitter optics (see Section 2.3.5 of Chapter 2). The two views are slightly offset due to the set up of the beam splitter optics.

To obtain particle trajectories, the particles are manually tracked from the video images, using the image analysis program ImageJ. Fig. 3.3 shows how the centre of masses are tracked in two cases: for millimetre-sized particles that are irregular or not

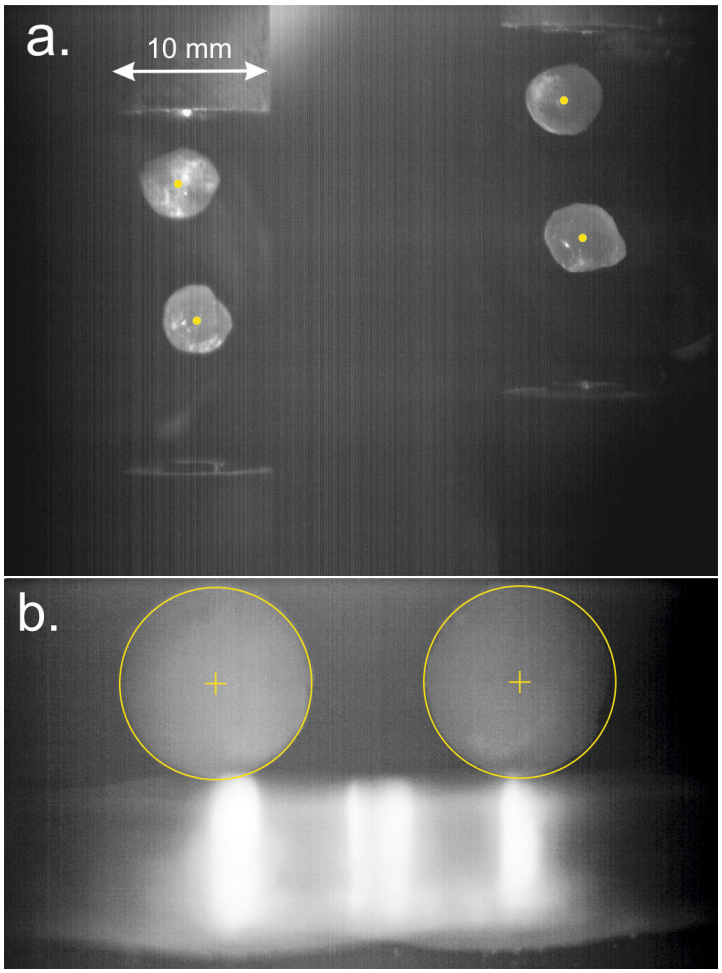

Figure 3.3: Images showing how particles are tracked **a.** by selecting the centre of mass point (indicated by a yellow circle) and **b.** by fitting a circle (yellow) to a spherical particle. The centre of the circles are indicated by crosses.

fully spherical (Fig. 3.3**a.**) and for spherical particles (Fig. 3.3**b.**). In both cases, two views of the particle(s) are present in the images, with the view on the left is separated from the view on the right by 60° (Fig. 3.3**a.**) or by 48.8° (Fig. 3.3**b.**).

For millimetre-sized particles, the video images are viewed frame by frame and the centre of mass of the particles is visually selected in each frame for each particle (shown by yellow dots in Fig. 3.3**a.**). Both views of the particles are tracked. Clicking on points within the image stores the position in pixels in a table (see Fig. 3.4) and when the full collision has been viewed and tracked, the table can be saved ready for further analysis.

For centimetre-sized fully spherical particles, a circle is drawn around each particle

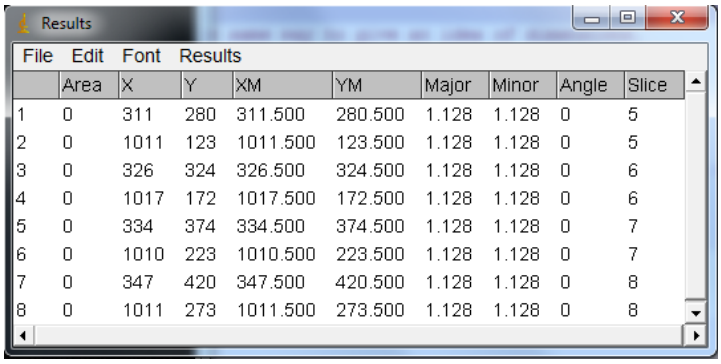

Results

File Edit Font Results

	Area	X	Y	XM	YM	Major	Minor	Angle	Slice
1	0	311	280	311.500	280.500	1.128	1.128	0	5
2	0	1011	123	1011.500	123.500	1.128	1.128	0	5
3	0	326	324	326.500	324.500	1.128	1.128	0	6
4	0	1017	172	1017.500	172.500	1.128	1.128	0	6
5	0	334	374	334.500	374.500	1.128	1.128	0	7
6	0	1010	223	1010.500	223.500	1.128	1.128	0	7
7	0	347	420	347.500	420.500	1.128	1.128	0	8
8	0	1011	273	1011.500	273.500	1.128	1.128	0	8

Figure 3.4: Table from Imagej of particle positions in pixels for one particle before a collision. The important columns are 'X' and 'Y' which give the x and y positions in pixels, and 'Slice' which gives the frame number. The two positions for each frame number are the left and right views of the particles respectively.

(shown in yellow in Fig. 3.3**b.**), and the centre of the circle (indicated by a yellow cross) is returned to the table as a centre of mass point as before. It is easier and more accurate to find the centre of mass in this way, and this method also allows the tracking of particles that are not fully visible in the video images by fitting a circle to the visible part of the particle and extracting the centre of mass using this circle (see Fig. 3.5). This can be done even if the centre of mass is outside the video image.

To convert the positions of the particles in pixels to their positions in metres, it is necessary to determine the conversion factor. This must be done by measuring the size of a known object in the images in pixels and using this as the conversion factor. In the case of Fig. 3.3**a.**, the piston guiding tubes are visible (and indicated by arrows); as they are 10 mm in diameter, their width in pixels can be used to convert the particle positions. In the case of Fig. 3.3**b.**, the particle size is known from the moulds they were formed in: 15 mm in diameter. An average of the diameters in pixels can be taken for several of these particles and this factor used for the position conversion to metres.

It is straightforward to determine the size of spherical or nearly spherical particles (not formed in moulds) as their diameters can be measured in pixels and then converted to metres (in the case of ice particle formation in moulds, the size is already known precisely). For irregularly shaped particles, it is less straightforward to determine the sizes. However, an estimate of the dimensions can be made by fitting ellipses to the

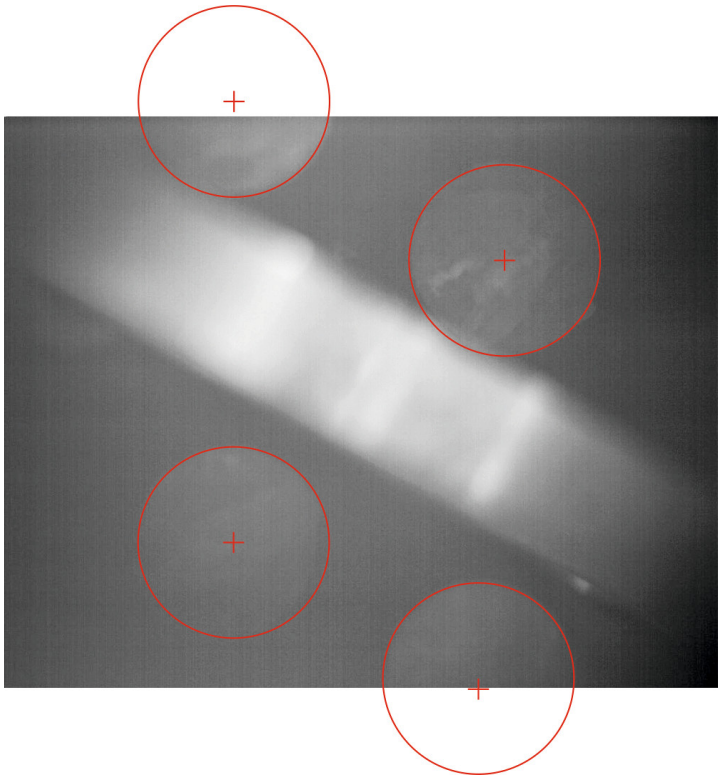

Figure 3.5: Images showing how spherical particles are tracked when one or more particles is not fully visible in the video images. The view of the particles on the left is separated from the view on the right by 48.8°. The particles are outlined in red and the centre of mass is shown by a red cross.

particles in the video images by manually drawing an ellipse on the image in ImageJ (Fig. 3.6). The major and minor axes of the ellipses are saved to a table ready for conversion into metres.

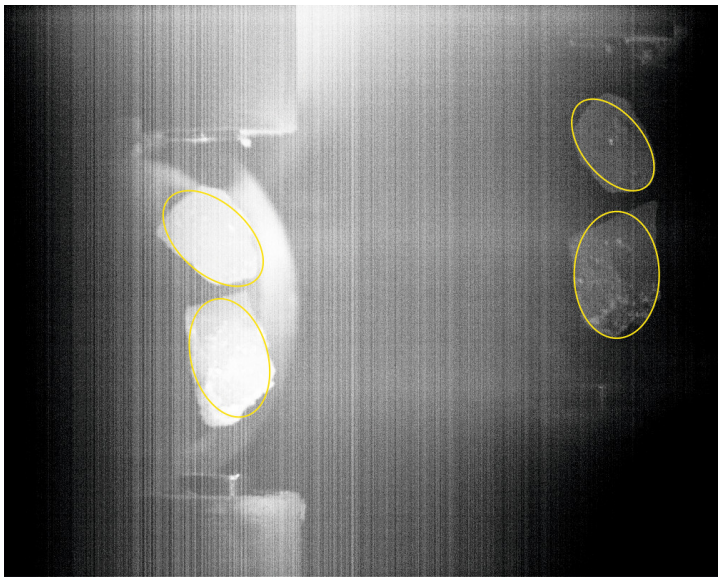

Figure 3.6: Image showing how ellipses (shown in yellow) are manually fitted to irregularly shaped particles to estimate their dimensions.

3.3 Analysis methodology

The equations used for extracting relative velocities, coefficient of restitution, normalised impact parameter, translational and rotational energy percentages and uncertainties are presented in this section. These equations form the basis of IDL programs that were used to automate the analysis and were written and developed by the current author. A worked example for extracting all of the parameters that follow can be found in Appendix A.

3.3.1 Coefficient of restitution and normalised impact parameter

The co-ordinate system chosen for the conversion of (x, y) positions in pixels to (x, y, z) positions in metres is shown in Fig. 3.7. The co-ordinates are defined as x' and z' for the left view and as x'' and z'' from the right view (Fig. 3.7) It should be noted that this choice of co-ordinate systems is completely arbitrary. The (x, y, z) co-ordinates were calculated from the centre of mass positions in pixels taken from the images as follows:

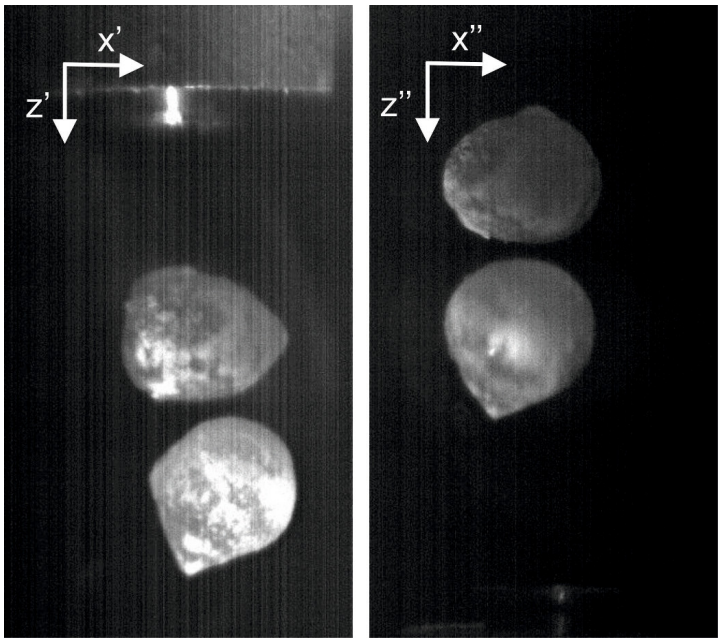

Figure 3.7: Image of two ice particles just before collision as seen from two different camera views; the view on the left is separated from the view on the right by 60°. The defined co-ordinate systems are indicated.

$$x = x' p \tag{3.3}$$

$$y = \frac{x'' - x' cos(\phi)}{sin(\phi)} p \tag{3.4}$$

$$z = \frac{z' + z''}{2} p \tag{3.5}$$

where p is the pixel size in metres.

To determine actual particle positions, particle trajectories before and after the collision are extracted from the (x, y, z) particle positions by performing linear fits in each dimension. Velocities of each particle before and after the collision in each dimension are calculated from the start ($i_{initial}$) and end (i_{final}) positions of the particle trajectories as follows:

$$v_i = \frac{i_{final} - i_{initial}}{t} \tag{3.6}$$

where $i = x, y, z$ and t is time, calculated from the number of frames (n) between the initial and final points divided by the frame rate of the camera (107 frames per second):

$$t = n/107 \tag{3.7}$$

For the target collisions, the velocity components are combined to yield the velocities before (v_b) and after (v_a) the collision:

$$v_b = \sqrt{v_{x,b}^2 + v_{y,b}^2 + v_{z,b}^2} \tag{3.8}$$

$$v_a = \sqrt{v_{x,a}^2 + v_{y,a}^2 + v_{z,a}^2} \tag{3.9}$$

The coefficient of restitution (ε) is calculated using Equation 3.1 with v_a and v_b in place of $v_{rel,a}$ and $v_{rel,b}$.

For the particle-particle collisions, the individual components of the relative velocity of the particles before ($v_{rel,b,i}$) and after ($v_{rel,a,i}$) the collision are calculated from the velocities of the individual particles:

$$v_{rel,b,i} = v_{i,b1} - v_{i,b2} \tag{3.10}$$

$$v_{rel,a,i} = v_{i,a1} - v_{i,a2} \tag{3.11}$$

where $i = x, y, z$ and 1 and 2 refer to each particle. The relative velocity of the particles before ($v_{rel,b}$) and after ($v_{rel,a}$) the collision is calculated from the individual components of relative velocity:

$$v_{rel,b} = \sqrt{v_{rel,b,x}^2 + v_{rel,b,y}^2 + v_{rel,b,z}^2} \tag{3.12}$$

$$v_{rel,a} = \sqrt{v_{rel,a,x}^2 + v_{rel,a,y}^2 + v_{rel,a,z}^2} \tag{3.13}$$

From the relative velocities before and after the collision, the coefficient of restitution is obtained using Equation 3.1.

For target collisions, the normalised impact parameter (b/R) is calculated as fol-

lows:

$$b/R = cos(\theta) \tag{3.14}$$

where θ is the angle between the target and the direction of travel of the particles. This is illustrated in Fig. 3.8.

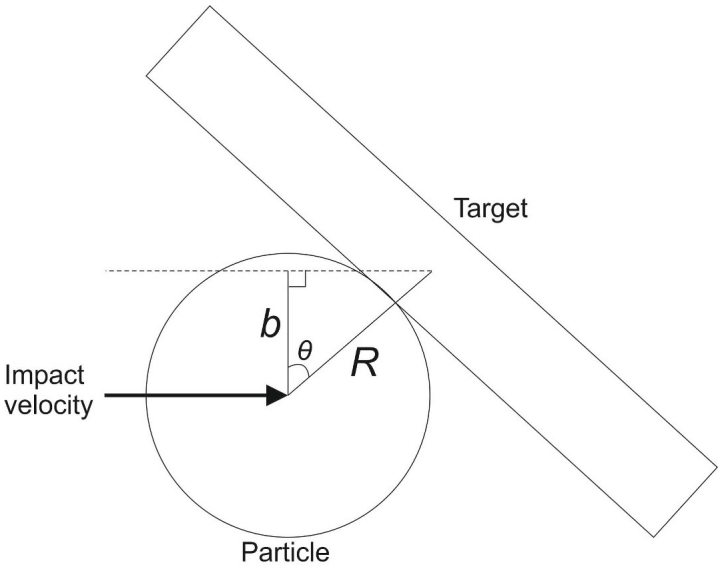

Figure 3.8: Diagram showing how the normalised impact parameter, b/R is related to the angle between the target surface and the direction of travel of the particle (θ).

For the particle-particle collisions, b/R is calculated as follows. The position of each particle at the point of collision is found by solving the simultaneous equations of the particle trajectories before and after the collision:

$$i = m_b t + c_b \tag{3.15}$$

$$i = m_a t + c_b \tag{3.16}$$

$$i_{col,j} = \frac{m_b c_a - m_a c_b}{m_b - m_a} \tag{3.17}$$

where $i = x, y, z,\ j = 1, 2$ and refers to each particle, $i_{col,j}$ refers to the position of the particle's centre of mass when the collision takes place, m and c are the gradient and intercept of the straight lines respectively and a and b refer to after and before the

collision.

R is then calculated:

$$R = \sqrt{(x_{col,1} - x_{col,2})^2 + (y_{col,1} - y_{col,2})^2 + (z_{col,1} - z_{col,2})^2} \tag{3.18}$$

Obtaining b requires the vector projection of R onto $v_{rel,b}$ ($\vec{R}_{v_{rel,b}}$):

$$\vec{R}_{v_{rel,b}} = \frac{\vec{v_{rel,b}}.\vec{R}}{v_{rel,b}^2}\vec{v_{rel,b}} = \frac{v_{b,x}R_x + v_{b,y}R_y + v_{b,z}R_z}{v_{b,x}^2 + v_{b,y}^2 + v_{b,z}^2}(v_{b,x}\vec{x} + v_{b,y}\vec{y} + v_{b,z}\vec{z}) \tag{3.19}$$

which then allows b to be calculated by simple trigonometry:

$$b = \sqrt{R^2 - R_{v_{rel,b}}^2} \tag{3.20}$$

and then the normalised impact parameter is b/R.

The normal and tangential coefficients of restitution ($\varepsilon_\perp$ and $\varepsilon_\parallel$) give further information about the distribution of energy after the collision. The normal coefficient of restitution gives information about particle rebound and the tangential coefficient of restitution gives information about particle scattering. They are calculated from the relative velocity components normal and tangential to the colliding surfaces ($v_\perp$ and $v_\parallel$). For collisions with a target surface at 90° to the direction of travel of the particle, the normal and tangential components of the velocity are simply:

$$v_\perp = v_z \tag{3.21}$$

$$v_\parallel = \sqrt{v_x^2 + v_y^2} \tag{3.22}$$

For collisions with a target surface at 60° to the direction of travel of the particle, the normal and tangential components of the velocity ($v_\perp$ and $v_\parallel$) are given by:

$$v_\perp = \frac{v\sqrt{3}}{2} \tag{3.23}$$

$$v_{\parallel} = \frac{v}{2} \tag{3.24}$$

For particle-particle collisions, the normal component of the relative velocity is calculated by taking a vector projection of v_{rel} onto R ($\vec{v_{relR}}$):

$$v_{\perp} = \vec{v_{relR}} = \frac{\vec{R}.\vec{v_{rel}}}{R^2}\vec{R} = \frac{R_x v_{rel,x} + R_y v_{rel,y} + R_z v_{rel,z}}{R_x^2 + R_y^2 + R_z^2}(R_x\vec{x} + R_y\vec{y} + R_z\vec{z}) \tag{3.25}$$

The tangential component is then calculated by trigonometry:

$$v_{\parallel} = \sqrt{v^2 - v_{\perp}^2} \tag{3.26}$$

The normal and tangential components of the velocities are calculated before and after the collision.

From the normal and tangential components of the velocities, the normal and tangential coefficients of restitution ($\varepsilon_{\perp}$ and $\varepsilon_{\parallel}$) are given by:

$$\varepsilon_{\perp} = \frac{v_{\perp,a}}{v_{\perp,b}} \tag{3.27}$$

$$\varepsilon_{\parallel} = \frac{v_{\parallel,a}}{v_{\parallel,b}} \tag{3.28}$$

where a and b refer to after and before the collision respectively.

3.3.2 Rotation

In some cases, it is possible to quantify particle rotation by tracking the angle through which a point on the particle moves from frame to frame. This can give information about the distribution of energy before the collision (i.e what percentage of the energy is in the form of translational kinetic energy and what percentage is in the form of rotational kinetic energy), and the distribution of energy after the collision (i.e. of the energy the particles had before the collision (translational plus rotational), what percentage is in the form of translational kinetic energy, what percentage is in the form of

rotational kinetic energy and what percentage remains unaccounted for). In calculating these percentages, it is assumed that the particles only possess translational and rotational kinetic energy *before* the collision. Comparing this value to the translational and rotational kinetic energy the particles possess *after* the collision gives the percentage of the original energy that is converted into translational and rotational kinetic energy, as well as the percentage that remains unaccounted for. This is illustrated in Fig. 3.9.

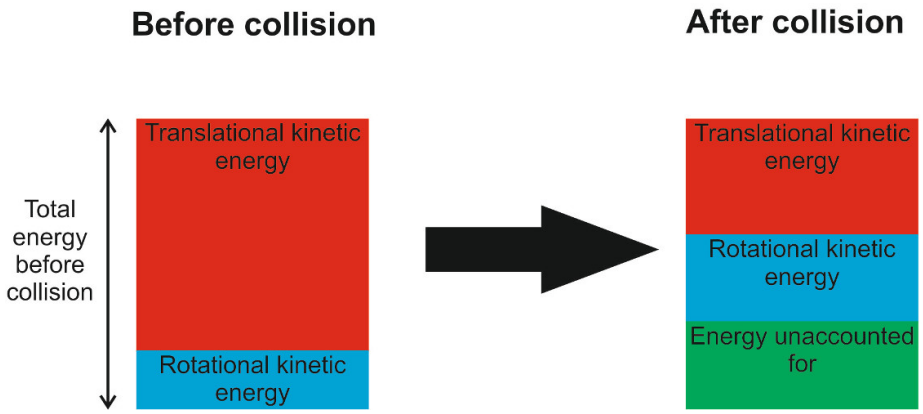

Figure 3.9: Diagram showing how particle energy before the collision (in the form of translational or rotational kinetic energy) is distributed into other forms after the collision (translational and rotational kinetic energy and energy unaccounted for).

Translational kinetic energy (E_{trans}) is calculated from the particle masses (m) and their relative velocity (v_{rel}) using the following equation:

$$E_{trans} = \frac{1}{2} m v_{rel}^2 \tag{3.29}$$

Rotational kinetic energy (E_{rot}) is calculated from the relative angular velocity (ω_{rel}) as follows:

$$E_{rot} = \frac{1}{2} I \omega_{rel}^2 \tag{3.30}$$

I is the moment of inertia:

$$I = \Sigma m_i r_i^2 \tag{3.31}$$

where m_i is each mass element of the particle and r_i is the radius of the mass element. However, it is not possible to obtain m_i or r_i from the limited shape information

available from the video images, and so the following approximation is used:

$$I = mr^2 \tag{3.32}$$

where m is the combined masses of the particles and r is equal to half the distant between the centre of masses of the two particles at the point of collision (i.e $R/2$). This introduces small uncertainties into the rotational kinetic energies, but these uncertainties do not significantly affect the overall conclusions about energy distribution before and after the collision.

The total kinetic energy before the collision ($E_{tot,b}$) is the some of the translational and rotational kinetic energy before the collision:

$$E_{tot,b} = E_{trans,b} + E_{rot,b} \tag{3.33}$$

The fraction of the total kinetic energy before the collision (translational and rotational) that is transferred into translational kinetic energy after the collision ($E_{trans,a}$) is:

$$\frac{E_{trans,a}}{E_{tot,b}} = \frac{v_{rel,a}^2}{v_{rel,b}^2 + r^2\omega_{rel,b}^2} \tag{3.34}$$

where a and b denote after and before the collision respectively. The fraction that is converted into rotational energy after the collision ($E_{rot,a}$) is:

$$\frac{E_{rot,a}}{E_{tot,b}} = \frac{r^2\omega_a^2}{v_b^2 + r^2\omega_b^2} \tag{3.35}$$

The fraction of energy unaccounted (E_{unacc}) for is:

$$\frac{E_{unacc}}{E_{tot,b}} = 1 - \frac{E_{trans,a} + E_{rot,a}}{E_{tot,b}} \tag{3.36}$$

Relative velocities before and after collision and R values (which are used to calculate r values) are calculated using the methods described above. Angular velocities for

each particle are calculated by taking a point to track on the particle and estimating the degrees rotated from the first image frame to the final image frame to the nearest 30°. This leads to an uncertainty of ± 28 rad s^{-1}. The rates of rotation are therefore approximate but are sufficient to determine whether or not all the energy before the collision is accounted for after the collision. The particle must be rotating within the field of view of one of the camera views to be able to perform this analysis. An example is shown in Fig. 3.10.

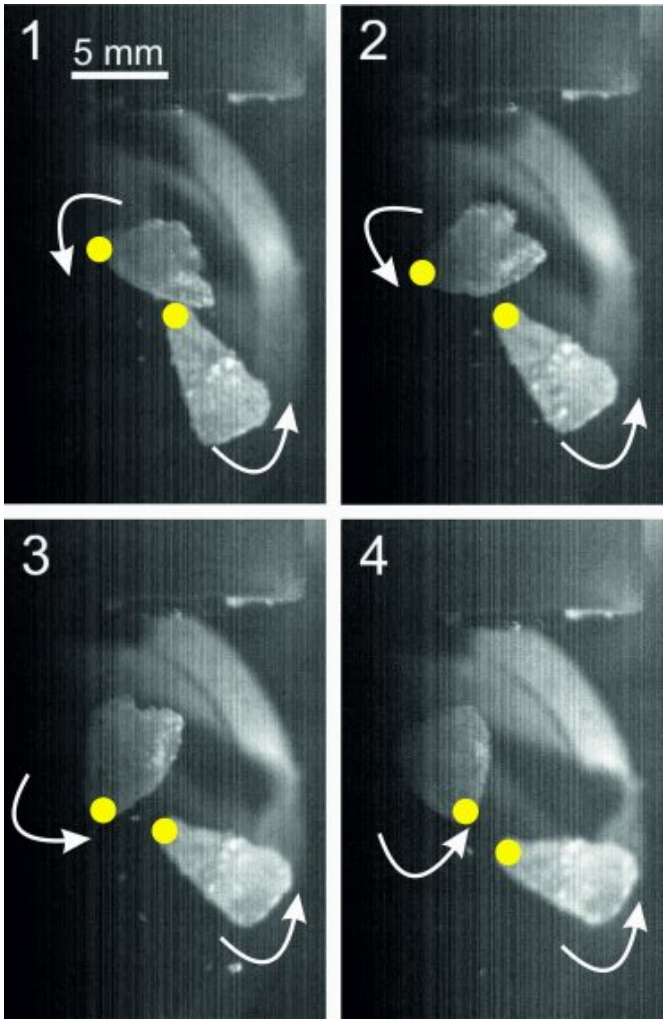

Figure 3.10: Image sequence of two ice fragments rotating after a collision. The angular velocities are -28 rad s^{-1} (top fragment) and -11 rad s^{-1} (bottom fragment) where rotation in the clockwise direction is defined as positive. The time difference between each successively numbered image is 2/107 s. The spots that were tracked are marked in yellow and the curly arrows indicate the direction of rotation.

3.3.3 Uncertainty analysis

The uncertainties on the velocity and coefficient of restitution were calculated using standard methods for the propagation of uncertainties. This method of calculating uncertainties has not previously been used for low velocity ice particle collisions due to its complexity.

The squared uncertainty on a parameter z (σ_z^2) is the sum of the squared uncertainties of the dependent variables (σ_j^2) multiplied by the square of the partial differential of the function with respect to each variable $\left(\left(\frac{\partial f}{\partial j}\right)^2\right)$:

$$\sigma_z^2 = \sum^{n} \sigma_j^2 \left(\frac{\partial f}{\partial j}\right)^2 \tag{3.37}$$

if the measurements of the variables are independent.

The position of each particle (where $i = x, y, z$) is given by:

$$i = mt + c \tag{3.38}$$

Partially differentiating with respect to all variables gives:

$$\frac{\partial i}{\partial m} = t \tag{3.39}$$

$$\frac{\partial i}{\partial t} = m \tag{3.40}$$

$$\frac{\partial i}{\partial c} = 1 \tag{3.41}$$

Hence the squared uncertainty on the position (σ_i^2) is:

$$\sigma_i^2 = t^2\sigma_m^2 + m\sigma_t^2 + \sigma_c^2 \tag{3.42}$$

As $\sigma_t \approx 0$ and there is an uncertainty on estimating the particle centre of mass (e_p),

Equation 3.42 becomes:

$$\sigma_i^2 = t^2\sigma_m^2 + \sigma_c^2 + e_p \tag{3.43}$$

The velocity components (where $i = x, y, z$) are given by:

$$v_i = \frac{i}{t} \tag{3.44}$$

Partially differentiating with respect to i gives:

$$\frac{\partial v_i}{\partial i} = \frac{1}{t} \tag{3.45}$$

Hence the squared uncertainty on each velocity component ($\sigma_{v_i}^2$) is:

$$\sigma_{v_i}^2 = \frac{\sigma_i^2}{t^2} \tag{3.46}$$

The overall velocity of each particle (v) is given by:

$$v = \sqrt{(v_x^2 + v_y^2 + v_z^2)} \tag{3.47}$$

Partially differentiating with respect to each component gives:

$$\frac{\partial v}{\partial v_i} = \frac{v_i}{\sqrt{(v_x^2 + v_y^2 + v_z^2)}} \tag{3.48}$$

Hence the squared uncertainty on the overall velocity is:

$$\sigma_v^2 = \frac{v_x^2\sigma_{v_x}^2 + v_y^2\sigma_{v_y}^2 + v_z^2\sigma_{v_z}^2}{v_x^2 + v_y^2 + v_z^2} \tag{3.49}$$

These equations are valid for before and after the collision.

If the collision is a particle-target collision, the coefficient of restitution (ε) is cal-

culated from the velocity of a single particle before (v_b) and after (v_a) the collision:

$$\varepsilon = \frac{v_a}{v_b} \tag{3.50}$$

Partially differentiating this with respect to all variables gives:

$$\frac{\partial \varepsilon}{\partial v_a} = \frac{1}{v_b} \tag{3.51}$$

$$\frac{\partial \varepsilon}{\partial v_b} = \frac{-v_a}{v_b^2} \tag{3.52}$$

Hence the squared uncertainty on the coefficient of restitution (σ_ε^2) is:

$$\sigma_\varepsilon^2 = \frac{\sigma_{v_a}^2}{v_b^2} + \frac{v_a^2 \sigma_{v_b}^2}{v_b^4} \tag{3.53}$$

If the collision is a particle-particle collision, the components of the relative velocity ($v_{rel,i}$) are calculated from the velocities of the individual particles (v_{i1} and v_{i2}):

$$v_{rel,i} = v_{i1} - v_{i2} \tag{3.54}$$

where $i = x, y, z$ and 1 and 2 refer to each particle. Partially differentiating this with respect to both velocities gives:

$$\frac{\partial v_{rel,i}}{\partial v_{i1}} = 1 \tag{3.55}$$

$$\frac{\partial v_{rel,i}}{\partial v_{i2}} = 1 \tag{3.56}$$

Hence the squared uncertainty on the relative velocity components ($\sigma_{v_{rel,i}}^2$) is:

$$\sigma_{v_{rel,i}}^2 = \sigma_{v_{i1}}^2 + \sigma_{v_{i2}}^2 \tag{3.57}$$

The overall relative velocity (v_{rel}) is given by:

$$v_{rel} = \sqrt{v_{rel,x}^2 + v_{rel,y}^2 + v_{rel,z}^2} \tag{3.58}$$

Partially differentiating with respect to each component gives:

$$\frac{\partial v_{rel}}{\partial v_{rel,i}} = \frac{v_{rel,i}}{\sqrt{(v_{rel,x}^2 + v_{rel,y}^2 + v_{rel,z}^2)}} \tag{3.59}$$

Hence the squared uncertainty on the overall relative velocity is given by:

$$\sigma_{v_{rel}}^2 = \frac{v_{rel,x}^2 \sigma_{v_{rel,x}}^2 + v_{rel,y}^2 \sigma_{v_{rel,y}}^2 + v_{rel,z}^2 \sigma_{v_{rel,z}}^2}{v_{rel,x}^2 + v_{rel,y}^2 + v_{rel,z}^2} \tag{3.60}$$

These equations are valid for before and after the collision.

The coefficient of restitution is calculated from the relative velocity before ($v_{rel,b}$) and after ($v_{rel,a}$) the collision:

$$\varepsilon = \frac{v_{rel,a}}{v_{rel,b}} \tag{3.61}$$

Partially differentiating this with respect to all variables gives:

$$\frac{\partial \varepsilon}{\partial v_{rel,a}} = \frac{1}{v_{rel,b}} \tag{3.62}$$

$$\frac{\partial \varepsilon}{\partial v_{rel,b}} = \frac{-v_{rel,a}}{v_{rel,b}^2} \tag{3.63}$$

Hence the squared uncertainty on the coefficient of restitution (σ_ε^2) is:

$$\sigma_\varepsilon^2 = \frac{\sigma_{v_{rel,a}}^2}{v_{rel,b}^2} + \frac{v_{rel,a}^2 \sigma_{v_{rel,b}}^2}{v_{rel,b}^4} \tag{3.64}$$

The average uncertainty on b/R for the particle-particle collisions is calculated by considering typical percentage uncertainties on the measurement of the positions of the particles. First, ellipses are fitted to the particles as described above. This returns the length of the major and minor ellipse axes and the ellipse area, both in pixels. The percentage uncertainty on the position of a particle's centre of mass (e_{pos}) is therefore given by:

$$e_{pos} = \left(\frac{e_p}{r} + \frac{e_p}{r}\right) \times 100 \tag{3.65}$$

where p is the estimated uncertainty on the centre of mass position in pixels and r is the radius of the particle in pixels. b depends on the position of two particles, therefore the uncertainty on b (e_b) is given by:

$$e_b = 2e_{pos} \tag{3.66}$$

R is a distance, the uncertainty on which is $2e_p$:

$$e_R = \left(\frac{2e_p}{R}\right) \times 100 \tag{3.67}$$

where $R = 2r$. Therefore, the percentage uncertainty on the normalised impact parameter ($e_{b/R}$) is given by:

$$e_{b/R} = \sqrt{(e_b^2 + e_R^2)} \tag{3.68}$$

3.4 Conclusions

Bouncing collisions are described in terms of their coefficient of restitution (the ratio of relative velocity after and before the collision) and their normalised impact parameter (the perpendicular distance between the centre of masses of the two particles at the point of collision normalised to the distance between the centre of masses at the point of collision). The coefficient of restitution gives a measure of how much translational kinetic energy is lost in the collision and the normalised impact parameter gives a measure of how head-on or glancing the collision is. These parameters are extracted from the video images by tracking each particle frame by frame, converting the positions in pixels to the positions in metres and performing linear fits to these positions to extract particle trajectories. The relative velocities before and after the collision (and hence the coefficient of restitution and normalised impact parameter) are calculated from these trajectories. When a particle is rotating within the field of view of the camera, it is possible to extract rotational energy as a percentage of the total energy (translational plus rotational) of the system before collision. This allows deductions to be made about the

dissipation of energy after the collision. Finally, it is possible to calculate uncertainties on the relative velocities and coefficients of restitution by using standard methods for calculating the propagation of uncertainties. Uncertainties on the normalised impact parameter are simply expressed as percentage uncertainties.

The ice particle collisions presented in this thesis were all analysed using the methods described in this chapter. Chapter 4 describes particle-particle collisions of millimetre-sized ice sphere and fragments, and Chapter 5 describes particle-target and particle-particle collisions of centimetre-sized ice spheres composed of pure water ice and water ice containing 5% methanol or formic acid.

Chapter 4

Collisions of small ice particles under microgravity conditions [1]

This study investigates whether the presence of crystalline water ice in planet-forming regions can overcome the so-called "bouncing barrier" that prevents dust particles from sticking at relevant collisional velocities. Low velocity collisions of millimetre-sized ice particles (both spheres and irregularly shaped fragments) were studied under microgravity conditions on parabolic flights (as described in Chapter 2) prior to the start of this work. The data reduction, analysis and interpretation was carried out by the author of this thesis as described in Chapter 3. Coefficients of restitution, normalised impact parameter, rotation, fragmentation and the effect of temperature are presented to characterise the ice collisions.

4.1 Introduction

As outlined in Chapter 1, understanding ice collisions in protoplanetary disks is vital for understanding and modeling the early stages of planet formation. The so-called

[1]This chapter is based on a previously published paper(C. R. Hill, D. Heißelmann, J. Blum, H. J. Fraser (2015), "Collisions of small ice particles under microgravity conditions" A&A, 573, A49) of which the author of this thesis is first author, and is the result of a collaboration between members of the Physics & Astronomy department of Technische Universität Braunschweig and the Department of Physical Sciences at The Open University.

"bouncing barrier" (described in Chapter 1) whereby dust particles tend to bounce rather than stick at relevant collision velocities is a major problem with the theory of planet formation by dust aggregation and it is possible that the presence of ice beyond the snowline may help to overcome the "bouncing barrier". However, to date, there have been no studies investigating the collisions of millimetre-sized ice particles in free space. This study investigates these collisions to see whether the presence of millimetre-sized ice grains could help to overcome the "bouncing barrier" and lead to particle sticking.

Colliding ice particles in conditions analogous to those in protoplanetary disks presents something of an experimental challenge. Early experiments investigating ice collisions utilised a disk pendulum and an ice target (Bridges et al., 1984; Hatzes et al., 1988; Supulver et al., 1995). It was found that coefficients of restitution decrease with increasing impact velocity, while glancing collisions yielded high coefficients of restitution (i.e. very little loss of kinetic energy in collision). The presence of a "frost" surface layer (condensed water vapour) or a roughened surface reduced the coefficient of restitution. Another method of ice particle collision used was that of dropping an ice sphere onto an ice target (Higa et al., 1996, 1998). These experiments were carried out with ice spheres with diameters between 0.28 and 7.2 cm, finding a constant coefficient of restitution below a critical velocity, above which the coefficients of restitution decreased with increasing impact velocity and the particles began to fracture.

Accessing low collision velocities in free space requires experiments to be conducted under microgravity conditions. Collisions of 1.5 cm diameter ice spheres were performed on a parabolic flight by Heißelmann et al. (2010) using a similar experimental set up to that described in Chapter 2. Coefficients of restitution were spread between 0.0 and 0.84, normalised impact parameters between 0.0 and 0.6 and relative impact velocities between 0.06 and 0.22 m s^{-1}. They found no correlation between the coefficient of restitution and relative impact velocity or normalised impact parameter. The spread of coefficients of restitution was thought to be caused by the rough, anisotropic surfaces of the ice particles.

The work in this chapter builds on the results of Heißelmann et al. (2010), colliding millimetre-sized ice spheres and ice fragments together at relative impact velocities between 0.27 and 0.51 m s^{-1} under microgravity conditions. The rest of the chapter is structured as follows. A brief summary of the experimental set up used and an explanation of how the ice particles were made is given in Section 4.2. The types of collisions obtained are described in Section 4.3 along with the reasons for including them in or excluding them from the resulting analysis. The results of the analysed collisions (coefficients of restitution, normalised impact parameter, particle rotation, particle fragmentation and the effect of temperature) are shown in Sections 4.4.1-4.4.4. The results and conclusions are summarised in Section 4.5.

4.2 Experimental methods

The experimental set up is described in detail in Chapter 2. For these experiments, it was used in configuration 1 (shown in Fig. 2.4**a.**). Briefly, ice particles were stored in a copper colosseum capable of storing 180 particles in compartments of 8 mm in diameter. The set up was passively cooled with liquid nitrogen prior to take-off and was kept at cryogenic temperatures by incorporating a copper thermal reservoir. The particles were collided together using a hydraulically driven piston assembly and the collisions were recorded with a high speed camera. For a full description of this set up, the reader is referred to Section 2.3 in Chapter 2.

4.2.1 Ice particles

Two different shapes of ice particles were used in these experiments: ice spheres and ice fragments. The ice spheres were prepared by freezing water droplets into liquid nitrogen. The needle end of a syringe of 18 Ohm purified water was placed under the surface of the liquid nitrogen and droplets were released one at a time, rapidly freezing to form ice spheres. When each droplet was released, the liquid nitrogen was allowed to quiesce until the ice particle was in equilibrium with the liquid nitrogen before the

formation of the next particle. Rapidly freezing ice particles in this way produces hexagonal polycrystalline ice. If the droplet size was significantly smaller, around a few microns in size, hyperquenched glassy water (a form of amorphous ice) would be expected to form. This can only be formed in this way if the particles are less than a few microns in size because if they are larger, it is not possible to dissipate the energy released in freezing and this allows the ice to crystallise. (Mayer & Brüggeller, 1982; Hallbrucker et al., 1989b; Angell, 2004).

The polycrystalline ice has a cloudy appearance because of light scattering from the sheer number of grain boundaries in the ice. The surface of the ice is rough and anisotropic. These properties can be seen in Fig. 4.1. Examples of "good" ice particles which are representative of those chosen for experiment are outlined with a solid black circle. These particles were spherical in shape and around 5 mm in diameter. Particles that were non-spherical were rejected (such as those indicated by a dashed line for a hemispherical shape and those indicated by a cross for a large and irregular shape). Fig. 4.2 shows an image sequence of a typical in-flight collision of two spheres.

The second type of ice particle was produced by submerging a spoonful of water into liquid nitrogen and crushing the resulting ice with a pestle and mortar. This results in highly irregularly shaped ice fragments such as those shown in the in-flight example, Fig. 4.3. These fragments had diameters ranging from 4.7 to 10.8 mm. The diameter refers to the major axis of an ellipse that was fitted to the images (see Chapter 2).

All ice particles used in these experiments were stored under liquid nitrogen until loading, using the loading procedure described in Chapter 2 (by storing them in liquid nitrogen and then loading them into the pre-cooled colosseum) to minimise formation of a layer of condensed water vapour on the particle surfaces. The robustness of this procedure is proved by considering the data as a function of temperature in Section 4.4.4. The particles that were first to be loaded were the last to be collided, so if significant water condensation occurs on the particle surfaces during loading, those that were collided last will have reduced coefficients of restitution compared to those collided first (as a layer of condensed water vapour reduces the coefficient of restitu-

Figure 4.1: Examples of ice particles produced by freezing water droplets in liquid nitrogen. The cloudy appearance of the ice indicates crystallinity and the rough, anisotropic surfaces can also be seen. Particles that were spherical in shape (such as the particle indicated by a solid circle) were selected for the experiments, while particles that were hemispherical (such as the one indicated by a dashed circle) or irregular (indicated by a cross) were rejected.

tion, see Chapter 2). As temperature increases with time, if significant water vapour condensation occurred during particle loading, the collisions that took place at higher temperature (those that were loaded first) would have higher coefficients of restitution compared to the collisions that took place at lower temperature (and were loaded last).

4.3 Collision statistics

A typical parabolic flight campaign consists of three flights with 31 parabolas each, giving a total of 93 parabolas. Up to four collision attempts per parabola were possible, leading to a large number of potential collisions. However, not all collisions were successful and of those that were, not all were chosen for analysis at the present time. Table 4.1 shows the outcomes of successful collisions. Of the 104 successful collisions, 52 were binary collisions suitable for analysis and are discussed in Section 4.4.1.

Table 4.1: Clarification of collisional outcomes. The binary collisions are the subject of the resulting analysis. Fragmentation is discussed separately and the other collisions were excluded from the analysis.

Type of collision	Number of collisions
Binary collisions	52
Non binary	33
Poor image quality	7
Residual acceleration	4
Multiple hit	4
Fragmentation	4
Total	104

For a collision to be suitable for analysis in the way described in Chapter 3, it has to be binary i.e. involving only two particles. Examples of binary collisions suitable for analysis are shown in Figs. 4.2 and 4.3. Fig. 4.2 shows a collision of two spherical particles and Fig. 4.3 shows a collision of two irregularly shaped fragments. Two views of the collision are shown: the view on the left is separated from the view on the right by an angle of 60°.

For non-binary collisions, analysis is less straightforward. The frame rate of the camera (107 frames per second) is not high enough to be sure of capturing the moment of collision and so the moment of collision is rarely captured. For binary collisions, this is not a problem, as the position and time of collision can be extracted by considering the particle trajectory before and after the collision. However, if more than two particles are involved, the situation becomes more complex. If the moment of collision is not captured, it is very difficult to tell if the collision event involved repeated two body collisions or a multiple body collision event (or a combination of the two). Even if this information could be determined, it would be difficult to extract coefficients of restitution and normalised impact parameters for multiple body collisions that could reasonably be compared with those of binary collisions, and the quality of the images is such that tracking multiple particles would be difficult. As the main focus of the current work was to investigate binary collisions of ice particles, the 33 non binary collision events such as the one shown in Fig. 4.4 were excluded from the current analysis. However, it may be possible to analyse these collisions in the future; for a full

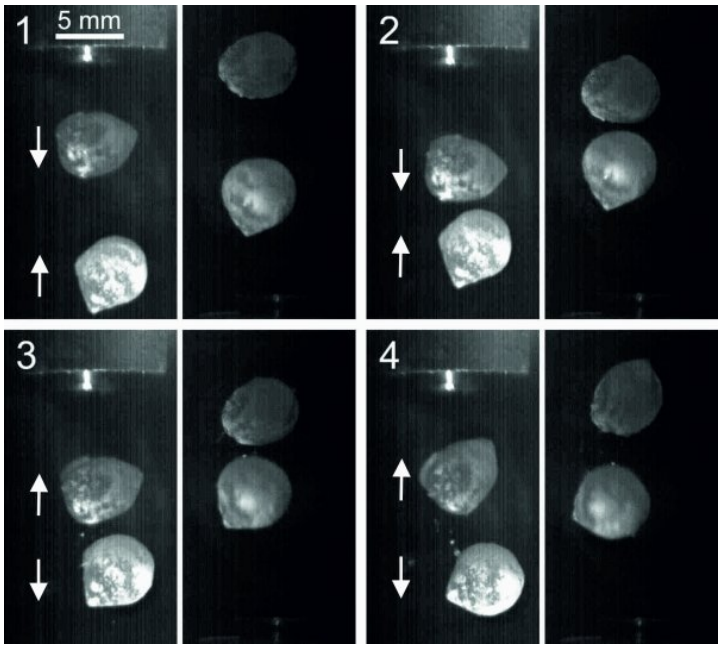

Figure 4.2: Image sequence of a collision between two ice spheres with a relative velocity of 0.42 m s^{-1}. Beam splitter optics were used to capture two views of the collision with the view shown on the left separated from the view shown on the right by 60°. The time difference between each successively numbered image is 1/107 s. The apparent offset of the two views is due to the set up of the beam splitter optics.

discussion of this, the reader is referred to Chapter 10.

After non binary collisions, the next second justification for exclusion was poor image quality, which rendered 7 collisions unsuitable for analysis. While the resolution and lighting used was sufficient to track most of the particles, in a few cases one or both particles could not be tracked throughout the collision and so these collisions were excluded. Again, it may be possible to extract collisional information from these collisions in future using image enhancement techniques and this is discussed in Chapter 10.

Next was residual acceleration of the aircraft (responsible for 4 exclusions) which is when the plane experienced turbulence, leading to a poor quality of microgravity. This is easily spotted when viewing the image sequences as the particles appear to move sideways with respect to the camera and in some cases move out of the field of view. As these particles appear to have another velocity component apart from that induced by the pistons or collision with each other, it is necessary to exclude them

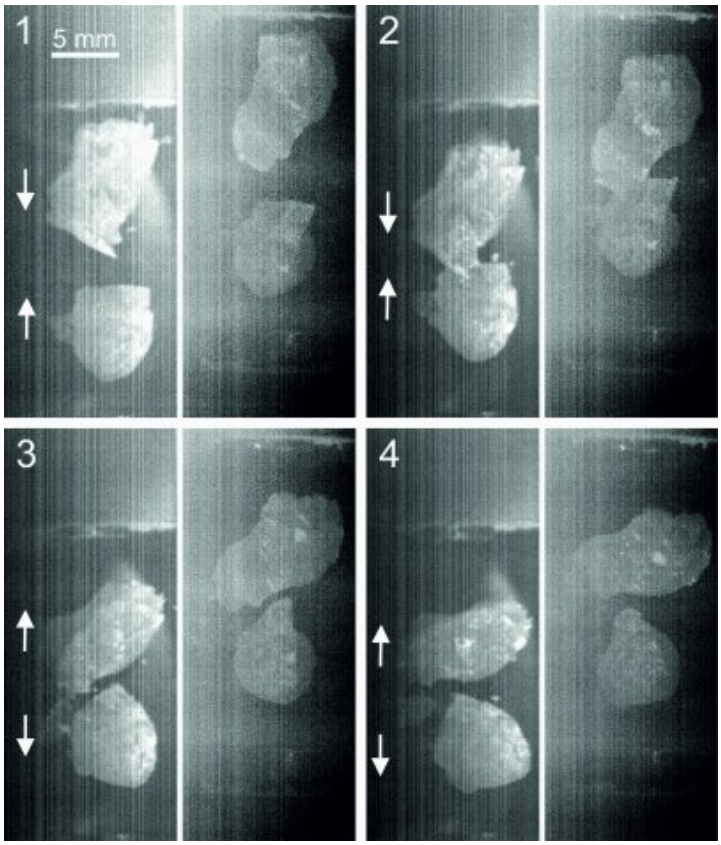

Figure 4.3: Image sequence of a collision between two ice fragments with a relative velocity of 0.36 m s^{-1}. Beam splitter optics were used to capture two views of the collision with the view shown on the left separated from the view shown on the right by 60°. The time difference between each successively numbered image is 1/107 s. The apparent offset of the two views is due to the set up of the beam splitter optics.

from analysis.

In 4 cases, collisions were removed from analysis because the particles involved hit each other more than once. While this is impossible with spheres, it is possible with irregularly shaped fragments; if a particle impacts another and induces rotation, it may hit the first particle again if the particles have not moved far enough apart. This is illustrated in Fig. 4.5. In these cases, there are not sufficient images between the two impacts for a velocity after collision to be extracted and so these collisions can not be analysed. The effects of rotation on the distribution of energy after the collision are discussed in Section 4.4.2.

Finally, fragmentation occurred as a collisional outcome in 4 cases. To obtain an accurate relative velocity after the collision in this scenario would require the tracking

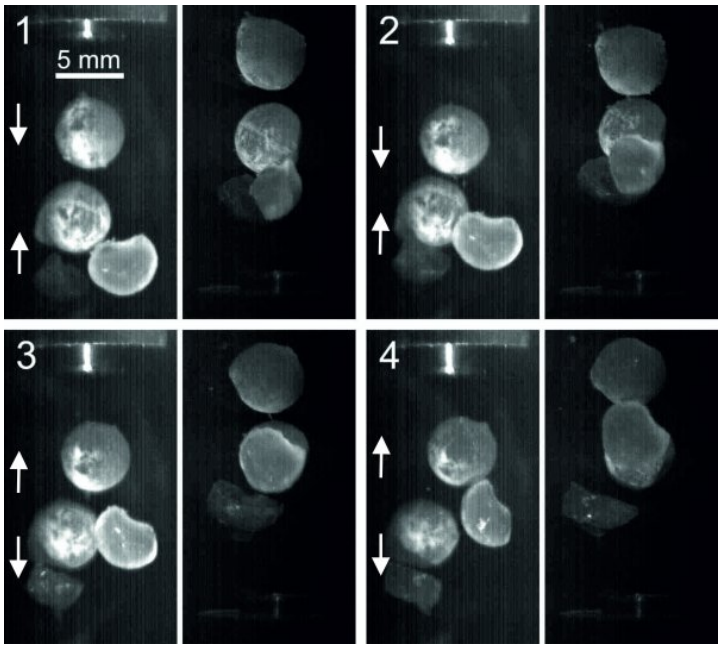

Figure 4.4: Image sequence of a collision between four ice particles. Beam splitter optics were used to capture two views of the collision with the view shown on the left separated from the view shown on the right by 60°. The time difference between each successively numbered image is 1/107 s. The apparent offset of the two views is due to the set up of the beam splitter optics.

of all of the fragments - some of which are very small and not clearly visible in the video images. It was therefore necessary to exclude them from the main analysis but they are discussed separately in Section 4.4.3.

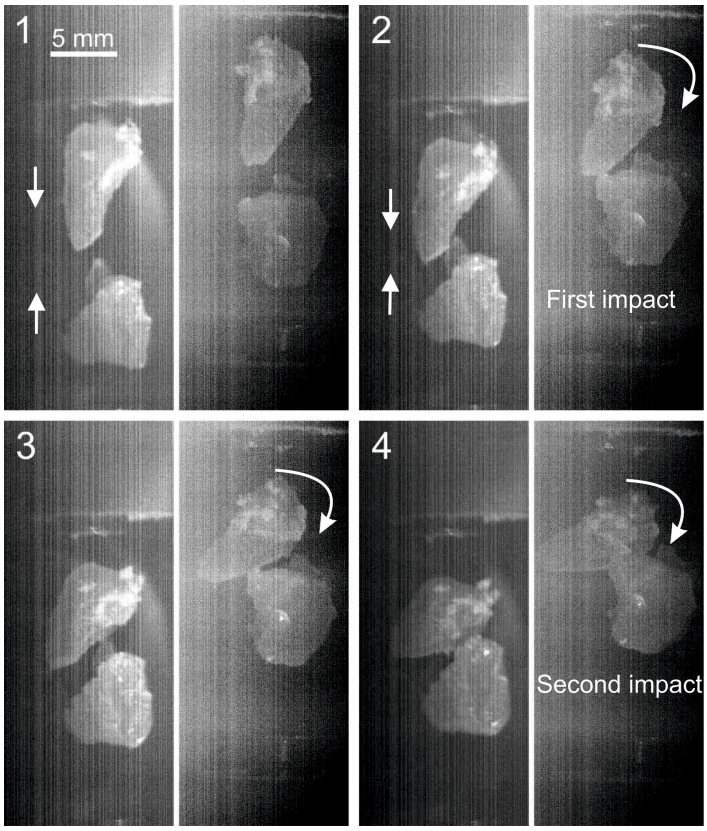

Figure 4.5: Image sequence of a multiple hit collision between two ice fragments with a relative impact velocity of 0.34 m s^{-1}. The direction of rotation is indicated by curved arrows. The particles first make contact in frame 2 and impact one another again in frame 4. Images after the collisions are not shown as both particles hit the top piston before they separated. Beam splitter optics were used to capture two views of the collision with the view shown on the left separated from the view shown on the right by 60°. The time difference between each successively numbered image is 1/107 s. The apparent offset of the two views is due to the set up of the beam splitter optics.

4.4 Results

4.4.1 Coefficient of restitution and impact parameter

As is clear from the image sequences shown in Figs. 4.2-4.5, the collisional outcomes were almost exclusively bouncing, apart from the 4 cases of fragmentation mentioned above and detailed in Section 4.4.3. Particle sticking did not occur in any case. This demonstrates that if ice particles have a "bouncing barrier" as dust particles do (Güttler et al., 2010; Zsom et al., 2010; Weidling et al., 2012; Kothe et al., 2013), it will be less than 0.26(91)±0.0009 m s^{-1} (the lowest collision velocity observed in these experiments) for particles of this size.

Coefficient of restitution

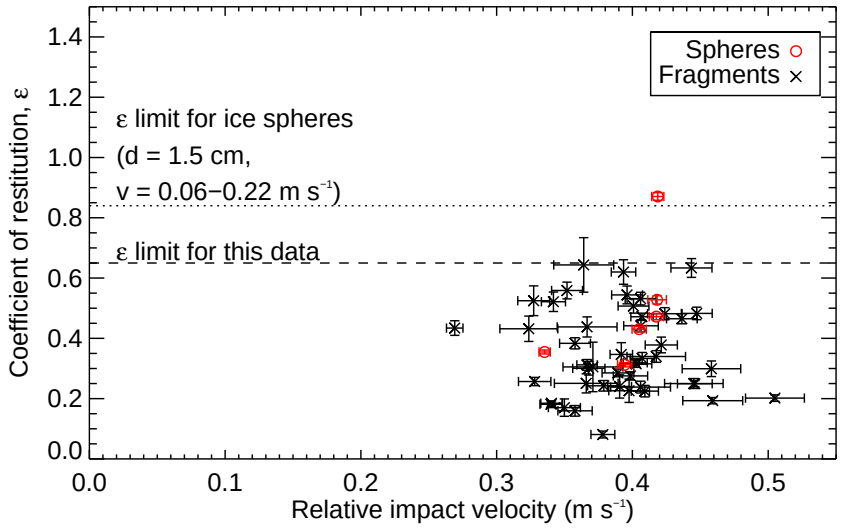

Figure 4.6: Coefficient of restitution as a function of relative impact velocity. The dashed lines show the limits of coefficient of restitution for this data and for collisions of 1.5 cm ice spheres in the velocity range 0.06-0.22 m s^{-1} (previously reported by Heißelmann et al. (2010)).

Fig. 4.6 shows the coefficients of restitution as a function of relative impact velocity. The impact velocities are spread from 0.26(91)±0.0009 to 0.50±0.02 m s^{-1} and the coefficients of restitution are spread from 0.08±0.01 to 0.87±0.01. Cumulative plots of these quantities demonstrate over which regions they are evenly distributed. Relative impact velocity is distributed evenly between 0.32 and 0.46 m s^{-1} (Fig. 4.7) and can be fitted with a linear function for the fragments. A linear cumulative plot indicates that the velocities are uniformly distributed within limits, while completely random events would produce a Gaussian distribution and result in a hysteresis-type plot. A good linear fit is not possible for the spheres but this is not a cause for concern as there are only 6 data points. Fig. 4.8 shows the distribution of the coefficients of restitution; these are evenly spread between 0.08±0.01 and 0.64±0.09 with good linear fits obtained for both the spheres and the fragments. This leaves one outlier at 0.87±0.01 which is discussed later in the chapter. The median value of the coefficient of restitution (for the fragments only) is 0.32 ± 0.01.

Apart from the single outlier, there appears to be a clear upper limit to the coefficients of restitution at around 0.65. This is indicated in Fig. 4.6 by a dashed line. The dotted line in this figure indicates the upper limit of 0.84 found by Heißelmann et al. (2010) for 1.5 cm (diameter) ice spheres colliding at relative velocities of 0.06-0.22 m s^{-1} (no uncertainties given). This demonstrates that the upper limit of coefficient of restitution decreases with increasing relative impact velocity, corroborating previous results by Güttler et al. (2012) and Krijt et al. (2013). While this is the most likely explantation, it is also possible that the upper limit of coefficient of restitution is lower than that reported by Heißelmann et al. (2010) because of the smaller particle size or because of deviation from sphericity (compared to the ice particles in the work of Heißelmann et al. (2010) which were completely spherical).

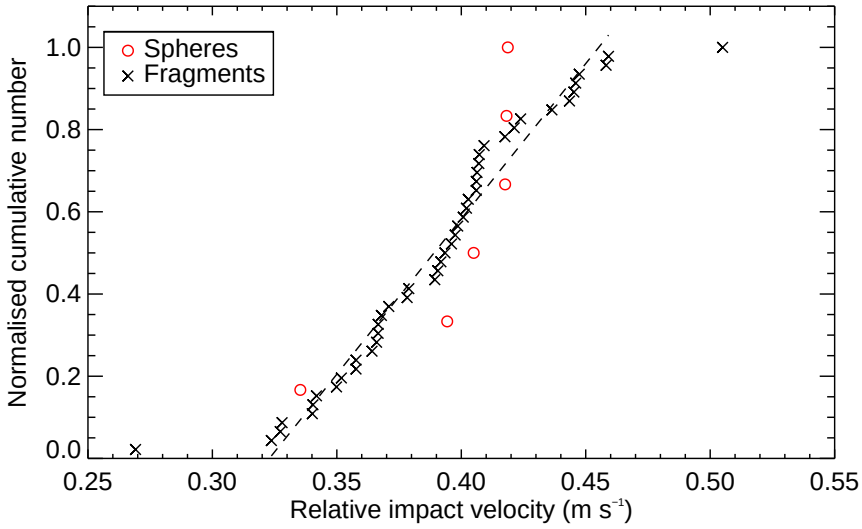

Figure 4.7: Normalised cumulative number for collisions with relative impact velocity $\leq v$. The dashed line indicates a linear fit between 0.32 and 0.46 m s^{-1} for the fragments (dashed line). A linear fit is not shown for the spheres because of the limited number of data points. Error bars have been omitted for clarity.

A visual inspection of Fig. 4.6 reveals no obvious correlation between coefficient of restitution and impact velocity. To test the strength of correlation mathematically, the linear Pearson correlation coefficient was computed:

$$r = \frac{\sum_{i=0}^{n}(y_i - \bar{y})(x_i - \bar{x})}{\sqrt{\sum_{i=0}^{n}(y_i - \bar{y})^2}\sqrt{\sum_{i=0}^{n}(x_i - \bar{x})^2}} \tag{4.1}$$

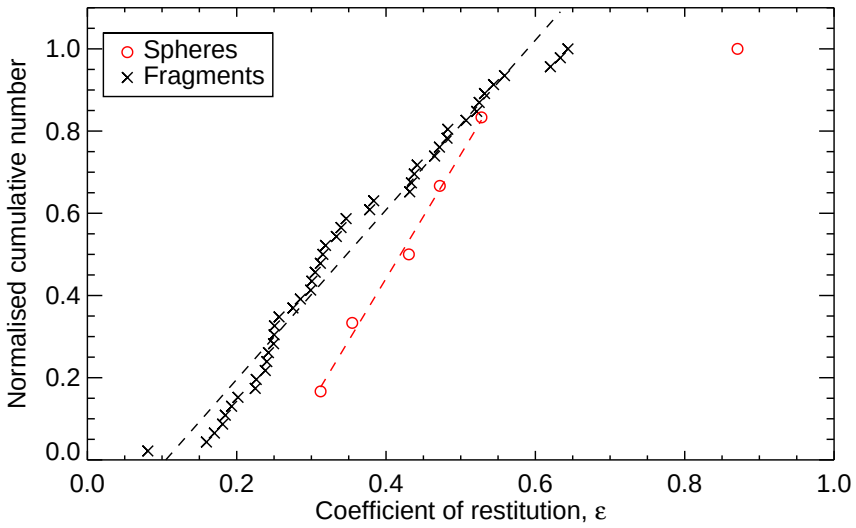

Figure 4.8: Normalised cumulative number for collisions with coefficient of restitution $\leq \varepsilon$. The dashed lines indicate linear fits across the entire range for the fragments and between 0.31 and 0.53 for the spheres. Error bars have been omitted for clarity.

n is the number of points and $\bar{x}$ and $\bar{y}$ are the mean values of x and y respectively. r is a number between 1 and -1 which gives the strength of correlation between the variables x and y. A value of 1 indicates perfect positive correlation, a value of -1 indicates perfect negative correlation and a value of 0 indicates no correlation. Uncertainties on these values were calculated using jackknife resampling (where the calculation is repeated with each point missing in turn and the difference between the average of these values and the original value is the uncertainty).

The linear Pearson correlation coefficient for the correlation between coefficient of restitution and relative impact velocity was $-0.05(1) \pm 0.003$ for the fragments. Clearly there is no correlation between these parameters for the fragments; as for the spheres, the number of data points (6) is too low for a correlation coefficient to indicate reliable correlation (or non-correlation). Hence the coefficient of restitution does not depend on relative impact velocity for these particles in this velocity range.

At this point, it is instructive to consider how these results compare to those published previously. The present findings are in agreement with those of Heißelmann et al. (2010) but do not replicate the findings of earlier studies (e.g. Hatzes et al.

(1988); Higa et al. (1996, 1998)). Table 4.2 shows the experimental conditions of these earlier studies and the current work. The first thing to note is that the pressure and temperature regimes of this work and that of Heißelmann et al. (2010) are different to those of the other studies, at 10^{-5} mbar and 130-180 K. These conditions are necessary to prevent condensation of water vapour onto the particle surface or roughening by sublimation, both of which have been found to lower the coefficient of restitution (Hatzes et al., 1988). In addition, the surfaces of the ice particles in the current work are rough and anisotropic, similarly to those of Heißelmann et al. (2010), in contrast to those of Hatzes et al. (1988), Higa et al. (1996) and Higa et al. (1998), where care was taken to obtain smooth surfaces. When surfaces were covered in condensed water vapour or roughened, each particle was coated or roughened to virtually the same extent; there was no anisotropy in the surfaces. This "uneven" surface roughness in the current work (and Heißelmann et al. (2010)) is the most likely explanation for the broad range of coefficients of restitution (as each coefficient of restitution is lowered by a different extent compared to that which would be expected for smooth particles) and their non-dependence on relative impact velocity. In addition, the method of particle collision in this work and the work of Heißelmann et al. (2010) (free collisions induced by pistons under microgravity conditions) is completely different to those of previous work, where collisions were carried out using a pendulum or other dropping arrangement. These collision methods do not allow access to all the translational and rotational degrees of freedom that are available to particles colliding in free space. The method of collision used in the current work is arguably more analogous to those occurring in protoplanetary disks, and it is possible that this method of collision will produce different results to others, regardless of ice particle properties.

Table 4.2: Comparison of the particle sizes and experimental conditions in previous ice collision studies with those of the current study. The particle sizes, method of collision, surface properties, collision velocities, temperature and pressure are compared. "Frost" here refers to a layer of condensed water vapour on the particle surface.

Study	Size of particle(s) (diameter)	Collision method	Surface properties	Relative collision velocities (m s^{-1})	Temperature (K)	Pressure (mbar)
Hatzes et al. (1988)	50 mm ice sphere and ice block	Pendulum	Smooth, roughened and "frosted"	0.00015-0.02	85-145	$1.3 \times 10^{-3} - 1.3 \times 10^{-4}$
Higa et al. (1996	30 mm ice sphere and ice block	Free fall	Smooth	0.01- 7	113-269	10
Higa et al. (1998)	2.8- 72 mm sphere and ice block	Free fall	Smooth	0.01-10	261	1000
Heißelmann et al. (2010)	15 mm spheres	Pistons, microgravity	Rough, "unfrosted"	0.06-0.22	130-180	Not stated but likely to be around 10^{-5}
Present work	4.7-10.8 mm spheres and fragments	Pistons, microgravity	Rough, "unfrosted"	0.26-0.51	130-160	10^{-5}

Normalised impact parameter

Fig. 4.9 shows the distribution of coefficient of restitution with normalised impact parameter. The average uncertainty on the parameters is indicated. The cumulative distribution of the normalised impact parameter is shown in Fig. 4.10. The solid line indicates the expected distribution of normalised impact parameter if the collisions were uniformly distributed. The distribution of normalised impact parameters falls slightly below this line at low normalised impact parameters and slightly above it at high normalised impact parameters; this indicates that this experimental set up produces collisions that are slightly more head-on as opposed to glancing. This is to be expected as the experimental set up was designed to perform head-on collisions using diametrically opposed pistons. The linear Pearson correlation coefficient was once again computed to test for correlation between coefficient of restitution and normalised impact parameter. The value of the correlation coefficient was $0.22(7) \pm 0.009$ for the fragments. This value indicate no correlation between the parameters. This is in contrast to the work of Supulver et al. (1995) where glancing collisions had very high coefficients of restitution, indicating little loss of translational kinetic energy. Once again, the anisotropic surface roughness is the dominant factor in explaining the coefficients of restitution. However, it can be seen from Fig. 4.9 that the outlier with a coefficient of restitution of 0.87 ± 0.01 was a very glancing collision with a normalised impact parameter of 0.95. In this case, it appears that the glancing collision of two spheres has had very little loss of kinetic energy, leading to the higher coefficient of restitution.

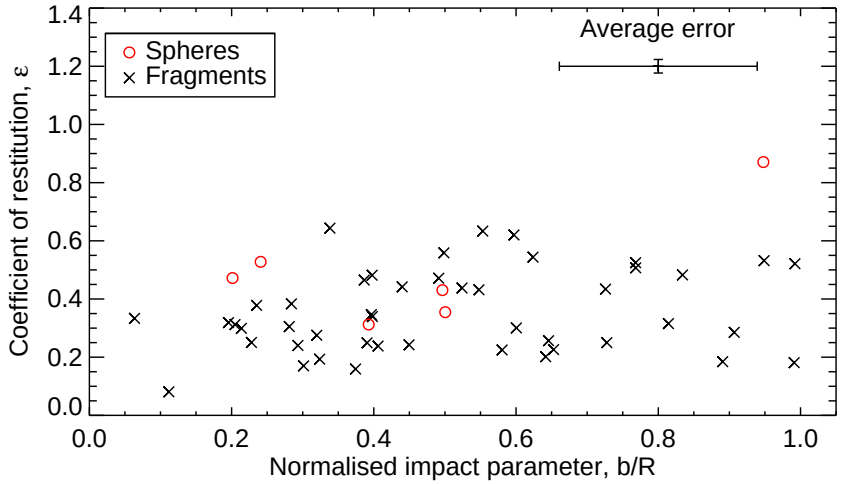

Figure 4.9: Coefficient of restitution as a function of normalised impact parameter.

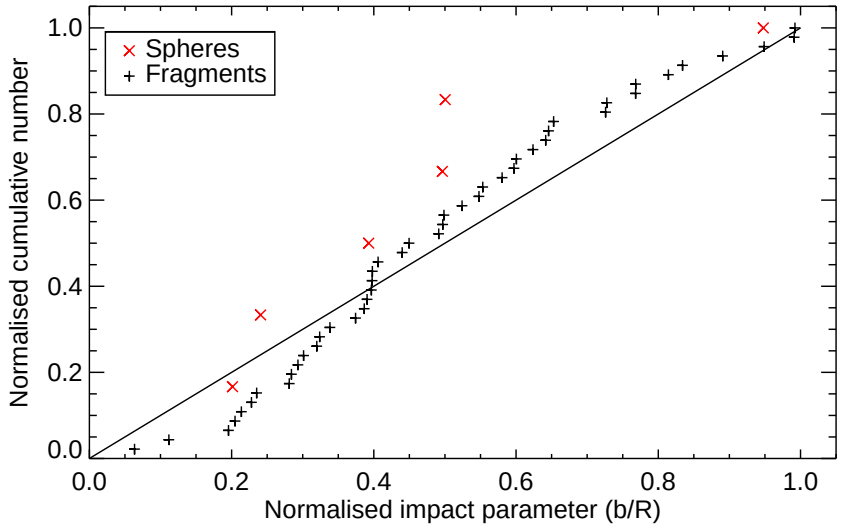

Figure 4.10: Normalised cumulative number for collisions with squared normalised impact parameter $\leq b/R$. The solid line indicates the distribution that would be expected if the collision geometry was completely random. The distribution shows that this apparatus slightly favours head on collisions over glancing ones.

Normal and tangential coefficients of restitution

Figs. 4.11-4.12 show the coefficient of restitution resolved into components normal ($\varepsilon_\perp$) and tangential ($\varepsilon_\parallel$) to the colliding surfaces versus the normal and tangential relative impact velocities respectively (Fig. 4.11) and the normalised impact parameter (Fig. 4.12). The normal and tangential coefficients of restitution are calculated according to Equations 3.27 and 3.28. These values give further information about the distribution of translational kinetic energy after the collision; $\varepsilon_\perp$ gives information about the particle rebound and $\varepsilon_\parallel$ gives information about the particle scattering. While a value of ε that is greater than 1 means that the particles have gained translational kinetic energy in collision, a value of $\varepsilon_\perp$ or $\varepsilon_\parallel$ that is greater than 1 simply means that translational kinetic energy has been transferred from one velocity component to another, such that the velocity component is greater after the collision than before it. This is clearly evident for the values of $\varepsilon_\parallel$ (Fig. 4.11**b.** and Fig. 4.12**b.**) which range from 0 to 2.1.

Fig. 4.13 shows the distribution of normal and tangential relative impact velocities. The normal relative impact velocities are spread from 0.04 to 0.45 m s^{-1} with the greatest concentration between 0.30 and 0.40 m s^{-1}. In contrast, the values of the tangential relative impact velocities are spread from 0.025 to 0.40 m s^{-1} with the greatest concentration between 0.070 and 0.27 m s^{-1}. The average value of normal relative impact velocity is 0.32 m s^{-1} whereas the average value of tangential relative impact velocity is 0.19 m s^{-1}. Therefore, the particles on average have a greater component of normal relative impact velocity than tangential impact velocity. This confirms that the apparatus slightly favours head-on collisions over glancing ones.

Fig. 4.14 shows the distribution of $\varepsilon_\perp$ and $\varepsilon_\parallel$. The values of $\varepsilon_\perp$ are evenly distributed between 0 and 0.65 apart from two cases. The limit of normal coefficient of restitution is identical to the overall coefficient of restitution; a fact that is unsurprising given the greater average component of normal relative impact velocity compared to tangential relative impact velocity. In contrast the values of $\varepsilon_\parallel$ are evenly distributed

below 0.4, between 0.5 and 0.6 and between 0.7 and 1.0. There are only a few values greater than 1.0. The overall coefficient of restitution is clearly dominated by the normal component.

However, the spread of the normal and tangential coefficients of restitution clearly indicates that significant energy is transferred into rebound and scattering. As there is no correlation between overall coefficient of restitution and relative impact velocity or normalised impact parameter, any correlation shown between the components of the coefficient of restitution and the components of relative impact velocity or normalised impact parameter will indicate the tendency to transfer energy between components. There is possibly very slight negative correlation between the components of coefficient of restitution and their respective components of relative impact velocity (correlation coefficient of -0.51 ± 0.03 for the normal component and -0.50 ± 0.03 for the tangential component, fragments only). This is somewhat speculative as the correlation is not very strong, but if this was the case, as the velocity component increases, the energy remaining in that component after the collision decreases, i.e. the greater the component of relative impact velocity, the greater the likelihood of transferring energy into the other velocity component after the collision. It should however be noted that this is not a strong tendency. There is also a possible very slight negative correlation between $\varepsilon_{\|}$ and b/R (correlation coefficient of -0.53 ± 0.02 for the fragments), i.e. the more head-on the collision, the more likely that the rebound component will be converted into scattering after the collision. However there is no correlation between $\varepsilon_{\perp}$ and b/R (correlation coefficient of 0.40 ± 0.02 for the fragments). Neither head-on or glancing collisions are associated with an increased tendency to convert energy from rebound to scattering. As all of the correlations discussed in this section are weak or non-existent, this suggests that another factor is needed to explain the range of normal and tangential coefficients of restitution. As with the overall coefficients of restitution, the rough, anisotropic surfaces of the particles is likely to be responsible for the broad range of normal and tangential coefficients of restitution observed.

The results in this section show that a minimum of 58% (1-ε^2 for $\varepsilon_{max} = 0.65$) of

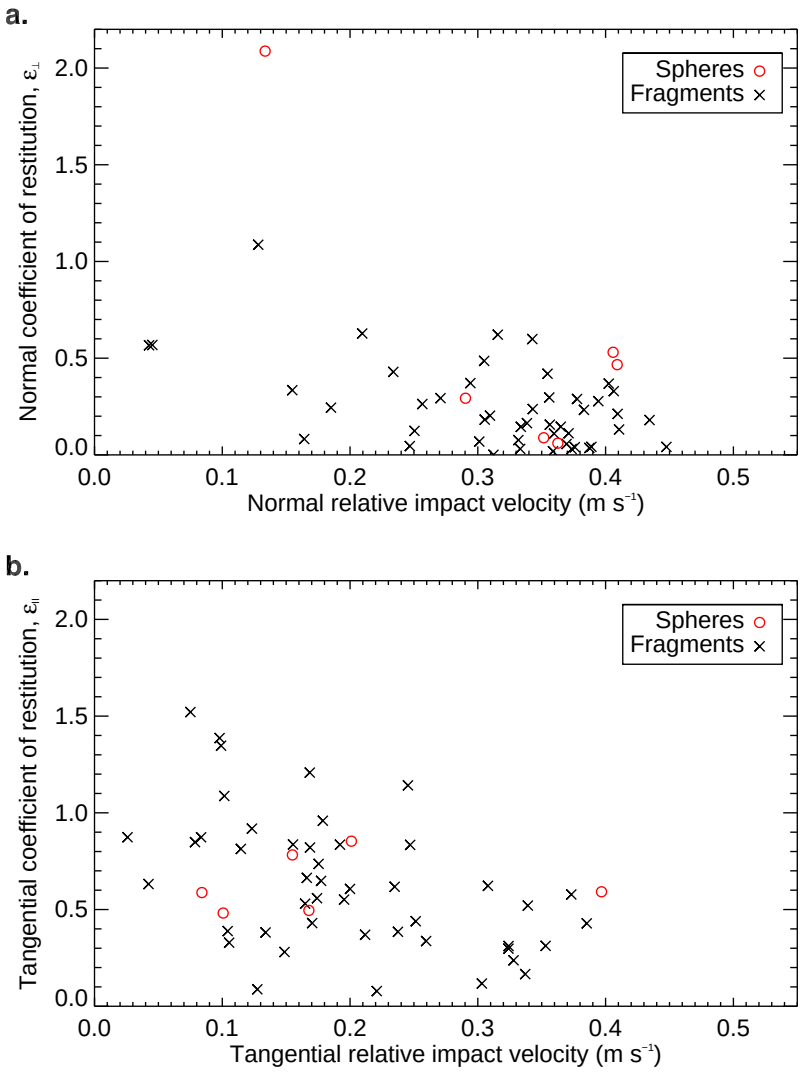

Figure 4.11: **a.** Normal coefficient of restitution as a function of normal relative impact velocity. **b** Tangential coefficient of restitution as a function of tangential relative impact velocity.

translational kinetic energy is lost in the collisions and in some cases, considerably more energy is lost. It can been seen from the collision videos that some of this energy is converted into rotational energy after the collision. The extent of this energy transfer in these experiments is the subject of the next section.

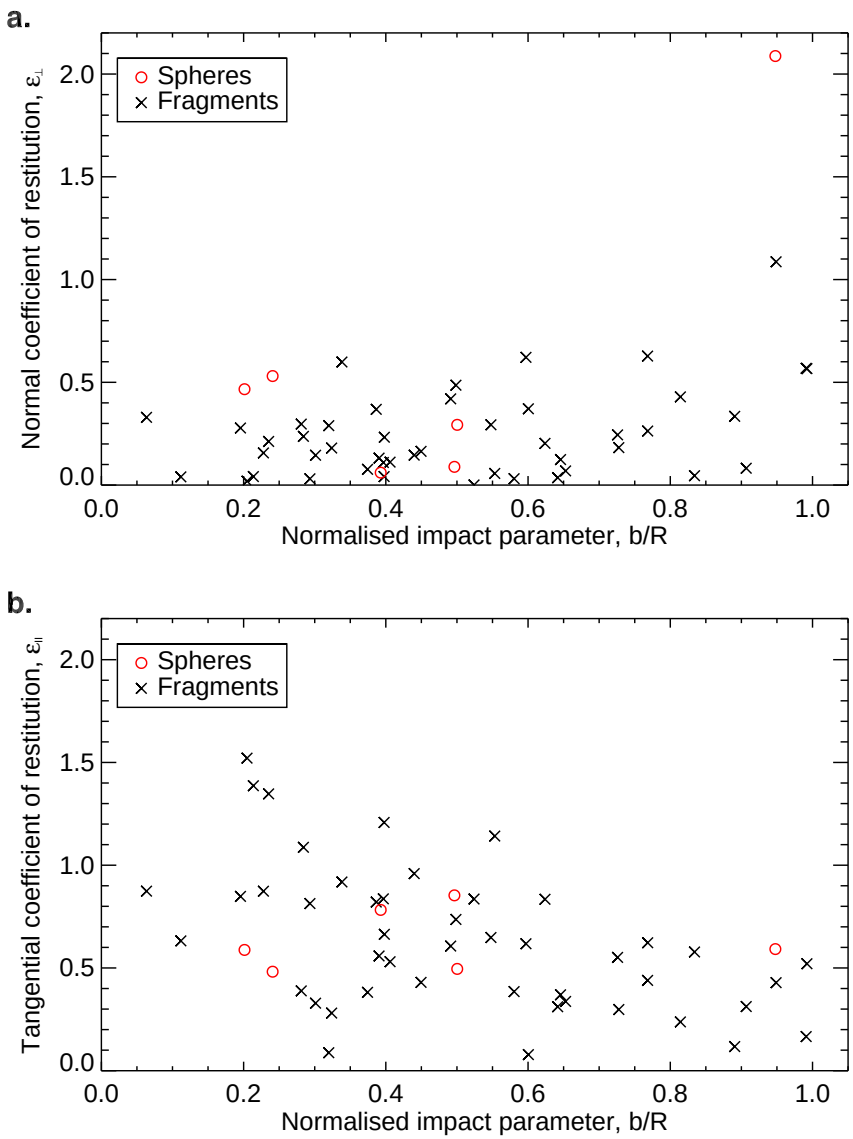

Figure 4.12: **a.** Normal coefficient of restitution as a function of normalised impact parameter. **b** Tangential coefficient of restitution as a function of normalised impact parameter.

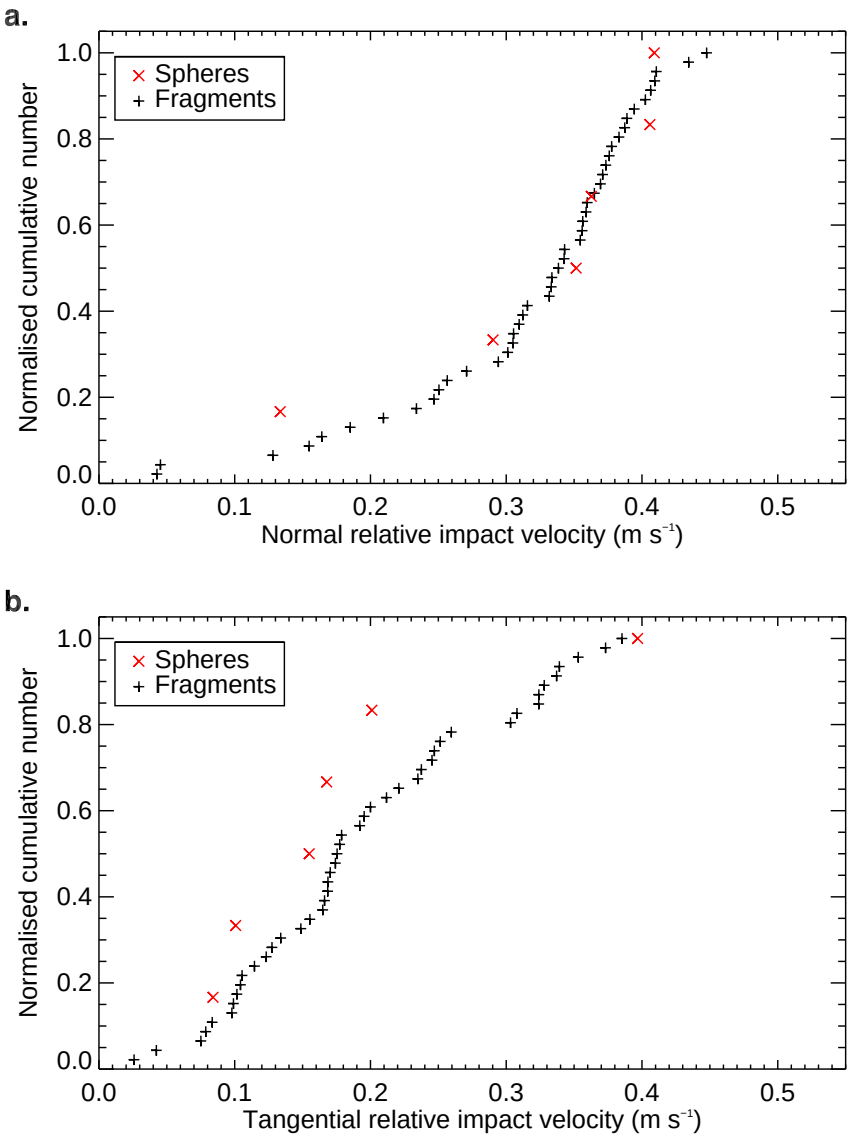

Figure 4.13: Normalised cumulative number for collisions with **a.** normal relative impact velocity $\leq v_{\perp}$ **b.** tangential relative impact velocity $\leq v_{\parallel}$.

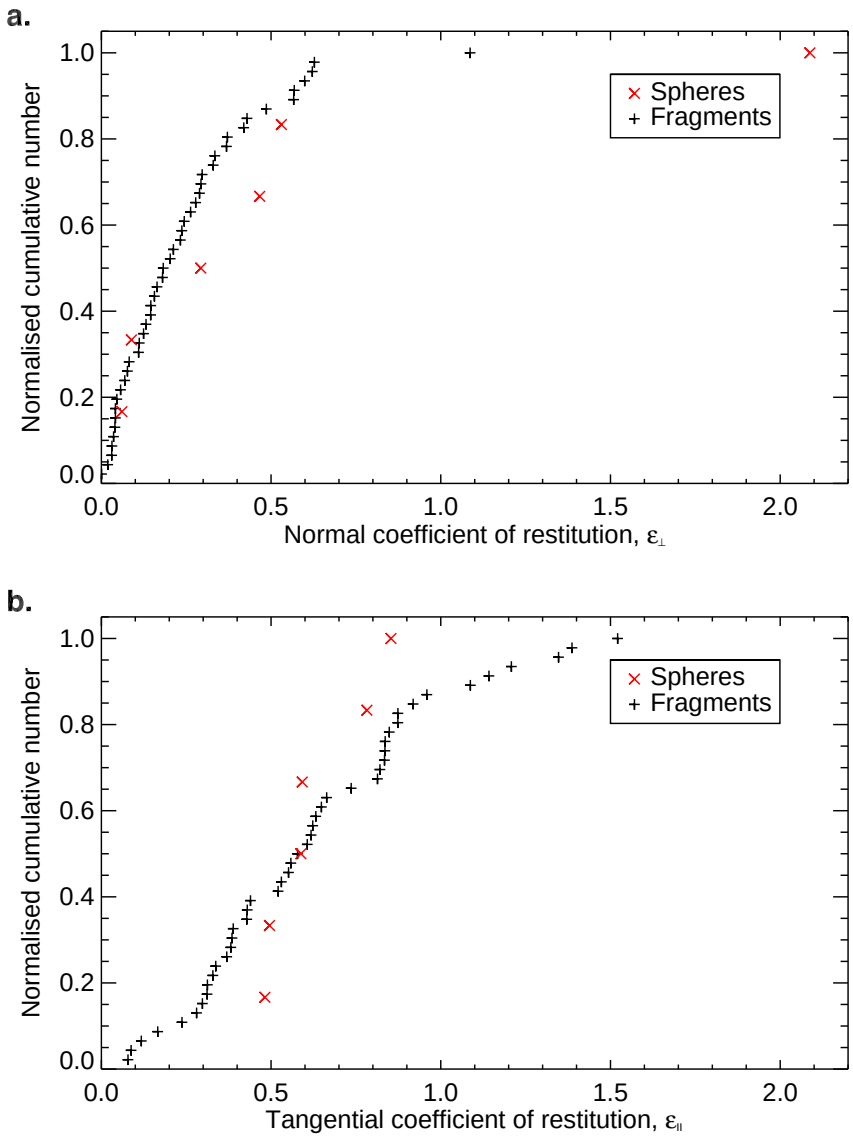

Figure 4.14: Normalised cumulative number for collisions with **a.** normal coefficient of restitution $\leq \varepsilon_{\perp}$ **b.** tangential coefficient of restitution $\leq \varepsilon_{\parallel}$.

4.4.2 Rotation

In simulations, ice particles can convert translational kinetic energy into rotational kinetic energy in collisions, with particles with normalised impact parameters greater than 0.5 tending to rotate (Schäfer et al., 2007). However, before this work, ice particle rotation had not been studied experimentally in a quantitative way. This is likely to be because of the considerable challenges inherent in measuring particle rotation. It is fairly straightforward to determine by visual inspection of the collision videos whether or not a particle is rotating, but the extent of the rotation is more difficult to determine.

Table 4.3: Percentage of particles involved in binary collisions that rotate and do not rotate before and after the collision.

	Rotates (%)	Does not rotate (%)	Unclear (%)
Before	10	89	1
After	84	6	10

Table 4.3 shows the percentage of particles rotating before and after collision for the binary collisions that were discussed in the preceding section. The majority of the particles (89%, 93 out of 104) did not rotate before the collision but after collision, most particles (84%, 87 out of 104) were rotating. All of the particles that were rotating before the collision were still rotating after the collision; collision did not stop particle rotation in any case. In all cases, there was at least one particle rotating after the collision; all collisions resulted in at least some rotation.

To take the analysis further and quantify the rotational energy possessed by a particle is far from straightforward. The particle must be rotating within one of the fields of view of the camera and must have a distinguishing mark that allows it to be tracked. The method of ice particle production used here does not allow the particles to be marked (such marking would change the ice structure and hence its collisional properties) which effectively prevents rotational information being extracted for the spheres. However, the irregular shapes of the ice fragments lend themselves to such tracking, allowing rotational energies to be extracted. To determine how much energy is converted into rotational energy after a collision, the rotation of both particles must be tracked

before and after the collision. This condition excludes some collisions where it is not possible to track the rotation of both particles throughout. In total, it was possible to track sufficient particle rotation in 10 cases; this is around 20% of the total number of collisions so should provide a representative sample. The translational kinetic energy and rotational energy before and after the collision was calculated as percentages of the original energy (translational plus rotational) before the collision as described in Chapter 2.

Table 4.4 shows the translational and rotational kinetic energy before and after the collision as a percentage of the total kinetic energy before the collision (translational plus rotational), as well as the percentage of energy after the collision that remains unaccounted for. Between 0.08 and 17% of the original kinetic energy was converted into rotational energy after the collision while 4-41% of the original kinetic energy went into translational kinetic energy. This leaves between 58 and 96% of the energy unaccounted for. While some energy goes into rotation, it is clear that this cannot account for all the energy lost. It is not clear where this energy goes. Recent work by Zamankhan (2010) has indicated that most of the translational kinetic energy dissipated in collision goes into fracturing the ice surfaces. This cannot be confirmed or refuted here as such surface fracturing would not be visible in the video images (and the experimental procedures mean that particles are not retrieved after collision). Other possibilities for removal of energy include compaction or localised heating leading to desorption of surface material. It is not possible to observe these effects with the current apparatus but it provides interesting questions for future studies.

Table 4.4: Energy breakdown before and after the collision. The energies are shown as a percentage of the total translational and rotational kinetic energy before the collision. Coefficients of restitution are also shown for comparison.

Case number	Translational energy before (%)	Rotational energy before (%)	Translational energy after (%)	Rotational energy after (%)	Unaccounted for energy after (%)	Coefficient of restitution
1	100.00	0.00	8.14	17.17	74.68	0.29
2	94.02	5.98	26.60	1.70	71.70	0.53
3	100.00	0.00	9.95	3.33	86.72	0.32
4	100.00	0.00	2.54	1.55	95.91	0.16
5	100.00	0.00	5.12	1.31	93.57	0.23
6	100.00	0.00	3.73	0.08	96.18	0.19
7	100.00	0.00	31.22	3.80	64.98	0.56
8	100.00	0.00	5.78	2.60	91.62	0.24
9	100.00	0.00	41.43	0.20	58.37	0.64
10	100.00	0.00	19.51	12.57	67.92	0.44

4.4.3 Fragmentation

The vast majority of the particle collisions in this study resulted in bouncing. However, in 4 cases, collision resulted in fragmentation. In one case, the fragmentation resulted in the total break up of one particle (shown in Fig. 4.15). The other three cases showed only small amounts of fragmentation. Research on dust aggregation has shown that dust particles will fragment when collided above a certain velocity (Blum & Wurm, 2008; Beitz et al., 2011; Schräpler et al., 2012). The same is true of ice particles; Higa et al. (1998) found that the critical velocity for fragmentation was 1.24 m s^{-1} for ice spheres of 2.8 mm diameter and 0.702 m s^{-1} for ice spheres of 8 mm diameter. The ice particles in this study are between 4.7 and 10.8 mm in diameter, so a similar critical velocity for fragmentation would be expected.

However, the fragmentation events observed resulted from collisions at relative velocities between 0.34 and 0.42 m s^{-1}. These values are within the range of velocities that resulted in bouncing for the remainder of the collision events and are well below the value of 0.702 m s^{-1} that would be expected for fragmentation. Therefore, it is likely that these ice particles fragmented on collision because they were already structurally compromised before collision; e.g. they had already become partially fractured in their creation.

It is only possible to observe particle fragmentation when the fragments are larger than the observable pixel size of the camera, i.e. 39×39 μm^2. It is possible that fragmentation occurs on a level smaller than this in many of the collisions. Such fragmentation would require an input of energy to take place and so this would provide a partial explanation for the dissipation of energy after the collision.

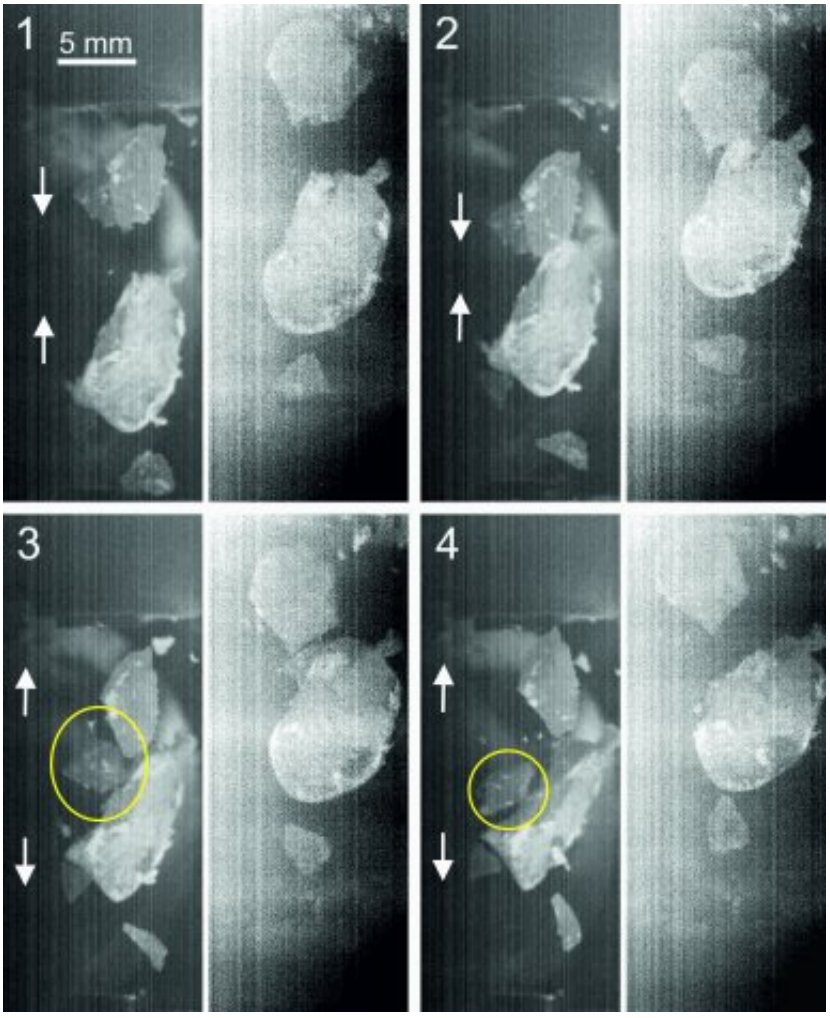

Figure 4.15: Image sequence of a collision between two ice fragments with a relative velocity of 0.42 m s^{-1} that resulted in fragmentation (one fragment is shown circled in yellow). Beam splitter optics were used to capture two views of the collision with the view shown on the left separated from the view shown on the right by 60°. The time difference between each successively numbered image is 1/107 s. The apparent offset of the two views is due to the set up of the beam splitter optics.

4.4.4 Effect of temperature

As discussed in Chapter 2, parabolic flight regulations do not permit the use of liquid nitrogen onboard the aircraft. The large copper thermal reservoir in the experiment helps to maintain a low temperature but there is an inevitable increase in the internal temperature of the chamber during the flight. This provides the opportunity to study the effects of temperature on the collisional properties of the ice.

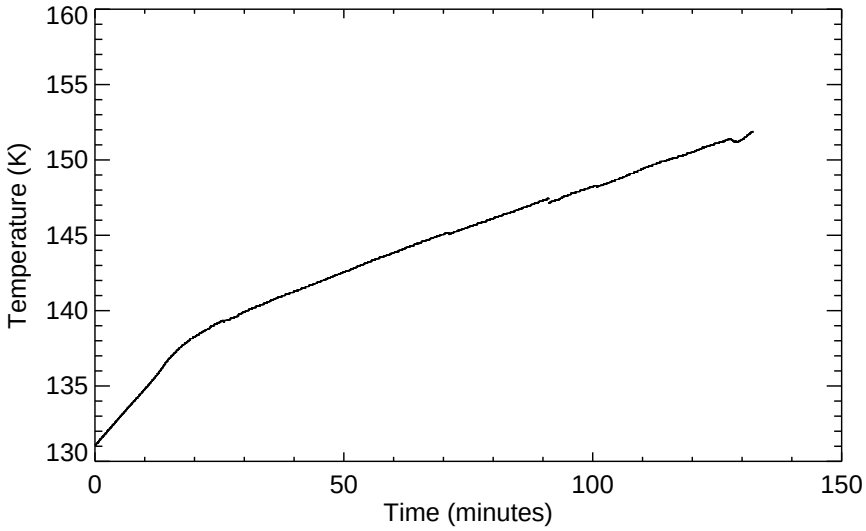

Figure 4.16: Increase in temperature over the course of the flight. The rate of temperature increase is 22.5 K h^{-1} for the first 20 minutes and 7.0 K h^{-1} for the remainder of the flight.

Fig. 4.16 shows the increase in temperature over time for the second flight on this campaign. The temperature increased at a rate of 22.5 K h^{-1} for the first 20 minutes and at a rate of 7.0 K h^{-1} for the remainder of the flight. The total temperature range was from 131 to 160 K. The discrepancy between the starting temperature (131 K) and the temperature to which the experiment was originally cooled (77 K) is due to the time taken to load the experiment onto the plane and for the plane to take off and travel to suitable airspace to execute the parabolas.

Fig. 4.17 shows the coefficients of restitution as a function of temperature. The correlation coefficient is $0.014(2) \pm 0.0004$ for the fragments: there is no correlation between coefficient of restitution and temperature over the range 131-160 K. The tem-

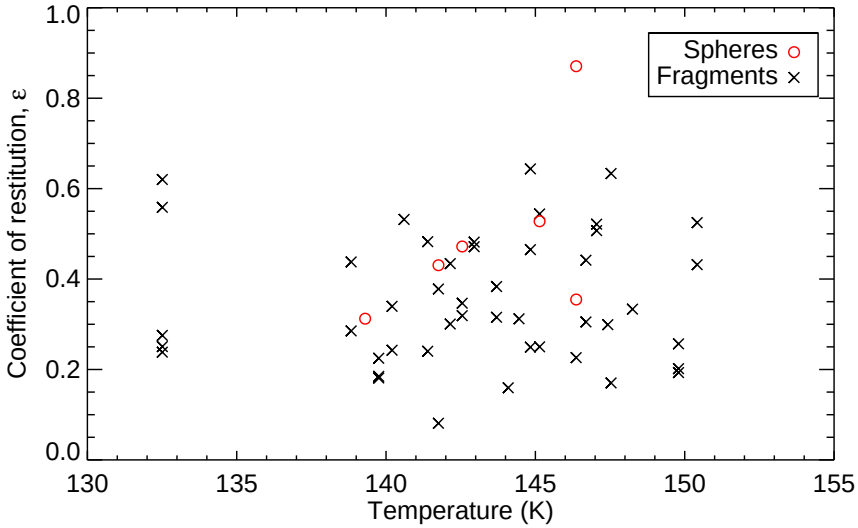

Figure 4.17: Coefficient of restitution as a function of temperature. No correlation was found between the two parameters.

peratures and pressures (10^{-5} mbar) in the chamber are too low for surface melting to take place. According to the phase diagram of water, surface melting could not take place below 10 mbar and around 260 K (Ehrenfreund et al., 2003), well above the temperatures and pressures in the current work. Sublimation (which could alter the surface and potentially the coefficient of restitution) would require a temperature of 175 K at a pressure of 10^{-5} mbar. Hence no changes can take place in the ice over this temperature range and hence the changing temperature has no effect. As the experiment was designed to operate over a temperature and pressure range where the ice could not melt or sublimate (Salter et al., 2009), this finding indicates that the experimental set up has produced the desired conditions.

Although temperatures in the range 131-160 K have no effect on the collisional properties of crystalline ice, it is possible that they may have an effect on the collisional properties of amorphous solid water, which has been detected in star forming regions (Smith & Wright, 2011) and around young stellar objects (Schegerer & Wolf, 2010). Amorphous solid water undergoes a phase change to cubic crystalline ice at around 137 K (Smith & Kay, 1999). If a collision takes place while this restructuring is occurring, it may be more likely to result in sticking as bonds could form between the

particle surfaces. This has already been proposed as a sticking mechanism (Supulver et al., 1997).

Finally, as previously mentioned in Section 4.2.1, the lack of temperature effects indicates that significant water condensation onto the particle surfaces did not occur during particle loading or during the course of the experiment. As temperature increases with time (Fig. 4.16), any time dependent effect will manifest itself as a temperature effect. Water condensation would be expected to reduce the coefficient of restitution (Hatzes et al., 1988) so the fact that the coefficient of restitution does not decrease with increasing temperature demonstrates that significant water condensation does not occur on the timescale of the experiment. It also shows that significant water condensation does not occur during the particle loading procedure; the experimental geometry dictates that the particles that are first to be loaded are the last to be collided. If significant water condensation occurred during this process, the collisions that occurred towards the end of the flight would be expected to have lower coefficients of restitution; the fact that they do not shows that the loading procedure is effective at preventing formation of a surface layer of condensed water vapour.

4.5 Conclusions

The question posed at the start of the chapter was: can millimetre-sized crystalline ice particles overcome the bouncing barrier in planet formation? To answer this, collisions of millimetre-sized ice spheres and fragments (4.7-10.8 mm in diameter) were carried out under microgravity conditions on parabolic flights. The apparatus was able to collide millimetre-sized particles with a broad range of normalised impact parameters (0.06-0.99) and relative impact velocities ranging from 0.26(91)$\pm$0.0009-0.50$\pm$0.02 m s^{-1}. The temperatures in the chamber were between 131 and 160 K and the residual pressure in the chamber was 10^{-5} mbar, preventing water condensation on the particle surfaces. The collisions were characterised according to relative impact velocity, coefficient of restitution, normalised impact parameter, and, where possible,

rotation. Cases of fragmentation were treated separately. The effect of temperature on the coefficient of restitution was also studied. The main conclusions of this work are as follows:

1. Particles did not stick in any case. Apart from four cases of fragmentation, universal bouncing was observed. If ice particles have a "bouncing barrier" as dust particles do, it will be below 0.26(91)$\pm$0.0009 m s^{-1} for particles of this size. Hence millimetre-sized ice particles cannot overcome the "bouncing barrier" in planet formation.

2. Coefficients of restitution ranged from 0.08$\pm$0.01 to 0.64$\pm$0.09 with an median value of 0.32 ± 0.01 (apart from one outlier with a coefficient of restitution of 0.87$\pm$0.01). The coefficients of restitution were evenly spread over this range. There was no correlation between coefficient of restitution and relative impact velocity. The rough, anisotropic surfaces of the ice particles was thought to account for the spread of coefficients of restitution and their lack of correlation with relative impact velocity. Therefore it is not appropriate to use a single value of coefficient of restitution in models of ice collisions; using a broad range would be more realistic.

3. The upper limit of coefficient of restitution was around 0.65. This is lower than was found by Heißelmann et al. (2010), where the upper limit was 0.84 for ice particles of 1.5 cm in diameter and relative impact velocities between 0.06 and 0.22 m s^{-1}. The lowering of the upper limit was thought to be because of the higher velocities in the present study, although it is possible that reduced particle size and irregular particle shape could also play a role.

4. There was no correlation between coefficient of restitution and normalised impact parameter, in contrast to previous results where glancing collisions had very high coefficients of restitution (Supulver et al., 1995). However, there was one very glancing collision ($b/R = 0.95$) with a much higher coefficient of restitution

than the others (0.87±0.01), providing some limited corroboration of the results of Supulver et al. (1995). The main factor affecting the coefficient of restitution was likely to be the particle surfaces, which outweighed any effect of normalised impact parameter.

5. Between 0.08% and 17% of the original kinetic energy was converted into rotational kinetic energy after the collision. When combined with translational kinetic energy, this leaves between 58% and 96% of the original kinetic energy unaccounted for after the collision. It is not possible to determine where this energy goes in these experiments, but it is possible that it leads to surface fracturing or surface heating and desorption of surface material.

6. Temperature did not affect the coefficients of restitution over the range studied. This is because the temperatures and pressures involved were too low for surface wetting or surface restructuring to take place.

It appears that millimetre-sized crystalline water ice particles cannot overcome the "bouncing barrier" in planet formation. However, the loss of energy in collisions may contribute towards particle "pile-ups" that can trigger planet formation via streaming and gravitational instabilities (Youdin & Goodman, 2005; Johansen et al., 2007; Nagel-Vega, 2010; Johansen & Klahr, 2011; Youdin, 2011). This work leaves a number of open questions that must be answered to fully describe collisions of icy particles in planet-forming regions. The ice particles used here were crystalline but the ice in protoplanetary regions is likely to be amorphous and may have different collisional properties. The dissipation of energy after the collision is also important. As up to 96% of the original translational and rotational energy remains unaccounted for after the collision, it is important to know where this missing energy goes. These questions are all beyond the scope of this thesis but are discussed in Chapter 10. One other obvious extension is to change the composition of the ice. Water, while abundant, is not the only molecule to have been detected in the solid phase in planet-forming environments. Collisions of ice particles incorporating two common molecules that

have been detected in protoplanetary regions (methanol and formic acid) will be the subject of the next chapter, to see if their inclusion changes the collisional properties and enables crystalline water ice particles to overcome the "bouncing barrier" in planet formation.

Chapter 5

Collisional properties of small "polluted" ice particles under microgravity conditions [1]

Protoplanetary ice (and the ice of planetary ring systems) is likely to be composed of a mixture of water ice and other chemicals. This study investigates the effects of including other chemicals within the ice particles. Collisions of 1.5 cm (diameter) ice spheres (containing either pure water, water with 5% methanol or water with 5% formic acid) with either a pure ice target or with each other were carried out on parabolic flights (as described in Chapter 2) prior to the start of this work. The data reduction, analysis and interpretation was carried out by the author of this thesis as described in Chapter 3 (with the exception of some of the particle tracking). The coefficients of restitution are compared to determine what effect, if any, including methanol and formic acid in the ice has on its collisional properties. Particle rotation and collision temperature are also discussed briefly.

[1] This chapter is based on a previously published paper(C. R. Hill, D. Heißelmann, J. Blum, H. J. Fraser (2015), "Collisions of small ice particles under microgravity conditions (II): Does the chemical composition of the ice change the collisional properties?" A&A, 575, A6) of which the author of this thesis is first author, and is the result of a collaboration between members of the Physics & Astronomy department of Technische Universität Braunschweig and the Department of Physical Sciences at The Open University.

5.1 Introduction

Understanding ice collisions is important for understanding both the process of planet formation and the dynamics and evolution of planetary ring systems. In contrast to the previous chapter, the particles studied in this chapter are 1.5 cm in diameter, meaning that their collisions are also relevant to planetary ring systems such as Saturn, where the rings consist of small icy bodies (Cuzzi & Pollack, 1978; Cuzzi et al., 1980, 2010) between 1 cm and 10 m in size (Zebker et al., 1985).

Most ice collision studies to date have focussed on collisions of pure water ice (e.g. Bridges et al. (1984); Hatzes et al. (1988); Supulver et al. (1995); Higa et al. (1996, 1998); Heißelmann et al. (2010); Hill et al. (2015a)). While water is abundant in planet-forming regions, many other simple molecules have been detected in the solid phase, including CO, CO_2, CH_3OH, CH_4, NH_3 and HCOOH (e.g. Pontoppidan et al. (2004), Oberg et al. (2011b), Aikawa et al. (2012), Noble et al. (2013)). It is therefore likely that icy particles in protoplanetary disks are composed of water ice and a multitude of these other chemicals. Further evidence for these substances being present in protoplanetary ices comes from recent work by Marboeuf et al. (2014) which found that the most abundant volatile species in planets of solar composition are H_2O, CO, CO_2, CH_3OH and NH_3. It is reasonable to assume that these species may also be present in planetary ring ices such as the rings of Saturn. While Saturn's rings are dominated by water ice, there is evidence of other species being present (Poulet et al., 2003; Cuzzi et al., 2009), particularly in the case of "old" rings which are residues from the formation of the planet. Therefore, the study of collisions of mixed ices is of relevance both to planet formation and ring system evolution.

Collisional data of mixed ices is somewhat lacking (hence the need for this study) but there is potential indirect evidence for altered collisional properties. Bridges et al. (1996) investigated the sticking properties of "frost" (i.e. condensed vapour) coated water ice at atmospheric pressure and temperatures between 110 and 150 K, and discovered that methanol frosts have stronger sticking forces (the sticking force between

two objects is the minimum force that needs to be applied to separate them) than water frosts. While no explanation for this was given, it is possible that this difference is caused by differing structural properties of these frosts, or more likely, surface melting. The melting point of methanol is 176 K at atmospheric pressure, so it is likely that the stronger sticking forces are due to surface melting. This same mechanism is responsible for ice aggregation in atmospheric clouds (Hobbs, 1965), making aggregation most efficient around the melting point of water (Hobbs et al., 1974). In protoplanetary disks and planetary rings, this process could not happen as the temperatures and pressures are too low for surface wetting to take place. The temperatures and pressures in this experiment are closer to those of protoplanetary disks and planetary rings, so the results of these experiments should be more applicable.

Methanol and formic acid have both been detected in protostellar regions in the solid phase (Schutte et al. (1999), Pontoppidan et al. (2004), Zasowski et al. (2009), Oberg et al. (2011b), Aikawa et al. (2012)) at the 1-30% abundance level relative to water ice for methanol and 1-5% level for formic acid (Boogert et al., 2008). The study presented in this chapter focusses on collisions of ice spheres containing 5% methanol or 5% formic acid and compares them with collisions of pure water ice to see if the chemical composition has any effect on the collisional properties. While many additional molecules are likely to be present, methanol and formic acid have been chosen as a starting point as they both exist in the solid phase at the temperatures at which the ice collisions experiment operates and they are both permitted on board parabolic flights. The ice particles were collided both with an ice target and with each other; the ice particles and target are described in Section 5.2, along with a brief summary of the experimental set up. The collision statistics are given in Section 5.3. In Section 5.4, the coefficients of restitution are presented and the collisional properties are discussed, comparing the collisions of the different ice compositions to see if there is any difference. In Section 5.5, the results are summarised and conclusions are drawn.

5.2 Experimental methods

The experimental set up is described in detail in Chapter 2. For these experiments, it was used in configuration 2 (shown in Fig. 2.4**b.**). Briefly, ice particles were stored in an aluminium colosseum capable of storing 64 particles in compartments of 16 mm in diameter. The set up was passively cooled with liquid nitrogen prior to take-off and was kept at cryogenic temperatures by incorporating a copper thermal reservoir. The particles were collided together using a master-and-slave driven piston assembly and the collisions were recorded with a high speed camera. For a full description of this set up, the reader is referred to Section 2.3 in Chapter 2.

5.2.1 Ice particles and target

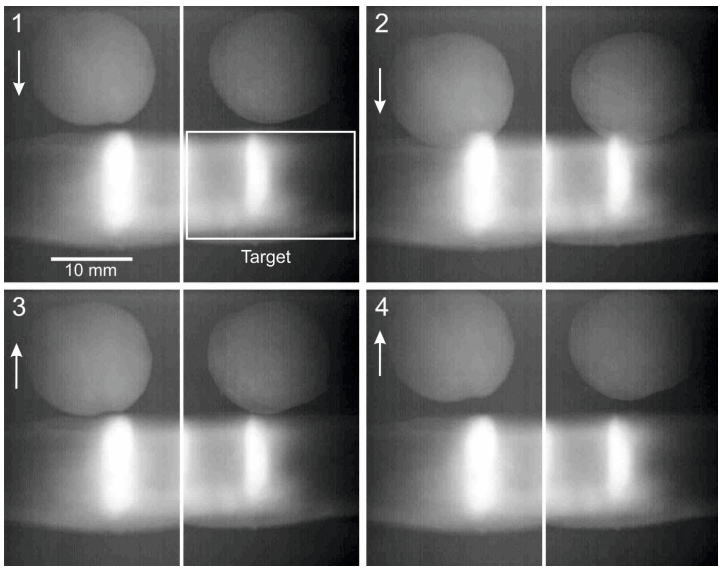

Figure 5.1: Image sequence of a collision between ice sphere containing 5% formic acid and a pure water ice target (indicated) at 90° to the direction of travel at a velocity of 0.08 m s^{-1}. Beam splitter optics were used to capture two views of the collision with the view shown on the left separated from the view shown on the right by 48.8°. The time difference between each successively numbered image is 4/107 s.

The particles used in this experiment were ice spheres with a diameter of 1.5 cm, composed of either pure distilled water or a 5% solution of methanol or formic acid in distilled water (see Fig. 5.1 for an in-flight example). The spheres were created by freezing the water/solution in spherical moulds. The moulds were composed of

two pieces of silicone with hemispherical insets that were joined together with clamps and sealed with a thin layer of Vaseline. The water/solution to be frozen was injected into the moulds through small holes in one side of the moulds. The moulds were then placed in a standard kitchen freezer to freeze the water/solution. When frozen, the silicone moulds were peeled off the ice spheres. This method of ice production produces crystalline ice with a rough, anisotropic surface (Heißelmann et al., 2010). The spheres were loaded into the colosseum as described in Chapter 2 (by storing them in liquid nitrogen and then loading them into the pre-cooled colosseum) to prevent water condensation on the particle surfaces which could affect the results.

The target was composed of pure crystalline water ice of thickness 10 mm. As described in Chapter 2, the target can be fixed in three orientations: at 90°, 60° and 30° to the direction of travel of the particles. This allows access to different normalised impact parameters. The angle (θ) between the target surface and the direction of travel of the particle is related to the normalised impact parameter b/R by Equation 3.14. Colliding a moving particle with a stationary target gives a lower relative impact velocity than colliding two moving particles with each other if the impact velocities of the individual particles are similar in both cases (see Fig. 5.2). The target was positioned at 90° on the first day of the flight campaign (giving $b/R = 0$ - completely head-on collisions), at 60° on the second day (giving $b/R = 0.5$) and at 30° on the third day (giving $b/R = \sqrt{3}/2$). However, technical problems prevented the collection of data in the 30° orientation and the chamber had to be opened during flight to remove the target, so particle-particle collisions were performed instead. During the opening of the chamber, the particles remained inside the sealed, cold colosseum so it is very unlikely that significant water condensation could have taken place on the particle surfaces; however, this possibility cannot be immediately ruled out. Fortuitously, the ice collisions performed by Heißelmann et al. (2010) were performed using the same experimental set up, virtually identical conditions and similar ice particles (1.5 cm pure water ice spheres created in the same way as the ones in the present study) but without the opening of the chamber during flight. Comparison of the pure water ice particle-particle

collisions in the present study with those of Heißelmann et al. (2010) clearly shows that the opening of the chamber had no effect on the collisional properties of the ice particles (see Section 5.4.1).

5.3 Collision statistics

Collision velocities were significantly lower than in the previous chapter, hence it was possible to fire the pistons up to 2 times per parabola. As a target was used on the first two days, this gives a maximum of 4 collision attempts per parabola (2 on each side of the target). On the third day, a target was not used, giving a maximum of 2 collision attempts per parabola. However, the limiting factor here is the number of particles that can be stored within the colosseum (a total of 64), meaning that a maximum of 64 collisions could take place on each flight with a target (just over 2 per parabola) and 32 particle-particle collisions could take place (just over 1 per parabola). This gives a maximum of 128 target collisions and 32 particle-particle collisions (160 in total).

The collisions obtained in this campaign are shown in Table 5.1. There were 120 successful collision attempts in total. However, not all of these were suitable for analysis. Some collisions had to be excluded from the analysis because of residual acceleration of the plane. This is when the plane experiences turbulence, the quality of microgravity is poor, and the system (including the camera) moves horizontally with respect to the particles. This was a particular problem on the second day of the campaign (target surface at 60° to the particles' direction of travel), excluding 41 collisions. Other collisions were excluded for poor image quality (making it impossible to accurately track the particle(s), although with improved image analysis techniques, it may be possible to analyse such collisions in the future - see Chapter 10) and there was one case of fragmentation. This was thought to be a result of a weakness in the sphere's formation rather than a real collisional outcome and therefore it was not analysed further.

Table 5.2 gives a breakdown of the collisions suitable for analysis by target ori-

Table 5.1: Collisional outcomes observed in this study. Angles refer to the angle between the direction of travel of the colliding particle and the target surface. Collisions that were suitable for analysis are discussed in Section 5.4. The other collisions were excluded from the analysis because of residual acceleration (poor quality of microgravity), poor image quality and fragmentation.

	Collisional outcome	Number of collisions
Target surface at 90°	Suitable for analysis	35
	Residual acceleration	1
	Poor quality	4
	Fragmentation	1
Target at surface 60°	Suitable for analysis	8
	Residual acceleration	41
	Poor quality	5
	Fragmentation	0
No target	Suitable for analysis	15
	Residual acceleration	3
	Poor quality	7
	Fragmentation	0
	Total	120

entation and chemical composition. The first day of the campaign (target surface at 90°) yielded the most collisions, with a good number of each composition, enabling the effect of the different compositions to be compared. The second day of the campaign (target surface at 60°) yielded only 8 collisions suitable for analysis, all of them involving pure water. The third day of the campaign (no target) yielded 15 collisions, allowing some limited comparison between the compositions. By comparing of the collisions with different target orientations, it can be seen if the normalised impact parameter has any effect on collisional properties.

Table 5.2: Break down by chemical composition of the analysed collisions. Angles refer to the angle between the direction of travel of the colliding particle and the target surface. The ice spheres were composed of pure crystalline water ice, 5% methanol in water and 5% formic acid in water.

Collision type	Pure water	5% methanol	5% formic acid	Total
Target surface at 90°	7	10	18	35
Target surface at 60°	8	0	0	8
No target	2	8	5	15
			Total	58

5.4 Results

5.4.1 Coefficient of restitution

As in Chapter 4, the only collisional outcome observed was bouncing (apart from the single case of fragmentation discussed in Section 5.3). This means that the critical velocity for the onset of bouncing in collisions of ice spheres 1.5 cm in diameter (composed of both pure water and water with 5% methanol or formic acid) will be less than $0.01(4)\pm0.003$ m s^{-1} (the lowest velocity collision in the current study). This immediately tells us that the inclusion of methanol and formic acid at a level of 5% does not change the collisional outcome from bouncing to sticking in this velocity range. However, it is possible that the varying chemical composition has a more subtle effect on collisional outcomes.

Fig. 5.2 shows the coefficients of restitution as a function of relative impact velocity for all the collisions suitable for analysis in the current study. It should be noted that for the particle-target collisions, relative velocity is simply the velocity of the colliding particle as the target is stationary. The different target orientations and chemical compositions are represented by different symbols and colours respectively. The data previously reported by Heißelmann et al. (2010) are plotted in grey. The data in the current study covers a similar velocity range to the previous data apart from two outliers at relative impact velocities around 0.01 m s^{-1}. There are two distinct velocity groupings in the current study: a low velocity group between 0.05 and 0.10 m s^{-1} and a high velocity group between 0.15 and 0.19 m s^{-1}. This is because when the piston velocities (and hence individual particle impact velocities) are similar, there is a difference between the relative velocity obtained when a moving particle collides with a stationary target (the low velocity group) and when two moving particles collide with each other (the high velocity group). The upper limit of coefficient of restitution in this study is around 0.81; this is very similar to the upper limit of coefficient of restitution in the results of Heißelmann et al. (2010) of 0.84.

A first look at the data in the current study shows no obvious differences between

the coefficients of restitution obtained for the different chemical compositions. As there is a good overlap between the coefficients of restitution for the two different target orientations, it is concluded that that changing b/R from 0 to 0.5 does not affect the coefficient of restitution.

Comparing the particle-particle data in the current study with that of the previous particle-particle data reveals no significant differences. Hence it is concluded that the brief opening of the chamber to remove the target during this flight did not cause the particle surfaces to become significantly covered in a layer of condensed water vapour which would have affected the results; if this had happened during that time, the coefficients of restitution would be expected to be lower, as seen in the results of Hatzes et al. (1988), where coating the ice particles in a "frost" layer reduced the coefficient of restitution.

Figs 5.3 and 5.4 show the cumulative plots of the relative impact velocities and coefficients of restitution respectively. Apart from two outliers with impact velocities between 0.01 and 0.02 m s^{-1}, the impact velocities are spread evenly between 0.05(1)$\pm$0.001 and 0.10(0)$\pm$0.003 m s^{-1} for the target surface at 90° (Fig. 5.3.a.). For the target surface at 60°, the impact velocities are spread evenly between 0.071$\pm$0.005 and 0.078$\pm$0.003 m s^{-1} with a couple of outliers above 0.09 m s^{-1} (Fig. 5.3.b.). The impact velocities are spread evenly between 0.15(2)$\pm$0.005 and 0.17(0)$\pm$0.005 m s^{-1} for the data with no target, with a couple of outliers above 0.18 m s^{-1} (Fig. 5.3.c.). The coefficients of restitution are evenly spaced between 0.24(4)$\pm$0.007 and 0.48(0)$\pm$0.01 and between 0.56(1)$\pm$0.001 and 0.61(0)$\pm$0.002 with outliers below 0.20 and above 0.70 for the target surface at 90°(Fig. 5.4a.), between 0.30(4)$\pm$0.007 and 0.63(4)$\pm$0.002 for the target surface at 60° (Fig. 5.4b.), and between 0.22$\pm$0.03 and 0.47$\pm$0.01 with an outlier around 0.60 for no target. The similar spreads of coefficient of restitution obtained for the collisions with a target and collisions without shows that colliding a sphere with a larger target has the same effect as colliding two spheres together; a result that is unsurprising considering the similarity in contact areas in both cases. Once again, these graphs do not reveal any differences between the chemical compositions.

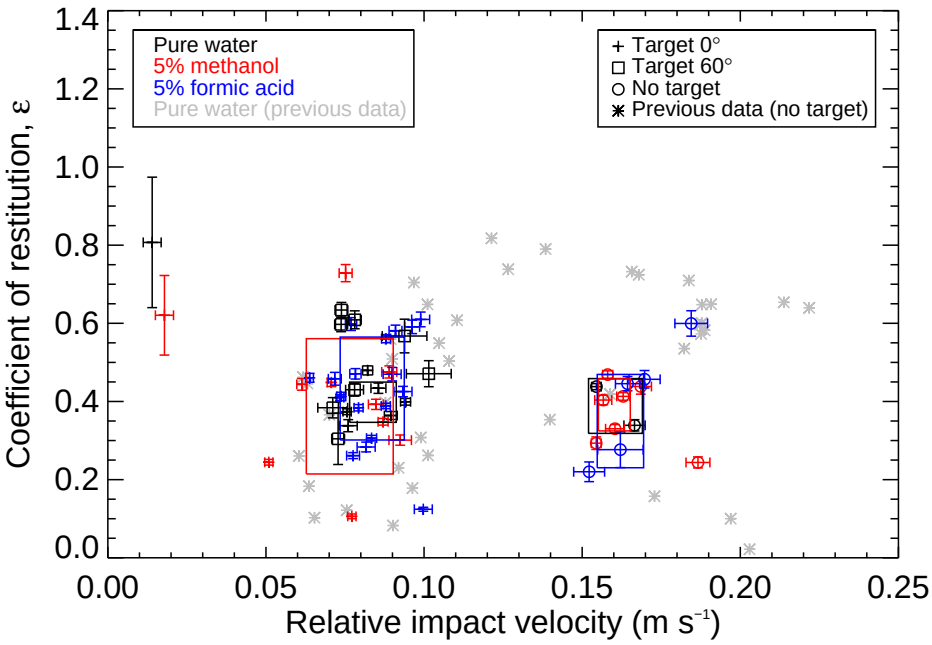

Figure 5.2: Coefficient of restitution as a function of relative impact velocity for collisions of 1.5 cm (diameter) ice spheres of varying chemical compositions with a pure water ice target. Collisions were performed with the target surface at 90° to the direction of travel (b/R = 0, shown by crosses), at 60° to the direction of travel (b/R = 0.5, shown by squares) and without a target (i.e. particle-particle collisions) (both this data (shown by circles) and data previously reported by Heißelmann et al. (2010) (shown by stars)). The chemical composition of the ice spheres is indicated by the colour of the symbol (black for water, red for methanol, blue for formic acid and grey for the previous data). The rectangles (black for pure water, red for 5% methanol in water and blue for 5% formic acid in water) show the data encompassed by one standard deviation of the mean (excluding any outliers) for the target surface at 90°to the direction of travel and for the particle-particle collisions (this study only).

For each composition and collisional set up, the mean and standard deviation of the mean were calculated. The rectangles on Fig. 5.2 show the data encompassed by one standard deviation of the mean. Comparing the data encompassed by one standard deviation of the mean shows if there are any significant differences in how each data set is spread. The outliers mentioned above were excluded from this analysis. There is also no rectangle plotted for the target surface at 60° as the only collisions suitable for analysis were those of pure water so the effect of chemical composition cannot be compared for this collisional set up. For the target surface at 90° and for the particle-particle collisions, there is a good overlap between all three rectangles. This shows

that there is no statistically significant difference between the collisional properties of pure water ice spheres and ice spheres incorporating 5% methanol or formic acid.

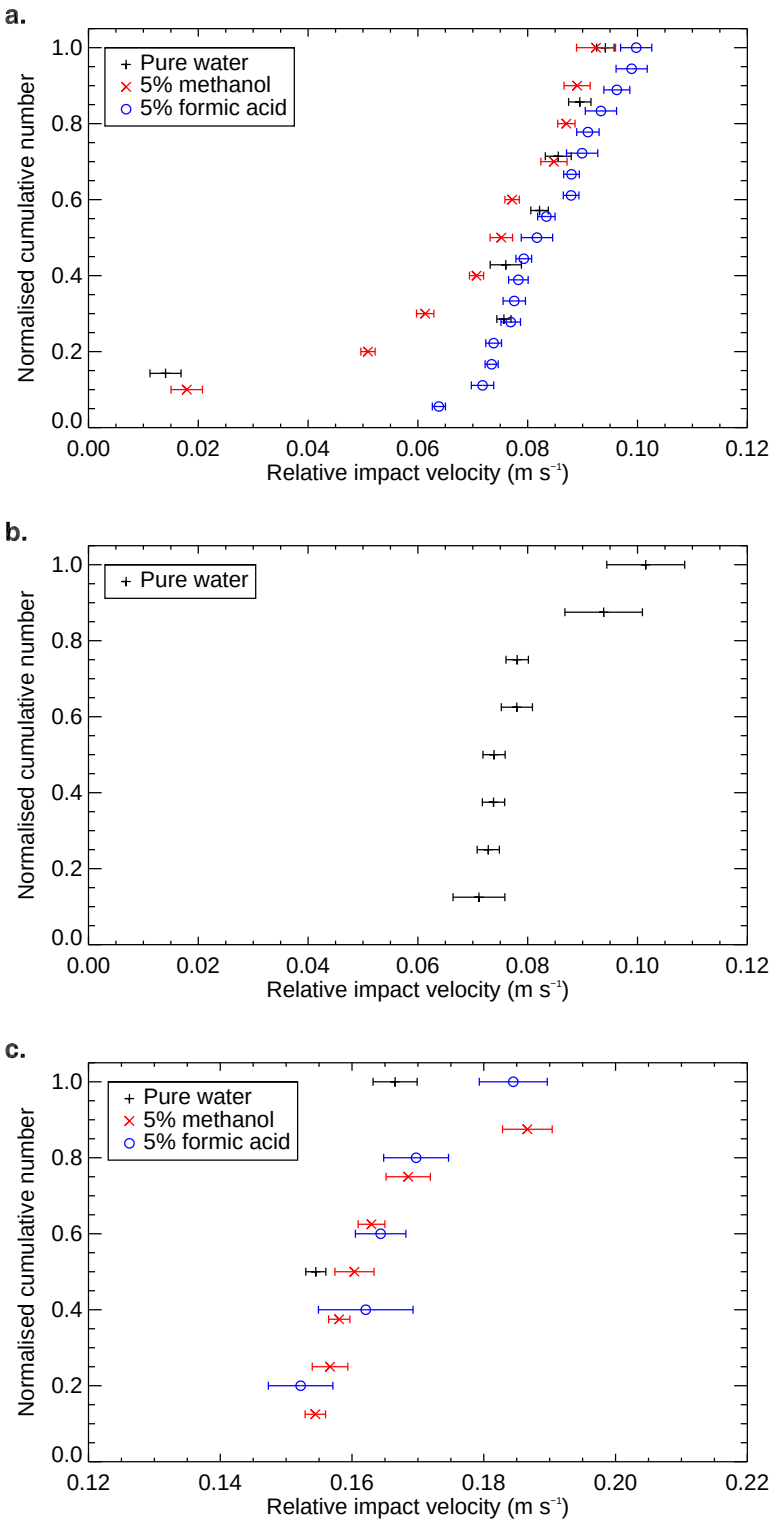

Figure 5.3: Normalised cumulative number for collisions with relative impact velocity $\leq v$. The chemical composition of the ice spheres is indicated by the colour of the symbol: black for water, red for methanol and blue for formic acid. **a.** Collisions of ice spheres with a target at 90° to the direction of travel. **b.** Collisions of ice spheres with a target at 60° to the direction of travel. **c.** Collisions of ice spheres with each other.

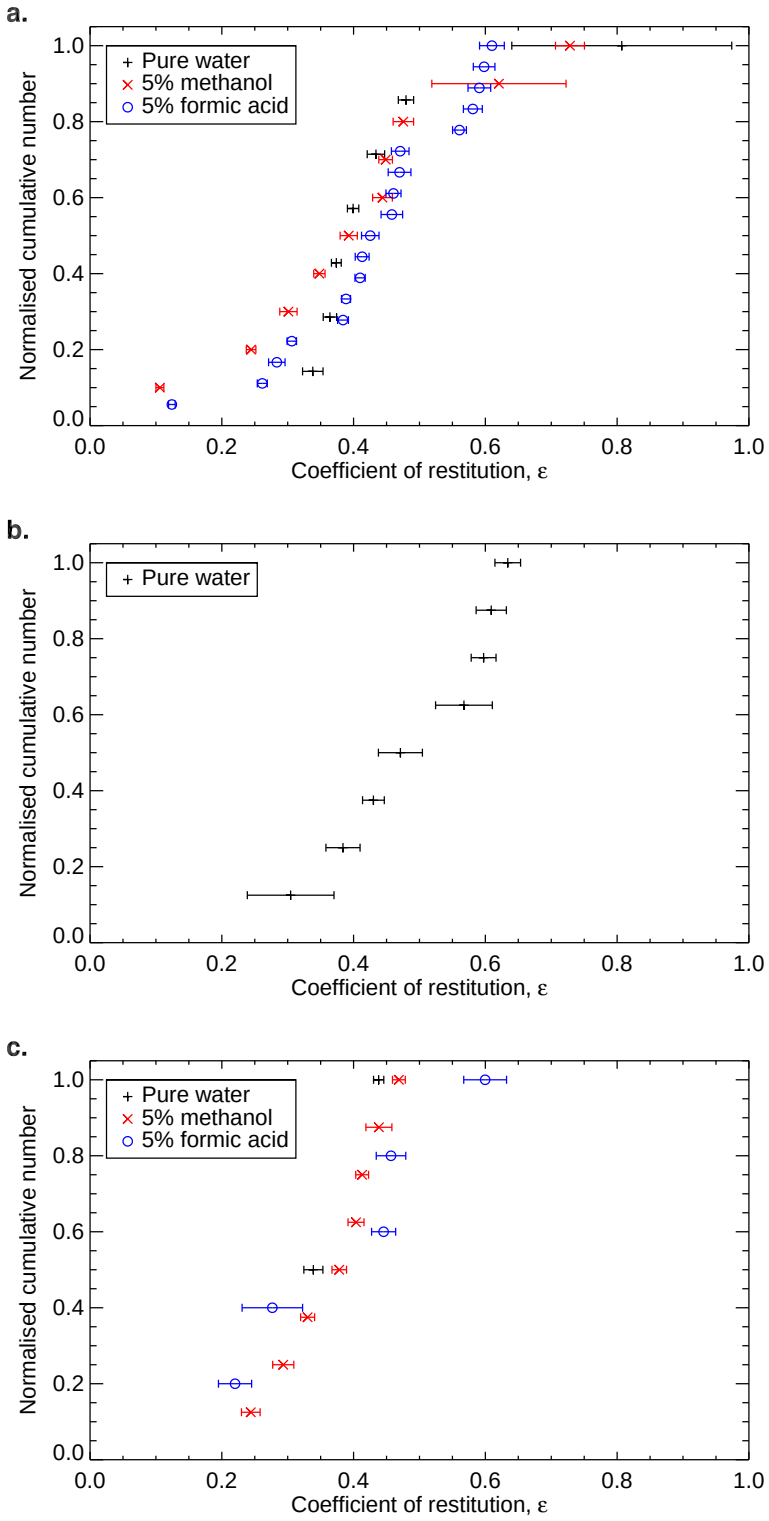

Figure 5.4: Normalised cumulative number for collisions with coefficient of restitution $\leq \varepsilon$. The chemical composition of the ice spheres is indicated by the colour of the symbol: black for water, red for methanol and blue for formic acid. **a.** Collisions of ice spheres with a target at 90° to the direction of travel. **b.** Collisions of ice spheres with a target at 60° to the direction of travel. **c.** Collisions of ice spheres with each other.

Discussion

The similarity of the ice collisions regardless of chemical composition is in contrast to the results of Bridges et al. (1996) where methanol "frosts" were found to be much stickier than water "frosts". However, given the temperature and pressure conditions in those experiments (110-150 K and atmospheric pressure), it is probable that the increased sticking forces seen were a result of surface melting. Surface melting is not possible for methanol, formic acid or water at the temperatures and pressures inside the chamber, and will not be possible in protoplanetary regions or planetary ring systems either. When considering the reasons for similarities between the data sets, it is also helpful to consider the freezing process used in creating the spheres and the probable location of the methanol and formic acid.

The temperature of a standard kitchen freezer such as that used to freeze the ice spheres is -18°C or 255 K. At this temperature, the water freezes. However, considering the phase diagram of methanol and water (Takaizumi & Wakabayashi (1997), Deschamps et al. (2010)), at this temperature, the methanol will still be liquid. The spheres will freeze from the outside in, excluding the methanol as the water freezes, leading to a water ice sphere with a liquid methanol core. When the sphere is placed into liquid nitrogen at 77 K, the methanol will freeze. Hence the surface of the ice will be essentially pure water, explaining the similarity in collisional properties.

In contrast, formic acid freezes at 282 K. This is a little higher than the freezing point of water (273 K) but it is likely that the presence of the water will slightly depress the freezing point of the formic acid. At the temperature of the freezer (255 K), both the formic acid and water will freeze and the similarity in freezing points means that the formic acid is likely to be evenly distributed through the ice. However, at a level of 5% formic acid, the structure is likely to be dominated by crystalline water ice which is similar enough to pure water ice to have similar collisional properties. The same will be true of the 5% methanol spheres if the methanol is in fact evenly distributed throughout the spheres. Tentative support for the theory that the surface of the methanol containing

ice spheres is composed of pure water but the formic acid is distributed throughout the ice can be found in Fig. 5.4**a.**, where the distribution of coefficients of restitution is similar for pure water and 5% methanol but different for 5% formic acid. If correct, this conclusion would explain why the chemical composition of the ice does not affect the collisional properties.

Correlation analysis

It has been demonstrated that the coefficient of restitution does not depend on chemical composition (for pure water, water with 5% methanol and water with 5% formic acid). The next step is to test for correlation between coefficient of restitution and relative impact velocity by computing the linear Pearson correlation coefficient using Equation 4.1. For the target surface at 90°, the correlation coefficients are 0.22 ± 0.017 for pure water, $0.06(2) \pm 0.006$ for 5% methanol and $0.05(20) \pm 0.0006$ for 5% formic acid (excluding outliers). For the target at 60°, the correlation coefficient is 0.13 ± 0.02 for pure water. For the particle-particle collisions, the correlation coefficient is 0.47 ± 0.09 for 5% methanol (excluding the outlier). The remaining data sets (particle-particle collisions for pure water and 5% formic acid) are too small for any correlation to be statistically significant. None of these values are high enough to indicate correlation and so it is concluded that coefficient of restitution does not depend on relative impact velocity over this velocity range for ice spheres of this size and these chemical compositions. As in Chapter 4, the surface roughness and anisotropy is likely to be the dominant factor in explaining the ranges of coefficient of restitution.

Normal and tangential coefficient of restitution

To give further information about the distribution of energy after the collision, the coefficients of restitution were resolved into components normal and tangential to the colliding surfaces as described in Section 3.3. As in Chapter 4, the normal coefficient of restitution gives information about particle rebound and the tangential component gives information about particle scattering. The normal and tangential coefficients of

restitution as a function of normal and tangential relative impact velocity respectively are shown in Figs. 5.5 and 5.6. In the cases of the target surface at 90° ($b/R = 0$) and the particle-particle collisions ($b/R = 0.0 - 0.33$), there is a small tangential component of relative impact velocity compared to the normal component (Figs. 5.5 and 5.6**a** and **c**). This is to be expected as these collisions are head-on (or nearly head-on) so most of the impact velocity is normal to the colliding surfaces. In these cases, there is a large spread of tangential coefficients of restitution (from around 0.10 to 1.3 for the target surface at 90° and from around 0.2 to 1.1 for particle-particle collisions). The spread of the normal coefficients of restitution is much lower (from around 0.0 to 0.60 for the target surface at 90° and from around 0.00 to 0.70 for particle-particle collisions). Therefore, head-on (or nearly head-on) collisions can result in both scattering and rebound. Energy can be transferred from rebound to scattering, as shown by the tangential coefficients of restitution that are greater than 1.The degree of scattering can vary significantly, from very little scattering to a large amount of scattering as shown by the large spread of tangential coefficient of restitution. In the case of the target surface at 60° ($b/R = 0.5$), the components of relative impact velocity are similar in size, although the normal component is on average slightly larger. The spreads of the normal and tangential coefficients of restitution are virtually identical, around 0.30 to 0.70. Hence in this case, there is a roughly equal distribution of energy into scattering and rebound after the collision as the normal and tangential coefficients of restitution are similar. This shows that the way in which the energy is distributed after the collision depends on normalised impact parameter. It should be noted that there is no visible effect of chemical composition on this energy distribution.

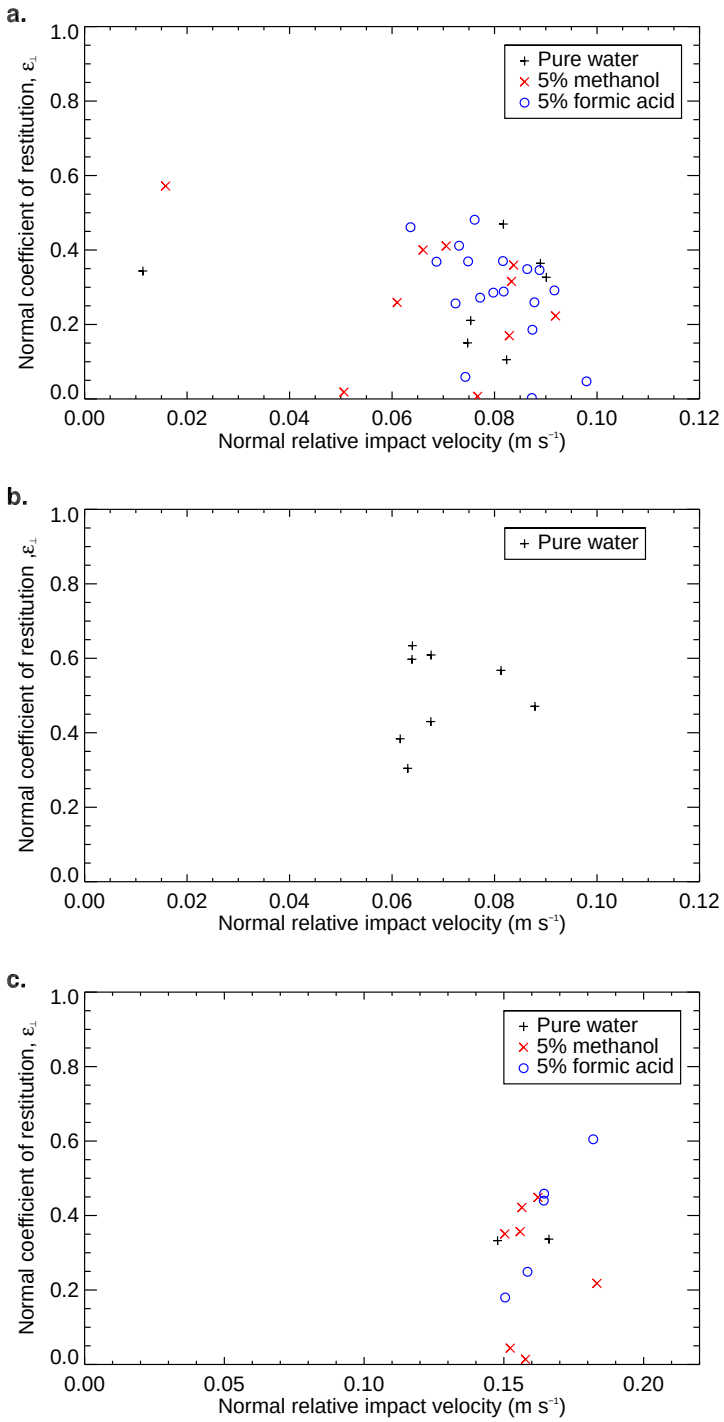

Figure 5.5: Coefficients of restitution normal to the colliding surfaces as a function of the normal impact velocity. Chemical compositions of the ice spheres are indicated by different colours and symbols: black plus symbols for pure water ice, red crosses for 5% methanol in water, and blue circles for 5% formic acid in water. **a.** Normal coefficient of restitution as a function of normal impact velocity for the target at 90° to the direction of travel (b/R = 0). **b.** Normal coefficient of restitution as a function of normal impact velocity for the target at 60° to the direction of travel (b/R = 0.5). **c.** Normal coefficient of restitution as a function of normal relative impact velocity for particle-particle collisions (b/R = 0.00-0.33).

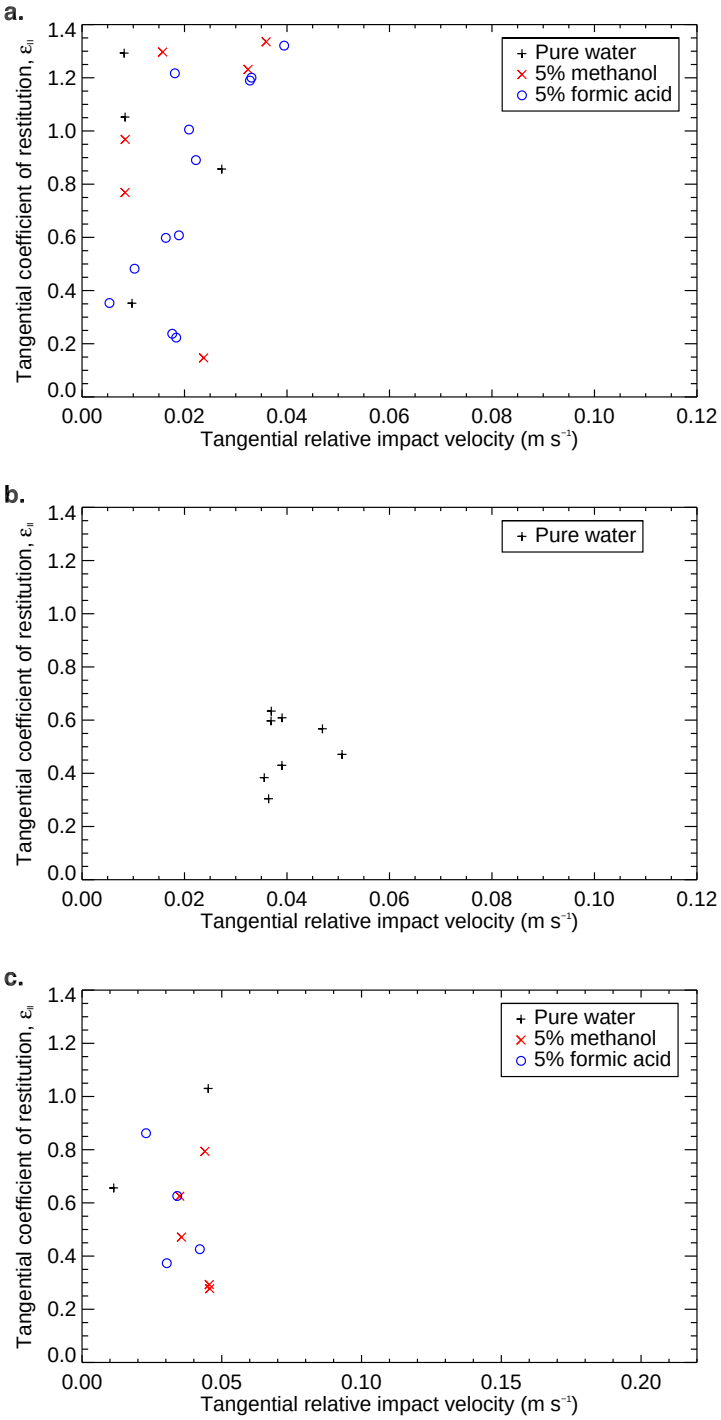

Figure 5.6: Coefficients of restitution tangential to the colliding surfaces as a function of the tangential impact velocity. Chemical compositions of the ice spheres are indicated by different colours and symbols: black plus symbols for pure water ice, red crosses for 5% methanol in water, and blue circles for 5% formic acid in water. **a.** Tangential coefficient of restitution as a function of tangential impact velocity for the target at 90° to the direction of travel (b/R = 0). **b.** Tangential coefficient of restitution as a function of tangential impact velocity for the target at 60° to the direction of travel (b/R = 0.5). **c.** Tangential coefficient of restitution as a function of tangential relative impact velocity for particle-particle collisions (b/R = 0.00-0.33).

Rotation

The last point to be considered is what happens to the translational kinetic energy lost in the collision. These results show that a minimum of 29% of the original translational kinetic energy was lost ($1-\varepsilon^2$ for $\varepsilon = 0.81$, the highest value in this study) and in some cases considerably more. In Chapter 4, it was shown that while only 10% of particles rotated before the collision, 84% were rotating afterwards and between 0.08 and 17% of the original kinetic energy was converted into rotational energy. Table 5.3 shows the percentage of particles rotating before and after the collision from the collisions suitable for analysis. The percentages are similar to Chapter 4 with 4% (5 out of 116) of particles rotating before the collision and 71% (82 out of 116) after. The percentage of cases where it is unclear whether the particles were rotating is higher than in Chapter 4 because of the spherical shape of the particles in the current study and their lack of distinguishing marks. For the same reasons it was not possible to extract quantitative information on the particle rotation for any particles in the current study. However, it is clear that some energy does go into rotation after the collision in the majority of cases. The fact that 10% (12 out of 116) of particles do not rotate after the collision indicates that, as before, rotation cannot account for all of the particles' energy loss. Once again, the hypotheses that energy goes into surface fracturing or surface heating followed by desorption cannot be confirmed or refuted with the current data.

Table 5.3: Percentage of particles from the collisions suitable for analysis that rotate and do not rotate before and after the collision.

	Rotates (%)	Does not rotate (%)	Unclear (%)
Before	4	89	7
After	71	10	19

5.4.2 Effect of temperature

As has been previously discussed (see Chapter 4 Section 4.4.4), the temperature of the chamber slowly increases during a parabolic flight as the liquid nitrogen used to cool it is not permitted on board the aircraft. Due to technical errors, temperature data was

not retained in this flight campaign so the warming profile from the previous chapter was used: temperature ranging from 131 to 160 K with a heating rate of 22.5 K h^{-1} for the first 20 minutes and 7.0 K h^{-1} for the remainder of the flight. The coefficients of restitution for the first two flights (target surface at 90° and target surface at 60°) are shown in Fig. 5.7. The differing chemical compositions and target orientations are indicated by different colours and symbols respectively. The particle-particle collisions have been excluded from this analysis because of the possibility of additional warming when the chamber was opened during flight to remove the target. The collisions from the second flight (target surface at 60°) all took place earlier in the flight than those available to analyse from the first flight. The linear Pearson correlation coefficient was computed and found to have a value of $-0.07(98) \pm 0.0002$. Therefore the coefficient of restitution does not depend on temperature over the range 131 to 160 K as before. Again, this lack of a temperature effect is likely to be because of the inability of surface melting to take place at the temperatures and pressures within the chamber.

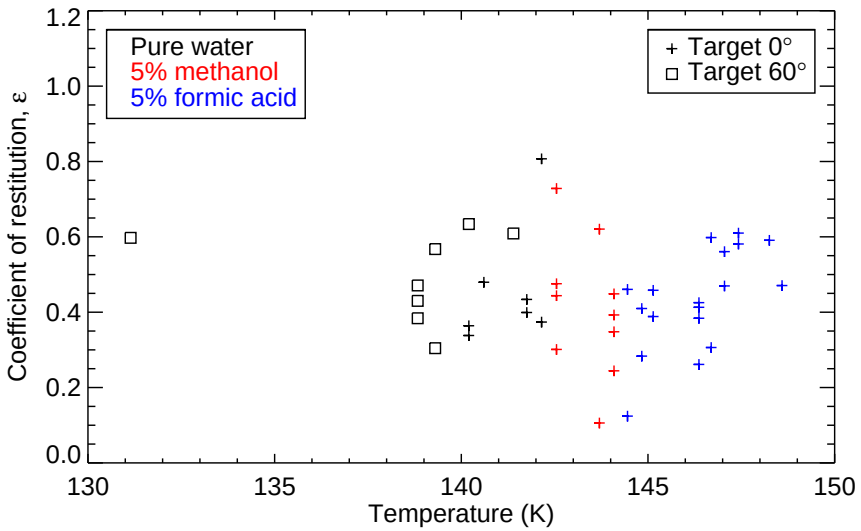

Figure 5.7: Coefficient of restitution as a function of temperature. Chemical compositions of the ice spheres are indicated by different colours: black for pure water ice, red for 5% methanol in water, and blue for 5% formic acid in water. The separation of the different chemical compositions is simply due to the order in which the particles were loaded into the colosseum (and hence the order in which they were collided). The target orientation is indicated by different symbols: a plus symbol for the target surface at 90°to the direction of travel, and a square for the target surface at 60°to the direction of travel. Particle-particle collisions are excluded from this analysis because of the possibility of additional warming when the chamber was opened to remove the target. There is no correlation between the two parameters.

5.5 Conclusions

Ice particles in protoplanetary regions and planetary ring systems are likely to be composed of water ice mixed with a plethora of other molecules which gives rise to the question: does the inclusion of these other molecules change the collisional properties and can such particles stick where pure crystalline water ice particles do not? Collisions of 1.5 cm (diameter) ice particles composed of pure water, water with 5% methanol and water with 5% formic acid with a pure ice target and with each other were carried out under microgravity conditions on a parabolic flight. As in Chapter 4, the temperature ranged from 131 to 160 K and the residual pressure in the chamber was 10^{-5} mbar, preventing water vapour condensation on the particle and target surfaces. The target was placed in two different orientations: at 90°to the direction of travel of the particles (giving $b/R = 0$) and at 60°to the direction of travel of the particles

giving $b/R = 0.5$). The particle-particle collisions had normalised impact parameters ranging from 0 to 0.33. The relative impact velocities ranged from 0.01±0.0028 to 0.19±0.0052 m s^{-1}. Collisions were characterised by relative impact velocity and coefficient of restitution.

The main conclusions of this work are as follows:

1. Universal bouncing was observed rather than particle sticking, meaning that the critical velocity for the onset of bouncing is less than 0.01(4)±0.003 m s^{-1} for ice particles of 1.5 cm in diameter. Including methanol or formic acid at a level of 5% does not change the collisional outcome from bouncing to sticking.

2. The limit of coefficient of restitution for this study (0.81) is similar to a previous study with the same sized ice particles and similar relative impact velocities (0.84) and higher than that in Chapter 4. This is thought to be because of the different velocity ranges used.

3. Changing the normalised impact parameter from 0 to 0.5 does not appear to affect the coefficients of restitution.

4. There is no observable difference between the target collisions and the particle-particle collisions, probably because the spherical shape of the particles gives rise to a similar contact area when they are collided with a flat surface or with each other.

5. Including methanol and formic acid within the ice spheres at a level of 5% does not change the coefficient of restitution. This is likely to be because the surface of the ice is either entirely composed of crystalline water ice or dominated by it in all cases, leading to similar coefficients of restitution.

6. Coefficient of restitution does not depend on relative impact velocity over the range studied. As in Chapter 4, the surface roughness and anisotropy is likely to be the dominant factor in explaining the range of coefficients of restitution.

7. Head-on collisions can both scatter and rebound, with some energy transferred from rebound to scattering in the collision. Collisions with a normalised impact parameter of 0.5 distribute energy roughly equally between scattering and rebound. Chemical composition does not affect the distribution of energy.

8. Some of the translational energy lost in the collision is converted into rotational energy but this cannot account for all the energy lost.

9. Increasing the temperature between 131 and 160 K does not affect the coefficient of restitution.

It appears that the inclusion of methanol or formic acid at a level of 5% cannot change the collisional outcome from bouncing to sticking over this velocity range and nor does it affect the coefficient of restitution. However, while the methanol ice was probably not mixed, the temperatures in protoplanetary disks and planetary rings are significantly lower than 255 K, meaning that a truly mixed ice can form. In addition, methanol has been detected in protostellar regions in the solid phase up to a level of 30% so could potentially have a greater effect on collisional properties than seen here. On the other hand, formic acid has not been detected above the 5% level and is already likely to be evenly distributed in the ice, so it is likely that the presence of formic acid will not change the coefficients of restitution. Saturn's rings are composed of 90-95% crystalline water ice (Cuzzi et al., 2010), meaning that methanol and formic acid are unlikely to be present at levels much higher than in the current study, so their inclusion will not change the coefficients of restitution in Saturn's rings.

Sticking has not been achieved for either pure ice particles of millimetre and centimetre sizes or ice particles containing 5% methanol or formic acid. However, the ice samples studied so far are crystalline, whereas at least some of the ice in protoplanetary regions is likely to be amorphous (Schegerer & Wolf, 2010; Smith & Wright, 2011). An obvious extension to this work would be to investigate collisions of amorphous solid water particles; this is beyond the scope of this thesis but is discussed in Chapter 10. As the differing structure of the ice is likely to influence the collisional

properties, it is important to understand the structure of amorphous solid water as well as possible. The remainder of this thesis focusses on the fundamental structural properties of amorphous solid water, in particular its porosity. As well as shedding light on many astrochemical processes, understanding the porosity of amorphous solid water will inform future studies on its collisional properties.

Chapter 6

Experimental methods II: neutron scattering

The porosity of amorphous solid water and the collapse of the pore network as the temperature is increased is relevant to many astronomical processes and may be relevant to the process of planet formation (see Chapter 1). Methods previously used to study porosity of amorphous solid water such as studying dangling bonds, gas adsorption and desorption, ice thickness and positron annihilation spectroscopy give somewhat limited information about the pores themselves. Neutron scattering is well suited to studying the porosity of amorphous solid water as it probes the structure of a material to give detailed structural information that other methods lack. The instrument used for these experiments is the Near and InterMediate Order Diffractometer, or NIMROD, which is based at the ISIS neutron source and is uniquely able to give structural information on a broad length scale. Amorphous solid water can either be grown in the laboratory and shipped to ISIS, or grown in situ on the beam line using a dedicated experimental set up.

6.1 Introduction

Amorphous solid water has been detected on interstellar dust grains (Leger et al., 1979), on comets (Patashni et al., 1974; Klinger, 1981; Smoluchowski, 1981; Delsemme, 1983) and planetary satellites (Smoluchowski, 1978), in star-forming regions (Smith & Wright, 2011) and around young stellar objects (Schegerer & Wolf, 2010). A key characteristic of amorphous solid water is its porosity, which decreases as the temperature is increased (Pletzer & Mayer, 1989; Buch & Devlin, 1991; Zondlo et al., 1997; Schriver-Mazzuoli et al., 2000; Ayotte et al., 2001; Horimoto et al., 2002; Hornekaer et al., 2005; Raut et al., 2007; Gálvez et al., 2008; Wu et al., 2010, 2011; Bossa et al., 2012; Mitterdorfer et al., 2014; Townrow & Coleman, 2015). Amorphous solid water grown at low temperatures is very porous (Stevenson et al., 1999; Kimmel et al., 2001) and is thought to undergo a phase change to a less porous form when the ice is heated (Jenniskens & Blake, 1994; Horimoto et al., 2002; Collings et al., 2003b). Studying the porosity of amorphous solid water is vital for understanding many astronomical processes, including the process of planet formation (see Chapter 1). Porosity in amorphous solid water has been studied using numerous experimental techniques which are discussed in detail in Chapter 1, such as studying dangling OH bonds (Buch & Devlin, 1991; Zondlo et al., 1997; Schriver-Mazzuoli et al., 2000), gas adsorption (Pletzer & Mayer, 1989; Ayotte et al., 2001; Horimoto et al., 2002; Boxe et al., 2007; Raut et al., 2007; Gálvez et al., 2008) and desorption (Hornekaer et al., 2005), ice thickness (Bossa et al., 2012; Isokoski et al., 2014) and positron annihilation spectroscopy (Wu et al., 2010, 2011; Townrow & Coleman, 2015). However, these methods cannot give information such as pore size and shape and can only give limited information about changes in porosity, including pore collapse.

Neutron scattering has previously been used to study various forms of water ice, including hyperquenched glassy water (Hallbrucker et al., 1991; Bellissentfunel et al., 1992), tetragonal ice (Besson et al., 1994), hexagonal ice (Li et al., 1994; Strauss et al., 1994; Nield & Whitworth, 1995) and amorphous solid water (Wenzel et al., 1975; El-

liott, 1995; Mitterdorfer et al., 2014). It is an ideal technique for studying the porosity of amorphous solid water as it is a non-invasive technique for probing the structure of a material, giving the detailed structural information that other studies of porosity lack. The theory of neutron scattering is described in Section 6.2.1. The neutron source used to conduct the experiments described in this thesis was the ISIS neutron source based at the Rutherford Appleton Laboratory in Oxfordshire, UK. The neutron source is described in Section 6.2.2 and the specific instrument used (the Near and InterMediate Order Diffractometer, or NIMROD) is described in Section 6.2.3. The experimental set ups for forming amorphous solid water for these experiments are presented in Section 6.3. Conclusions are drawn in Section 6.4.

6.2 Neutron scattering

6.2.1 Theory

Neutron scattering is a non-destructive technique used for probing the structure of a material. The basic concept is to place the sample under investigation in a beam of neutrons and detect the scattered neutrons at various angles. The way in which the neutrons are scattered gives information about the structure.

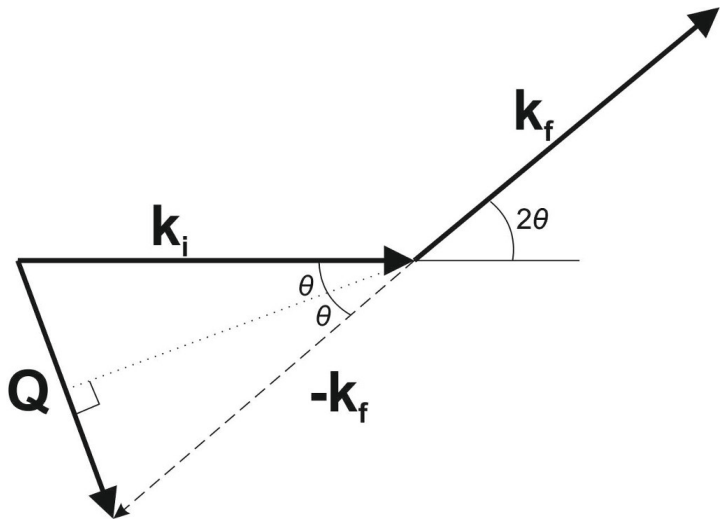

Figure 6.1: Idealised scattering case where a neutron with incident wavevector $\mathbf{k_i}$ is scattered by an angle 2θ has a scattered wavevector $\mathbf{k_f}$. $\mathbf{Q}$ is the wavevector transfer.

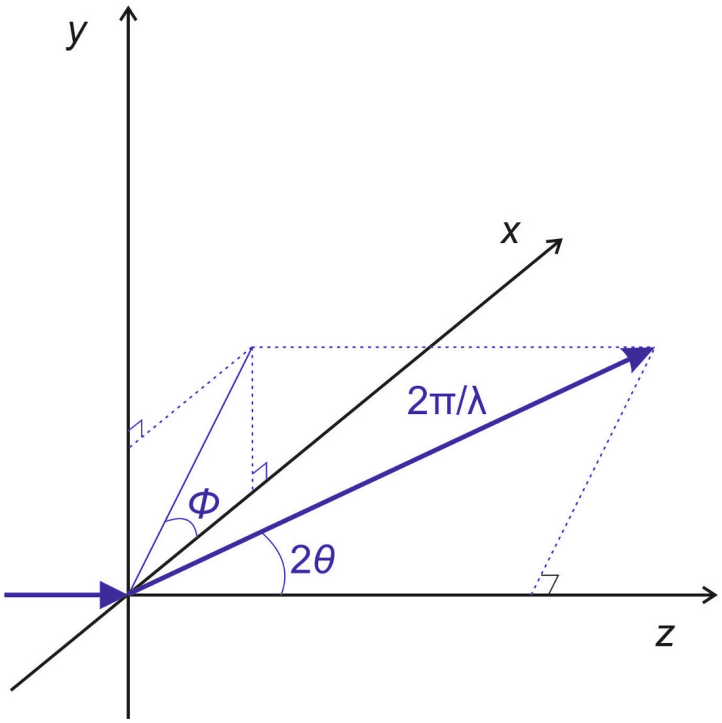

Figure 6.2: A neutron with incident wavevector $\mathbf{k_i}$ is scattered by 2θ and ϕ. It has a scattered wavevector $\mathbf{k_f}$. The z-axis has been chosen to be parallel with the incident neutron wavevector.

Fig. 6.1 shows the idealised scattering case. In this case, a neutron with incident wavevector $\mathbf{k_i}$ and angular frequency ω_i is scattered by an angle 2θ and has a scattered wavevector $\mathbf{k_f}$ and angular frequency of ω_f. The momentum transfer ($\mathbf{P}$) is given by:

$$\mathbf{P} = \hbar\mathbf{k_i} - \hbar\mathbf{k_f} = \hbar\mathbf{Q} \tag{6.1}$$

where $\mathbf{Q}$, the wavevector transfer, is given by:

$$\mathbf{Q} = \mathbf{k_i} - \mathbf{k_f} \tag{6.2}$$

The modulus of a wavevector $\mathbf{k}$ with wavelength λ is given by:

$$|k| = \frac{2\pi}{\lambda} \tag{6.3}$$

The energy transfer (E) is given by:

$$E = \hbar\omega = \frac{|\hbar\mathbf{k_i}|^2}{2m_n} - \frac{|\hbar\mathbf{k_f}|^2}{2m_n} \tag{6.4}$$

where

$$\omega = \omega_i - \omega_f \tag{6.5}$$

and m_n is the mass of a neutron. In the case of elastic scattering, the neutron does not lose any energy, hence E and ω are equal to 0. Therefore Equation 6.4 yields:

$$|k_i| = |k_f| = \frac{2\pi}{\lambda} \tag{6.6}$$

By visualising the incident and scattered wavevectors as shown in Fig. 6.1, it is possible to connect the wavevector transfer $\mathbf{Q}$ to the scattering angle θ and wavelength λ. $\mathbf{k_i}$, $\mathbf{k_f}$ and $\mathbf{Q}$ form an isosceles triangle, and by simple trigonometry:

$$Q = \frac{4\pi \sin\theta}{\lambda} \tag{6.7}$$

where $Q = |\mathbf{Q}|$.

Completely defining the scattering requires a second angle, ϕ, which measures the rotation about $\mathbf{k_i}$. This is shown in Fig. 6.2. The z-axis has been chosen to be parallel with the incident neutron, such that:

$$\mathbf{k_i} = \left(0, 0, \frac{2\pi}{\lambda}\right) \tag{6.8}$$

$\mathbf{k_f}$ is given by:

$$\mathbf{k_f} = \frac{2\pi}{\lambda}(\sin 2\theta \cos\phi, \sin 2\theta \sin\phi, \cos 2\theta) \tag{6.9}$$

Neutrons are scattered when the wavelength of the neutron is comparable to the distances between objects within the sample. These can range from atoms and small atomic structures to much larger objects such as pores, micelles and proteins. A con-

sideration of Equation 6.2 shows that as λ increases, Q decreases; so small values of Q correspond to large distances and vice versa.

A neutron scattering experiment aims to measure the number of neutrons scattered in various directions. The directions are defined by spherical polar co-ordinates 2θ and ϕ (see Fig. 6.2). The rate of arrival of neutrons scattered through angles of 2θ and ϕ into a detector that subtends a solid angle $\Delta\Omega$ steradians is given by R per unit time (s^{-1}). The differential cross section, $\frac{d\sigma}{d\Omega}$ is the ratio of the number of particles deflected by $(2\theta,\phi)$ per unit solid angle to the number of incident particles per unit area of beam (Φ):

$$\frac{d\sigma}{d\Omega} = \frac{R(2\theta,\phi)/\Delta\Omega}{\Phi} \tag{6.10}$$

The differential cross section is often quoted per atom by normalising to the number of atoms, N:

$$\frac{d\sigma}{d\Omega} = \frac{R(2\theta,\phi)}{N\Phi\Delta\Omega} \tag{6.11}$$

It can also be quoted as $I(Q)$ which has units of cm^{-1}. The cross section is related to the neutron scattering length (b) by:

$$\sigma = 4\pi|b| \tag{6.12}$$

The neutron scattering length is isotope specific, so hydrogen and deuterium have different values of b. It is specified by its mean ($\langle b\rangle$) and standard deviation (Δb):

$$b = \langle b\rangle \pm \Delta b \tag{6.13}$$

Rearranging Equation 6.13 gives:

$$\langle b^2\rangle = \langle b\rangle^2 + (\Delta b)^2 \tag{6.14}$$

Combining Equations 6.12 and 6.14 gives the average scattering cross section ($\langle\sigma_{scat}\rangle$)

as the sum of two quantities, the coherent (σ_{coh}) and incoherent (σ_{incoh}) cross sections:

$$\langle \sigma_{scat} \rangle = 4\pi \langle b^2 \rangle = 4\pi(\langle b \rangle^2 + (\Delta b)^2) = \sigma_{coh} + \sigma_{incoh} \tag{6.15}$$

The coherent cross section contains structural information while the incoherent cross section only contributes a featureless background signal. Hydrogen has a large incoherent cross section, and for this reason it is often substituted with deuterium for neutron scattering experiments.

For crystalline samples, sharp peaks are produced in the scattering signal. The positions of these peaks in Q are related to the distances between objects (d) by:

$$Q = \frac{2\pi}{d} \tag{6.16}$$

Combining Equations 6.7 and 6.16 gives Bragg's law:

$$N\lambda = 2d \sin\theta \tag{6.17}$$

which specifies the peak positions in d (N is an integer).

6.2.2 The ISIS neutron source

There are two main ways in which neutrons can be produced for neutron scattering experiments: by a nuclear reactor or by a spallation process. In a nuclear reactor, neutrons are produced through a process of neutron induced nuclear fission, where an atomic nucleus captures a neutron and splits into two nuclei, releasing high energy neutrons in the process. Typical choices for the original atomic nuclei are uranium or plutonium. An example of a reactor source is the Institut Laue-Langevin (ILL), which is situated in Grenoble in France. In a spallation source, protons are collided with a target (typically made of uranium, tantalum or tungsten), forming highly excited states which decay, producing neutrons. The ISIS neutron source (situated at the Rutherford

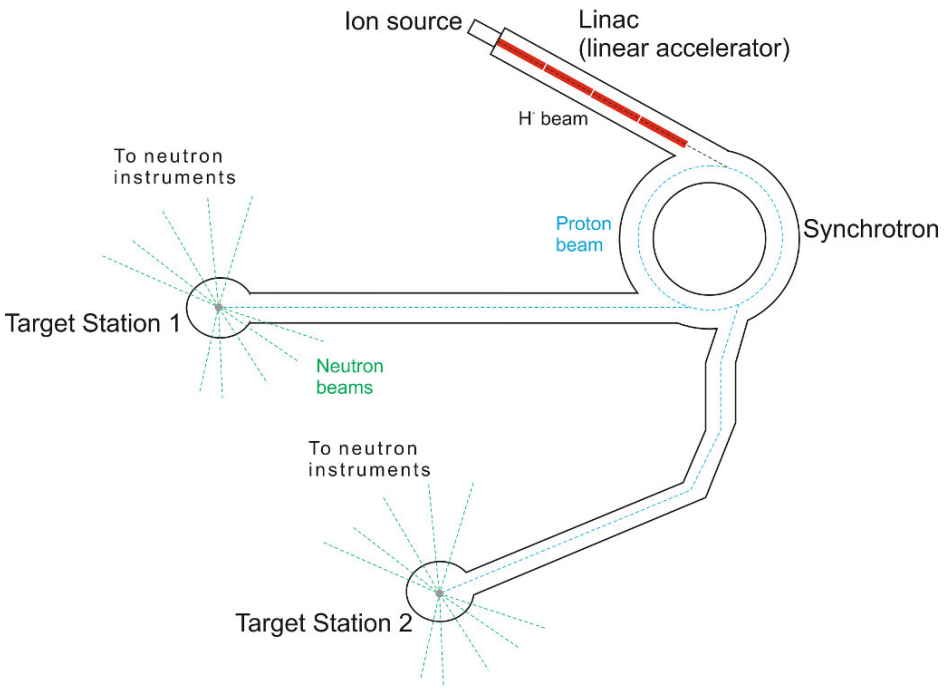

Figure 6.3: Schematic of the ISIS neutron source (not to scale). H^- ions are produced in the ion source, accelerated by the linear accelerator and passed into the synchrotron, where the electrons are removed to create a proton beam. In the synchrotron, the protons are accelerated to 84% of the speed of light. Bunches of protons are removed from the synchrotron by fast kicker magnets and directed to Target Station 1 or Target Station 2 where they collide with a tungsten target and produce neutrons. The neutrons are directed down beam lines to neutron instruments.

Appleton Laboratory in the UK and used for all the neutron scattering experiments presented in this thesis) produces neutrons by the spallation process.

A schematic of the ISIS neutron source is shown in Fig. 6.3. H^- ions are produced in an ion source that combines hydrogen gas and hot caesium vapour. A discharge plasma is formed and H^+ ions are attracted to the cathode where they receive electrons. The H^- ions are extracted in bunches and accelerated by a Radio Frequency Quadrupole accelerator (RFQ), before being passed into the linear accelerator (linac). In the linac, the bunches are further accelerated by passing through four 10 m long tanks containing copper drift electrodes. The H^- ions then enter the synchrotron, where they are stripped of their electrons on entry by a 0.3 μm thick aluminium oxide stripping foil to form H^+ ions (i.e. protons). The synchrotron consists of a 163 m circumference ring of powerful magnets that accelerate the protons to 84% of the speed of light. The proton bunches are extracted from the synchrotron by fast kicker magnets,

where they travel either to Target Station 1 or Target Station 2 and collide with a tungsten target. This excites the tungsten nuclei, and as they decay, they release neutrons which travel down beam lines to the neutron instruments.

The neutrons produced by this method are too energetic to be of use in scattering from atoms, so their energy must be reduced by use of a moderator. The moderator chosen depends on the desired neutron wavelength; a water moderator will produce neutrons of a higher energy (shorter wavelength) than a liquid hydrogen moderator.

6.2.3 The NIMROD instrument

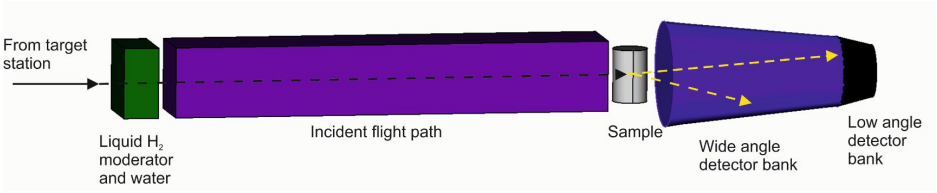

Figure 6.4: Diagram of the NIMROD instrument (not to scale). The neutrons pass through a liquid H_2 moderator and a water premoderator and travel down the beam line (grey dashed line). They are scattered by the sample (yellow dashed lines) and can be detected at low and wide angles.

The Near and InterMediate Range Order Diffractometer (NIMROD) is situated on Target Station 2 of ISIS and is depicted in Fig. 6.4. Its world-unique feature is that it is able to take measurements on a continuous length scale from <1 - 300 $Å^{-1}$ in a single measurement (Bowron et al., 2010). This is achieved by a combination of a liquid H_2 moderator at 17 K (for long wavelength neutrons) and a water premoderator (for short wavelength neutrons). Two sets of detector banks at both low and wide angles cover 2θ angles between 0.5° and 40°. The advantage of covering such a broad Q range is that NIMROD can obtain both molecular information (high Q) and mesoscale information (low Q). This makes it uniquely suitable for studying amorphous solid water, as changes relating to crystallisation are seen in the high Q region and changes relating to the pores are seen in the low Q region (as the pores are 10s of angstroms apart).

6.3 Formation of amorphous solid water

6.3.1 Formation in the laboratory

Amorphous solid water is formed in the lab by vapour deposition on a cold surface, so cold that the water molecules do not have sufficient energy to rearrange into a crystalline structure but instead stick where they fall. The amorphous solid water used in the experiments detailed in Chapter 8 was formed using the apparatus detailed in Fig. 6.5 (which is also described by Mayer & Pletzer (1984)). The ice was formed and the neutron scattering experiments carried prior to the start of this PhD. D_2O is used instead of H_2O as hydrogen has a large incoherent neutron cross section, whereas deuterium does not (see Section 6.2.1).

The D_2O vapour is deposited on a 50 mm thick copper plate that is cooled to 77 K by being in direct contact with liquid nitrogen. The copper plate is situated inside a glass vacuum chamber with a background pressure of 10^{-4} mbar. The D_2O is introduced into the chamber through a copper nozzle 13 mm in diameter by opening a needle valve connected to the D_2O reservoir so that the inlet pressure rises to 0.1 mbar (measured by a pirani manometer). The vapour is deposited for between 24 and 30 hours at a rate of 40 μm per hour. Placing a baffle between the D_2O entry point allows background deposition to take place. This causes the D_2O clusters that are released from the copper nozzle to break up into monomers so that mostly single water molecules are deposited (Mayer & Pletzer, 1984).

After deposition, the ice is scraped off the deposition plate with a spatula under liquid nitrogen. The ice is stored under liquid nitrogen, shipped to ISIS and then transferred to a null-scattering (i.e. it allows neutrons to pass through without being scattered) TiZr alloy cell (also under liquid nitrogen) which is placed in a helium cryostat, maintaining the sample temperature of 77 K. The cryostat is then placed on the beam line.

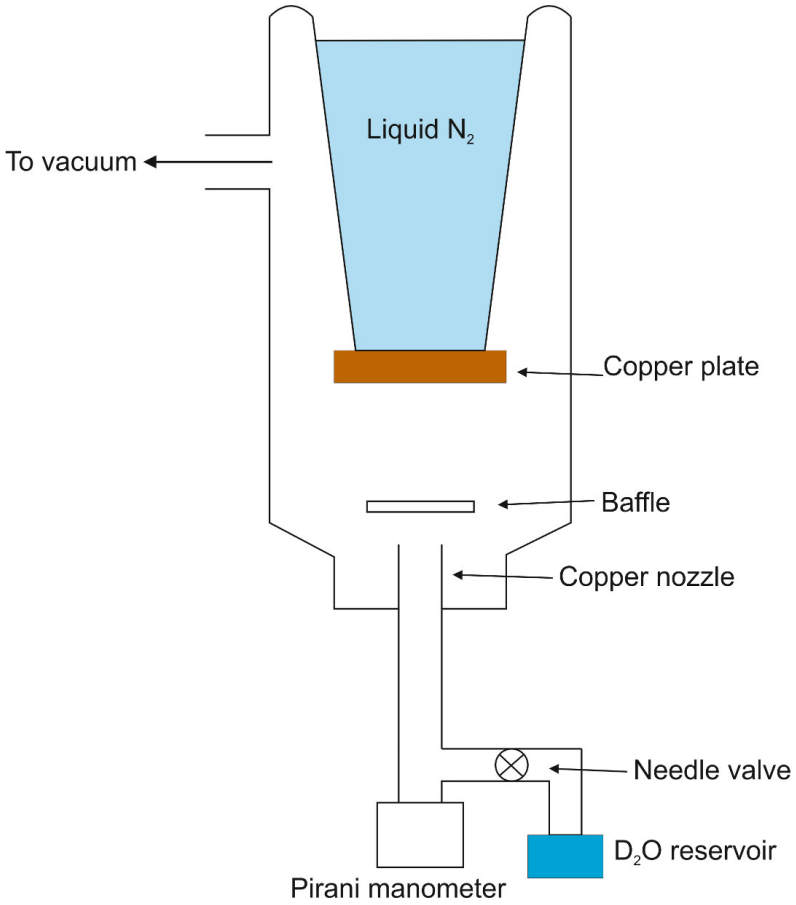

Figure 6.5: Diagram of the experimental set up used to prepare amorphous solid water in the laboratory. The set up consists of a copper plate that is cooled with liquid nitrogen and sits inside a glass vacuum chamber. The D_2O vapour enters through a copper nozzle from a liquid D_2O reservoir, passing around a baffle to ensure background deposition. Adapted from Mayer & Pletzer (1984).

6.3.2 Formation on the NIMROD beam line

Ice grown at 77 K can be transported under liquid nitrogen, maintaining a constant temperature so that the ice is stable. Transporting ice at temperatures below 77 K is far from straightforward as this is below the temperature of liquid nitrogen. Therefore, the following set up was developed to grow ice in situ on the NIMROD beam line. This has the added advantage of being able to study the ice as it forms. This apparatus was used by the current author to perform the experiments detailed in Chapter 9 in conjunction with an experimental team comprising scientists from The Open University and the ISIS neutron source. An overview of the set up is shown in Fig. 6.6. The ice is grown on a cold plate, cooled by a cryostat. The cold plate sits inside a vacuum chamber on

the beam line. D_2O vapour is passed in through the top flange.

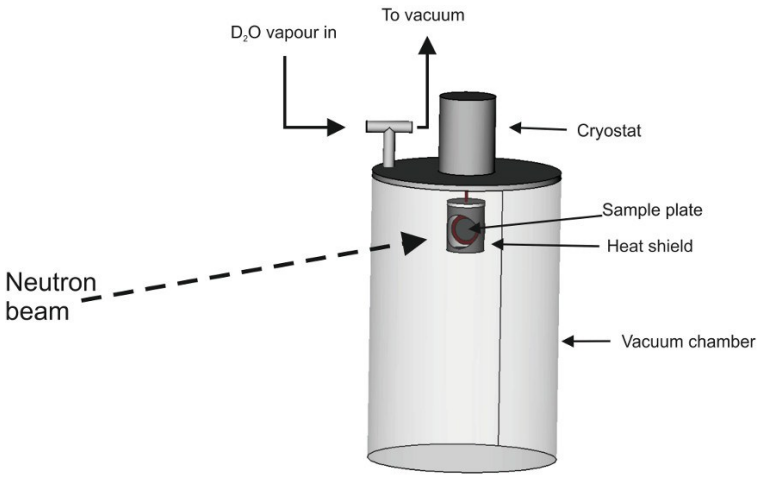

Figure 6.6: Computer aided design (CAD) schematic of the vacuum chamber on the NIMROD beam line. The ice is grown on the sample plate which is cooled using the cryostat. The D_2O vapour enters the vacuum chamber through the top flange.

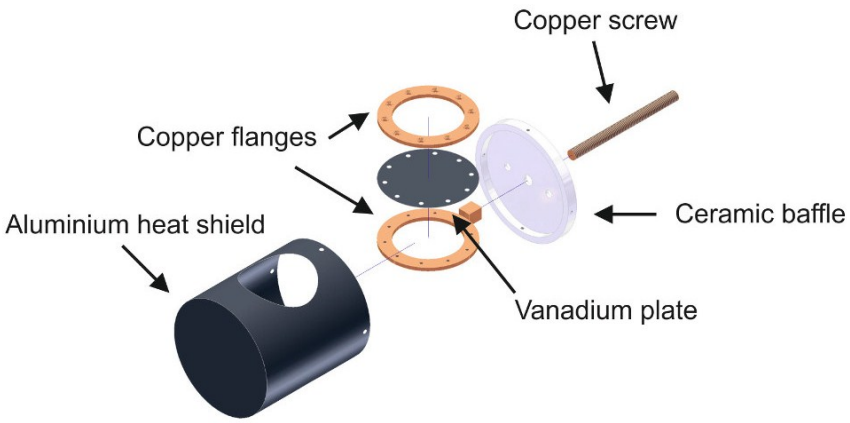

Figure 6.7: Computer aided design (CAD) schematic of the vanadium plate on which the ice is grown, aluminium heat shield and associated components. This schematic was produced by Chris Goodway of the pressure and furnaces group at ISIS and was labelled by the current author.

The system on which the ice is grown is shown in Figs. 6.7 and 6.8. The ice is grown on a 0.1 mm thick vanadium plate that is 70 mm in diameter. Vanadium is used because it has a very small coherent scattering length, so the differential cross section is mostly flat; hence it does not significantly contribute to the scattering signal. The vanadium plate is held in place by two copper flanges which are attached to the head of a helium cryostat with a copper screw. The vanadium plate is surrounded by an

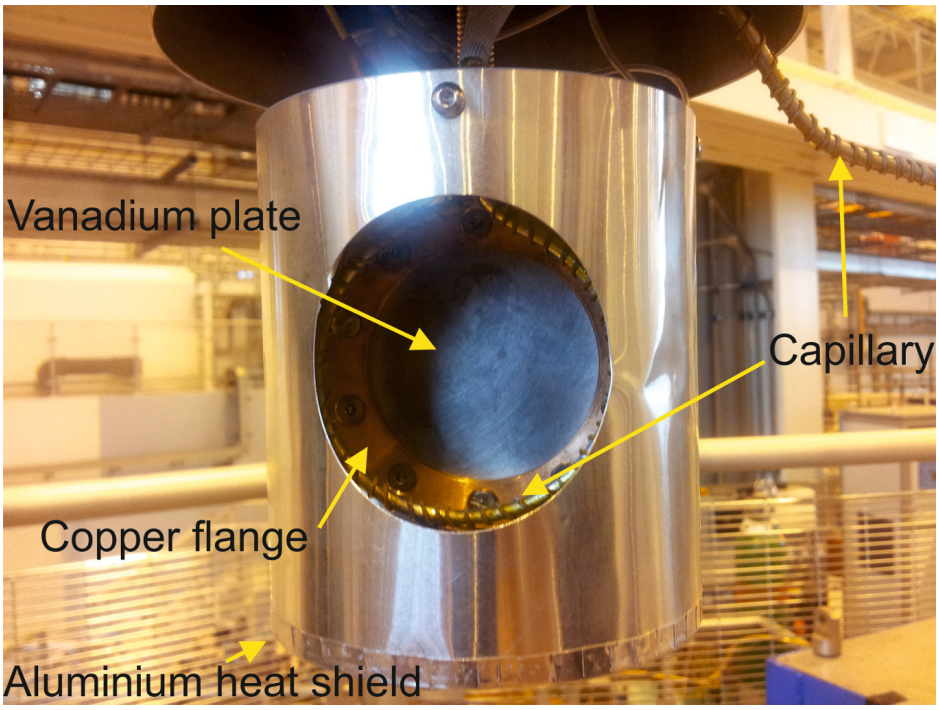

Figure 6.8: Photograph of the vanadium plate on which the ice is grown, aluminium heat shield and associated components.

aluminium heat shield which attaches to a ceramic disc, removing the thermal contact between the cold head of the cryostat and the heat shield. The heat shield contains two holes of 90 mm in diameter in front of and behind the face of the vanadium plate. The neutron beam passes through these holes and this ensures that the neutrons are only scattered from ice grown on the plate (which has a known temperature) and not from ice grown elsewhere on the set up (where the temperature is unknown). Thermal linkage of the vanadium plate (via two 50 mm copper studs connected by a stainless steel nut) to the helium cryostat cools the plate and a heater situated on the rear copper flange is used to heat the ice. This system allows the cryostat to reach a minimum temperature of 10.1 K and the sample plate to reach a minimum temperature of 48.3 K. To lower the minimum temperature that can be reached, the two copper studs and nut can be replaced by a single, 100 mm copper stud to improve the thermal linkage. The aluminium heat shield can be replaced with one that does not have holes where the beam passes through but has two small holes of 6 mm in diameter on ceramic flange to allow removal of D_2O vapour from inside the shield. A second heat shield, also

made of aluminium, is additionally fixed to the base of the cryostat (see Fig. 6.9). This has a small hole on the base (around 6 mm in diameter) to allow D_2O vapour to be pumped away. In this set up, the minimum temperature of the cryostat is 11.3 K and the minimum temperature of the sample is 14.7 K.

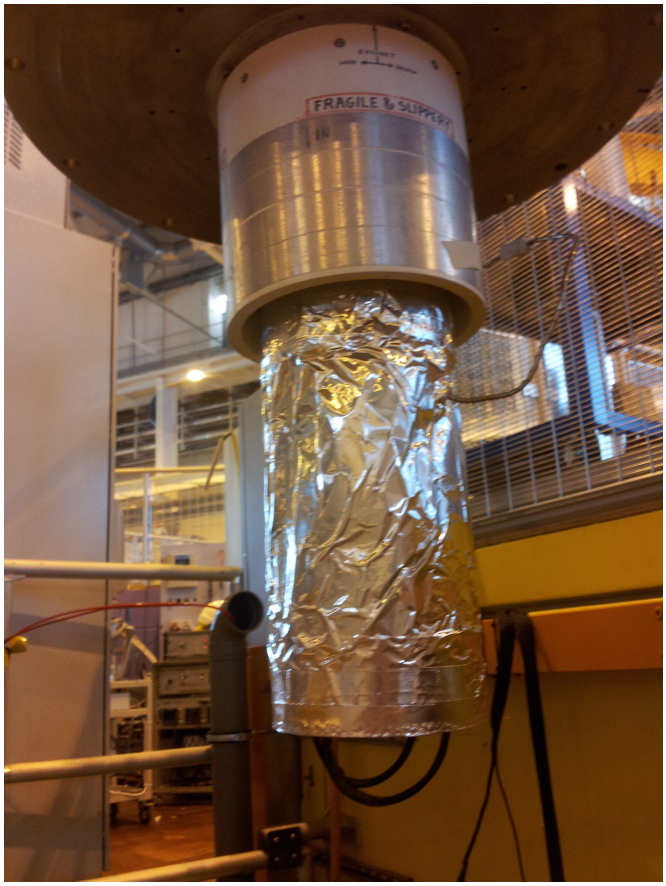

Figure 6.9: Photograph of the aluminium 10 K that surrounds the set up to lower the base temperature of the vanadium plate.

The amorphous solid water is formed by slowly depositing D_2O vapour through a stainless steel capillary of 1/8 inch diameter. The capillary is formed into a 60 mm diameter ring and sits close to the vanadium plate as shown in Fig. 6.8. The D_2O vapour leaves the capillary through around 20 holes 0.5 mm in diameter. The holes point directly towards the vanadium plate at an angle of 45°, so that ice only forms on the vanadium plate. The capillary is maintained at a temperature of around 5°C by use of a heating wire. This prevents the D_2O vapour from freezing inside the capillary. Thermocouples are attached to the capillary, the rear copper flange and the cryostat to

measure the temperatures of these components.

The vanadium plate is situated inside a vacuum chamber on the beam line. The chamber is evacuated by a turbomolecular pump that is backed by a scroll pump. This gives a residual pressure of around 5×10^{-5} mbar when the system is at room temperature and a residual pressure of 4×10^{-7} mbar when the cryostat is turned on. These pressures are significantly higher than the ultra high vacuum (UHV) pressures of around 10^{-9} mbar or less usually used in such experiments, as dedicated UHV equipment for use on the neutron beam line does not yet exist. Instead, the current set up was used to perform proof-of-concept experiments with a view to building a dedicated UHV chamber suitable for use on the neutron beam line in future.

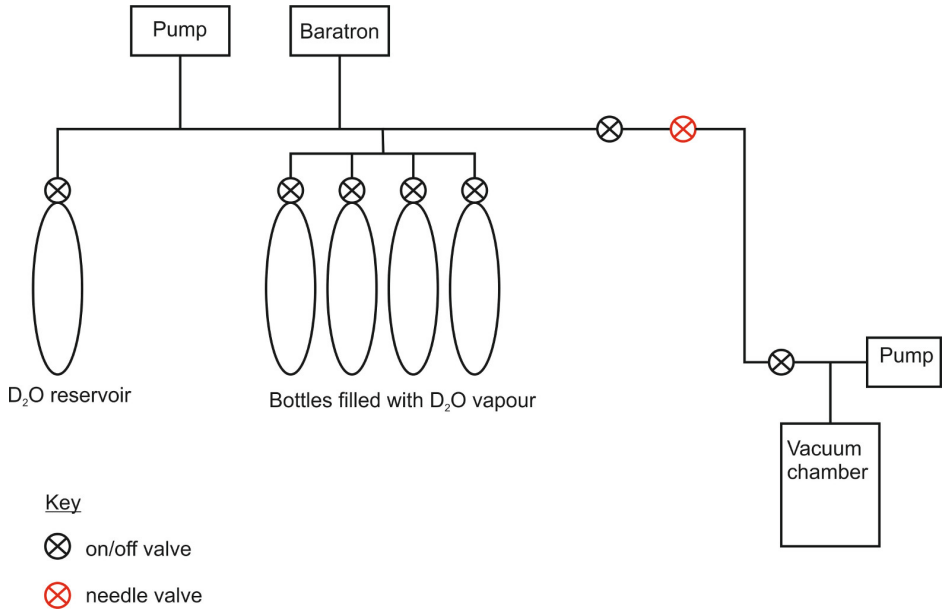

Figure 6.10: Diagram of the dosing line used to prepare D_2O vapour for deposition on the vanadium plate. The liquid D_2O is stored in a reservoir from which bottles on the dosing line are filled with D_2O vapour. This is then deposited onto the vanadium plate within the vacuum chamber.

D_2O vapour is produced from a reservoir of liquid D_2O on a dosing line connected to the vacuum chamber. The dosing line is shown in Fig. 6.10. Liquid D_2O is stored in a reservoir and undergoes repeated freeze-thaw processes prior to the start of the experiment to remove dissolved gases. To avoid accidentally drawing liquid D_2O through the system, the D_2O reservoir is never opened directly to the vacuum chamber. Instead, D_2O vapour is stored in bottles on the dosing line. Valves are used to close the

connection to the vacuum chamber. The connections to the bottles and the D_2O reservoir are then opened. The D_2O is frozen using liquid nitrogen and then heated with a heat gun to maximise the release of the D_2O vapour, filling the bottles. When the bottles have been filled with the maximum pressure of D_2O vapour, the connection to the D_2O reservoir is closed and the connection to the vacuum chamber is reopened to allow deposition to commence. When the pressure in the bottles has dropped to around 1-2 mbar, the connection to the vacuum chamber is closed and the bottles are refilled before continuing with deposition.

On the end of the dosing line is a needle valve (see Fig. 6.10). This is opened to flow the D_2O vapour into the chamber. The flow rate is set by opening the needle valve and observing the pressure rise within the chamber.

6.4 Conclusions

Neutron scattering is an ideal technique for studying the porosity of amorphous solid water because, unlike other techniques often used, it probes the structure of a material and so it can give information about pore size and shape. The NIMROD instrument at the ISIS neutron source is uniquely suited to studying amorphous solid water as it can measure both low Q and high Q information. This gives information related to crystallisation (in the high Q region) and porosity changes (in the low Q region). Amorphous solid water can be grown in the laboratory at 77 K and shipped to ISIS under liquid nitrogen. It is not practical to transport ice at temperatures lower than the temperature of liquid nitrogen (77 K), so a purpose-built set up is used to grow ice in situ on the NIMROD beam line at temperatures below 77 K. This additionally allows the ice to be studied as it grows.

The analysis of the data resulting from neutron scattering experiments of amorphous solid water is presented in Chapter 7. The results of neutron scattering experiments of amorphous solid water are presented in Chapters 8 and 9.

Chapter 7

Data reduction and analysis for neutron scattering experiments

Neutron scattering experiments studying the porosity of amorphous solid water can produce a large quantity of data for analysis. The raw data (in the form of neutron counts per unit time in each detector) must be processed to make it suitable for analysis using a purpose-built program called Gudrun (developed by scientists at ISIS). This program can be very time consuming to run and so Python programs written by the current author are used to batch process files using Gudrun. Parameters relating to porosity such as specific surface area, periodic spacings, radius of gyration and parameters relating to pore shape and pore surface roughness can be extracted from the processed data. Considering these parameters as a function of time or temperature gives information about porosity changes in the ice.

7.1 Introduction

Reducing and analysing neutron scattering data is a complex process. The raw data obtained from a neutron scattering experiment is in the form of neutron counts per unit time in each detector. This data must be reduced to obtain the differential cross section as a function of Q as described in Section 6.2.1 of Chapter 6. The reduction

is performed by a purpose-built program called Gudrun. The workings and operation of Gudrun, as well as Python programs written by the current author to batch process data files using Gudrun are presented in Section 7.2. Once the data has been reduced, parameters relating to the pores such as specific surface area, periodic spacings, pore size, shape and surface roughness can be extracted. The methods for extracting these parameters are described in Section 7.3. Conclusions are drawn in Section 7.4.

7.2 Reducing neutron scattering data: Gudrun

Gudrun is a purpose-built neutron scattering data reduction program developed by Alan Soper *et al.* at ISIS. A complete description of how Gudrun works is beyond the scope of this thesis but the basic steps are presented here.

7.2.1 Theory

The differential cross section, $\frac{d\sigma}{d\Omega}(\lambda,2\theta)$ is related to the number of particles scattered in the direction 2θ ($CNT(\lambda,2\theta)$) by:

$$\frac{d\sigma}{d\Omega}(\lambda,2\theta) = \frac{CNT(\lambda,2\theta)}{N\langle\Phi(\lambda,t)\rangle_t \Delta\lambda\Delta\Omega\Delta t} \tag{7.1}$$

where λ is the neutron wavelength, N is the number of atoms in the sample, $\langle\Phi(\lambda,t)\rangle_t$ is the average number of particles of radiation per unit area per unit time per unit wavelength, $\Delta\Omega$ is the solid angle through which the neutrons are scattered and Δt is the time. The number of counts in each detector for a given sample ($CNT_s(\lambda,2\theta)$) is given by:

$$CNT_s(\lambda,2\theta) = N_s\Sigma_s(\lambda,2\theta)\langle\Phi(\lambda,t)\rangle_t E_d(\lambda)\Delta\lambda\Delta\Omega\Delta t_s \tag{7.2}$$

where $\Sigma_s(\lambda,2\theta) = \frac{d\sigma}{d\Omega}(\lambda,2\theta)$ and E_d is the detector efficiency.

These equations hold if the sample is small enough so that the effects of self attenuation (where the neutron beam loses intensity as it passes through the sample) and multiple scattering (where a neutron is scattered by more than one atom) can be

ignored. In practice, a sample this small will give too low a count rate for useful information to be obtained, so self attenuation and multiple scattering must be taken into account. Adding these into Equation 7.2 gives:

$$CNT_s(\lambda,2\theta) = (A_{s,s}N_s\Sigma_s(\lambda,2\theta) + M_s)\,\langle\Phi(\lambda,t)\rangle_t\, E_d(\lambda)\Delta\lambda\Delta\Omega\Delta t_s \tag{7.3}$$

where $A_{s,s}$ refers to "scattering in the sample, attenuation by the sample" and M_s is the multiple scattering by the sample. As every detector is subject to a background count, a background factor ($B(\lambda,2\theta)$) must be added:

$$CNT_s(\lambda,2\theta) = (A_{s,s}N_s\Sigma_s(\lambda,2\theta) + M_s + B(\lambda,2\theta))\,\langle\Phi(\lambda,t)\rangle_t\, E_d(\lambda)\Delta\lambda\Delta\Omega\Delta t_s \tag{7.4}$$

Finally, a sample is usually placed in a container, which has its own scattering pattern. Equation 7.4 then becomes:

$$\begin{aligned} CNT_{s+c}(\lambda,2\theta) =& (A_{s,sc}N_s\Sigma_s(\lambda,2\theta) + A_{c,sc}N_c\Sigma_c(\lambda,2\theta) + M_{sc} \\ &+ B(\lambda,2\theta))\,\langle\Phi(\lambda,t)\rangle_t\, E_d(\lambda)\Delta\lambda\Delta\Omega\Delta t_{sc} \end{aligned} \tag{7.5}$$

where $CNT_{s+c}(\lambda,2\theta)$ is the total number of counts for scattering by the sample and container, $A_{s,sc}$ refers to "scattering in the sample, attenuation by the sample and container", $A_{c,sc}$ refers to "scattering in the container, attenuation by the sample and container", N_c is the number of atoms in the container, $\Sigma_c(\lambda,2\theta)$ is the differential cross section of the container and M_{sc} is the multiple scattering by the sample and container. The background and container factors are quantified by measuring the background counts (with no sample and container) and the counts of the container (with no sample). The calculation of the attenuation and multiple scattering factors is complex and beyond the scope of this thesis; the reader is referred to Soper & Egelstaff (1980) and Soper (1983) for further information.

Before the attenuation and multiple scattering factors are subtracted, the data must be put on an absolute scale. This is achieved by normalising the data to a scan of

vanadium. Vanadium has a very small coherent scattering length, so the differential cross section is mostly flat, apart from a few weak Bragg peaks, the positions of which are known precisely. This makes it ideal for calibration.

7.2.2 The Gudrun algorithm

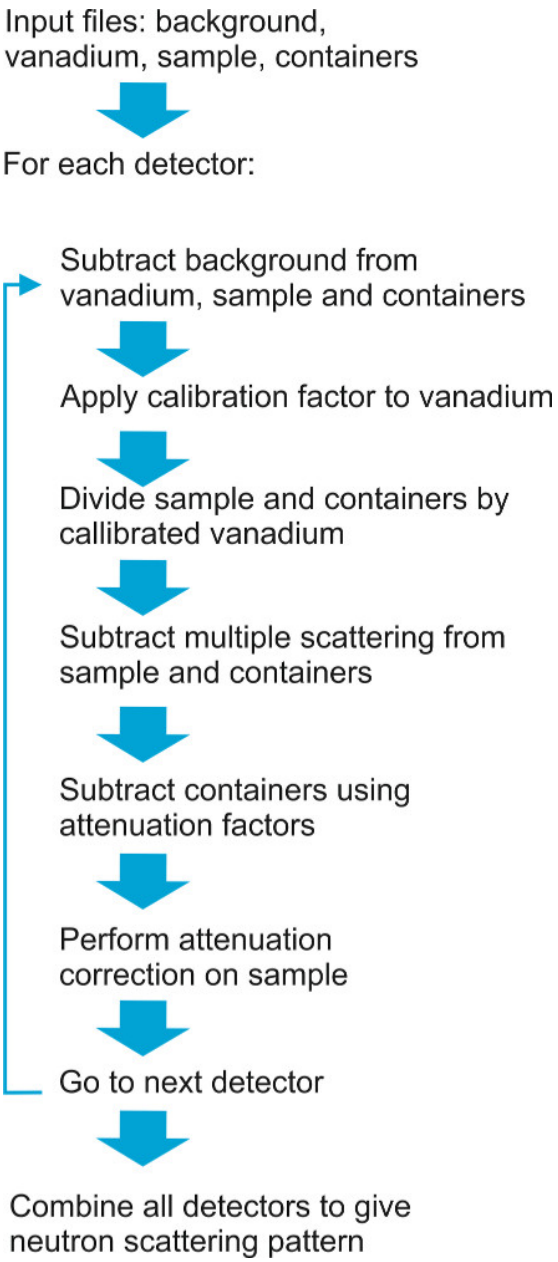

Figure 7.1: Gudrun algorithm (adapted from the Gudrun manual).

A basic representation of the Gudrun algorithm is presented in Fig. 7.1. The input files required are raw neutron counts for the background, vanadium, sample and any

containers. For each detector, the background is subtracted from the vanadium, sample and containers. A calibration factor is applied to the vanadium and the sample and containers are divided by the calibrated vanadium to put the data on an absolute scale. The multiple scattering is subtracted from the sample and containers. Containers are then subtracted using attenuation factors and the attenuation correction is performed on the sample. This process is repeated for each detector. The detectors are then combined in groups to yield overall differential cross section as a function of Q.

7.2.3 Running Gudrun

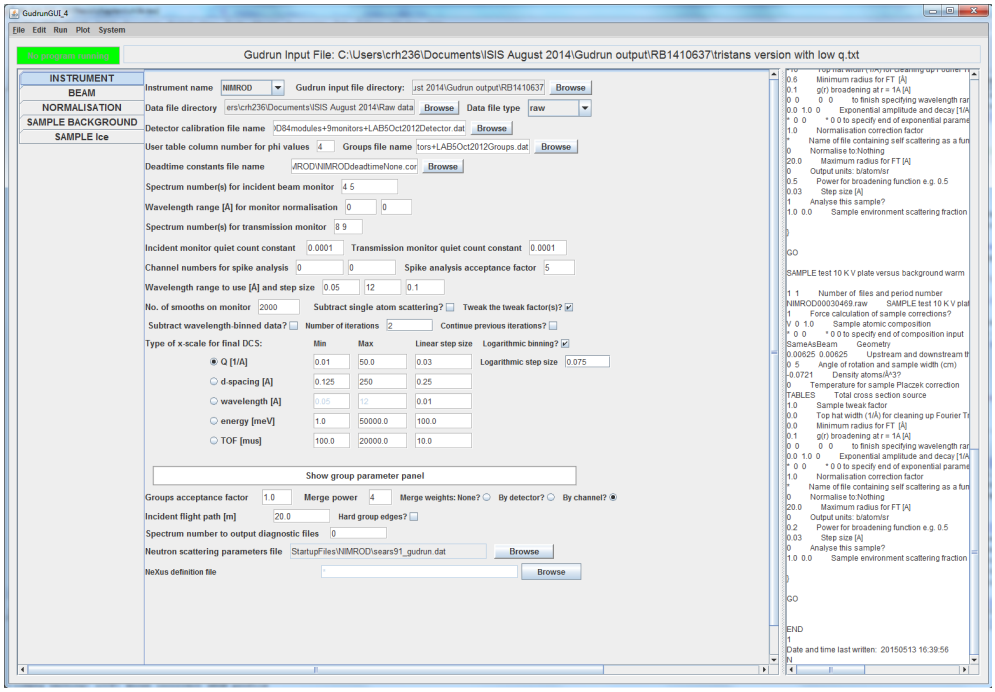

Figure 7.2: Screen shot of the Gudrun GUI. The "Instrument" and "Beam" tabs are used to specify details about the instrument and neutron beam respectively and the other tabs specify the input files.

The Gudrun executable is written in Fortran and is supplied with a Java based Graphical User Interface (GUI). The GUI is used to write input files for the Gudrun executable and run it. A screen shot of the GUI is shown in Fig. 7.2. The tabs on the GUI are "Instrument", "Beam", "Normalisation", "Sample background" and "Sample". Tabs can also be added for any containers. The "Instrument" and "Beam" tabs specify

details of the instrument and neutron beam respectively. The normalisation (vanadium), background and sample raw files are supplied in the relevant tabs. Multiple sample raw files can be supplied to obtain an average scattering pattern for all the files. In the sample tab, the "tweak factor" (inverse of the packing fraction) is specified for granular samples and the thickness is supplied for flat samples. The sample density is also supplied. The "tweak factor" or thickness are altered such that the output differential cross section is close to 100% of the expected level. The expected level in the high Q region is the calculated scattering cross section of the average atom in the sample in barns/steradians/atom. In practice, this means that a first guess of these parameters is supplied before running and looking at the output differential cross section level. The first guess for the tweak factor is 1, and the first guess of the thickness is calculated by estimating the thickness from the number of molecules of D_2O vapour released into the chamber (see Section 9.2.1 of Chapter 9 for calculations). The differential cross section level is supplied to a command prompt once Gudrun has finished running and is also written to a text file. The tweak factor or thickness is adjusted accordingly by the user and Gudrun is re-run. This process is repeated until the differential cross section is $\pm 0.3\%$ of the expected level.

7.2.4 Gudrun batch processing using Python

As a neutron scattering experiment may generate hundreds of raw files, processing them individually by the process above can be extremely time consuming. The Gudrun GUI has a built in feature for batch processing raw files, but they must all be run with the same input parameters. This is not practical for use with data of ice growing (where the thickness is constantly changing) or ice heating (where both the thickness and the density may change as the pores collapse). Therefore, two Python programs were written to automate the manual iteration of the sample thickness and density, one to process single files and one to process multiple files to produce averaged scattering patterns. These programs rely on the fact that Gudrun can be run by directly calling

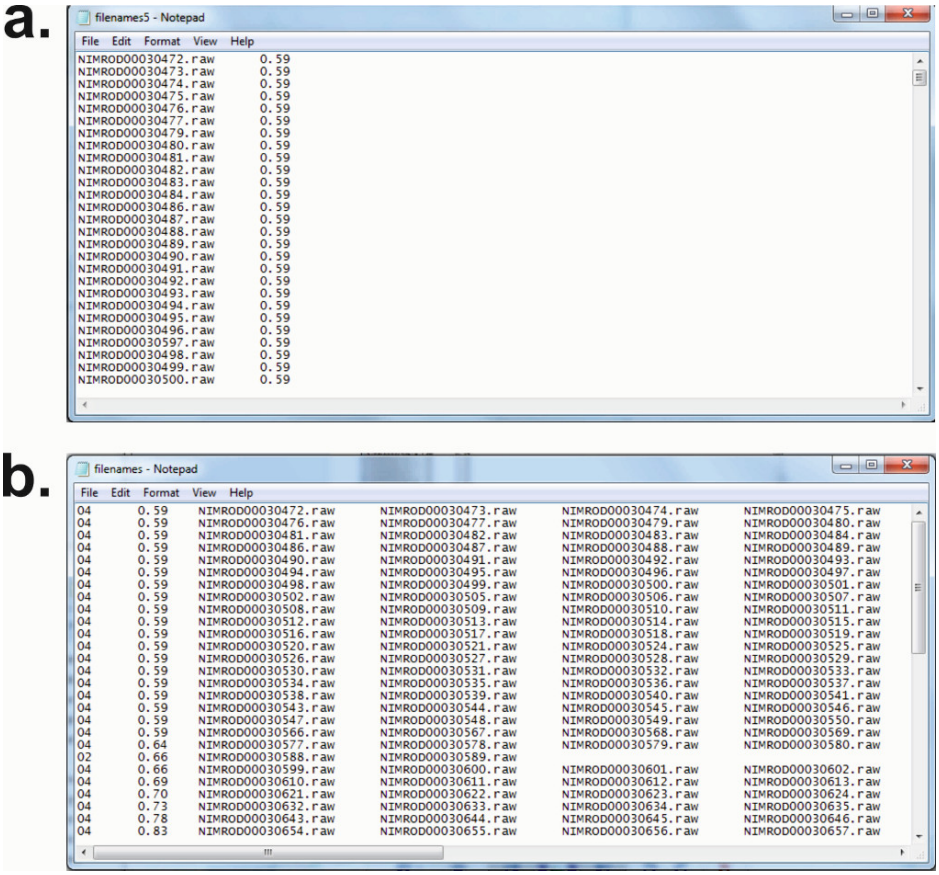

Figure 7.3: Example input files for Python programs used to process files using Gudrun. **a.** File names input file for processing single files. Each line of the text file contains the sample file followed by the density (tab separated). **b.** File names input file for processing multiple files and averaging them. Each line of the text file contains the number of sample files, the density and the sample files (all tab separated).

the Fortran executable instead of being run from the GUI. The GUI is used to write the original input file for Gudrun to ensure that it is set up correctly. Thereafter, the sample files, density and thickness are adjusted by Python. To start, the sample files and densities (estimated from those found by Brown et al. (1996)) are specified in a text file. For processing single files, each line of the text file contains the name of a sample file followed by the density to be used, with these two parameters separated by a tab. For processing multiple files and averaging, each line of the text file contains the number of files to be averaged, the density and the individual files, all separated by a tab. Screen shots of sample input files for the two programs are shown in Fig 7.3. The Python programs then read the file names input file. For each line of the file names input file, the program edits the Gudrun input file accordingly and runs Gudrun. When

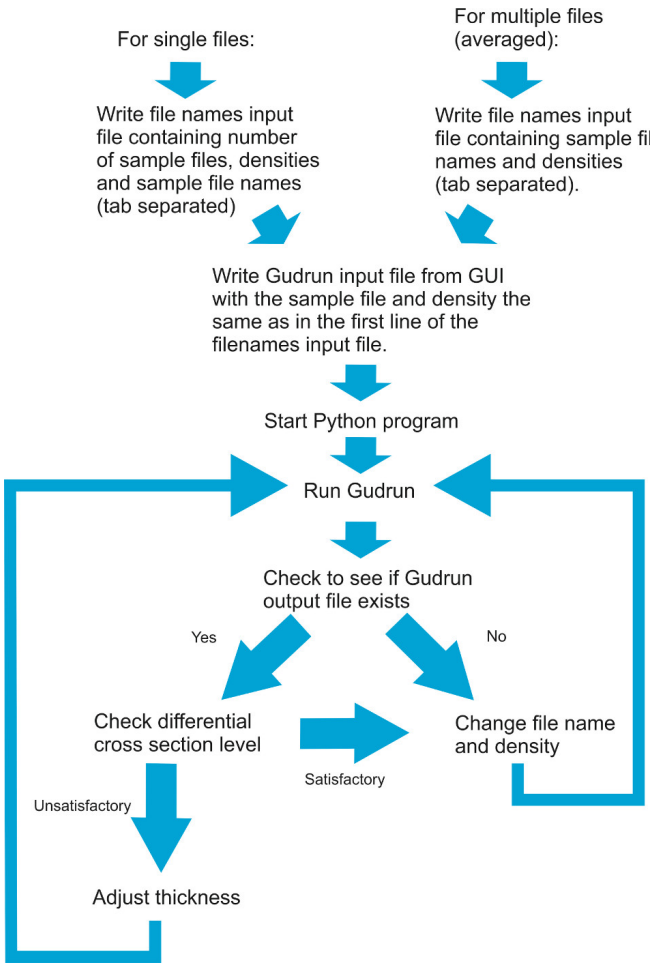

Figure 7.4: Flow chart showing operation of Python programs used to process files using Gudrun.

Gudrun has finished running, the program looks for the appropriate Gudrun output file containing the differential cross section level. If this file is not found, Gudrun has failed to run for this sample file and the program continues with the next sample file. If the Gudrun output file is found, the differential cross section is read. If it is not within 0.3% of the expected level, the thickness is adjusted in the Gudrun input file and Gudrun is run again. When a satisfactory differential cross section level has been reached, the program changes the sample file and density in the Gudrun input file and the process is repeated. A flow chart showing the operation of these programs is shown in Fig. 7.4. The programs themselves are presented in Appendix B.

7.3 Data analysis

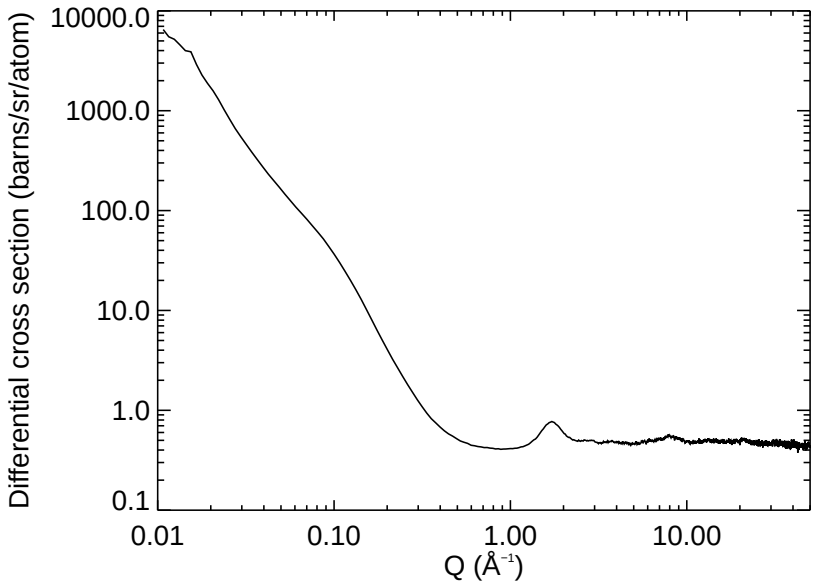

Figure 7.5: Example neutron scattering pattern for an amorphous solid water sample grown at 50 K.

An example neutron scattering pattern for an amorphous solid water sample grown at 50 K is shown in Fig. 7.5. The main features are a slope in the low Q region with a "hump" superimposed upon it around 0.1 Å^{-1} and a broad peak in the high Q region between 1 and 2 Å^{-1}. The slope is due to the granular nature of the material and corresponds to scattering from the grain surfaces. The "hump" is related to the pores in the ice. The broad peak in the high Q region is related to the average O-O distance in the ice (Elliott, 1995). The majority of the analysis focusses on the low Q region, from which the specific surface area, pore periodic spacings, pore radius of gyration, s parameter (relating to pore shape) and d parameter (relating to pore surface roughness) can be extracted. These properties are extracted from the neutron scattering patterns with IDL or Python programs as detailed in this section. The Python programs for calculating specific surface area and periodic spacing (which are identical to the IDL programs in operation) and the IDL program for performing a Guinier-Porod fit are presented in Appendix B.

7.3.1 Specific surface area

The specific surface area is calculated as follows. Paglia et al. (2004) state that the specific surface area (Σ_s) is related to the Porod constant (K):

$$\Sigma_s = \frac{\lim_{Q\to\infty}(I(Q).Q^4)}{2\pi\Delta\rho^2} = \frac{K}{2\pi\Delta\rho^2} \tag{7.6}$$

which, according to Equation 7.6, can be found from the intercept of the quasi-plateau of an $I(Q).Q^4$ plot. $\Delta\rho$ is the difference in scattering length density between the pore and the solid. The scattering length density difference for D_2O at a density of 0.94 g cm^3 is 5.414 $\times 10^{-6}$Å^{-2}. This value is used for all forms of amorphous solid water regardless of overall porosity as $\Delta\rho$ is the difference in scattering length density between the pore and the solid between the pores (the density of which is equal to that of non porous amorphous solid water, which has a density of 0.94 g cm^3).

Fig. 7.6 shows two examples of quasi-plateaus in $I(Q).Q^4$ plots. The position of the quasi-plateau (and hence the Porod constant K) is indicated by a solid line and the uncertainty is indicated by dashed lines. The first example in Fig. 7.6 **a.** shows a clear plateau. Here, the Porod constant is 3.03 $\times 10^{28} \pm 1.71 \times 10^{26}$ cm^{-5}, leading to a specific surface area of 165 ± 0.93 m^2 cm^{-3}. Not all plots of $I(Q).Q^4$ show plateaus; some merely show sloped linear regions such as that in Fig. 7.6 **b.**. In this case, K corresponds to the midpoint of the sloped linear region with upper and lower uncertainties at the start and end of the linear region. In the case of Fig. 7.6 **b.**, the Porod constant is 5.29 $\times 10^{28} \pm 3.78 \times 10^{27}$ cm^{-5} and the specific surface area is $287 \pm$ 21 m^2 cm^{-3}.

The linear region is selected in Python by computing the rate of change of $I(Q).Q^4$ and defining the linear region where the rate of change falls below a certain value. This "cut-off" point changes depending on the gradient of the linear region (i.e. it is lower when the gradient is lower) and therefore, setting the cut-off point is a matter of trial and error. The program which extracts the Porod constant is run, and the $I(Q).Q^4$

plots (such as those in Fig. 7.6) are visually examined to see if the linear region has been correctly chosen. It should be noted that choosing the linear region in this way is somewhat subjective. If it has not, the cut-off point is adjusted accordingly. In some cases, the quality of the data is too poor to produce a smooth linear region and the program fails to choose the start and end points correctly. When this occurs, the region is chosen manually. When all linear regions have been correctly selected, the specific surface area is calculated from the Porod constants according to Equation 7.6.

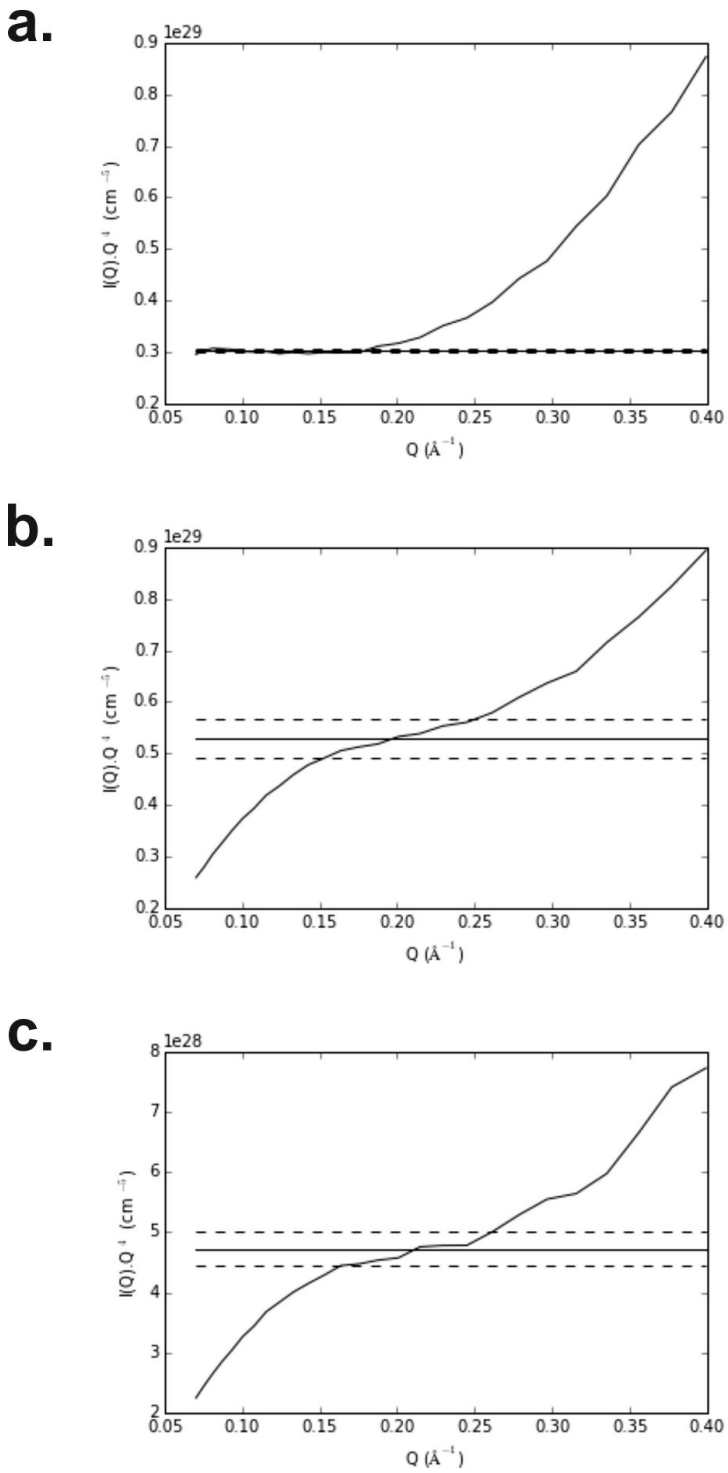

Figure 7.6: Example quasi-plateaus in $I(Q).Q^4$ plots. **a.** A plot with clear quasi-plateau, leading to a Porod constant of $3.03 \times 10^{28} \pm 1.71 \times 10^{26}$ cm^{-5} and a specific surface area of 165 ± 0.93 m^2 cm^{-3}. **b.** A plot with a sloped linear region with the upper and lower bounds indicated by dashed lines (corresponding to the uncertainty in the Porod constant). The solid line indicates the midpoint of the linear region which is chosen as the Porod constant. This gives a Porod constant of $5.29 \times 10^{28} \pm 3.78 \times 10^{27}$ cm^{-5} and a specific surface area of 287 ± 21 m^2 cm^{-3}. **c.** A plot where the linear region is chosen manually (the solid line indicates the Porod constant and the dashed line indicates the uncertainty. This gives a Porod constant of $4.72 \times 10^{28} \pm 2.82 \times 10^{27}$ and a specific surface area of 257 ± 15 m^2 cm^{-3}.

7.3.2 Periodic spacings

The Q position of the "hump" relating to the pores is linked to their periodic spacings (i.e. how far apart they are) (Hass et al., 2010) by:

$$d = \frac{2\pi}{Q} \tag{7.7}$$

where d is the periodic spacing of the pores. It should be noted that the Q position does not refer to the size of the pores but their spacings; the size is obtained from a Guinier-Porod fit (see Section 7.3.3). However, due to the broad shape of the "hump", it is difficult to extract a peak position. Multiplying the differential cross section by Q^a where $a = 2.5$ or 3 transforms the "hump" into a more pronounced peak, or "pseudopeak". While the peak position could in theory be extracted by differentiating the curve, this method is used as it is standard practice in the field. The position of this peak in Q is used to calculate the periodic spacings according to Equation 7.7.

The positions of the pseudopeaks are selected in Python by computing the rate of change and observing the turning point (i.e. where the gradient becomes negative). This point is selected to be the peak. This method is somewhat crude but works well for pronounced peaks which make up the majority of the data (see Fig. 7.7**a.**). For less pronounced peaks, the peak position is not always chosen correctly, so in these cases, the peak position is selected manually (Fig. 7.7 **b.**). Uncertainties on the pseudopeak positions are found by taking the difference between points either side of the peak position and dividing by 2. Uncertainties on the periodic spacings are calculated from these using standard methods for the propagation of uncertainties (see Chapter 3 Section 3.3.3). The choice of the value of a simply depends on which value produces the clearest and most pronounced pseudopeak.

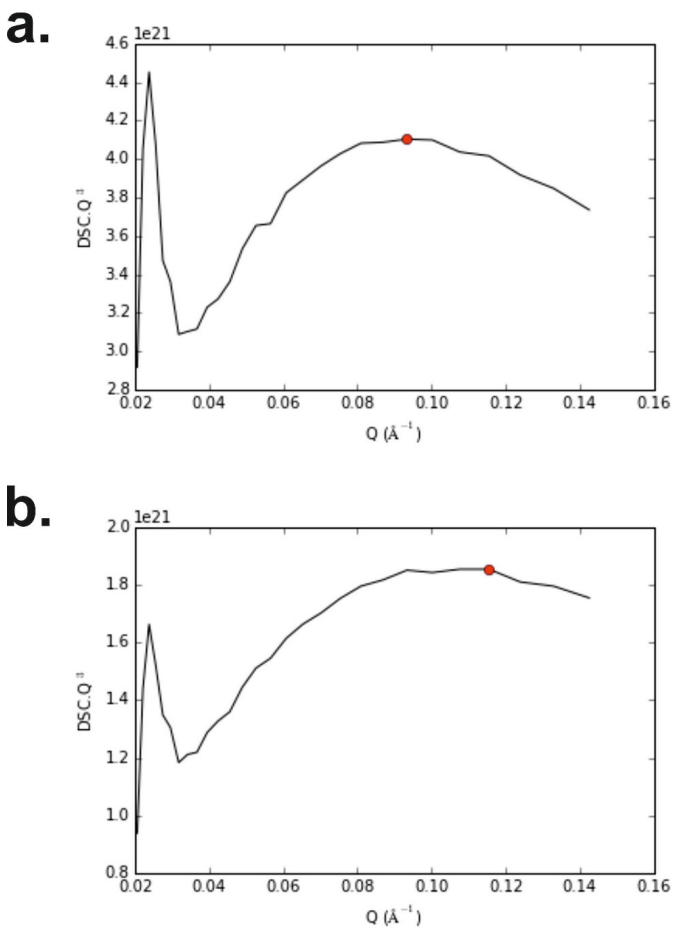

Figure 7.7: Example pseudopeaks in $I(Q).Q^3$ plots. **a.** A plot with a pronounced pseudopeak where the peak position has been correctly chosen. **b.** A plot with a less pronounced pseudopeak where the peak position has been incorrectly chosen. In cases such as these, the peak position is chosen manually.

7.3.3 Guinier-Porod analysis

To extract information about pore size, shape and surface roughness, a Guinier-Porod function can be fitted to the "hump":

$$\begin{aligned} I(Q) &= \frac{G}{Q^s} exp(\frac{-Q^2 {R_g}^2}{3-s}) \text{ for } Q \leq Q_1 \\ I(Q) &= \frac{D}{Q^d} \text{ for } Q \geq Q_1 \\ Q_1 &= \frac{1}{R_g}\left[\frac{(d-s)(3-s)}{2}\right]^{1/2} \end{aligned} \tag{7.8}$$

where G and D are scaling factors, R_g is the radius of gyration, s is a parameter related to pore shape (where $s = 0$ indicates spheres, $s = 1$ indicates cylinders and $s = 2$ indi-

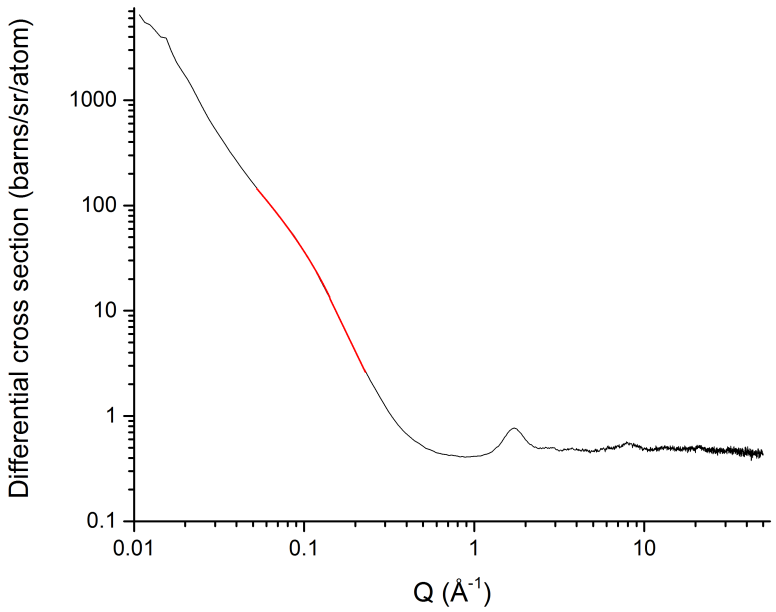

Figure 7.8: Example neutron scattering pattern for an amorphous solid water sample. The Guinier-Porod fitting region is shown in red.

cates platelets) and d is a parameter related to surface roughness (where $d = 3$ for very rough surfaces and $d = 4$ for very smooth surfaces). Fig. 7.8 shows the region over which the Guinier-Porod function is fitted.

The Guinier-Porod function was developed by Hammouda (2010) from the standard Guinier functions for spheres, cylinders and platelets and the Porod function (Glatter & Kratky, 1982). The Guinier function for a sphere is:

$$I(Q) = \frac{G}{Q^3} exp(\frac{-Q^2 {R_g}^2}{3}) \tag{7.9}$$

For a cylinder it is:

$$I(Q) = \frac{G}{Q^2} exp(\frac{-Q^2 {R_g}^2}{2}) \tag{7.10}$$

For a platelet it is:

$$I(Q) = \frac{G}{Q} exp(-Q^2 {R_g}^2) \tag{7.11}$$

The Porod function is simply:

$$I(Q) = \frac{D}{Q^d} \tag{7.12}$$

These functions are widely used to extract information about the size and surface roughness of objects from small angle neutron scattering data. Combining them in the Guinier-Porod function allows shape information to be easily extracted. This function has already been used to extract information about the pores in amorphous solid water (Mitterdorfer et al., 2014).

Changes in the s parameter indicate changes in pore shape. Fig. 7.9 shows the shapes indicated by different values of s. For non-integer value of s, the shapes will vary between those indicated by integer values e.g. if s is between 0 and 1, the shape is an ellipsoid.

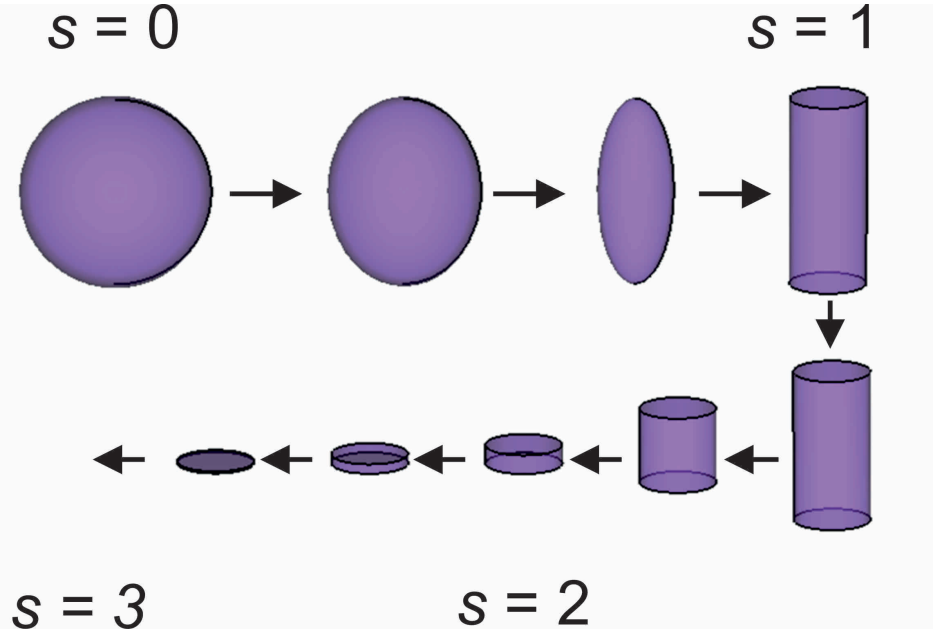

Figure 7.9: Shapes indicated by s parameter. $s = 0$ corresponds to a sphere, $s = 1$ corresponds to a cylinder, $s = 2$ corresponds to a platelet and $s = 3$ corresponds to pore disappearance. For non-integer values of s, the shape varies between these shapes as shown.

7.4 Conclusions

Raw data obtained from a neutron scattering experiment in the form of neutron counts per unit time in each detector is reduced using Gudrun to give differential cross section as a function of Q. As input parameters such as the sample thickness and density must be adjusted to obtain the best differential cross section level, running Gudrun manually is very time consuming. To overcome this, Python programs were written to batch process files. Once the neutron scattering patterns are produced, parameters such as specific surface area, periodic spacings, radius of gyration, s parameter and d parameter can be extracted. These parameters characterise the porosity of the ice.

Considering these parameters as a function of time or temperature gives information about porosity changes in the ice. The results from neutron scattering experiments of amorphous solid water are presented in the following chapters. Chapter 8 describes results of an experiment using ice grown at 77 K and Chapter 9 describes results of experiments using four ices grown at temperatures between 17 K and 52 K.

Chapter 8

The process of pore collapse in amorphous solid water[1]

Amorphous solid water (ASW) is of great astrochemical importance as it is found in multiple environments in space and is thought to play a role in many astronomical processes, including possibly the process of ice aggregation in protoplanetary disks and hence planet formation. ASW can contain pores which collapse upon heating the ice. Here, neutron scattering was used to study porosity changes, including pore collapse, when ASW grown at 77 K was heated between 78 K and 144 K. The experiments were carried out prior to the start of this work (as described in Chapter 6) and the data was reduced and analysed by the current author (as described in Chapter 7). The specific surface area, pore periodic spacings and parameters relating to the pore size, shape and surface roughness were extracted. These parameters give information about both the process of pore collapse and the glass transition in ASW.

[1]Part of this chapter is based on a paper of which the author of this thesis is the first author (C. R. Hill, C. Mitterdorfer, T. G. A. Youngs, D. T. Bowron, H. J. Fraser, T. Loerting, "Neutron scattering analysis of water's glass transition and micropore collapse in amorphous solid water"). The paper has been submitted to Physical Review Letters. The work in this chapter is based on (but does not include) the work of a previously published paper (C. Mitterdorfer, M. Bauer, T. G. A. Youngs, D. T. Bowron, C. R. Hill, H. J. Fraser, J. L. Finney, T. Loerting (2014), "Small-angle neutron scattering study of micropore collapse in amorphous solid water", PCCP, 16, 16013) of which the author of this thesis is a co-author. Both papers are the result of a collaboration between scientists at the Institute of Physical Chemistry at the University of Innsbruck, the ISIS neutron facility at RAL and the Department of Physical Sciences at The Open University.

8.1 Introduction

As described in Chapter 1, amorphous solid water (ASW) has been detected in multiple environments in space, including on interstellar dust grains (Leger et al., 1979), on comets (Patashni et al., 1974; Klinger, 1981; Smoluchowski, 1981; Delsemme, 1983) and planetary satellites (Smoluchowski, 1978), and it has been suggested that it may play a role in planet formation (Ehrenfreund et al., 2003). It has been detected in star forming regions (Smith & Wright, 2011) and around young stellar objects (Schegerer & Wolf, 2010) and therefore it must be taken into account when considering ice aggregation in planet-forming regions. Studying the collisional properties of amorphous solid water particles is beyond the scope of this thesis, but a detailed understanding of the structural properties of this ice is necessary to fully understand the results of future collision experiments. The structural properties of ASW, in particular the porosity and how this changes with temperature and time is the subject of this chapter.

The results of numerous experiments investigating the porosity of ASW by studying dangling OH bonds (Buch & Devlin, 1991; Zondlo et al., 1997; Schriver-Mazzuoli et al., 2000), gas adsorption and trapping (Pletzer & Mayer, 1989; Ayotte et al., 2001; Horimoto et al., 2002; Raut et al., 2007; Gálvez et al., 2008) and desorption (Hornekaer et al., 2005), ice thickness (Bossa et al., 2012; Isokoski et al., 2014) or positron annihilation spectroscopy (Wu et al., 2010, 2011; Townrow & Coleman, 2015) show that the pores collapse on heating. However, these methods can only probe the fact of pore collapse and not the nature of the collapse itself. Information such as pore size and shape cannot be determined by these methods, so they are unable to lead to a description of the process of pore collapse. In addition, some of these methods may not actually probe porosity at all. For example, it has been shown that the absence of dangling OH bonds does not necessarily imply the absence of porosity (Isokoski et al., 2014).

As described in Section 1.2.4 of Chapter 1 and Section 6.1 of Chapter 6, neutron scattering is an ideal tool for studying the porosity of ASW, giving information about the pore size and shape which is inaccessible via other techniques. A small angle neu-

tron scattering study by Mitterdorfer et al. (2014) investigated for the first time the nature of the pore collapse and shape of the pores. Amorphous solid water samples were heated from 77 K to 160 K at a rate of 0.3 K min^{-1}. Measurements were taken at 10 K intervals, maintaining the temperature of the ice for 30 minutes while the measurements were taken before resuming heating. The pores collapsed from cylinders to platelets between 120 and 140 K, with the temperature of the collapse depending on the mode of deposition - for baffled samples (grown by background deposition), the pores collapsed between 110 K and 120 K and for non-baffled samples (grown by directional deposition), the pores collapsed between 130 K and 140 K. The rate of deposition did not appear to affect the pore collapse. There was also evidence of pores clustering prior to collapse. As measurements were only taken every 10 K, the exact temperature at which the pore collapse took place could not be determined.

Other open questions still remain about the nature of the pore collapse. Pore collapse has often been assumed to be an autocatalytic process that will take place given sufficient time regardless of temperature (Collings et al., 2003a), but this has not been studied experimentally. Pore clustering has often been observed prior to pore collapse (Wu et al., 2010; Mitterdorfer et al., 2014; Cazaux et al., 2015) but it is not known whether this is a universal process or whether it only occurs under certain conditions. The first aim of this chapter is to explain the nature of the pore collapse in amorphous solid water.

Porosity changes can also be used to study the glass transition of amorphous solid water. The glass transition in amorphous materials is the transition from a hard, brittle state into a molten state, with increased molecular mobility such that the material can behave as a liquid. Increased molecular mobility would be required for the pores to collapse and so by studying the pore collapse, deductions can be made about the glass transition. The glass transition in water was first detected by a subtle increase in heat capacity close to 137 K (McMillan & Los, 1965). Since then, the nature of the glass transition has been disputed. The following suggestions have been made:

1. The glass transition is a transition from a glassy state to a super cooled, ultra

viscous liquid state. This is associated with long range, translational motion of water molecules (i.e. diffusion) (Johari et al., 1987; Hallbrucker et al., 1989a,c; Elsaesser et al., 2010).

2. The glass transition is a transition from one glassy state to another glassy state. Water molecules undergo reorientation but not translation (Fisher & Devlin, 1995).

3. The glass transition is caused by impurities at the surface causing enhanced surface mobility (McCartney & Sadtchenko, 2013).

The glass transition has been previously studied by calorimetry scans, in which the sample is heated and the heat capacity measured as a function of temperature. The glass transition is indicated by an increase in heat capacity. However, enthalpy relaxation effects can cause a decrease in heat capacity that can obscure the glass transition and so, to minimise this effect, ice samples are annealed prior to the calorimetry scan. Typically, samples are heated to 129 K, kept at 129 K for 90 minutes and then cooled back to 77 K for the calorimetry scan (Johari et al., 1987; Hallbrucker et al., 1989a,c; Elsaesser et al., 2010). The glass transition temperature depends on the heating rate and has been found to be 124 K for a heating rate of 0.17 K min^{-1} (Handa & Klug, 1988), 136 K for a heating rate of 30 K min^{-1} (Johari et al., 1987; Hallbrucker et al., 1989a,c; Elsaesser et al., 2010), and 176 K for a heating rate of 6×10^6 K min^{-1} (Sepulveda et al., 2012). Studying the glass transition of amorphous solid water via the pore collapse negates the need for an annealed sample as enthalpy relaxation effects do not obscure the pore collapse. The second aim of this chapter is to explain the nature of the glass transition of amorphous solid water.

The pore collapse of amorphous solid water was studied using neutron scattering. The experimental procedures used are described in Section 8.2. The neutron scattering patterns and parameters extracted from these which describe porosity (specific surface area, periodic spacing, radius of gyration, s parameter and d parameter) are presented in Section 8.3. The relationship of the results to the process of pore collapse

is discussed in Section 8.3.5 and the relationship of the results to the glass transition is described in Section 8.3.6. Conclusions are drawn in Section 8.4.

8.2 Experimental

A sample of amorphous solid water was formed using the experimental set up described in Section 6.3.1 of Chapter 6. Briefly, the ice was formed by depositing D_2O vapour on a copper plate at 77 K. A baffle between the D_2O entry point and the plate ensured background deposition. The deposition time was between 24 and 30 hours and the deposition rate was 40 μm per hour. After growth, the ice was removed from the plate and stored under liquid nitrogen before being shipped (also under liquid nitrogen) to ISIS. Once at ISIS, the granular sample was ground under liquid nitrogen using a pestle and mortar before being loaded into a cold, null scattering (i.e. it allows neutrons to pass through without being scattered) TiZr cell. The cell was cooled with a closed cycle helium cryostat. The entire assembly (cell plus cryostat) was placed on the NIMROD beam line. Measurements were taken every 5 minutes while the ice was heated up using the following heating procedure.

8.2.1 Heating profile

The ice was heated indirectly by heating the cryostat and relying on the thermal linkage between the sample and cryostat to heat the ice sample. The cryostat was heated at a rate of between 0.59 and 2.4 K min^{-1}. There was a thermal lag between the cryostat and the sample, leading to non-linear heating of the sample, particularly when heating was stopped. While the cryostat was being heated, the heating of the sample was approximately linear with rates of 0.4-0.5 K min^{-1}.

Measurements were taken while the sample was being heated and while the sample temperature was kept constant, to see if the porosity of the ice changed when the temperature was constant or if the porosity only changed when the temperature was increasing. The isothermal temperatures at which the cryostat was held were 95 K,

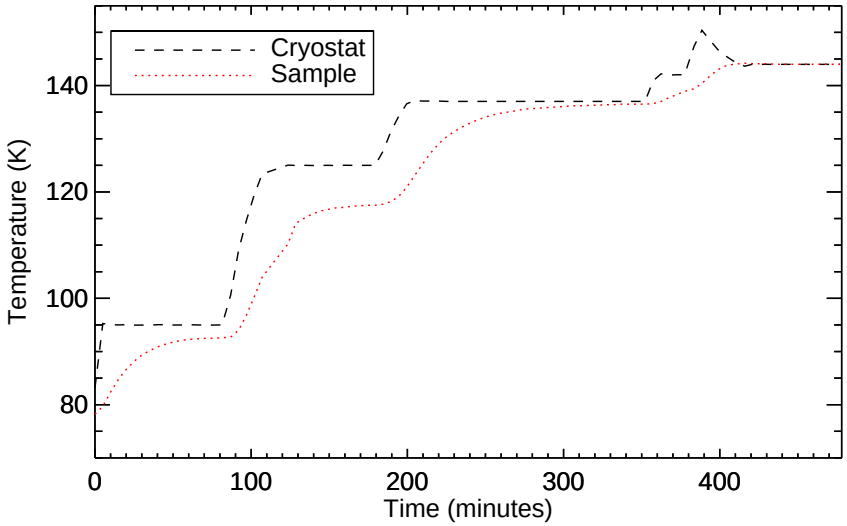

Figure 8.1: Comparison of the temperature of the cryostat, which was heated directly (shown by the black dashed line) and the temperature of the sample, which was indirectly heated by the cryostat (shown by the red dotted line).

125 K, 137 K and 144 K. This led to isothermal sample temperatures of 92 K, 117 K, 136 K and 144 K. The heating profiles of the cryostat and sample are shown in Fig. 8.1.

8.3 Results

8.3.1 Neutron scattering patterns

Figs. 8.2 and 8.3 show the neutron scattering patterns obtained for heating the sample between 78 and 144 K. The heating regions are shown as a function of temperature and the isothermal regions are shown as a function of time, with different temperatures and times represented by different colours. The low Q region (Q <1 $Å^{-1}$) features a slope with a "hump" superimposed upon it at around 0.1 $Å^{-1}$ (indicated in Figs. 8.2 and 8.3 by dotted lines). The slope is indicative of a granular material and is due to scattering from the surfaces of the grains (Mitterdorfer et al., 2014). The "hump" flattens between 117 and 136 K; such a flattening of this "hump" has been found to be indicative of pore collapse (Mitterdorfer et al., 2014). In the high Q region (Q >1 $Å^{-1}$), Bragg peaks appear between 1 and 5 $Å^{-1}$ when the sample is held at 144 K, indicating crystallisation

to cubic ice (I_c). The lack of Bragg peaks prior to this indicates that the sample is fully amorphous, not crystalline. The fact that the hump has flattened long before these Bragg peaks appear shows that pore collapse is independent of crystallisation.

It is immediately apparent that the "hump" between 0.05 and 0.2 $Å^{-1}$ undergoes the most substantial changes during heating, particularly between 117 and 136 K when it undergoes significant flattening, which has been previously linked to pore collapse (Mitterdorfer et al., 2014). At 92 and 117 K there are no visible changes to this feature. Therefore, the pores appear to be stable at these temperatures for at least 35 minutes (the time that the sample was held at 117 K). There are subtle changes when heating to 92 K and at 136 K and above. Between 92 and 117 K, the feature grows slightly.

Fig. 8.4 shows this feature as a contour plot for all heating and isothermal regions. Again, it is apparent that this feature does not change when the sample is held at 92 or 117 K. The slight growth can be seen between 92 and 117 K and the flattening of the hump between 117 and 136 K is obvious. The blue dashed line indicates the start of this flattening at 121 ± 1 K. The contour plot does not show observable changes to this feature in any other region.

The peak intensity of the "hump" in differential cross section is shown in Fig. 8.5 as a function of time until the "hump" disappears at 136 K. Again, the "hump" does not change in the isothermal regions of 92 K and 117 K. Between 92 K and 117 K, the peak intensity increases as the "hump" grows. Between 117 K and 136 K, the peak intensity decreases as the "hump" flattens. The time at which the temperature reaches 121 K (when the "hump" begins to flatten as seen in Fig. 8.4) is indicated on the graph and it can be seen that this occurs at the start of the reduction in peak intensity.

Fig. 8.6 shows a contour plot of all the data in the high Q region ($Q = 1.0 - 5.0$ $Å^{-1}$) as a function of time. At around 435 minutes (when isothermal measurements at 144 K were being taken), the broad peak between 1 and 2 $Å^{-1}$ narrows and three other Bragg peaks appear between 2 and 5 $Å^{-1}$. This indicates crystallisation to cubic ice. The crystallisation does not take place as soon as the temperature of 144 K is reached but after the ice has been held at 144 K for around 27 minutes.

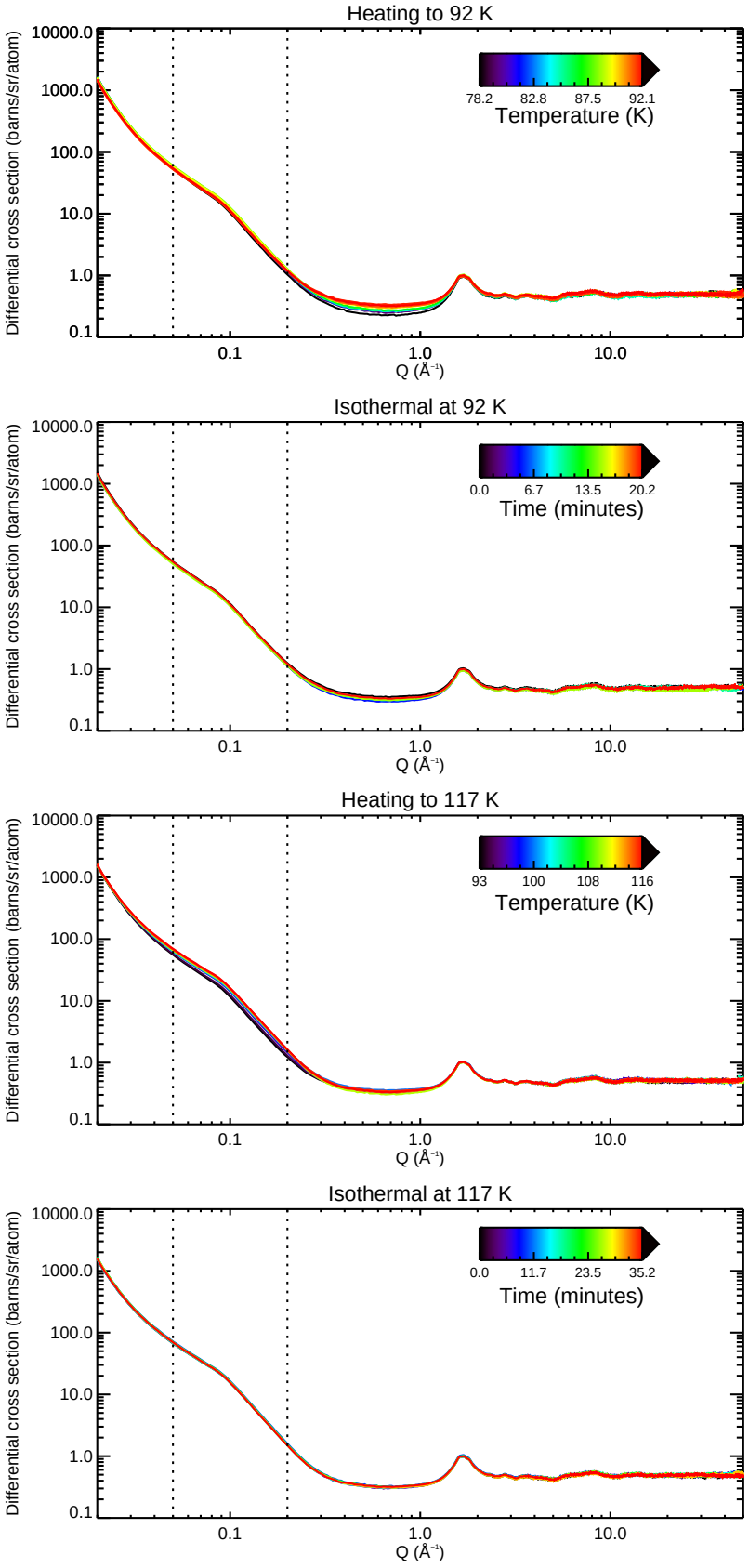

Figure 8.2: Neutron scattering patterns for the heating of the ice between 78 and 117 K. Data in an isothermal region is shown as a function of time and data in a heating region is shown as function of temperature (where different times and temperatures are indicated by different coloured lines). The "hump" indicating porosity appears between the vertical dotted lines.

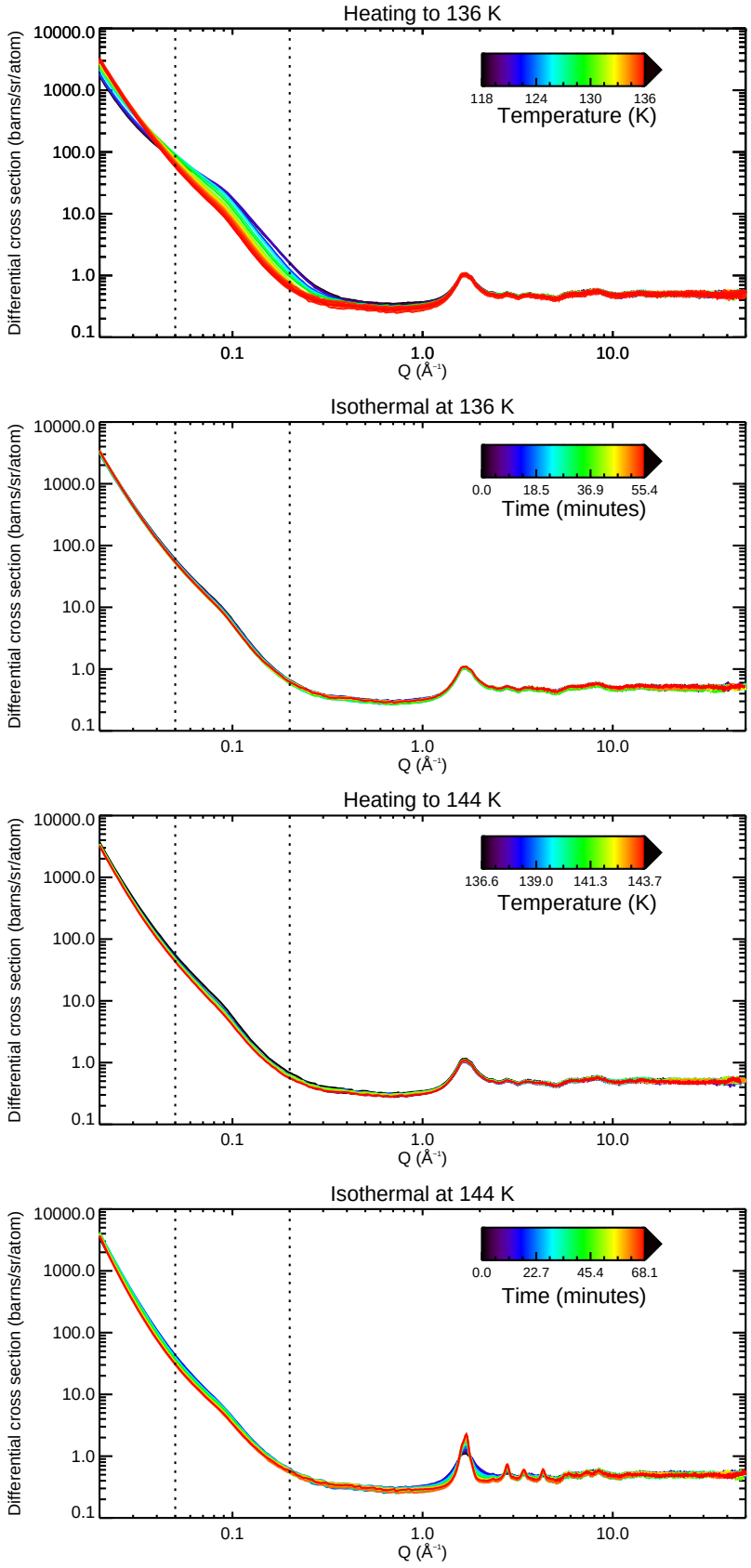

Figure 8.3: Neutron scattering patterns for the heating of the ice between 117 and 144 K. Data in an isothermal region is shown as a function of time and data in a heating region is shown as function of temperature (where different times and temperatures are indicated by different coloured lines). The "hump" indicating porosity appears between the vertical dotted lines.

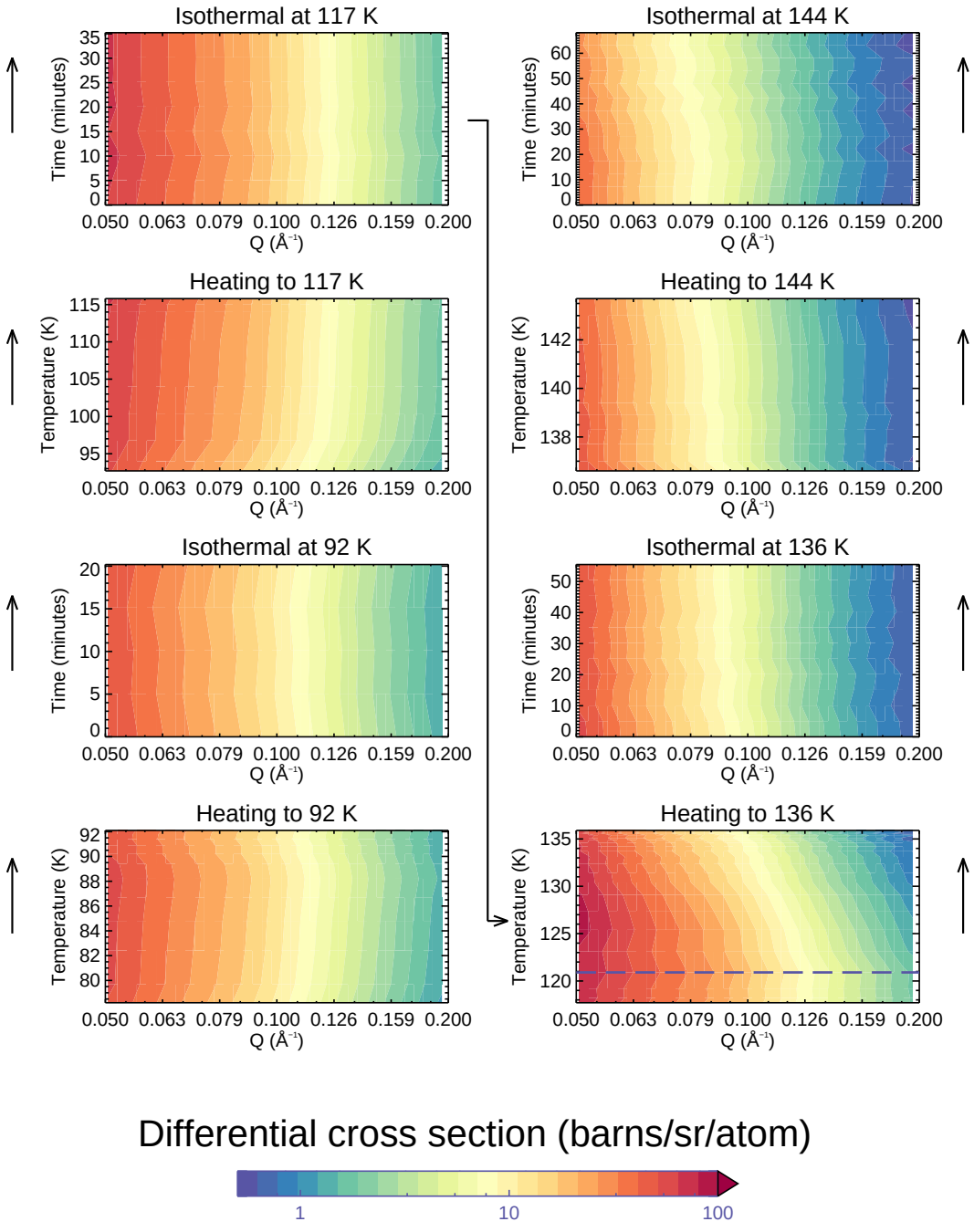

Figure 8.4: Contour plots of the neutron scattering patterns in the region where the "hump" appears ($Q = 0.05 - 0.2$ Å^{-1}, corresponding with the dotted lines in Figs. 8.2 and 8.3). Data in an isothermal region is shown as a function of time and data in a heating region is shown as function of temperature. The dotted line indicates the onset of the flattening of the hump, and hence pore collapse.

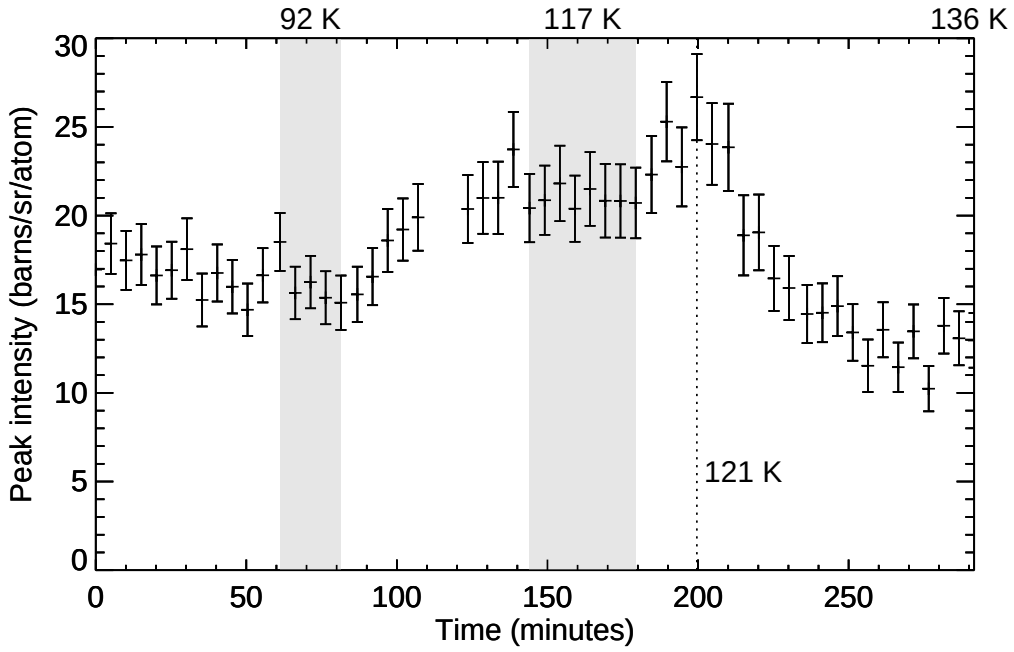

Figure 8.5: Peak intensity of the "hump" as a function of time. Isothermal regions at 92 and 117 K are indicated by grey shading. The dotted line indicates the temperature (121 K) where the "hump" begins to flatten. The peak position cannot be extracted after 136 K as the peak has virtually disappeared.

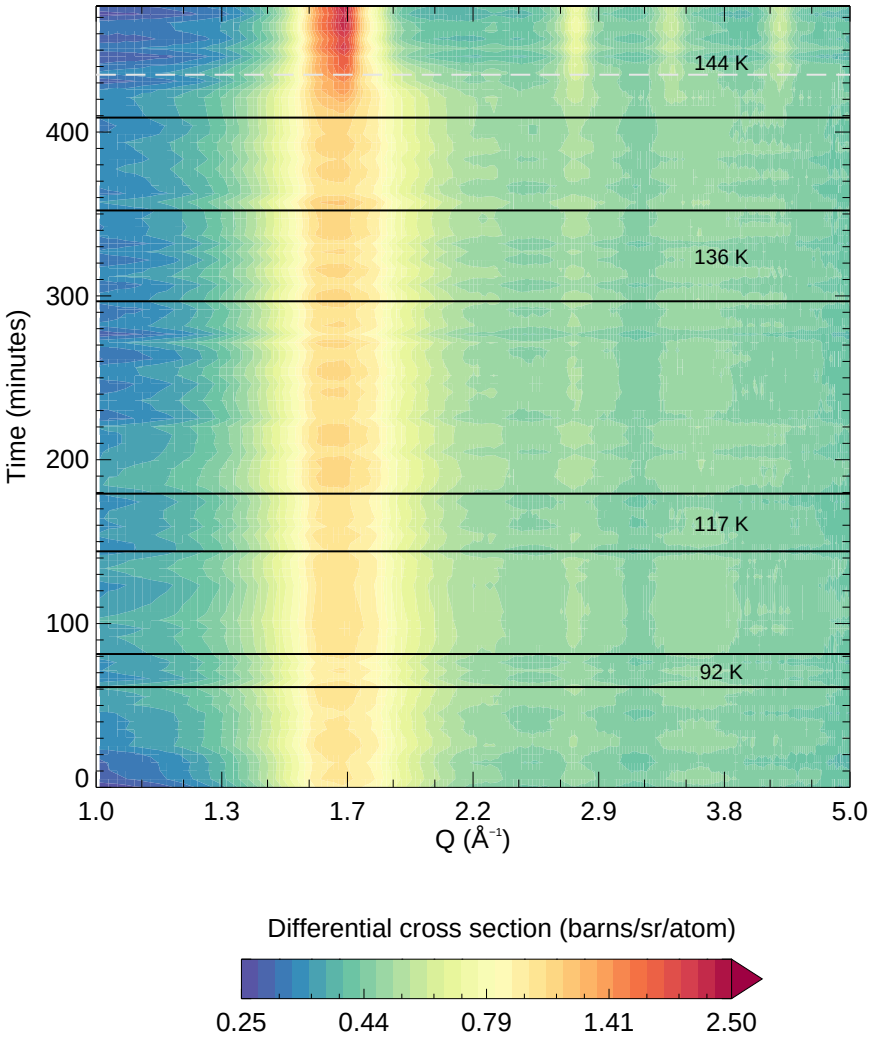

Figure 8.6: Neutron scattering patterns in the high Q ($Q = 1.0 - 5.0$ Å^{-1}) as a function of time. The breaks between the heating and isothermal regions are indicated by solid lines and the temperatures of the isothermal regions are printed where appropriate. The appearance of Bragg peaks can be seen at around 435 minutes (when the ice is isothermal at 144 K and indicated by the grey dashed line).

8.3.2 Specific surface area

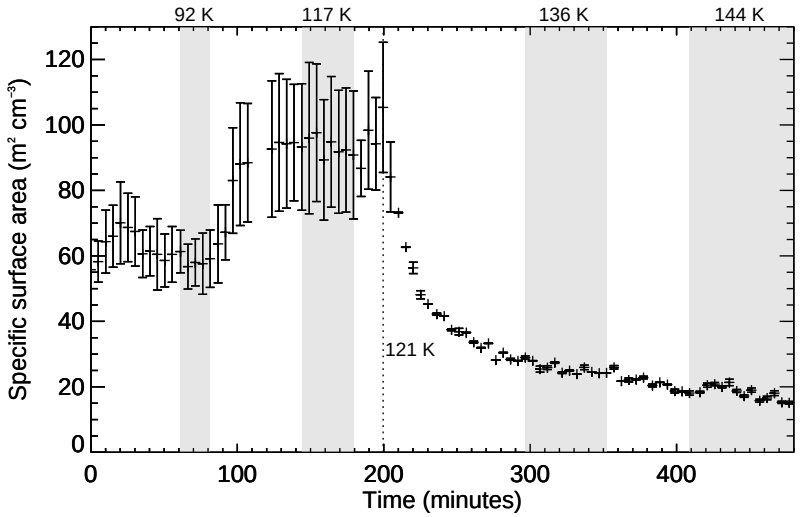

Figure 8.7: Specific surface area as a function of time for temperatures between 78 K and 144 K. Isothermal regions are indicated by grey shading. Where there is no grey shading, the ice was heated between the isothermal temperatures according to the heating profile shown in Fig. 8.1. The temperature of 121 K is marked by a dotted line, indicating the start of the "hump" flattening and hence pore collapse.

The Porod constants were extracted from the data as described in Section 7.3.1 of Chapter 7. The quasi-plateaus from which the Porod constants were extracted are shown in Figs. 8.8 and 8.9. The different colours indicate different temperatures (for heating regions) and times (for isothermal regions). The quasi-plateaus do not undergo any changes in the isothermal regions of 92 K and 117 K. Between 92 K and 117 K, the positions of the quasi-plateaus increase in height. The quasi-plateaus flatten significantly between 117 K and 136 K, with flattening continuing while the ice is isothermal at 136 K, when heating to 144 K and while the ice is isothermal at 144 K.

The specific surface areas were calculated from the Porod constants as described in Section 7.3.1 of Chapter 7. The results are shown in Fig. 8.7. The larger error bars at lower temperatures are due to the sloped linear regions instead of actual plateaus seen in Fig. 8.8. Once the quasi-plateaus begin to flatten, the uncertainties become much smaller. The specific surface area is constant within uncertainties when the ice is isothermal at 92 K and 117 K. It increases from around 60 m^2 cm^{-3} to around

95 m^2 cm^{-3} between 92 K and 117 K and then drops sharply to around 20 m^2 cm^{-3} starting at 121 K $\pm$1 K. This decrease is mostly complete by 136 K but continues slowly all the way to 144 K. A decrease in specific surface area with increasing temperature is expected due to pore collapse, however the increase between 92 K and 117 K is unexpected and is discussed later in the chapter.

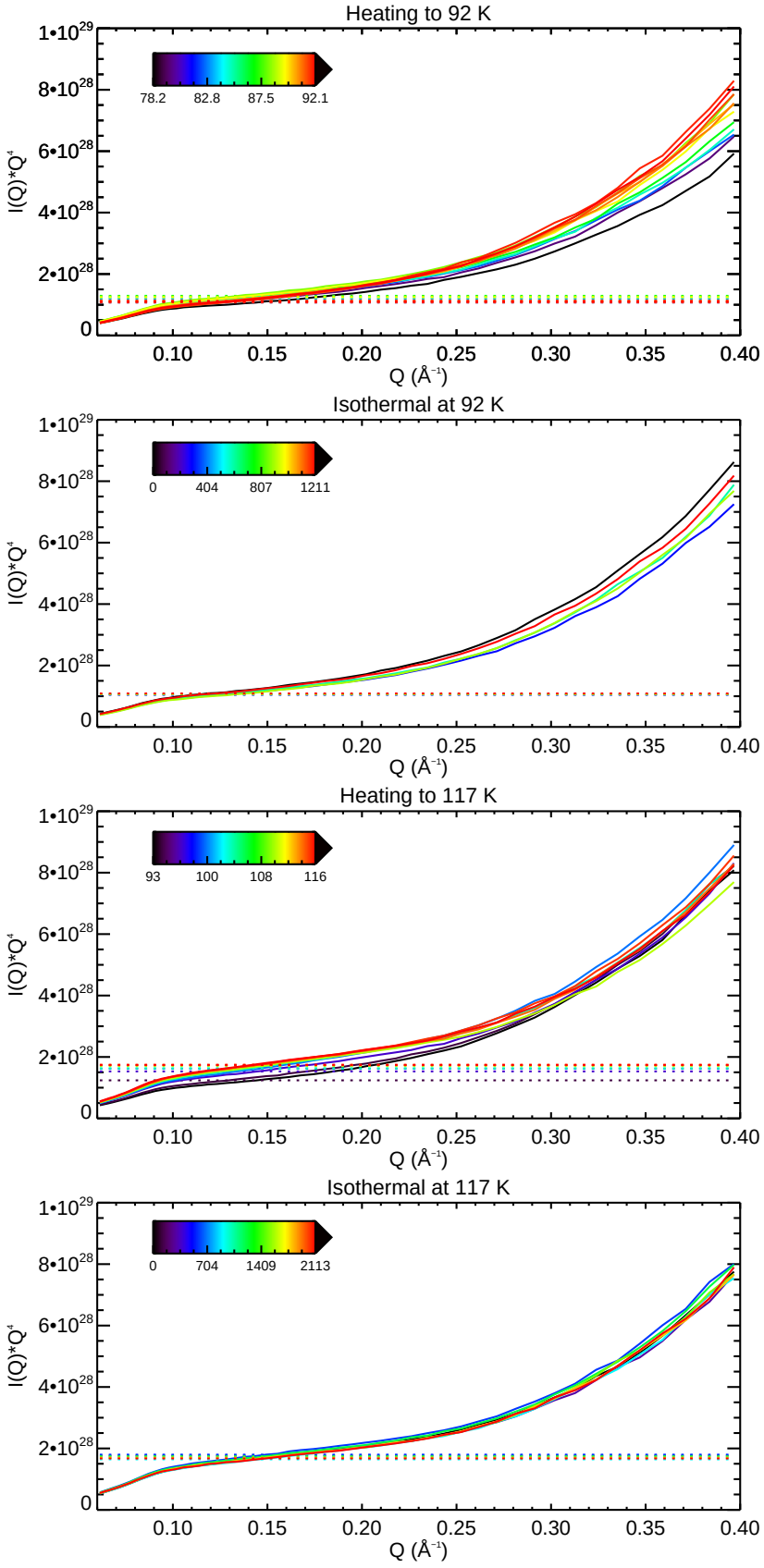

Figure 8.8: $I(Q) * Q^4$ vs. Q between 78 and 117 K, showing the quasi-plateaus from which the Porod constant (and hence the specific surface area) was extracted. Different colours indicate different temperatures (for heating regions) and times (for isothermal regions).

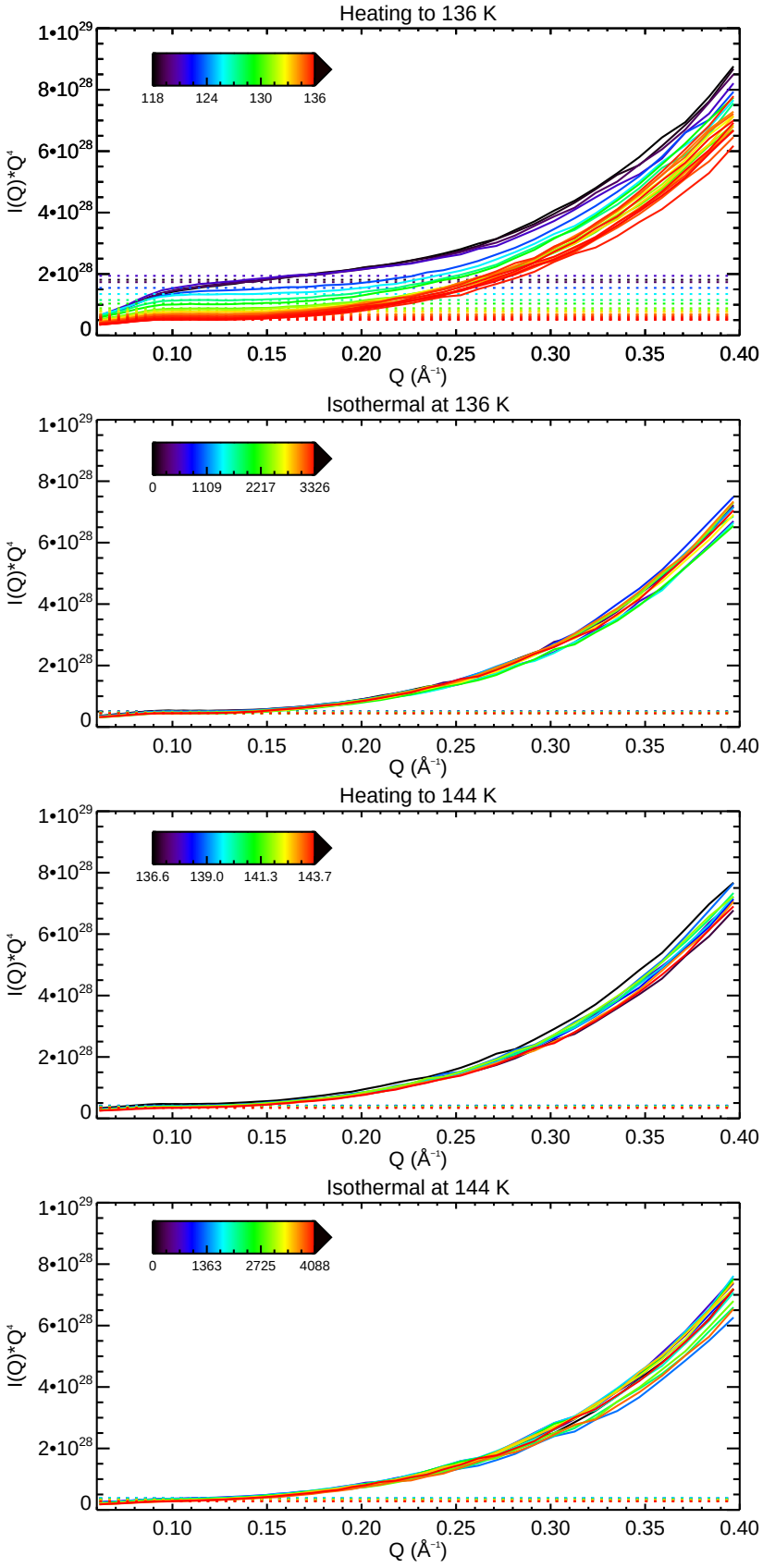

Figure 8.9: $I(Q) * Q^4$ vs. Q between 117 and 144 K, showing the quasi-plateaus from which the Porod constant (and hence the specific surface area) was extracted.

8.3.3 Periodic spacings

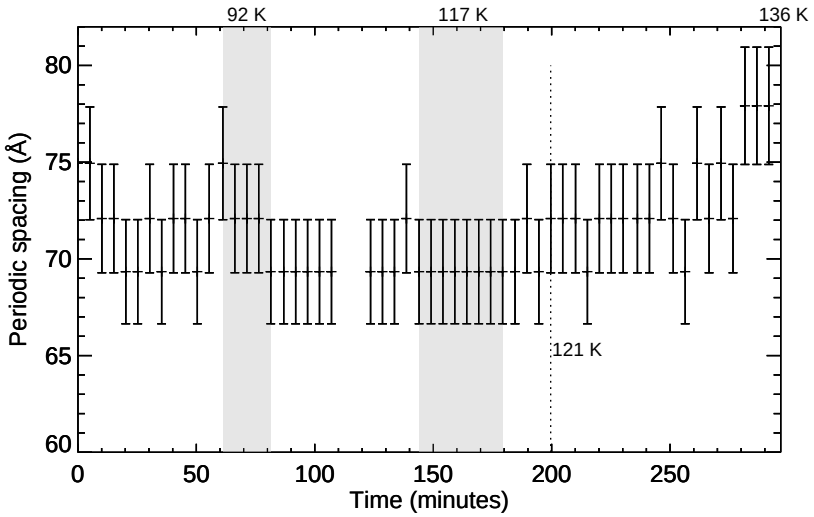

Figure 8.10: Periodic spacings as a function of time for temperatures between 78 K and 136 K. Isothermal regions are indicated by grey shading. Where there is no grey shading, the ice was heated between the isothermal temperatures according to the heating profile shown in Fig. 8.1. The temperature of 121 K is marked by a dotted line, indicating the start of the "hump" flattening and hence pore collapse.

The periodic spacings of the pores were determined by transforming the "hump" in the original data to a "pseudopeak" as described in Section 7.3.2 of Chapter 7. Figs. 8.11 and 8.12 show $I(Q) * Q^{2.5}$ vs. Q and Figs. 8.13 and 8.14 show $I(Q) * Q^3$ vs. Q.

$I(Q) * Q^{2.5}$ vs. Q produces the clearest peak until the temperature reaches 127 K; after that, $I(Q) * Q^3$ vs. Q produces the clearest peak. The peak disappears around 136 K, so after this, the periodic spacings cannot be extracted. The peak remains at the same Q position until its disappearance.

The periodic spacings extracted from the pseudopeaks are shown in Fig. 8.10. The periodic spacings are around 70 Å , in good agreement with Mitterdorfer et al. (2014) and are constant within uncertainties. This indicates that the pores do not cluster prior to collapse, in contrast to previous results (Wu et al., 2010; Mitterdorfer et al., 2014; Cazaux et al., 2015).

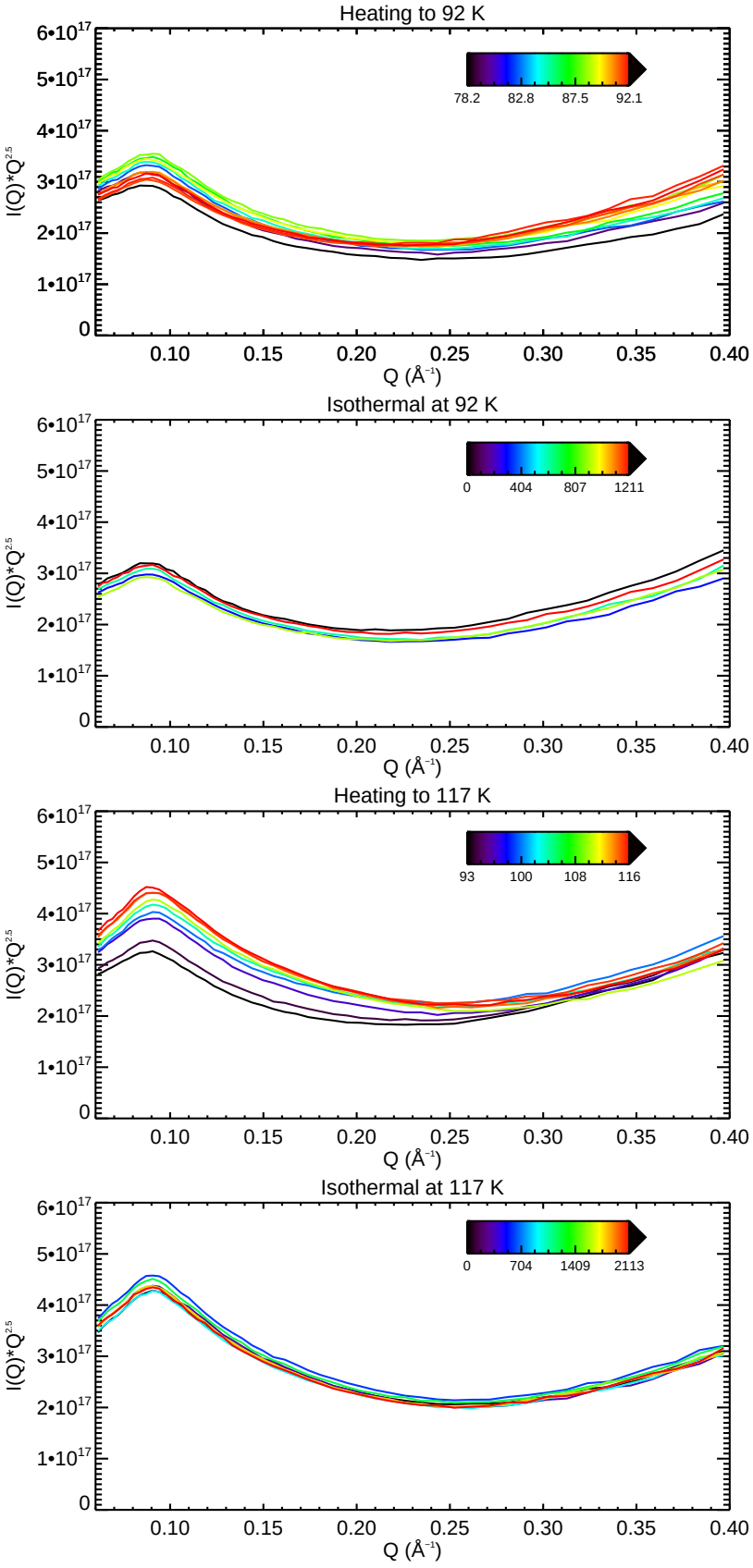

Figure 8.11: $I(Q) * Q^{2.5}$ vs. Q between 78 and 117 K, showing the pseudopeaks from which the periodic spacing of the pores can be extracted. Different colours indicate different temperatures (for heating regions) and times (for isothermal regions).

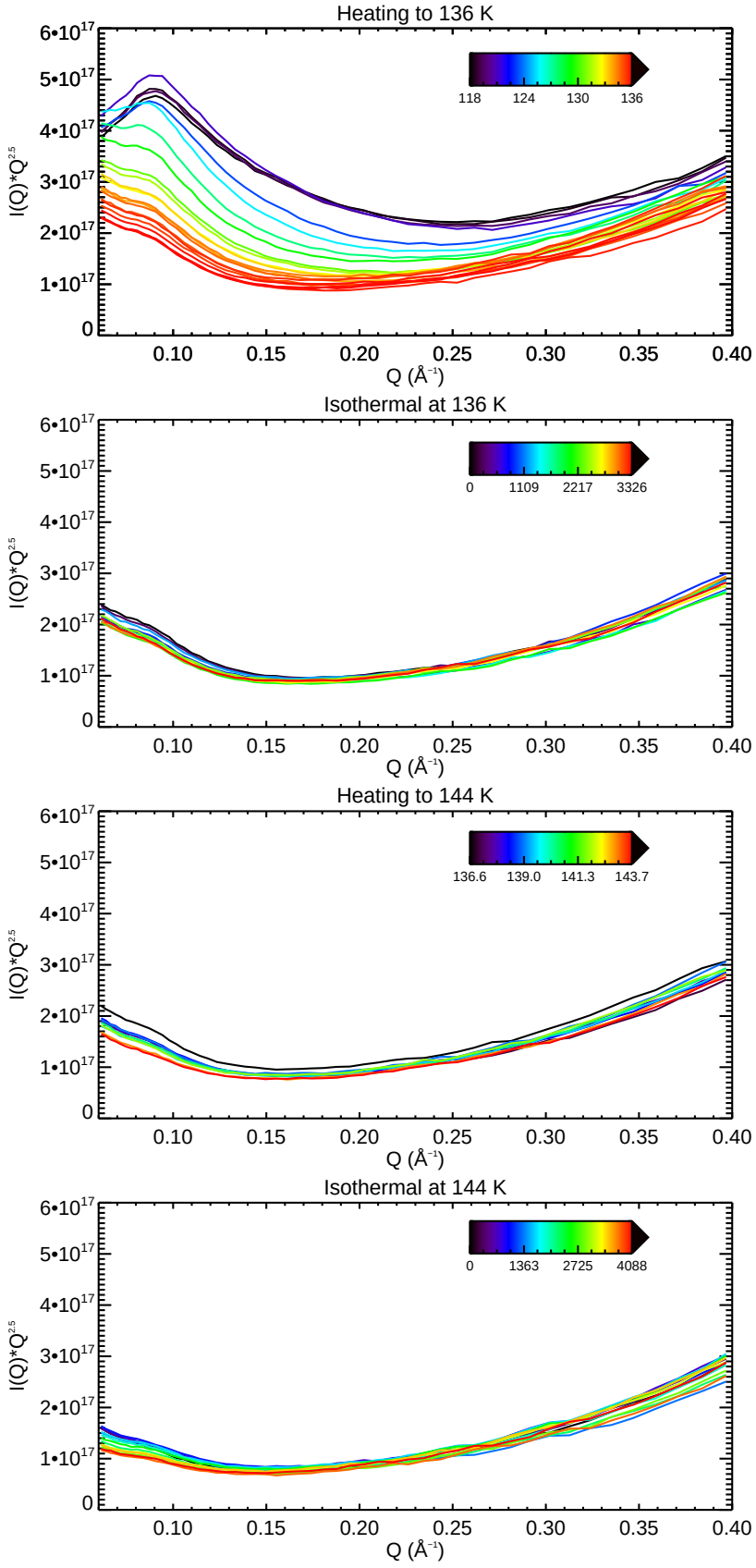

Figure 8.12: $I(Q) * Q^{2.5}$ vs. Q between 117 and 144 K, showing the pseudopeaks from which the periodic spacing of the pores can be extracted. Different colours indicate different temperatures (for heating regions) and times (for isothermal regions).

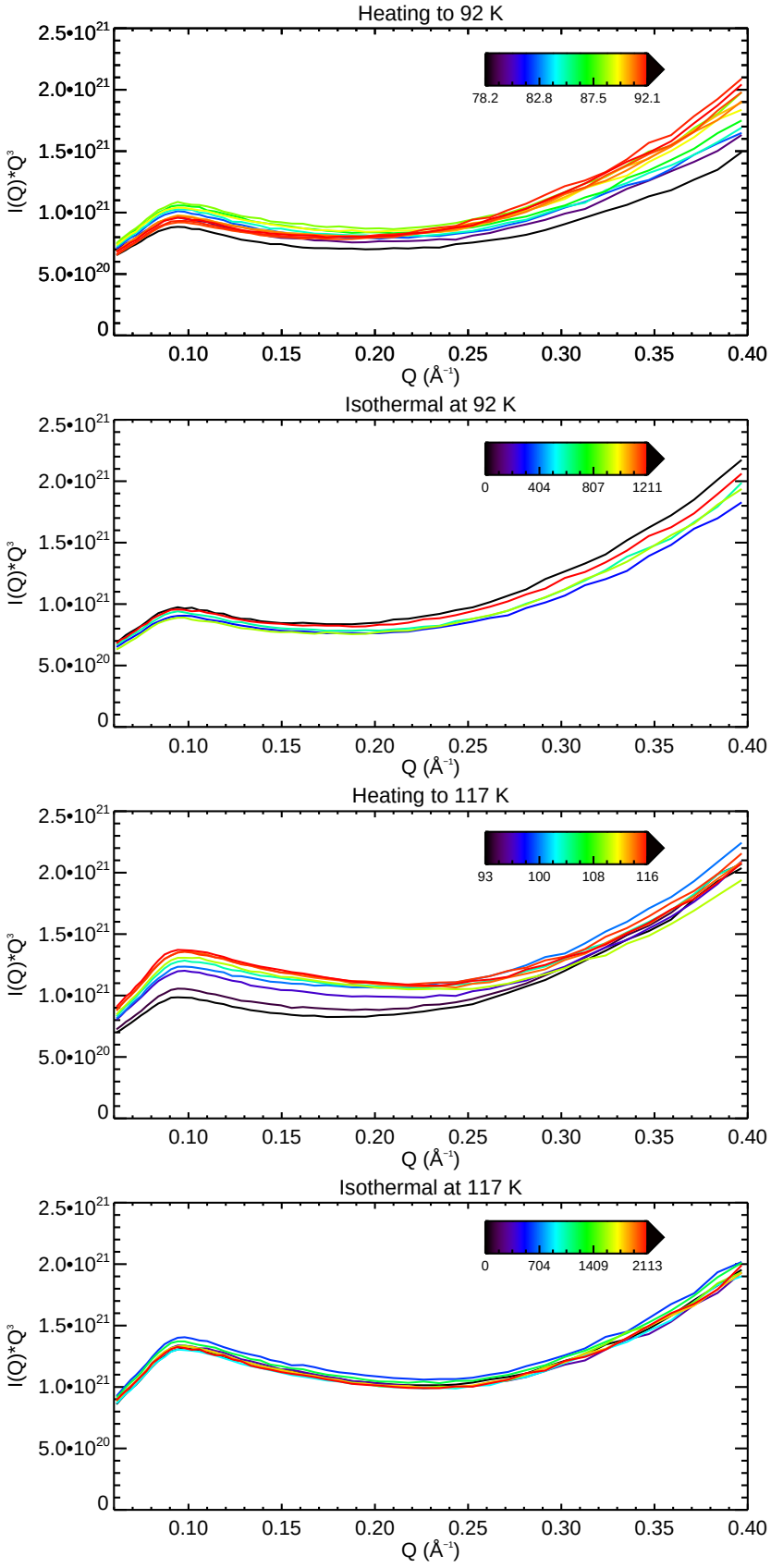

Figure 8.13: $I(Q) * Q^3$ vs. Q between 78 and 117 K, showing the pseudopeaks from which the periodic spacing of the pores can be extracted. Different colours indicate different temperatures (for heating regions) and times (for isothermal regions).

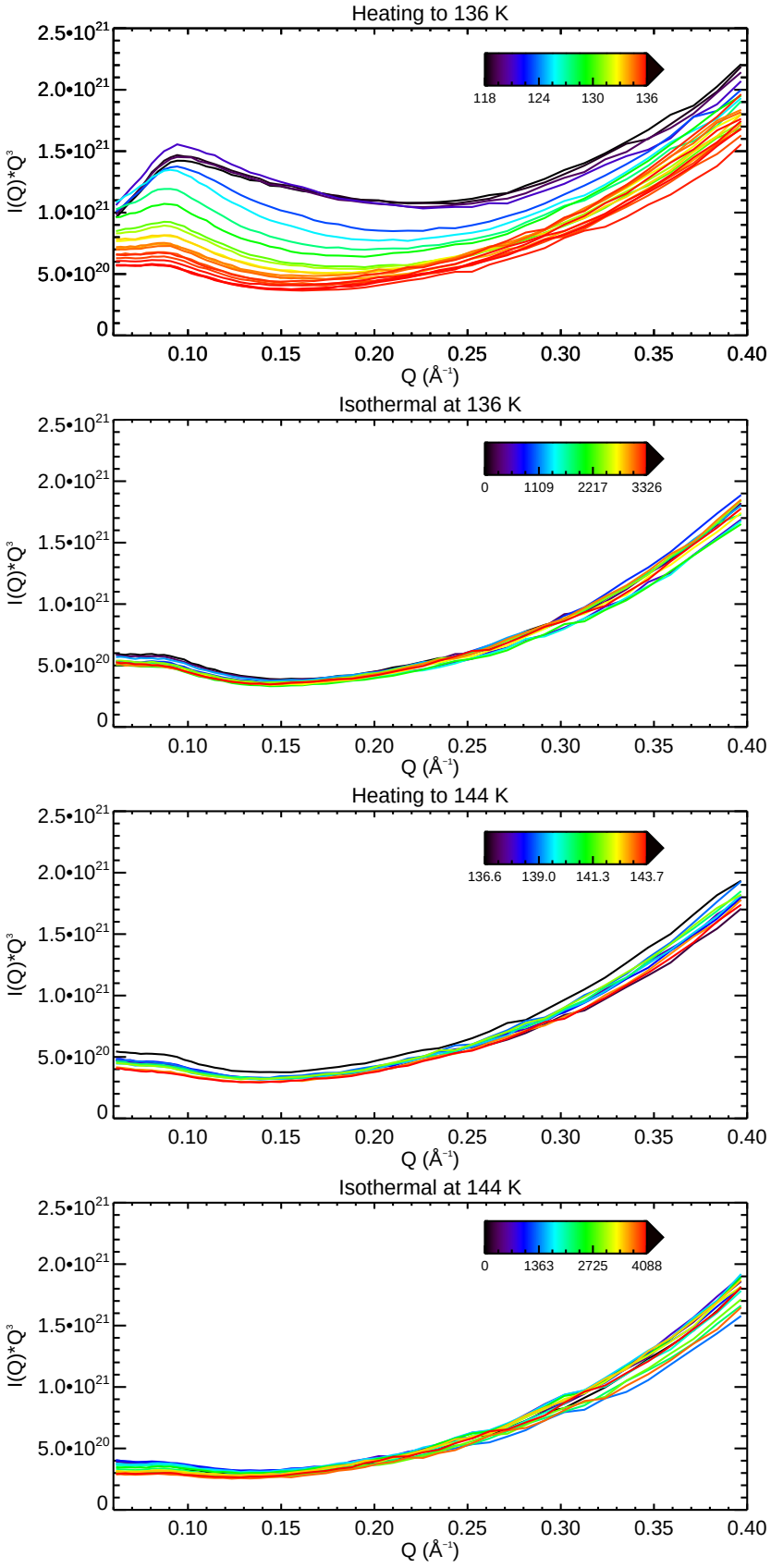

Figure 8.14: $I(Q) * Q^3$ vs. Q between 117 and 144 K, showing the pseudopeaks from which the periodic spacing of the pores can be extracted. Different colours indicate different temperatures (for heating regions) and times (for isothermal regions).

8.3.4 Guinier-Porod fits

The "hump" was fitted with a Guinier-Porod function as described in Section 7.3.3 of Chapter 7. This gives the radius of gyration of the pores (R_g) which gives a measure of pore size, the s parameter which describes pore shape ($s = 0$ for spheres, $s = 1$ for cylinders, $s = 2$ for platelets and $s = 3$ for no pores) and the d parameter which describes pore surface roughness ($d = 3$ for very rough surfaces and $d = 4$ for very smooth surfaces). These parameters are shown in Fig. 8.15 as a function of time between the temperatures of 78 K and 136 K. Beyond 136 K, the "hump" is gone and a Guinier-Porod fit can no longer be performed.

The radius of gyration is constant in all isothermal regions (92 K, 117 K and 136 K) and is constant within uncertainties between 78 K and 92 K. It increases slightly between 92 K and 117 K from 10 Å to 11 Å. Between 117 K and 136 K, the radius of gyration decreases to around 2 Å. This reduction in pore size is clearly indicative of pore collapse.

The s parameter is also constant in all isothermal regions (92 K, 117 K and 136 K) and within uncertainties between 78 K and 92 K. s starts around 1.5, indicating cylindrical pores. Between 92 and 117 K, s decreases to around 1.2. Between 117 K and 136 K, s increases, rising to nearly 3. This indicates a collapse from cylinders to platelets ($s = 2$), corroborating the results of Mitterdorfer et al. (2014), and then total collapse as s approaches 3.

The initial values of d are around 3.35. Between 78 and 92 K, the pores roughen slightly as indicated by the decrease in d to a value of 3.2. d then begins to increase again between 92 K and 117 K. d is mostly constant at 117 K but then continues to increase when heating resumes and increases very rapidly between 117 K and 136 K (as the same time as pore collapse is occurring), increasing to a value of 3.8. This suggests a smoothing process. As pore collapse continues, d fluctuates between 3.6 and 3.8, settling at around 3.7, showing that the surface of the pores is undergoing constant restructuring as they collapse.

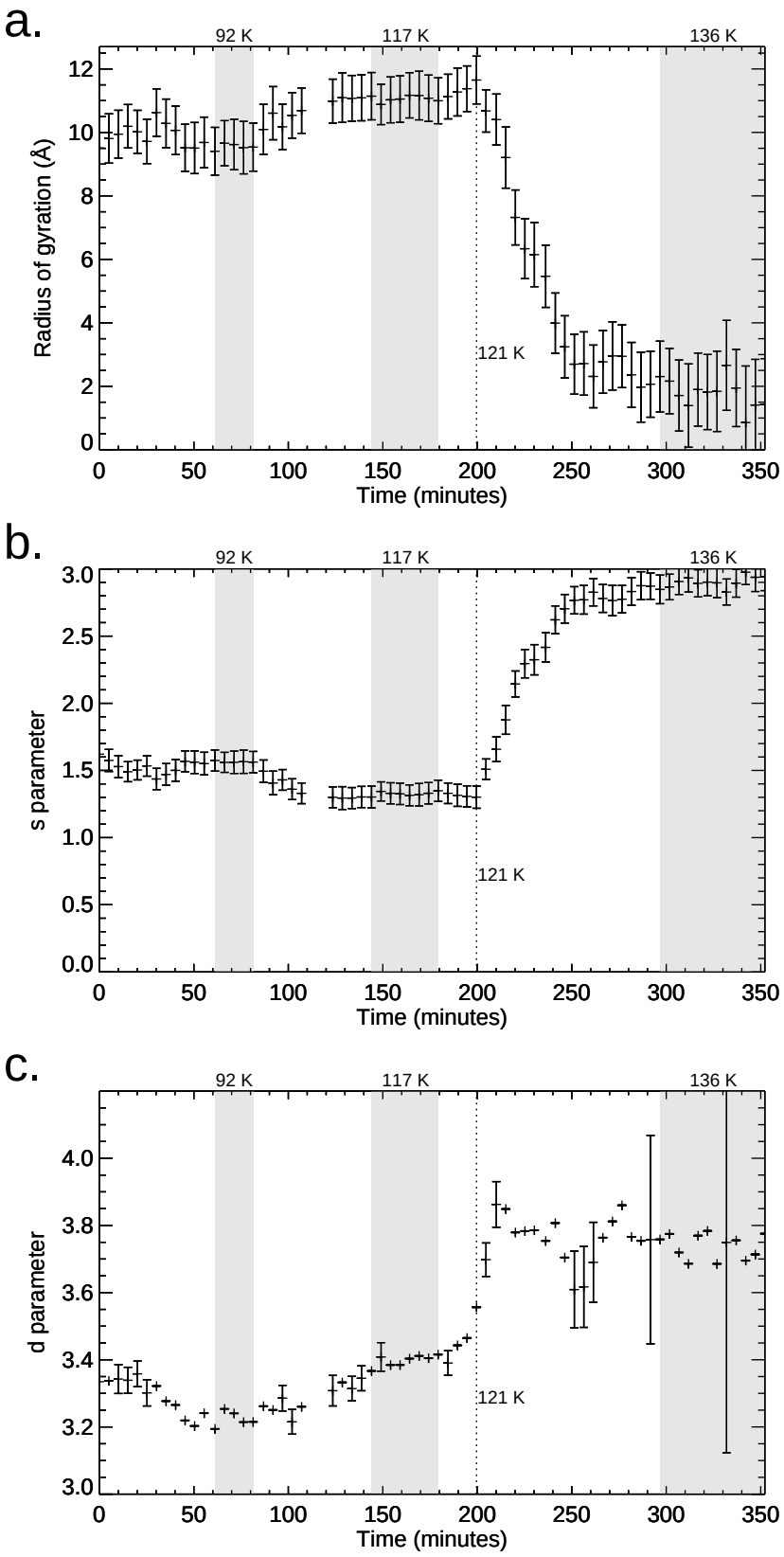

Figure 8.15: Radius of gyration (**a.**), *s* parameter (**b.**) and *d* parameter (**c.**) as a function of time for temperatures between 78 K and 144 K. Isothermal regions are indicated by grey shading. Where there is no grey shading, the ice was heated between the isothermal temperatures according to the heating profile shown in Fig. 8.1.

8.3.5 Porosity changes as a function of time: the process of pore collapse

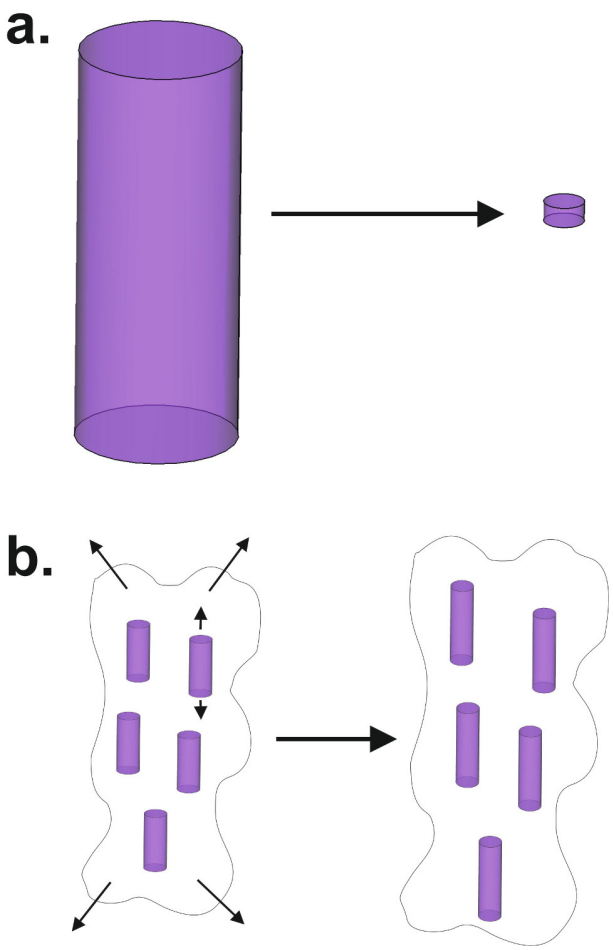

Figure 8.16: **a.** Pore size and shape changes during pore collapse. The pores collapse from cylinders to platelets. **b.** Ice expansion leading to pore elongation and increased specific surface area.

Fig. 8.17 shows the parameters relating to ice porosity (specific surface area (SSA) of the ice, pore radius of gyration (R_g), s parameter relating to pore shape, d parameter referring to pore surface roughness and periodic spacing (PS) of the pores) as a function of time. Isothermal regions are indicated by grey shading and the ice temperature is also shown.

The specific surface area, radius of gyration and s parameter undergo two main changes during the experiment. The first is an increase in specific surface area and R_g and a decrease in s, all starting around 90 minutes. The second is a decrease in

specific surface area and R_g and an increase in s starting around 200 minutes. The latter process is clearly pore collapse, as the pores get significantly smaller (R_g decreases from around 11 Å to around 2 Å between 200 minute and 280 minutes). The specific surface area also decreases significantly, from around 95 m^2 cm^{-3} at 200 minutes to around 20 m^2 cm^{-3} at 480 minutes and this decrease can also be associated with pore collapse. At 200 minutes, the s parameter is around 1.3 which indicates cylindrical pores. Between 200 minutes and 220 minutes, s increases to 2. This suggests a pore collapse from cylinders to platelets, corroborating the results of Mitterdorfer et al. (2014). The size and shape changes are illustrated in Fig. 8.16**a.**. Between 220 minutes and 280 minutes, s increases further from 2 to 3. This shows the complete collapse of the pores. A close examination of Fig. 8.17 shows that the pore collapse starts at 121 K. R_g and s stop decreasing and increasing respectively at 136 K and this is the end of the pore collapse. After the isothermal stop at 136 K, it is not possible to perform a Guinier-Porod fit as the "hump" has disappeared and so it is not possible to extract R_g or s beyond this time. The specific surface area continues to decrease slowly after R_g and s have stopped changing, with the slow decrease continuing until the end of the experiment. These small changes are likely to be related to restructuring of the ice surface as the pores have completely collapsed by this point. The pore collapse is complete well before crystallisation occurs (during the isothermal stop at 144 K) and so pore collapse and crystallisation are independent processes.

The slight increases in R_g and specific surface area and slight decrease in s between 92 K and 117 K suggests a slight pore expansion. An increase in R_g from around 10 Å to around 11 Å between 90 minutes and 130 minutes suggests an increase in pore size, albeit a small one. The specific surface area increases from around 60 m^2 cm^{-3} to around 95 m^2 cm^{-3} in the same time period. During this time period, s decreases from around 1.6 to around 1.3. As a value of 1 indicates cylinders and a value of 2 indicates platelets, this change suggests the pores are becoming more cylindrical, i.e. the pores are undergoing a process of elongation (see Fig. 7.9). The elongation starts at 94 K and is complete by 110 K. This elongation could be due to expansion of the pores alone or

expansion of the whole ice, leading to pore expansion as well. As the specific surface area increases significantly while R_g and s only undergo small changes, it is likely that the whole ice is expanding which would lead to an increased surface area at the grain surface as well as within the pores. This is illustrated in Fig. 8.16**b.**.

The d parameter does not follow the same trends as the specific surface area, radius of gyration and s parameter. d starts around 3.35 and decreases to around 3.2 between 20 minutes and 50 minutes, suggesting the pore surfaces roughen slightly. d remains around 3.2 until 120 minutes when it begins to slowly increase to 3.4 by the time the isothermal stop at 117 K is reached. It continues to increase slightly during the isothermal stop and shortly afterwards. At 200 minutes, d begins to rise steeply until 210 minutes, finishing at a value of 3.85. After this, d falls slightly to 3.6, rises back to 3.85 and then falls again, settling at a value of around 3.7 during the isothermal stop at 136 K. These changes indicate that the pores start to become smoother around 120 minutes (at a temperature of 115 K), with the smoothing happening faster after 200 minutes (121 K) when pore collapse starts. As the pore collapse finishes, the pore surfaces undergo restructuring that makes them become rougher and smoother again and by the end of the collapse they are fairly smooth. Hence pore collapse causes the pores to become smoother and the smoothing process starts before pore collapse, although the rate of smoothing increases once pore collapse starts.

The periodic spacings of the pores is around 70 Å and is constant within uncertainties until the periodic spacing can no longer be extracted due to pore collapse (at 136 K). An increase in periodic spacing has previously been attributed to pore clustering (Mitterdorfer et al., 2014); the constant periodic spacing here appears to indicate a lack of pore clustering. Pore clustering has also been seen in other experiments (eg. Wu et al. (2010); Cazaux et al. (2015)) and so it seems that pore clustering occurs in some ices before pore collapse but does not always occur, i.e. it is not a necessary process accompanying pore collapse.

R_g and s appear to be constant within uncertainties in all the isothermal regions they can be extracted (92 K, 117 K and 136 K). The specific surface area appears to be

Table 8.1: Gradients and chi-squared (χ^2) values obtained for linear fits of specific surface area (SSA), radius of gyration (R_g) and the s parameter as a function of time at different temperatures.

Temperature (K)	Gradient	χ^2
SSA		
92	$-9.8 \times 10^{-2} \pm 4.83 \times 10^{-1}$	0.23
117	$-1.01 \times 10^{-1} \pm 6.09 \times 10^{-1}$	0.10
136	$-4.55 \times 10^{-2} \pm 1.46 \times 10^{-3}$	1100
144	$-6.83 \times 10^{-2} \pm 5.73 \times 10^{-3}$	98
R_g		
92	$2.34 \times 10^{-3} \pm 4.75 \times 10^{-2}$	0.067
117	$1.76 \times 10^{-3} \pm 2.20 \times 10^{-2}$	0.14
136	$1.06 \times 10^{-2} \pm 2.11 \times 10^{-2}$	0.97
s		
92	$3.69 \times 10^{-4} \pm 4.96 \times 10^{-3}$	0.015
117	$4.41 \times 10^{-4} \pm 2.41 \times 10^{-3}$	0.23
136	$1.25 \times 10^{-3} \pm 1.68 \times 10^{-3}$	1.4

constant within uncertainties in the isothermal regions of 92 K and 117 K but decreases slowly in the isothermal regions of 136 K and 144 K. Figs. 8.18-8.20 show R_g, s and specific surface area as a function of time for 92 K, 117 K and 136 K. Fig. 8.21 shows specific surface area as a function of time for 144 K. Linear fits to this data are shown in red, with the gradients and chi-squared (χ^2) values shown in Table 8.1. For R_g and s, the gradients are very small and are zero within the uncertainty of the fit in all isothermal regions. The gradients for specific surface area are similarly close to zero within the uncertainty of the fit at 92 and 117 K. The quality of the fit is somewhat poor in the cases of specific surface area at 136 K and 144 K (as shown by the high χ^2 values) but the gradients and uncertainties on the gradients do indicate a decrease. The linear Pearson correlation coefficient (see Equation 4.1 in Chapter 4) is -0.77 ± 0.0022 for specific surface area at 136 K and -0.69 ± 0.0053 for specific surface area at 144 K. These values indicate negative correlation and hence the decrease in specific surface area at these temperatures is real. As R_g and s are effectively constant in all isothermal regions of study and specific surface area is constant at 92 and 117 K, it appears that pore collapse is not an autocatalytic process below 117 K.

This experiment can be viewed as the first step towards a kinetic model of pore

collapse in amorphous solid water. It is not possible to extract quantitative kinetic information from the current data as both temperature and time are changing while the pores are collapsing, hence it is impossible to determine to what extent the pores are collapsing as a function of temperature and to what extent they are collapsing as a function of time. A series of isothermal experiments would need to be carried out around the temperature that pore collapse begins to see how the rate changes as a function of temperature. A series of different experiments studying the pore collapse at different heating rates would complement the first set of experiments. This is discussed further in Chapter 10. However, it is possible to draw some qualitative conclusions about how the rate of pore collapse changes with heating rate, as the heating rate was not constant between 121 K and 136 K. A visual examination of Fig. 8.17 reveals that the temperature increases linearly until around 130 K and exponentially thereafter. s increases linearly at first, then the rate of change decreases as the heating rate decreases. Therefore the rate of pore shape change appears to be linked to the heating rate, although it is not possible to describe this in a quantitative manner with the current data. Conversely, there are no obvious changes to the rate of decrease of specific surface area before and after 130 K (220 minutes) and therefore its decrease may be independent of heating rate. The rate of decrease of R_g appears to be constantly changing and so it is not possible to conclude anything about how its rate of decrease may be linked to or independent of the heating rate.

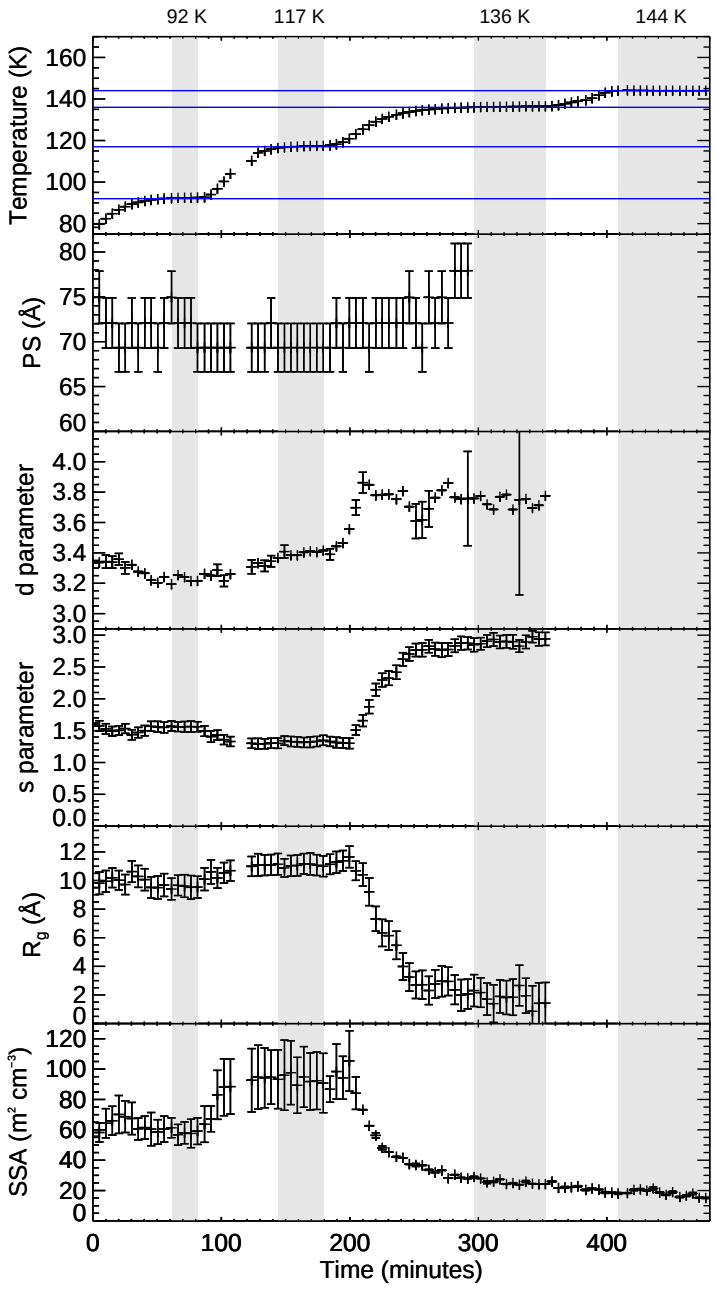

Figure 8.17: Parameters pertaining to porosity and structure changes in the ice as a function of time: specific surface area (SSA) of the ice, pore radius of gyration (R_g), s parameter relating to pore shape, d parameter referring to pore surface roughness and periodic spacings (PS) of the pores. The ice temperature is also shown. Isothermal regions are indicated by grey bars.

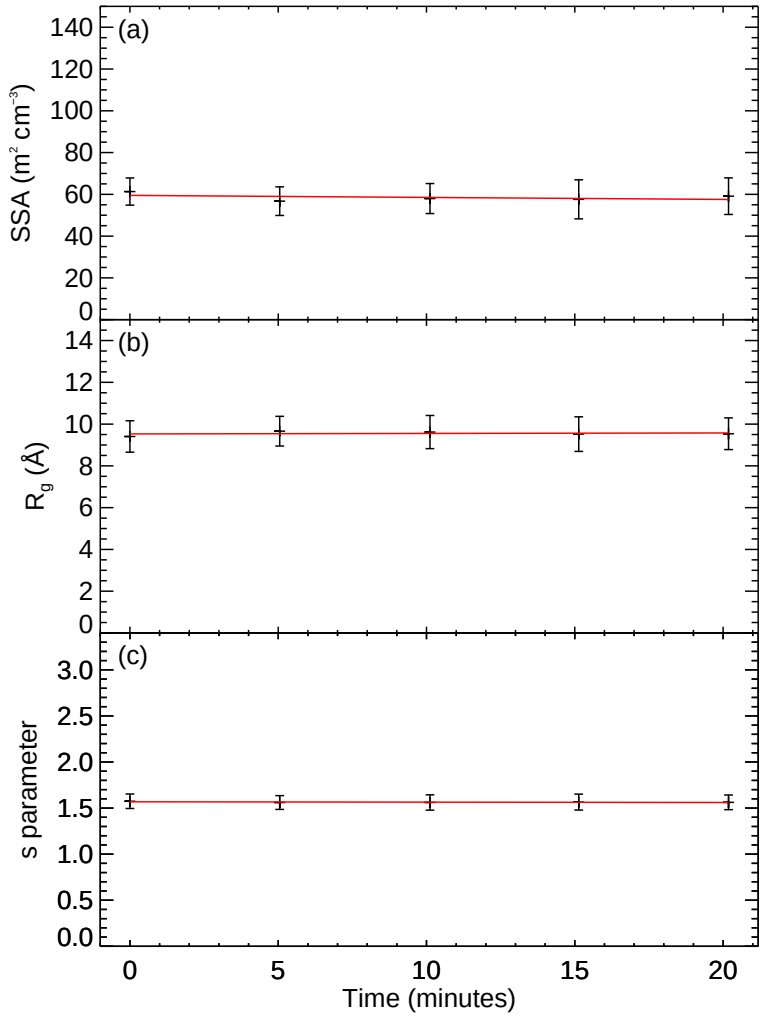

Figure 8.18: Specific surface area (SSA) (**a.**), radius of gyration (R_g), (**b.**) and s parameter (**c.**) as a function of time for isothermal at 92 K. Linear fits are shown in red. The gradients of the fits and the chi-squared values are shown in Table 8.1.

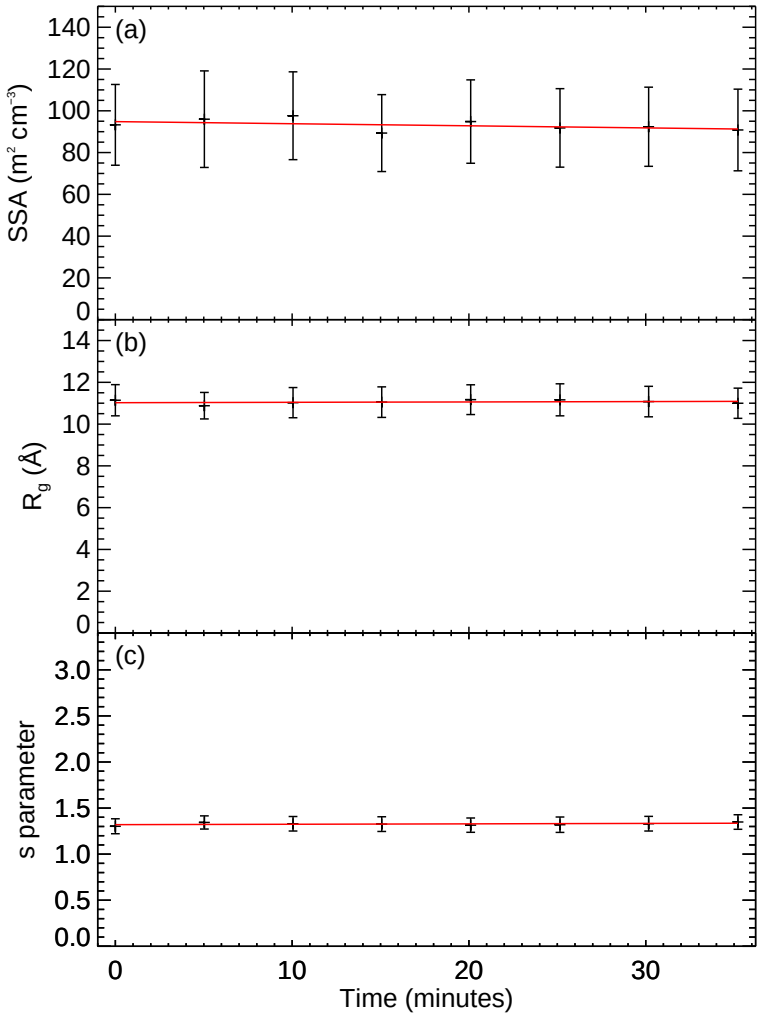

Figure 8.19: Specific surface area (SSA) (**a.**), radius of gyration (R_g), (**b.**) and s parameter (**c.**) as a function of time for isothermal at 117 K. Linear fits are shown in red. The gradients of the fits and the chi-squared values are shown in Table 8.1.

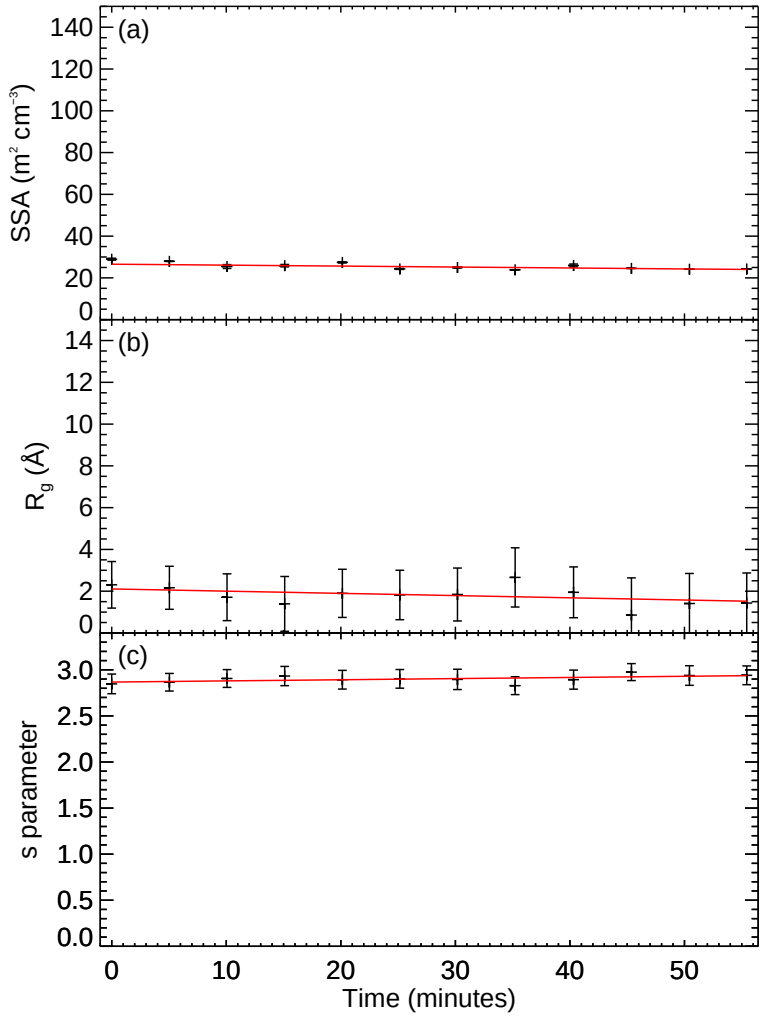

Figure 8.20: Specific surface area (SSA) (**a.**), radius of gyration (R_g), (**b.**) and s parameter (**c.**) as a function of time for isothermal at 136 K. Linear fits are shown in red. The gradients of the fits and the chi-squared values are shown in Table 8.1.

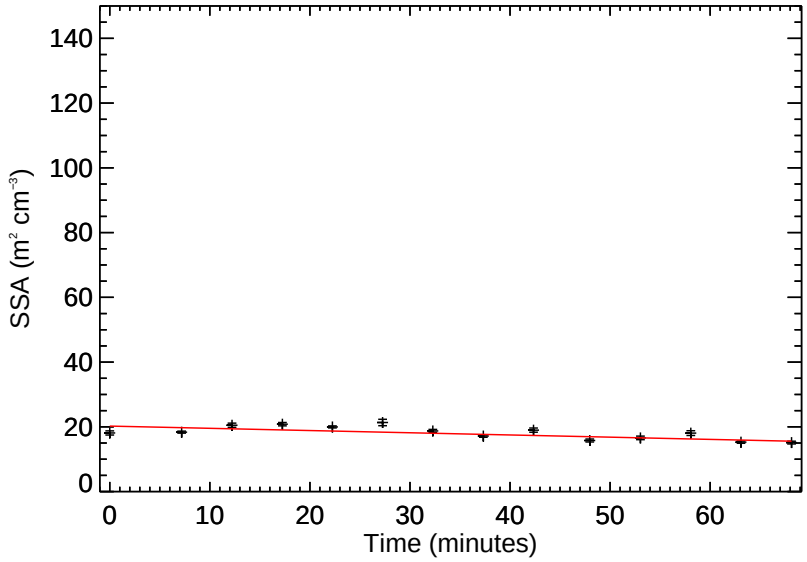

Figure 8.21: Specific surface area (SSA) as a function of time for isothermal at 144 K. Linear fits are shown in red. The gradients of the fit and the chi-squared value are shown in Table 8.1.

8.3.6 Porosity changes as a function of temperature: the glass transition of amorphous solid water

As discussed in the introduction to this chapter, the nature of water's glass transition is disputed and several different explanations have been proposed. The main suggestions are: that the glass transition is from a glassy state to a super cooled ultra viscous state (achieved by long range diffusive, translational motion of water molecules); that the glass transition is from one glassy state to another glassy state (achieved by reorientation of water molecules alone); and that the glass transition is driven by impurities causing enhanced surface mobility. In this work, the glass transition is studied by considering the porosity changes in amorphous solid water associated with the collapse of the pores.

The key parameters associated with the pores in amorphous solid water are shown in Fig. 8.22 (specific surface area, radius of gyration, s parameter, d parameter and periodic spacings) as a function of temperature. The isothermal temperatures of 92 K, 117 K, 136 K and 144 K are indicated in grey. Other than the slight changes to the radius of gyration, s parameter and specific surface area between 92 K and 117 K that are associated with ice expansion (see Section 8.3.5), the radius of gyration, s parameter and specific surface area remain constant until 121 K, where they undergo rapid changes. The radius of gyration and specific surface area both decrease and the s parameter increases. As described in Section 8.3.5, these changes indicate pore collapse from cylinders to platelets. Achieving this collapse requires long range translation of water molecules. Therefore, 121 K is the temperature required for the onset of translational motion of water molecules (i.e. diffusion) for this ice and is taken to be the starting temperature for the glass transition. This conclusion confirms that the pore elongation seen between 94 K and 110 K is related to ice expansion rather than just pore expansion as the latter process would require long range translation of water molecules. R_g and s continue to change until 136 K but do not change further once this temperature is reached. The specific surface area undergoes the most dramatic change

between 121 K and 136 K, although it continues to decrease thereafter. Therefore 136 K is taken to be the end point of the glass transition as by then, pore collapse is complete.

The d parameter starts to increase (corresponding to pore surface smoothing) around 115 K. As smoothing requires rotational movement of water molecules but not necessarily translational movement, it appears that the onset of rotational motion occurs at 115 K. The d parameter continues to rise until 125 K and then decreases slightly, indicating a smoothing effect followed by slight roughening as the pore collapse process comes to an end.

The onset temperature of the glass transition is related to the heating rate and, from calorimetry experiments, is expected to be around 124 K for heating rates of 0.4 K min^{-1} (Handa & Klug, 1988). This is very close to the temperature of 121 K seen here for the onset of translational diffusive motion and therefore it appears that the glass transition seen in calorimetry experiments is associated with long range, translational diffusion of water molecules. Reorientation of individual water molecules would not achieve pore collapse and so these mechanisms cannot be responsible for water's glass transition. The impurity driven surface mobility mechanism can also be ruled out as the pore collapse is a bulk effect and not a surface effect, so increasing surface mobility alone would not result in pore collapse. These results confirm the suggestion of Townrow & Coleman (2015) that pore collapse in ASW is associated with the glass transition.

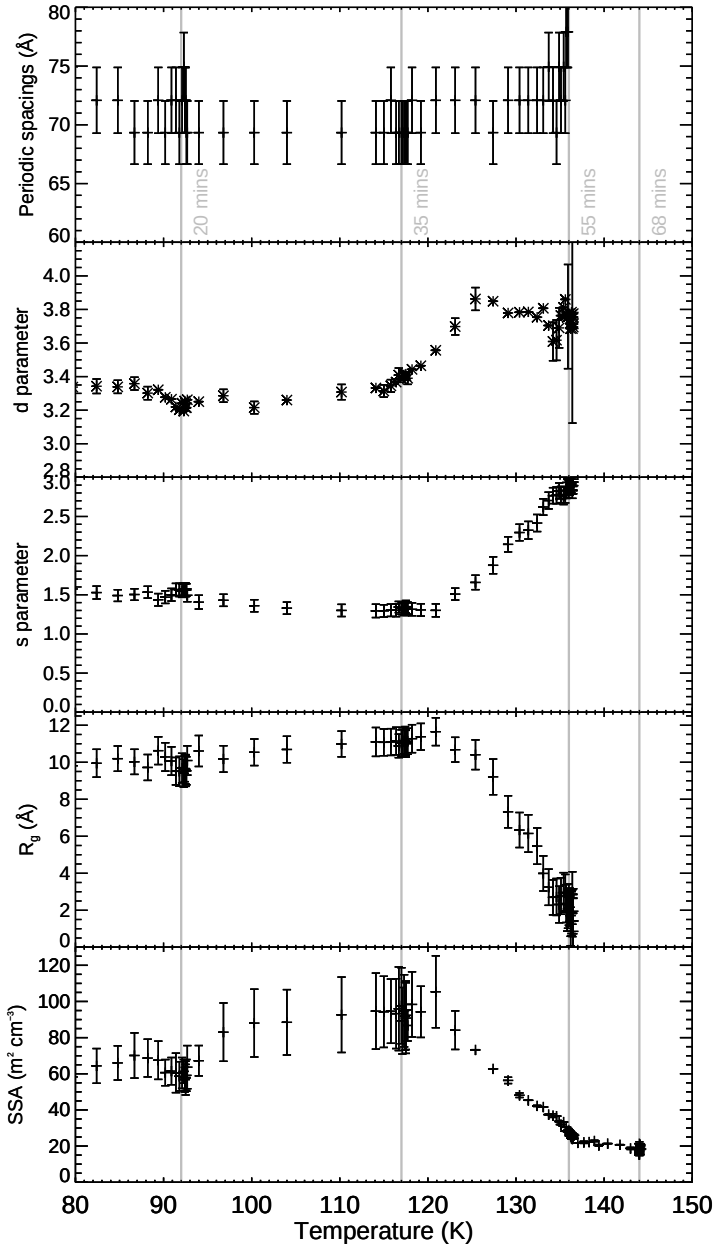

Figure 8.22: Parameters pertaining to porosity and structure changes in the ice as a function of temperature: specific surface area (SSA) of the ice, pore radius of gyration (R_g), *s* parameter relating to pore shape, *d* parameter referring to pore surface roughness and periodic spacings of the pores. The isothermal temperature are indicated by grey lines with the time spent at each temperature also given in grey.

8.4 Conclusions

Amorphous solid water formed at 77 K was studied using neutron scattering while heating and while isothermal to observe porosity changes in the ice. The ice was heated from 78 K to 144 K with isothermal stops at 93 K, 117 K, 136 K and 144 K. The c-ASW that was grown was porous, with pore collapse occurring when heating from 121 K to 136 K. Crystallisation occurred while the ice was held at 144 K. The main conclusions of this work are as follows:

1. Pore collapse begins at 121 K, indicated by a decrease in specific surface area and radius of gyration. The s parameter increases from 1.5 to 2 between 121 K and 128 K, indicating collapse from cylinders to platelets. The s parameter then increases to 3 between 128 K and 136 K, indicating total collapse of the pores. R_g and s stop decreasing at 136 K, signifying the end of pore collapse. Specific surface area continues to decrease further between 136 K and 144 K, which is attributed to surface restructuring.

2. Before pore collapse occurs, R_g and specific surface area increase a little and s decreases a little. This is attributed to ice expansion which results in pore elongation.

3. The d parameter begins to change before pore collapse starts. It increases, indicating pore smoothing. It increases faster once pore collapse starts.

4. The periodic spacing of the pores remains constant within uncertainties throughout the heating and pore collapse (until it can no longer be extracted due to disappearance of the "hump"). This shows that pore clustering is not taking place and hence pore clustering is not a necessary process accompanying pore collapse.

5. R_g and s do not change (within uncertainties) in any of the isothermal regions for which they can be extracted (92 K, 117 K and 136 K). The specific surface area does not change (within uncertainties) at 92 K or 117 K and therefore, pore

collapse is not likely to be an autocatalytic process below 117 K. The specific surface area does undergo small changes during the isothermal stops at 136 K and 144 K.

6. The rate of increase of s changes as the heating rate of the ice changes. This suggests that it depends on the heating rate. The rate of change of specific surface area does not appear to depend on the heating rate and so this decrease may be independent of heating rate. The rate of decrease of R_g is constantly changing and so it is not clear whether it is linked to the heating rate or not.

7. The glass transition of amorphous solid water involves a transition from a glassy state to an ultra cooled liquid state. This is the only suggestion able to account for pore collapse. For this ice, it begins at 121 K and ends at 136 K.

From this experiment, the nature of pore collapse in amorphous solid water is now clearer. It is clearly not an autocatalytic process below 117 K on the timescale of the present experiment. As there is no evidence for the pores changing at all when the temperature is constant below 117 K, it is likely that amorphous solid water in space will remain porous for as long as the temperature is below this value. This has implications for planetisimal formation as more porous particles are known to have greater sticking probabilities (Langkowski et al., 2008; Shimaki & Arakawa, 2012). Pore collapse is not necessarily preceded by pore clustering, although this has been seen to occur in other experiments. Studying the pore collapse has also shed light on the glass transition in amorphous solid water, showing that it involves long range, translational diffusion of water molecules. This diffusive motion could promote sticking during the glass transition as as sintering could occur, which could bind ice particles together.

The next step is to study the porosity of ices grown at temperatures below 77 K as these are thought to be more porous. This is the subject of the next chapter.

Chapter 9

Low temperature growth and pore collapse of amorphous solid water

The work presented in the previous chapter answered important questions about the process of pore collapse in amorphous solid water grown at 77 K. It has been suggested that amorphous solid water undergoes a phase transition from a more porous to a less porous form between ∼30 K and ∼70 K, so the porosity and process of pore collapse may be different for ices grown at temperatures below 77 K. To investigate this, four ices were grown in situ on the NIMROD beam line at deposition temperatures of 50 K, 52 K, 17 K and 17 K as described in Chapter 6. The porosity was studied while growing the ice and while heating the ice to 180 K. Once again, the specific surface area, pore periodic spacings and parameters relating to pore size, shape and surface roughness were extracted as described in Chapter 7. These parameters are compared to investigate the similarities and differences between the porosity changes in amorphous solid water grown at different temperatures.

9.1 Introduction

The previous chapter shed light on the process of pore collapse in amorphous solid water grown at 77 K. The pores collapse from cylinders to platelets once the onset of

the glass transition temperature has been reached (around 121 K in this case). The pore collapse is not auto-catalytic at temperatures of 117 K and below and is not necessarily preceded by pore clustering. However, amorphous solid water grown at temperatures below 77 K is known to be very porous (Stevenson et al., 1999; Kimmel et al., 2001) and may have increased porosity with respect to ices grown at 77 K. The low temperature, higher porosity form is sometimes referred to as porous ASW (p-ASW) and the higher temperature, lower porosity form is referred to as compact ASW (c-ASW), although it should be noted that c-ASW is still porous (Horimoto et al., 2002; Collings et al., 2003b; Isokoski et al., 2014). In addition, it is postulated that p-ASW undergoes a phase change to c-ASW between ∼30 K and ∼70 K (Jenniskens & Blake, 1994; Horimoto et al., 2002; Collings et al., 2003b). It has been suggested that p-ASW contains open pores whereas c-ASW contains only closed pores. This enables gas to be trapped inside the pores during the phase change from p-ASW to c-ASW (Horimoto et al., 2002; Collings et al., 2003b). This leaves a number of open questions. How do the pore sizes and shapes differ when ASW is grown at temperatures below 77 K and does the periodic spacing and specific surface area change? Does the deposition temperature affect the temperature at which pore collapse takes place? Does a phase change really occur between 30 K and 70 K and if so, what is the nature of the phase change? This chapter seeks to answer these questions and functions as a proof-of-concept study for growing ASW on the NIMROD beam line. In addition, it is not known how the porosity of ASW changes as it is grown. The apparatus described in Chapter 6 and used in the experiments described in this chapter is capable of studying the growth of ASW as well as porosity changes that take place on heating and so is suitable for answering the question of how the porosity evolves as the ice grows.

Four different ices were grown at deposition temperatures of 50 K, 52 K, 17 K and 17 K. The deposition and heating procedures are described in Section 9.2. The results, both the basic data and derived parameters (specific surface area, periodic spacing, radius of gyration, s parameter and d parameter) are presented in Section 9.3. The implications of the results are discussed in Section 9.4 and conclusions are drawn in

Section 9.5.

9.2 Experimental methods

9.2.1 Deposition

The experiments were carried out using the experimental set up described in Section 6.3.2 of Chapter 6. Briefly, D_2O vapour was deposited on a cold vanadium plate connected to a cryostat. The vanadium plate was situated inside a vacuum chamber on the beam line such that the neutron beam passed through the plate. In the first experimental run the set up used was that depicted in Figs. 6.7 and 6.8, with a single aluminium heat shield with two large holes for the beam to enter and exit through. Two ices were grown using this set up at deposition temperatures of 50 K and 52 K. The second experimental run used the modified set up depicted in Fig. 6.9 with two aluminium heat shields (without beam-in and beam-out holes surrounding the vanadium plate). Two additional ices were grown using this set up, both at deposition temperatures of 17 K.

For the 50 K deposition and the first 17 K deposition, the D_2O vapour was deposited for around 20 hours to ensure a sufficiently thick sample of ice to give good neutron scattering data. The 52 K deposition and the second 17 K deposition had deposition times of around 12 hours due to time restrictions on beam time. Although in some cases, the smaller amount of ice made the data analysis more difficult (particularly when analysing short scans), this deposition time still gave a sufficient quantity of ice to be able to analyse the data effectively. Scans were taken approximately every 15 minutes during deposition.

The D_2O vapour was stored in bottles on the dosing line with a total capacity of 4 litres in the first experimental set up and a total capacity of 8 litres in the second. This supply of D_2O vapour lasted for a few hours before the bottles needed to be refilled as described in Section 6.3.2 of Chapter 6. While the bottles were being filled, deposition

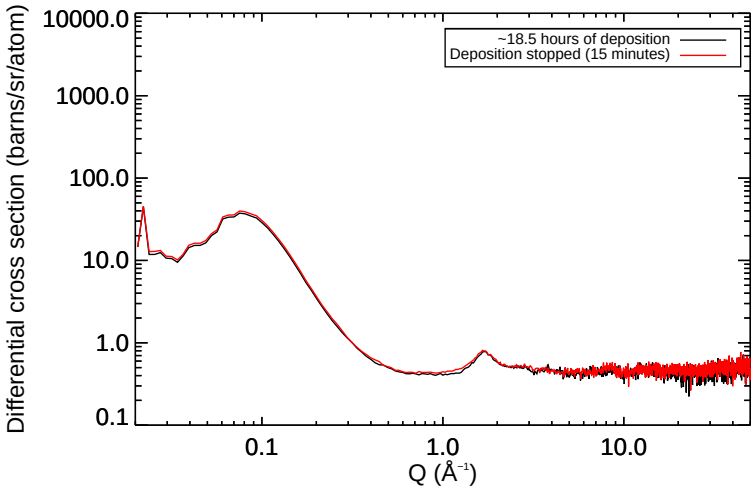

Figure 9.1: Comparison of neutron scattering pattern obtained after ∼18.5 hours of deposition at 50 K with neutron scattering pattern taken after deposition was stopped for 15 minutes.

was stopped, typically for 5-15 minutes. The results of Chapter 8 suggest that the ice would be stable on these timescales at these temperatures. To confirm this, scans were taken while deposition had stopped and the bottles were being refilled. These scans showed no changes to the ice when deposition was stopped. An example is shown in Fig. 9.1.

The temperature of the vanadium plate did not remain constant throughout deposition but underwent the changes depicted in Fig. 9.2. For the 50 K and the 52 K deposition (Fig. 9.2**a.** and **b.** respectively), the temperature increased as deposition took place. This is likely to be because not all of the energy released in deposition could be removed by the cryostat, leading to a slow temperature rise. The temperature increased faster during the 52 K deposition despite similar rates of growth (see later). As the temperature of the cryostat only increased to 120 K when heating to remove the ice (unlike the vanadium plate which was heated to approximately 300 K), it is possible that ice was formed on the copper stud linking the vanadium plate with the cold head of the cryostat during the first deposition and remained there during warm up. The presence of this ice could have reduced the thermal linkage between sample and cryostat, thus causing the faster temperature increase. In contrast, the temperature

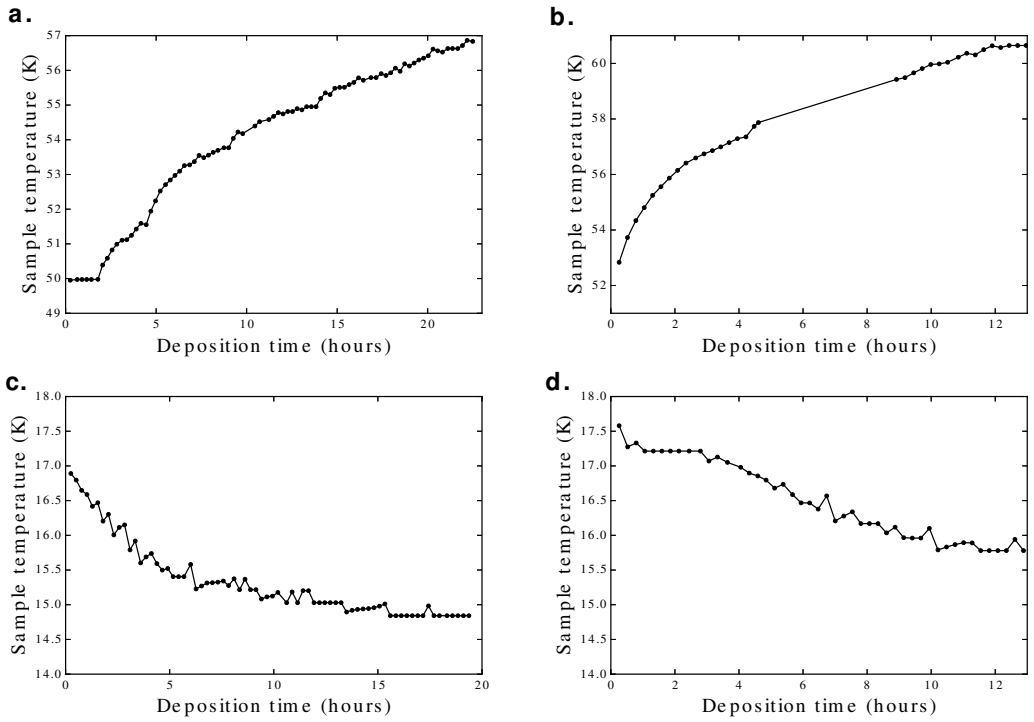

Figure 9.2: Sample temperature during deposition. **a.** 50 K deposition. **b.** 52 K deposition. **c.** 17 K first deposition. **d.** 17 K second deposition.

of the vanadium plate decreased during deposition for both 17 K depositions. For these later experiments, the thermal linkage between the vanadium plate and the cryostat was improved (see Chapter 6) and was sufficient to remove the heat released in deposition. The decrease in temperature is likely to be due to starting deposition before the base temperature of the vanadium plate had been reached (the temperature of the cryostat also decreased during deposition).

The flow rate of D_2O vapour into the chamber was set when the entire system was at ambient temperature by opening the needle valve and observing the pressure rise in the chamber. For the 50 K and 52 K depositions, the pressure in the chamber at ambient temperature was 3.4×10^{-4} mbar and the flow of D_2O was set such that the pressure rose to 4.1×10^{-4} mbar. For the first 17 K deposition, the pressure in the chamber at ambient temperature was 4.3×10^{-5} mbar and the flow of D_2O was set such that the pressure rose to 6.0×10^{-5} mbar. Due to timing restrictions, the flow for the second 17 K deposition had to be set while the system was cold and hence the flow rate is unknown.

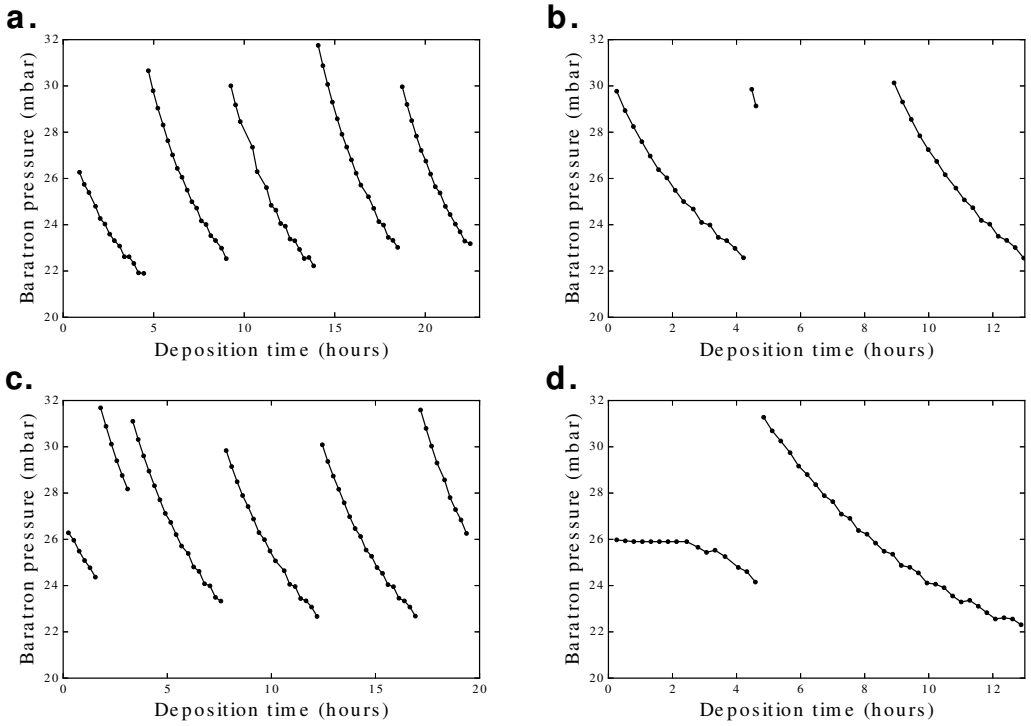

Figure 9.3: Pressure measured in the dosing line during deposition. The baratron had an offset of approximately 18 mbar. **a.** 50 K deposition. **b.** 52 K deposition. **c.** 17 K first deposition. **d.** 17 K second deposition.

Table 9.1: Depletion rate of D_2O vapour for 50 K deposition.

Cycle	Depletion rate (mbar hour^{-1})
1	1.24
2	1.82
3	1.68
4	1.94
5	1.80

It is also possible to estimate the flow of D_2O vapour into the chamber by observing the depletion rate of the D_2O vapour from the storage bottles on the dosing line. The pressures measured on the dosing line during deposition are shown in Fig. 9.3. It should be noted that the baratron used to measure the pressure had an offset of approximately 18 mbar. The discontinuities in the data result from the refilling of the D_2O bottles. The D_2O depletion rates (calculated from the data presented in Fig. 9.3 by performing linear fits to this data) are given in Tables 9.1-9.4 in mbar hour^{-1}. There is a slight variation between different deposition cycles but depletion rates were usually between 1 mbar hour^{-1} and 3 mbar hour^{-1}. The only exceptions are the second

Table 9.2: Depletion rate of D_2O vapour for 52 K deposition.

Cycle	Depletion rate (mbar hour^{-1})
1	1.74
2	5.46
3	1.8

Table 9.3: Depletion rate of D_2O vapour for 17 K first deposition.

Cycle	Depletion rate (mbar hour^{-1})
1	1.49
2	2.71
3	1.81
4	1.59
5	1.61
6	2.39

deposition cycle for the 52 K deposition and the first deposition cycle for the second 17 K deposition. The second deposition cycle for the 52 K deposition only has two pressure points as the neutron beam was off for around 4 hours, halting the collection of all data (including pressure data that was collected electronically for each scan), although deposition of D_2O continued. Therefore the depletion rate is unlikely to be very accurate as it was only calculated from two points. The first deposition cycle for the second 17 K deposition initially had a very low depletion rate of D_2O as the flow was still being set. It should be noted that the total volume of D_2O stored on the dosing line was doubled for the 17 K depositions (8 litres instead of 4 litres) and so the in the first 17 K deposition, the D_2O vapour was actually depleted twice as fast as in the 50 K and 52 K depositions.

The final way to assess the D_2O flow rate is to look at the thickness of ice grown. The thickness can be estimated from Gudrun as it is the parameter that is adjusted to achieve the required differential cross section level (see Section 7.2.3 of Chapter 7). The thicknesses of the ices are shown in Fig. 9.4. The points indicated by crosses come from reducing the raw $\sim$15 minute scans in groups of four. The points indicated by circles come from reducing 3 hour long scans once deposition has stopped and should produce the most accurate thicknesses due to the longer timescales used to obtain the data. These values were used to calculate the growth rates in μm hour^{-1}

Table 9.4: Depletion rate of D_2O vapour for 17 K second deposition.

Cycle	Depletion rate (mbar hour^{-1})
1	0.35
2	1.09

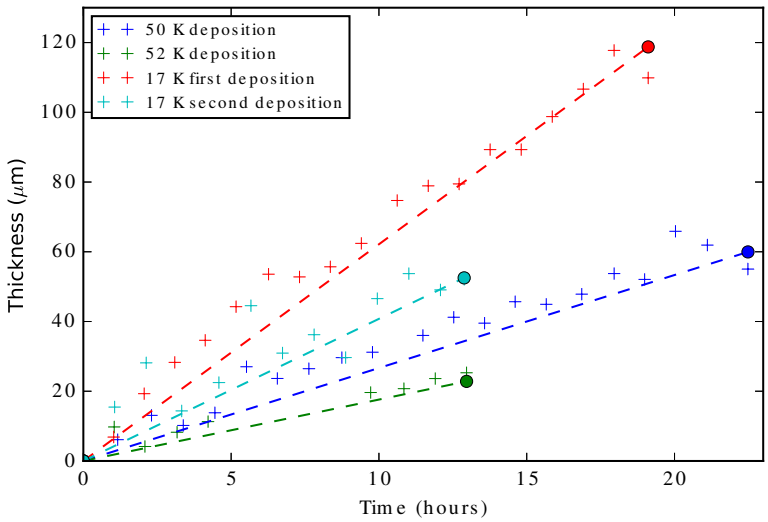

Figure 9.4: Growth rates of ices grown at different temperatures. The circles indicate the final thickness of the ice determined from the long scan (3 hours) and the dashed lines are drawn between this point and the origin. The growth rates were extracted from these lines. The crosses indicate the thicknesses determined from the ∼1 hour averaged scans.

and these are shown in Table 9.5. The 50 K and 52 K ices were grown at similar rates of 2.67 μm hour^{-1} and 1.76 μm hour^{-1} respectively (although the 50 K ice was grown a little faster) and the 17 K ices were grown a lot faster, at 6.22 μm hour^{-1} for the first deposition and 4.08 μm hour^{-1} for the second deposition.

The D_2O depletion rate and ice thickness can also be used to estimate how much of the D_2O vapour released into the chamber sticks on the vanadium plate. According to the ideal gas law, the number of moles of D_2O released from the gas line (n_g) is given by:

$$n_g = \frac{pV}{RT} \tag{9.1}$$

where p is the pressure, V is the volume, R is the universal gas constant and T is the temperature. The number of moles of D_2O on the vanadium plate (n_s) (which has a

Table 9.5: Growth rates for the four ices calculated from the thickness obtained from the 3 hour long scans.

Deposition	Growth rate (μm hour^{-1})
50 K	2.67
52 K	1.76
17 K (first)	6.22
17 K (second)	4.08

diameter of 5 cm) is given by:

$$n_s = \frac{\rho \pi r^2 t}{20} \tag{9.2}$$

where ρ is the density of the ice, r is the radius of the plate, t is the thickness of the ice and 20 is the molecular mass of D_2O in g mol^{-1}. The proportion of molecules which stick to the vanadium plate (p_s) is then given by:

$$p_s = \frac{n_s}{n_g} \tag{9.3}$$

For the 50 K deposition and the 52 K deposition, the proportions of molecules that stuck to the plate were 67% and 42% respectively. For the 17 K depositions, the proportions of molecules that stuck to the plate were 64% for the first deposition and 87% for the second deposition. The high proportion of molecules that stuck to the plate during the second 17 K deposition compared to the 50 K and 52 K depositions is likely to be due to the lower deposition temperature. The lower proportion of molecules that stuck to the plate for the first 17 K deposition compared to the second 17 K deposition is probably due to the higher flow rate in the first case.

9.2.2 Heating

Once deposition was stopped, a 3 hour long scan was taken of the ice with the temperature kept constant. The long scan time gives good data quality and allows parameters relating to porosity to be accurately determined before heating. The ice was then heated up at a rate of 0.5 K min^{-1} in 10 K steps. Scans were taken every 3 minutes while heating. Isothermal data was taken every 10 K. The waiting time was approximately 1 hour

for the 50 K and first 17 K depositions and 30 minutes for the 52 K and second 17 K depositions (the shorter time was due to timing restrictions). During isothermal steps, scans were taken every 15 minutes for temperatures of 110 K and below. From 120 K onwards, scans were taken every 6 minutes, as this was close to the temperature at which pore collapse started for the ice described in Chapter 8. Once the temperature reached 180 K, the sample plate was heated to 300 K to remove the ice and the sample plate was re-cooled to begin deposition again.

9.3 Results

9.3.1 Neutron scattering patterns

Figs. 9.5-9.8 show averaged neutron scattering patterns for the four ices grown at temperatures of 50 K, 52 K, 17 K and 17 K. The deposition graphs show the results of averaging four scans corresponding to around an hour of deposition. The heating scans show the results of averaging isothermal scans at the indicated temperatures. Individual deposition, heating and isothermal scans are shown in the supplementary material at the back of this thesis. Error bars have been omitted for clarity.

In the deposition scans, the data is quite noisy at first, becoming significantly less noisy as more ice is deposited. This is due to the increasing sample size, which leads to better quality of data. The first deposition scan in particular is very noisy for three out of four of the ices (50 K deposition, 52 K deposition and 17 K second deposition). Considering the growth rates detailed in Section 9.2 (2.67 μm hour^{-1} for the 50 K ice, 1.76 μm hour^{-1} for the 52 K ice, 6.22 μm hour^{-1} for the first 17 K ice and 4.08 μm hour^{-1} for the second 17 K ice), this is because the growth rate of the first deposition at 17 K is much higher than for the other three ices, so a larger sample was produced in one hour. The "hump" relating to the pores in the ice can clearly be seen in the 50 K and 52 K depositions, with the former exhibiting a much more pronounced peak between $\sim$8 and 19 hours. The "hump" can also be seen in both 17 K depositions,

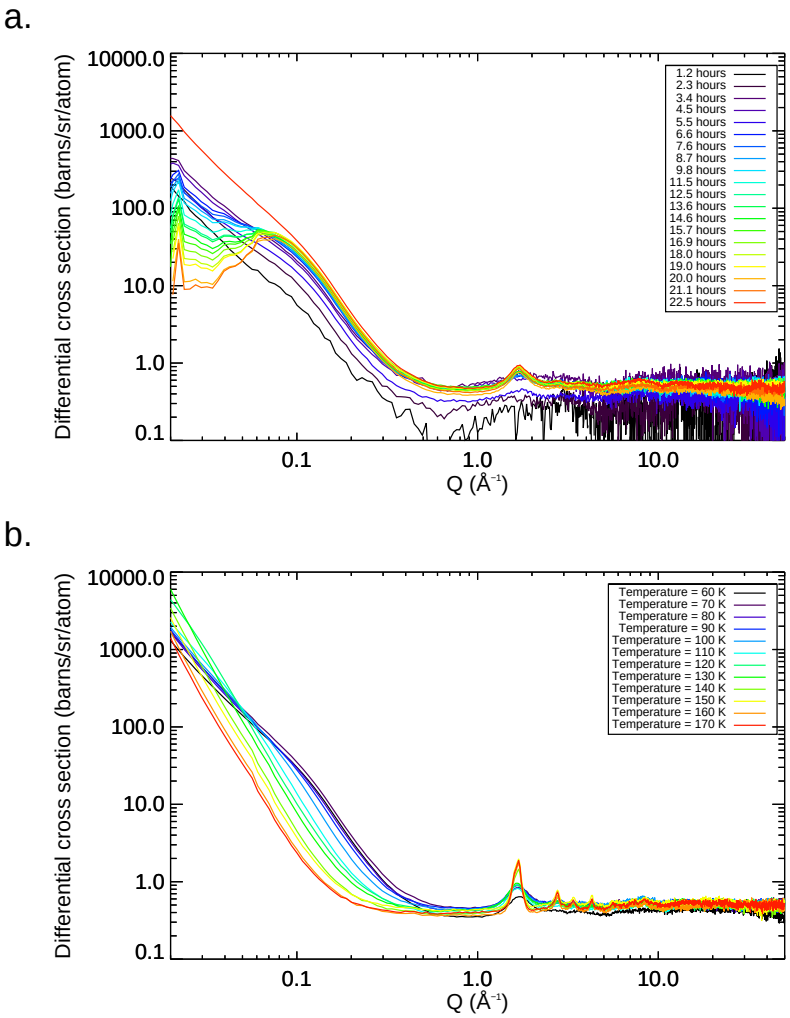

Figure 9.5: Neutron scattering patterns for ice deposited at 50 K. **a.** Neutron scattering patterns for deposition. **b.** Neutron scattering patterns for heating.

although it is much less pronounced. In all cases, the broad peak between 1 and 2 Å^{-1} (related to the average O-O distance in the ice) is visible. Therefore, this experimental apparatus is clearly capable of growing amorphous solid water.

In the heating scans, the peak flattens and disappears between 100 and 130 K, suggesting pore collapse. The broad peak between 1 and 2 Å^{-1} grows and narrows into a more pronounced peak around 140 K and the other 3 Bragg peaks appear around the same time, indicating crystallisation to cubic ice. While the 50 K, 52 K and second 17 K deposition show significant growth and narrowing of the first peak on crystallisation, and no sign of the additional three peaks prior to this, the first 17 K deposition shows a much less significant growth and narrowing of the first peak, and a close in-

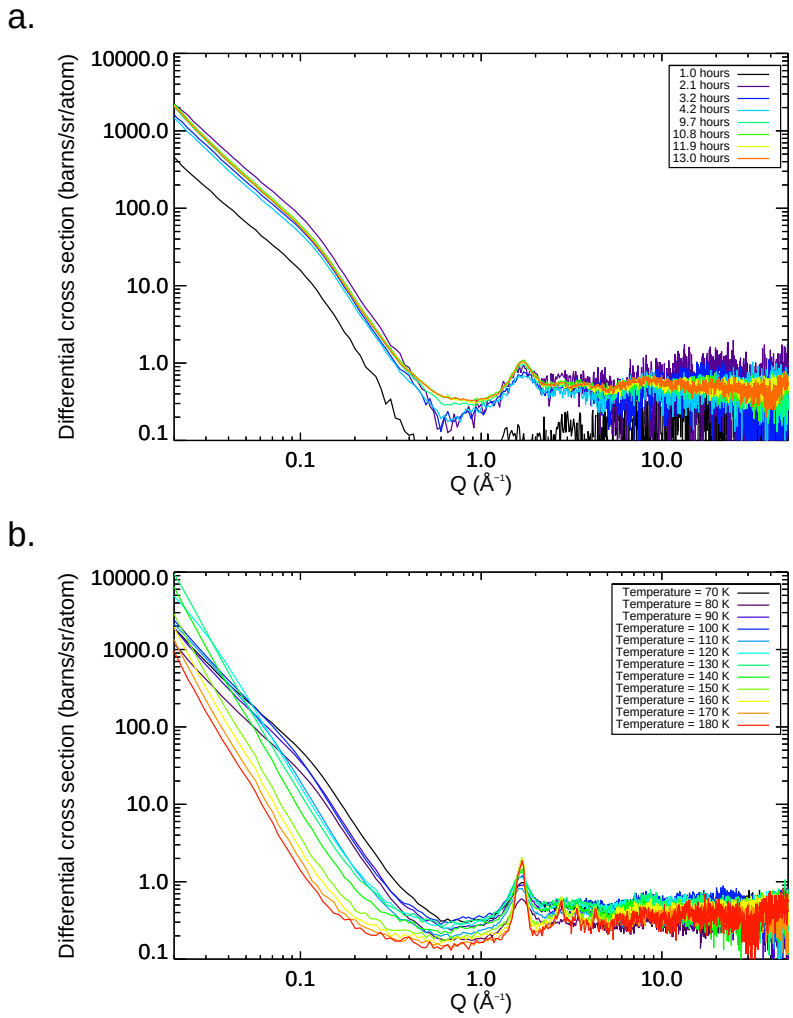

Figure 9.6: Neutron scattering patterns for ice deposited at 52 K. **a.** Neutron scattering patterns for deposition. **b.** Neutron scattering patterns for heating.

spection of Fig. 9.7**a.** shows small but visible Bragg peaks between 2 and 5 $Å^{-1}$ by the end of the deposition. This suggests that this ice has some crystalline character before heating. This was discovered when the ice temperature had reached 150 K and the experiment was immediately aborted, hence the lack of data beyond 150 K. It is possible that this was caused by the high growth rate of this ice, although this seems unlikely as the ice described in the previous chapter was grown at a faster rate and was clearly all amorphous. More likely, the fact that the holes for pumping out the cryo shields surrounding the vanadium plate were extremely small, hence leading to a high partial pressure of D_2O vapour surrounding the plate, is responsible for the crystalline character of this ice. Modifications to the experimental apparatus to prevent this occurring

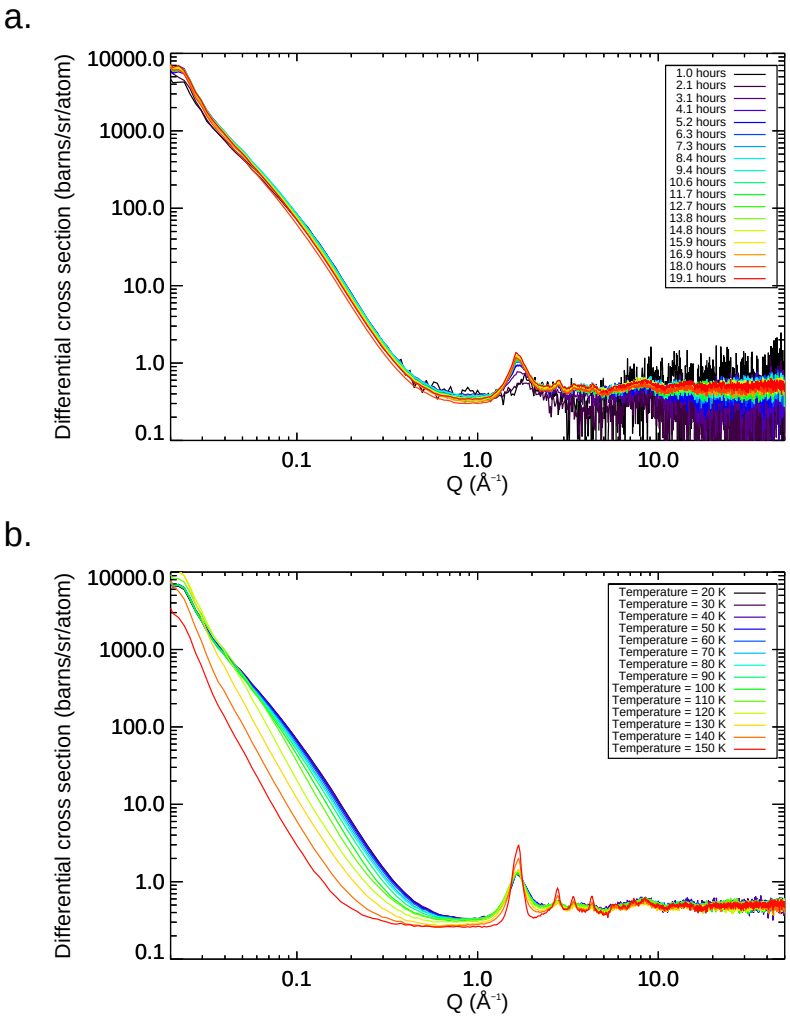

Figure 9.7: Neutron scattering patterns for first ice deposited at 17 K. **a.** Neutron scattering patterns for deposition. **b.** Neutron scattering patterns for heating.

are discussed in Chapter 10.

Considering the energy released in deposition of the first 17 K ice also sheds light on the reasons for its crystalline character. Using Equation 9.2 with a density of 0.59 g cm^2 and a growth rate of 6.22 μm hour^{-1} (0.0017 μm s^{-1}), the number of moles of water deposited per second is 0.030 mol s^{-1}. The heat of sublimation (ΔH_{sub}) of water is approximately 51 kJ mol^{-1}. Therefore, the energy released into the ice film is:

$$0.030 \times 51 = 1.5 \text{ kJ s}^{-1}$$

The activation energy for crystallisation of amorphous solid water is approximately 77 kJ mol^{-1} Dohnalek et al. (2000). As there are 0.030 mol of water deposited per

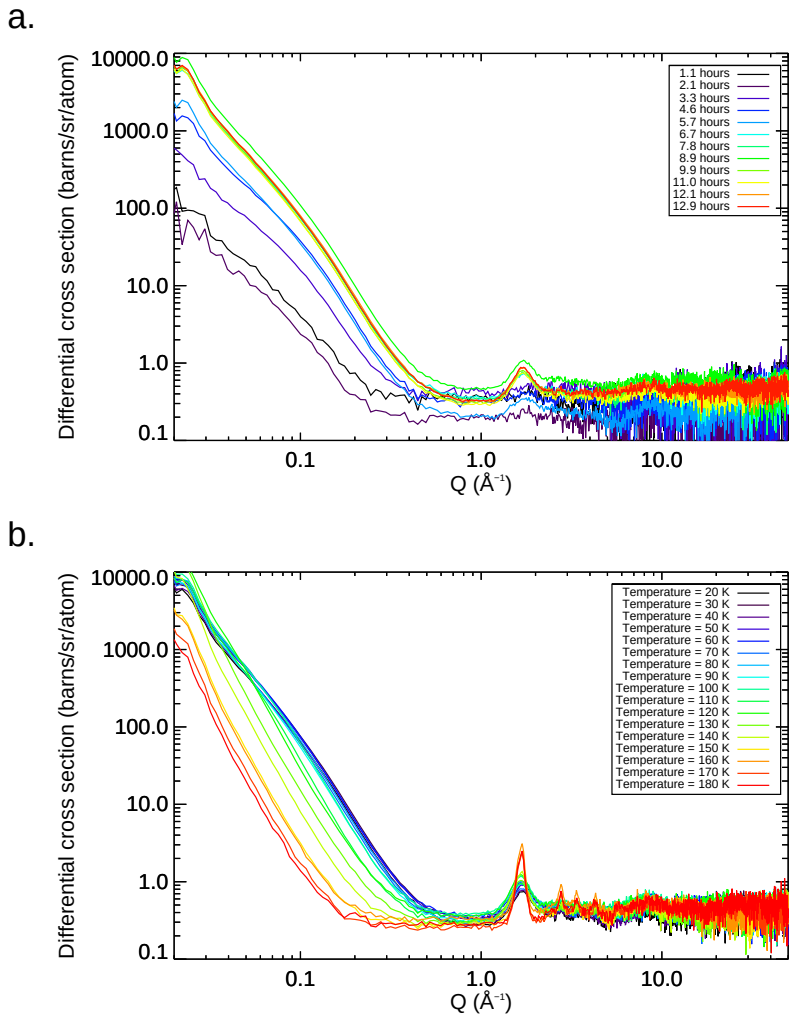

Figure 9.8: Neutron scattering patterns for second ice deposited at 17 K. **a.** Neutron scattering patterns for deposition. **b.** Neutron scattering patterns for heating.

second, the energy required to crystallise the ice is:

$$0.030 \times 77 = 2.3 \text{ kJ s}^{-1}$$

This is less than the energy released in depositing the ice, but if the energy cannot be removed from the film at a rate of at least 1.5 kJ s^{-1}, the energy will build up and eventually allow crystallisation to occur. The likely high partial pressure of D_2O vapour surrounding the plate would release even more energy into the system, making crystallisation increasingly likely.

Fig. 9.9 shows the 3 hour long scans for all four ices after deposition was stopped but before heating took place. The difference of the first 17 K deposition to the other ices is now clearly apparent. The peak between 1 and 2 $Å^{-1}$ is much taller and nar-

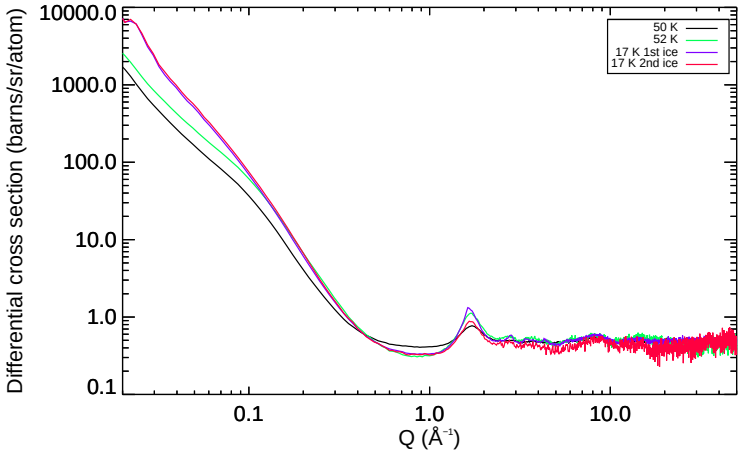

Figure 9.9: Neutron scattering patterns for 3 hour long scans of all four ices.

rower for the first 17 K deposition compared to the other ices. Comparing the ices in this way also shows the differences between the 50 K and 52 K depositions and the 17 K ones, with the latter having a much less pronounced "hump" around 0.1 $Å^{-1}$. This suggests that the 50 K and 52 K ices are more porous than the 17 K ones.

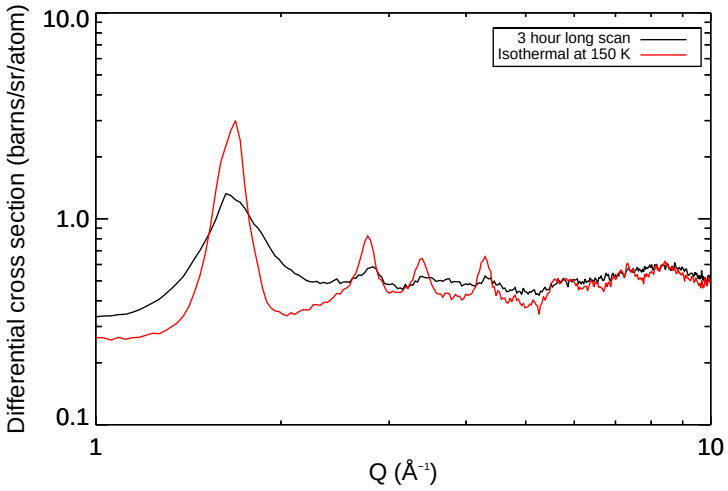

Figure 9.10: Comparison of the high Q region of the 3 hour long scan and the 150 K isothermal scan for the 17 K first deposition.

Fig. 9.10 shows the high Q region of the 3 hour long scan for the 17 K first deposition prior to heating, compared to the isothermal scan at 150 K when the ice had crystallised. The three Bragg peaks between 2 and 5 $Å^{-1}$, while small, can be seen

in the scan prior to heating. As this ice is not fully amorphous, it cannot be used to draw conclusions about the nature of porosity changes in pure amorphous solid water. However, it is useful as a comparison to the fully amorphous ices to see what effect the crystalline character had on the porosity. The two 17 K depositions are differentiated in the rest of the chapter by referring to the first deposition as 17 K (AC) (amorphous-crystalline) and the second deposition as 17 K (A) (amorphous).

9.3.2 Specific surface area

The specific surface area was extracted from the data as detailed in Section 7.3.1 of Chapter 7. Fig. 9.11 shows the results for deposition, both single (Fig. 9.11**a.**) and averaged (Fig. 9.11**b.**) scans. Fig. 9.12 shows the results for heating, both single heating (Fig. 9.12**a.**) and averaged isothermal (Fig. 9.12**b.**) scans. The 77 K deposition that is the subject of Chapter 8 is also shown in Fig. 9.12. Specific surface areas for the individual isothermal scans are shown in the supplementary material at the back of this thesis. The error bars on the single scans, both for deposition and heating but particularly for heating are very large. This is because the quality of the data is poorer in these shorter scans, making it much more difficult to determine the positions of the quasi-plateaus (which are shown in the supplementary material at the back of this thesis). Although the error bars are large for the single deposition scans, the data follows the same trend as the averaged deposition scans. The error bars are too large on the single heating scans to draw any such conclusions. The following discussion therefore focuses on the averaged deposition and isothermal scans (Fig. 9.11**b.** and Fig. 9.12**b.**).

In Fig. 9.11**b.**, the 50 K, 52 K and 17 K (A) depositions all start with a specific surface area of less than 100 m^2 cm^{-3} after a deposition of 1 hour, whereas the specific surface area of the 17 K (AC) ice is between 300 and 400 m^2 cm^{-3} after depositing for 1 hour. This could be due to the higher growth rate for the 17 K (AC) ice. The specific surface area of the 17 K (AC) ice decreases slightly to just under 300 m^2 cm^{-3}

over the course of deposition, which is possibly due to some crystallisation occuring. In contrast, the specific surface area of the other three ices increases with deposition time. The 52 K ice and the 17 K (A) ice have a similar specific surface area at the end of the deposition (just over 300 m^2 cm^{-3}), whereas the 50 K ice has a much smaller specific surface area (just over 200 m^2 cm^{-3}).

When the ices are heated (Fig. 9.12**b.**), the specific surface area decreases. For the 50 K and 52 K ices, the specific surface area begins to decrease at 70 K. The specific surface area of the 17 K (A) ice begins to decrease at 100 K. In contrast, the decrease in specific surface area for the 17 K (AC) ice starts at a much lower temperature (40 K), and this ice exhibits a much slower decrease in specific surface area compared to the others. This difference could be related to the crystalline component of this ice, which may inhibit the restructuring required for a decrease in specific surface area. Comparing the four ices described in this chapter to the 77 K deposition described in the previous chapter, the current ices were grown with much higher specific surface areas. However, as the 52 K and the 17 K (A) ices have similar specific surfaces areas before heating, despite the different deposition temperatures, it is not clear whether the differences between the 77 K ices and the current ices are due to the different deposition temperatures or the different experimental set ups. The 77 K ice also exhibits an increase in specific surface area between 92 K and 120 K which was thought to be due to expansion of the ice (see Section 8.3.5 of Chapter 8). The 50 K ice has a very slight increase in specific surface area between 60 K and 70 K but due to the size of this increase compared to the uncertainties, it is not possible to determine whether or not the increase is genuine. None of the other ices show this increase. By around 150 K, the specific surface areas of all the ices have decreased to similar levels.

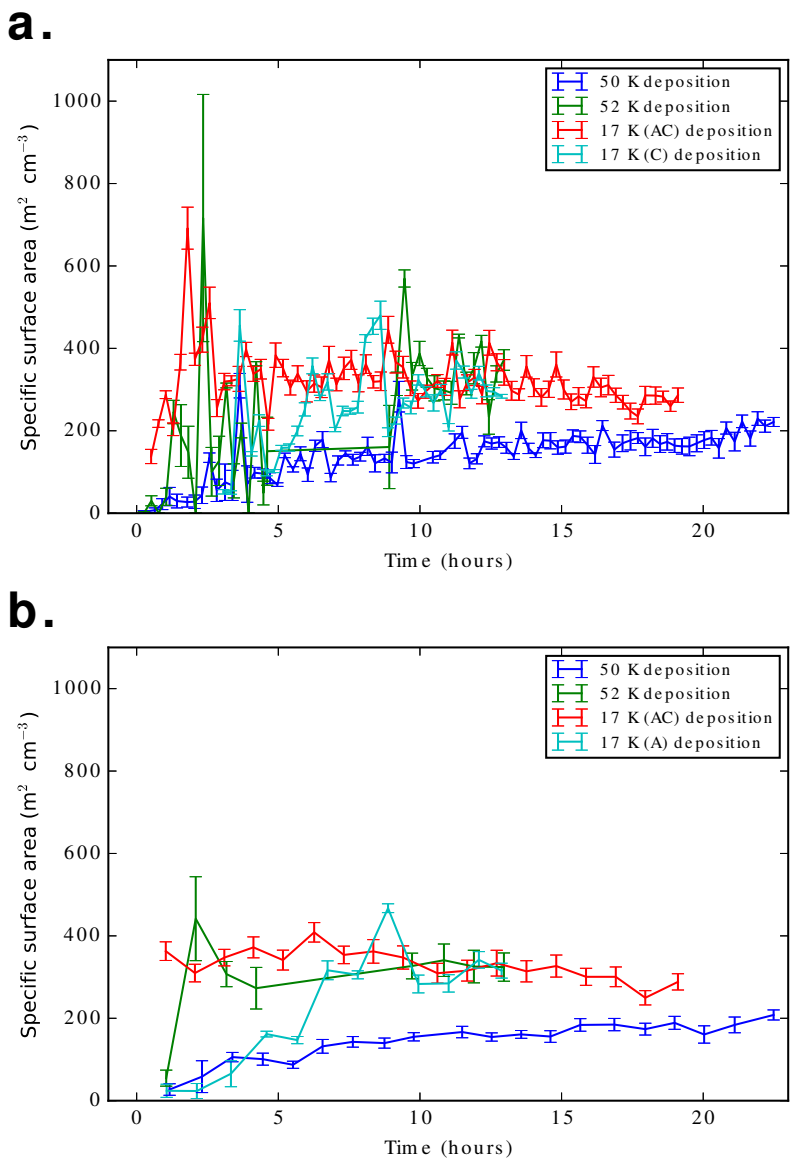

Figure 9.11: Specific surface area during deposition for all four ices. The different ices are indicated by different colours. Results from both single (**a.**) and averaged (**b.**) scans are shown.

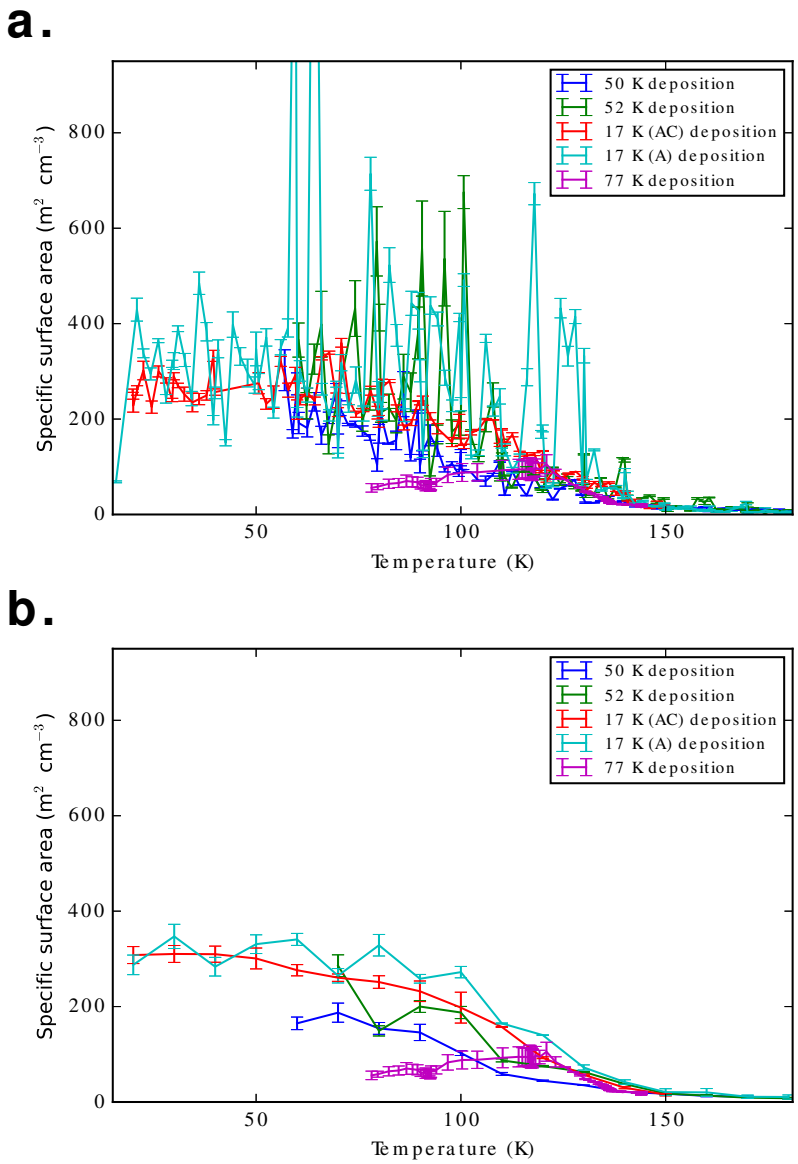

Figure 9.12: Specific surface area during heating for all four ices. The different ices are indicated by different colours. Results from both single heating (**a.**) and averaged isothermal (**b.**) scans are shown.

9.3.3 Periodic spacings

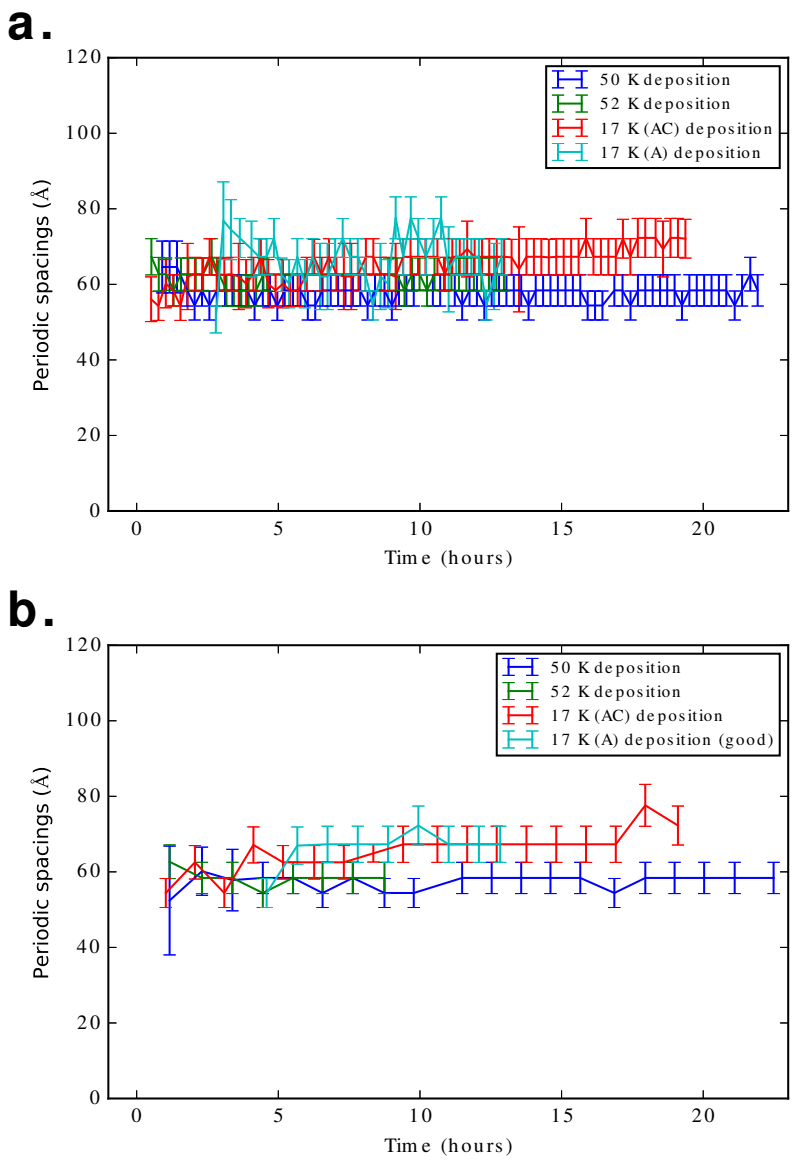

Figure 9.13: Periodic spacings during deposition for all four ices. The different ices are indicated by different colours. Results from both single (**a.**) and averaged (**b.**) scans are shown.

The periodic spacings of the pores were extracted from the data as described in Section 7.3.2 of Chapter 7. Fig. 9.13 shows the results for deposition, both single (Fig. 9.13**a.**) and averaged (Fig. 9.13**b.**) scans. Fig. 9.14 shows the results for heating, both single heating (Fig. 9.14**a.**) and averaged isothermal (Fig. 9.14**b.**) scans. The 77 K deposition that is the subject of Chapter 8 is also shown in Fig. 9.14. Periodic spacings for the individual isothermal scans (and the pseudopeaks used to extract peri-

odic spacings for all scans) are shown in the supplementary material at the back of this thesis. The uncertainties on the periodic spacings are slightly larger for the single deposition and heating scans compared to the averaged deposition and isothermal scans, but not so large as to render the data incomprehensible.

The periodic spacings are mostly constant throughout deposition (Fig. 9.13) and are similar in all four ices, with values around 60 Å. This is a little lower than the 77 K ice in Chapter 8, which had periodic spacings of around 70 Å. Again, it is unclear whether the lower deposition temperatures in the current study or the different experimental set ups are responsible for this distance. Both the 17 K ices show a slight increase in periodic spacings as the deposition time increases and by the end of deposition, the periodic spacings are slightly larger than for the 50 K and the 52 K ices. As the pores in the 17 K ices start off at similar distances apart to the 50 K and 52 K ices and get slightly further apart; this suggests that the ices start off with similar numbers of pores, but there are fewer pores in the 17 K ices by the end of deposition than in the 50 K and 52 K ices.

When the ices are heated (Fig. 9.14), the periodic spacings increase. This increase starts at 90 K for the 50 K ice, 100 K for the 52 K ice, 60 K for the 17 K (AC) ice and 50 K for the 17 K (A) ice. The increase is much more dramatic for the 50 K and 52 K ices which undergo very large increases starting at 110 K and 100 K respectively. The 17 K ices show only moderate increases in periodic spacings. The increase in periodic spacings is attributed to pore clustering prior to collapse which has been seen in earlier work (Wu et al., 2010; Mitterdorfer et al., 2014; Cazaux et al., 2015) and is in contrast to the results of the previous chapter where the periodic spacings remained constant until the pores collapse. As the periodic spacings increase much more for the 50 K and 52 K ices compared to the 17 K ices, pore clustering happens to a greater extent in the former ices. In the case of the 50 K and 52 K ices, the periodic spacings rise to almost 300 Å. This is close to the limit of 314 Å that can be observed by NIMROD (indicated by the dotted lines on Figs 9.14**a.** and **b.**) and so it is possible that the pores cluster to an even greater extent at higher temperatures but this cannot be observed by

NIMROD.

Fig. 9.15 shows the pseudopeaks used to extract the periodic spacings (as described in Chapter 7) for the averaged isothermal scans for all four ices. For the 50 K and 52 K ices, the pseudopeak shifts to lower Q values with increasing temperature and appears to shift to lower Q values that cannot be observed by NIMROD, suggesting that the pores cluster to an even greater extent in these ices. For the 17 K ices, the pseudopeak does not shift as much but disappears around 100-110 K. This suggests that the pores do not cluster further but collapse at this point instead.

Both the 50 K and the 52 K ices show a discontinuity in periodic spacings obtained from the single heating scans at 110 K and 120 K respectively. Fig. 9.16 shows the periodic spacings for the isothermal scans at these temperatures. In contrast to the other isothermal temperatures (shown in the supplementary material at the back of this thesis), the periodic spacings increase at these temperatures, leading to the discontinuity seen in Fig. 9.14**a.**.

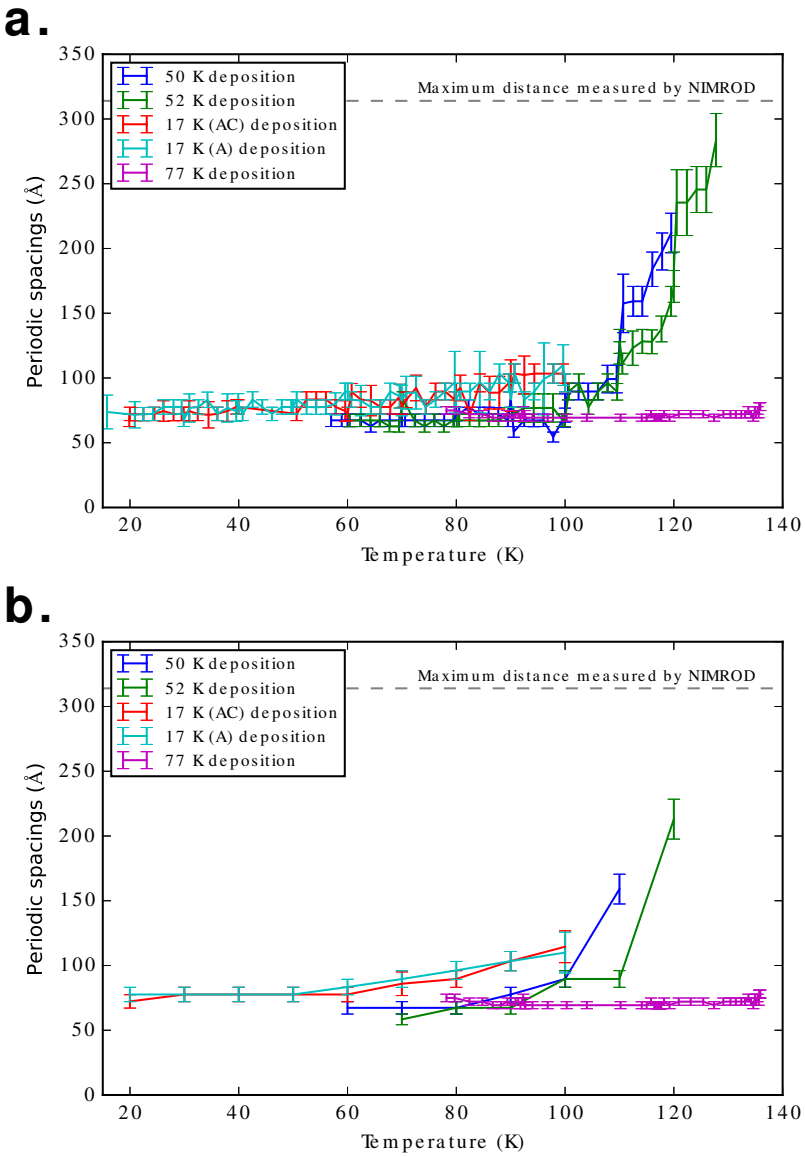

Figure 9.14: Periodic spacings during heating for all four ices. The different ices are indicated by different colours. Results from both single heating (**a.**) and averaged isothermal (**b.**) scans are shown.

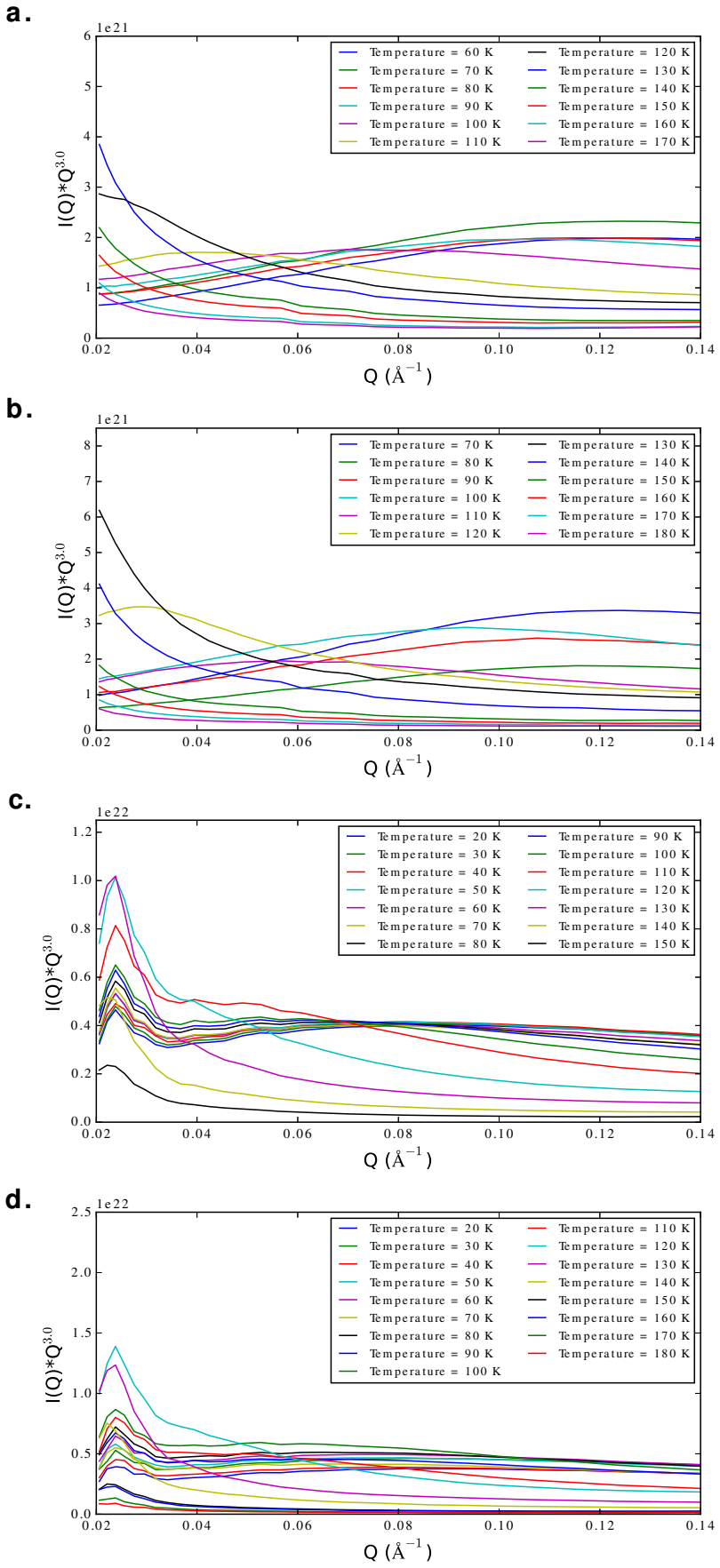

Figure 9.15: Pseudopeaks in $I(Q) * Q^3$ vs. Q for **a.** 50 K deposition, isothermal scans. **b.** 52 K deposition, isothermal scans. **c.** 17 K deposition (AC), isothermal scans. **d.** 17 K deposition (A), isothermal scans.

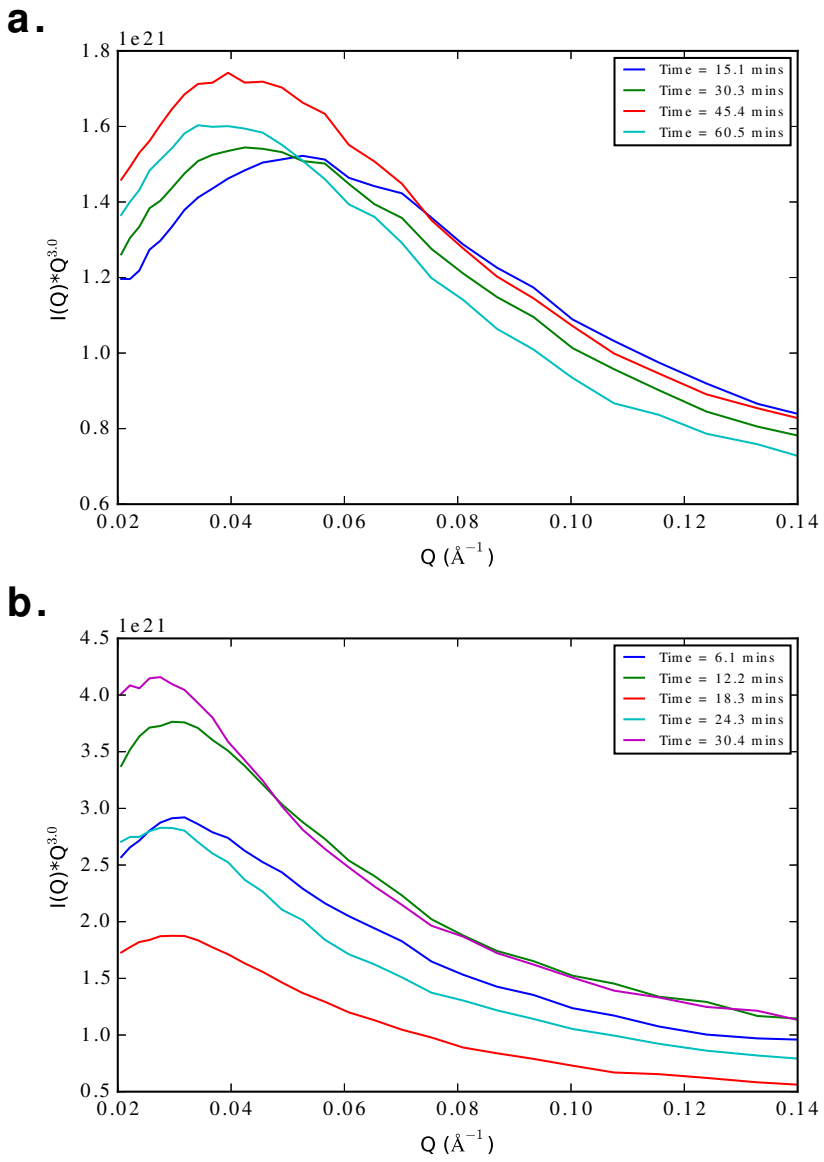

Figure 9.16: Pseudopeaks in $I(Q) * Q^3$ vs. Q for **a.** 50 K deposition, isothermal at 110 K. **b.** 52 K deposition, isothermal at 120 K.

9.3.4 Guinier-Porod fits

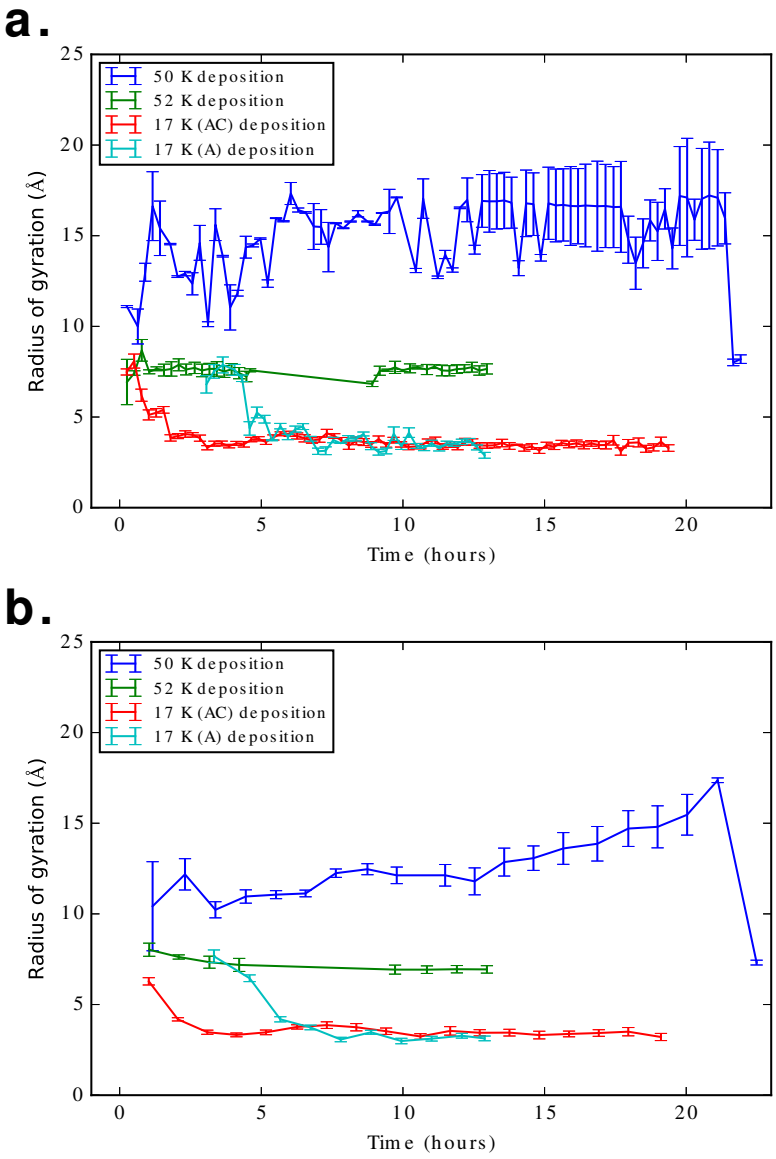

Figure 9.17: Radius of gyration (R_g) during deposition for all four ices. The different ices are indicated by different colours. Results from both single (**a.**) and averaged (**b.**) scans are shown.

Guinier-Porod fits were performed on the data as described in Section 7.3.3 of Chapter 7, extracting the radius of gyration indicating the size of the pores (R_g), the s parameter describing pore shape and the d parameter describing pore surface roughness. Fig. 9.17 shows the radius of gyration for deposition, both single (Fig. 9.17**a.**) and averaged (Fig. 9.17**b.**) scans. Fig. 9.18 shows the radius of gyration for heating, both single heating (Fig. 9.18**a.**) and averaged isothermal (Fig. 9.18**b.**) scans. The

77 K deposition that is the subject of Chapter 8 is also shown in Fig. 9.18. Radii of gyration for the individual isothermal scans are shown in the supplementary material at the back of this thesis. The error bars are larger for the single scans than for the averaged scans (in the case of the 50 K deposition they are a lot larger) but the trends followed are the same in both cases.

The radius of gyration undergoes some changes as the ice is deposited (Fig. 9.17). For the 50 K deposition, R_g starts off around 10 Å and begins to increase after around 6 hours of deposition. It increases to around 17 Å but drops sharply to around 7 Å after 21 hours. For the 52 K deposition, R_g is initially around 8 Å and slightly decreases to around 7 Å by the end of deposition. For the 17 K (AC) deposition, R_g starts around 6 Å but starts decreasing almost immediately to around 4 Å by the end of deposition. The 17 K (A) deposition has an R_g value of around 7 Å after 3 hours of deposition, but this quickly falls to around 4 Å as well. By the end of deposition, the 50 K and 52 K ices have pores of similar sizes that are larger than the pores in the 17 K ices.

R_g also changes when the ices are heated (Fig. 9.18). When the 50 K ice is heated, R_g initially decreases slightly from 6.4 Å to 5.7 Å when the temperature is increased from 60 K to 80 K. This suggests that a small pore collapse is taking place between these temperatures. A very subtle decrease from 7.1 Å to 6.8 Å is seen between 70 K and 80 K for the 52 K ice in the averaged data (Fig. 9.18**b.**) but this is not apparent in the single data (Fig. 9.18**a.**). R_g then increases very sharply to around 10 Å at 110 K for the 50 K ice and to around 20 Å at 120 K for the 52 K ice. This fits with the understanding of pore clustering taking place between these temperatures. The 52 K ice also shows a sharp increase in R_g at 120 K, coinciding with the sharp increase in periodic spacing at the same temperature. At higher temperatures, the "hump" has shifted to low Q values beyond the range of NIMROD and so a Guinier-Porod fit cannot be performed at these temperatures. The 17 K (A) ice also shows a very slight decrease in R_g when the temperature is increased from 20 K to 30 K and a slight increase after 50 K, indicating slight pore collapse at lower temperatures and slight pore clustering at higher temperatures. These differences are only apparent in the averaged scans. The

17 K (AC) ice has a very slight increase in R_g with temperature after 60 K (which could indicate very slight pore clustering) but no real decrease in R_g prior to this.

Fig. 9.19 shows the s parameter for deposition, both single (Fig. 9.19**a.**) and averaged (Fig. 9.19**b.**) scans. Fig. 9.20 shows the s parameter for heating, both single heating (Fig. 9.20**a.**) and averaged isothermal (Fig. 9.20**b.**) scans. The 77 K deposition that is the subject of Chapter 8 is also shown in Fig. 9.20. s parameters for the individual isothermal scans are shown in the supplementary material at the back of this thesis. The error bars are larger for the single scans than for the averaged scans (in the case of the 50 K deposition they are a lot larger) but the trends followed are the same in both cases.

When the ice is deposited (Fig. 9.19), the s parameter starts around 1 for the 50 K ice. It then decreases to 0 as the deposition time increases. This suggests a transition from cylinders to spheres. After 21 hours, the s parameter jumps to around 1.6, suggesting a sudden transition to shorter cylinders. The 52 K ice appears to grow with these shorter cylinders from the start as the s parameter starts around 1.5 and increases to around 1.6 over the course of the deposition. The s parameter for the 17 K (A) ice starts around a similar value and increases almost immediately to around 2.5. This suggests a collapse from cylinders to platelets occurring between 3 and 5 hours of deposition. The s parameter starts around 2 for the 17 K (AC) ice, which indicates platelets. It then increases to 2.5, suggesting a further collapse of these platelets as the ice is deposited.

When the ice is heated (Fig. 9.20), the s parameter increases in all cases, indicating further collapse when the ice is heated. A decrease in the s parameter on heating (as seen for the 77 K deposition between 92 K and 117 K) is not seen for any of the current ices. The 50 K and 52 K ices show an increase of s to 2.4 and 2.2 respectively before the "hump" shifts to low Q values that cannot be observed by NIMROD. The 17 K ices show an increase to just over 2.5 before the "hump" becomes too unclear to fit to. The 77 K ice shows s increasing to almost 3 before the "hump" disappears. It is possible that this final increase to a value of almost 3 happens between 100 K and 110 K (for

the 17 K (AC) ice) or between 90 K and 100 K (for the 17 K (A) ice) but cannot be observed as it is not possible to fit the Guinier-Porod function to poor quality data (such as the 3 minute heating scans) where the "hump" is very small.

Fig. 9.21 shows the d parameter for deposition, both single (Fig. 9.21**a.**) and averaged (Fig. 9.21**b.**) scans.) Fig. 9.22 shows the d parameter for heating, both single heating (Fig. 9.22**a.**) and averaged isothermal (Fig. 9.22**b.**) scans. The 77 K deposition that is the subject of Chapter 8 is also shown in Fig. 9.22. d parameters for the individual isothermal scans are shown in the supplementary material at the back of this thesis. The error bars for the single scans are very large (particularly for the deposition) and so the remainder of this discussion will focus on the averaged deposition and isothermal scans.

During deposition (Fig. 9.21), the d parameter differs for all the ices. The 50 K ice and the 17 K (A) ice show an increase in d over the course of the deposition, indicating that the pore surfaces become smoother. In contrast, the 52 K ice and the 17 K (AC) ice show a decrease in d, indicating a roughening of the pore surfaces over the course of deposition. By the end of deposition, the 17 K ices have pores with smoother surfaces than the other two ices. The 50 K deposition has the roughest pores of all. The reasons for these differences are unclear, but they highlight the complex nature of ASW.

When heating the ice (Fig. 9.22), the d parameter increases in all cases, indicating a smoothing of the pore surfaces. This increase is also seen for the 77 K ice. The increase is more pronounced in the 50 K and 52 K ices than in the 17 K ices. The 17 K (AC) and the 17 K (A) ices have the smoothest pores by 100 K (both with a d value of 3.87), and by 120K, the pores of the 52 K ice are nearly as smooth (with a value of 3.85). The pores of the 50 K ice are slightly less smooth by the time the "humps" disappear, with a final d value of 3.74.

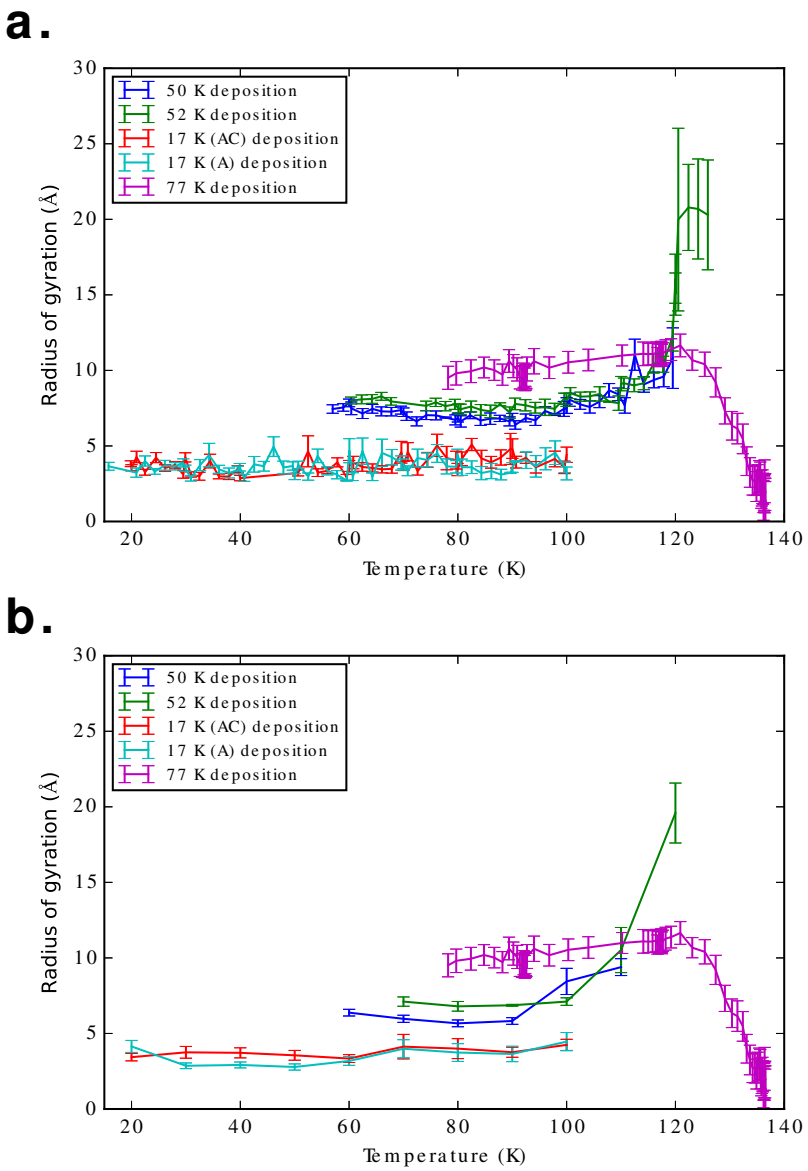

Figure 9.18: Radius of gyration (R_g) during heating for all four ices. The different ices are indicated by different colours. Results from both single heating (**a.**) and averaged isothermal (**b.**) scans are shown.

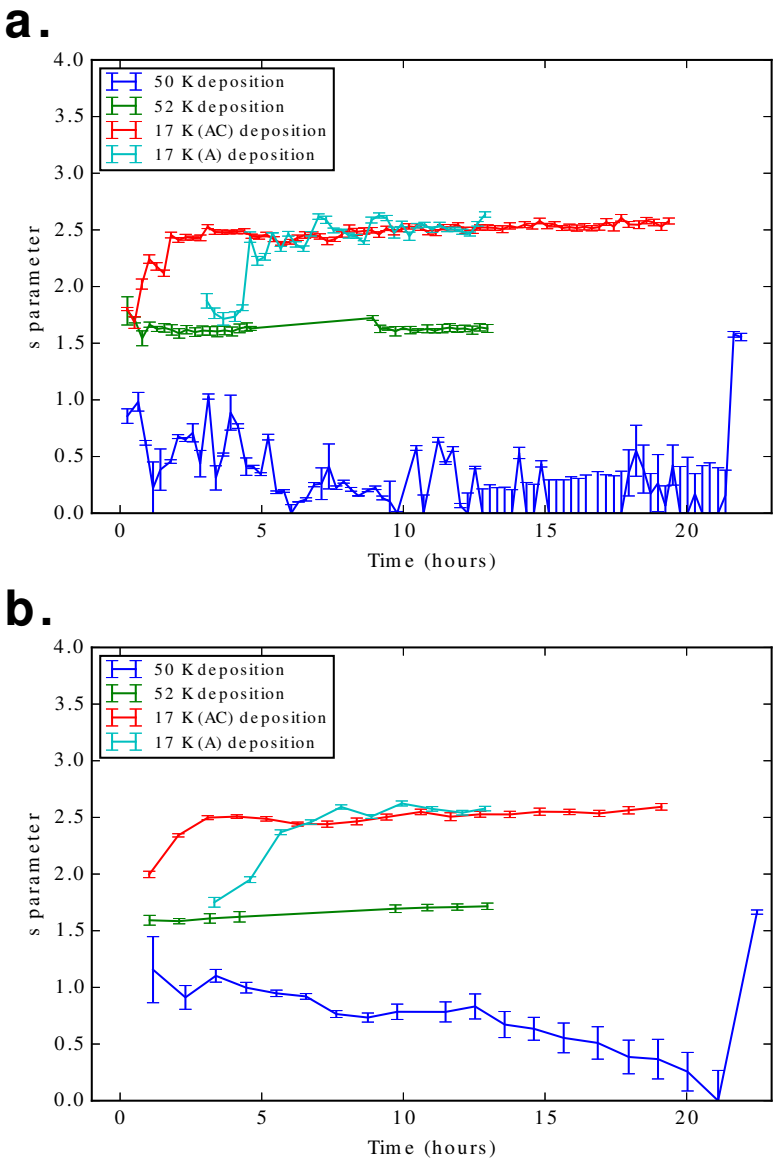

Figure 9.19: *s* parameter during deposition for all four ices. The different ices are indicated by different colours. Results from both single (**a.**) and averaged (**b.**) scans are shown.

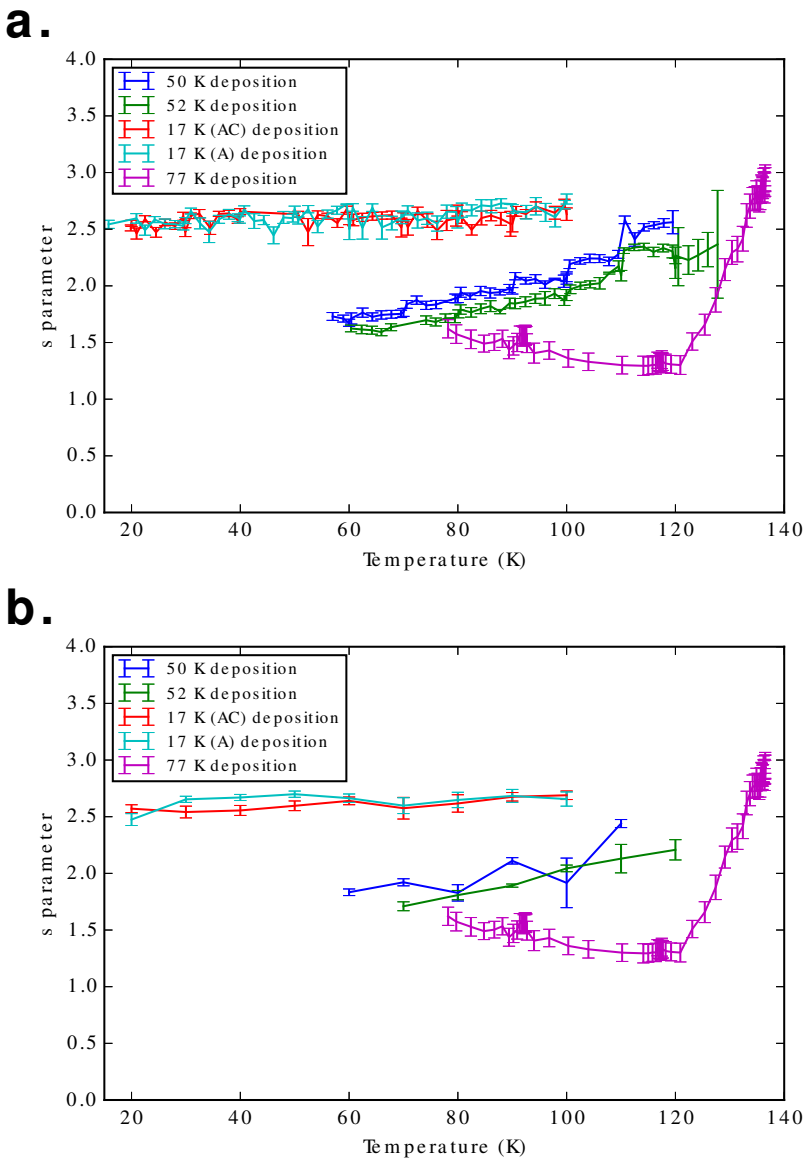

Figure 9.20: *s* parameter during heating for all four ices. The different ices are indicated by different colours. Results from both single heating (**a.**) and averaged isothermal (**b.**) scans are shown.

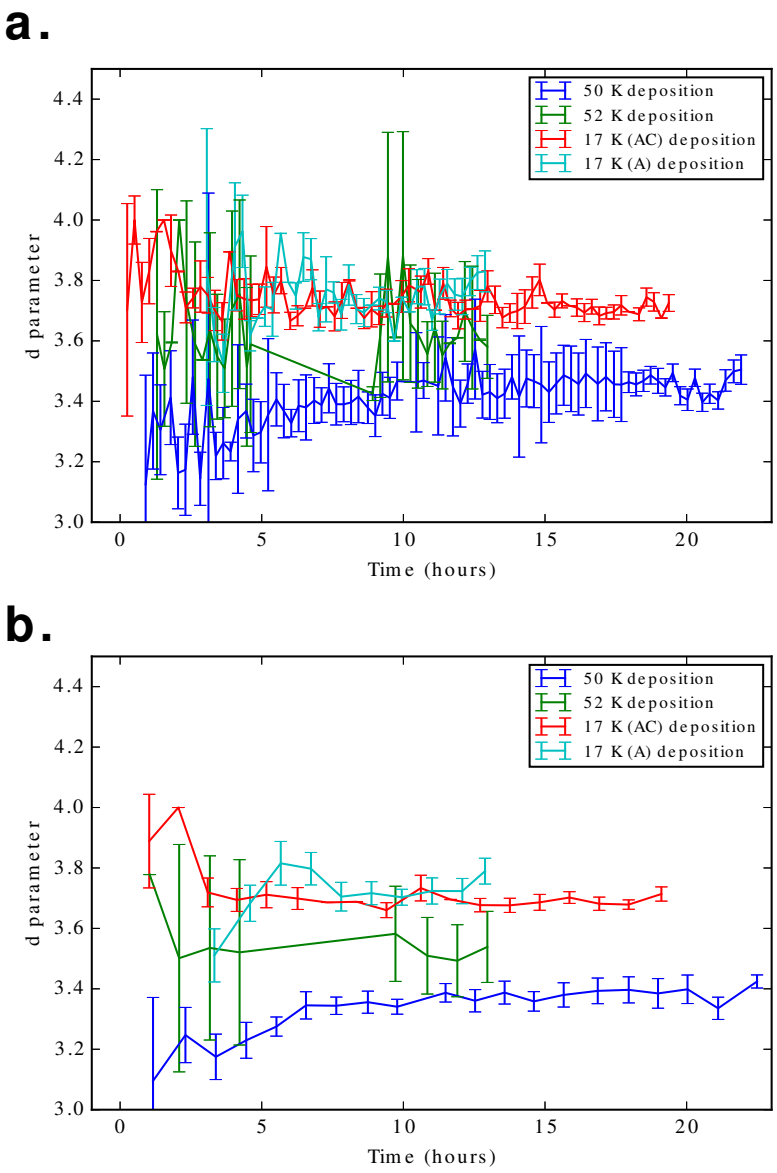

Figure 9.21: *d* parameter during deposition for all four ices. The different ices are indicated by different colours. Results from both single (**a.**) and averaged (**b.**) scans are shown.

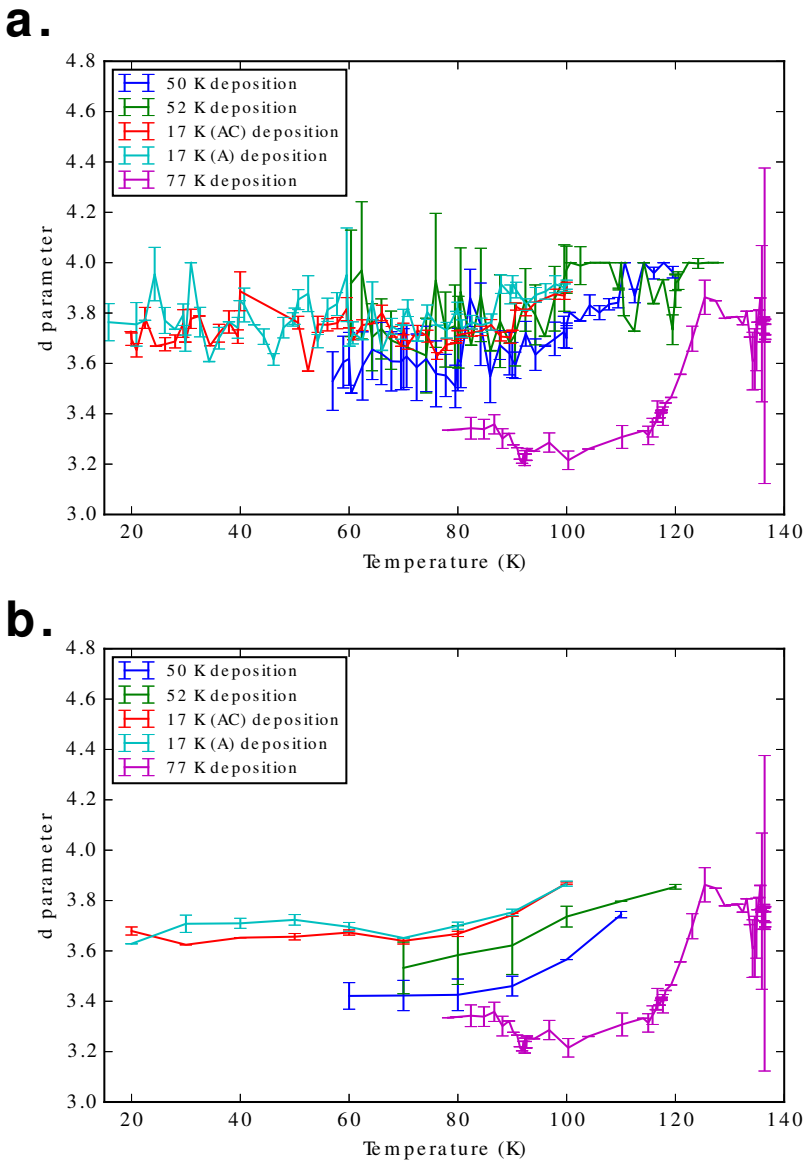

Figure 9.22: *d* parameter during heating for all four ices. The different ices are indicated by different colours. Results from both single heating (**a.**) and averaged isothermal (**b.**) scans are shown.

9.4 Discussion

Figs. 9.25-9.33 show all the parameters pertaining to ice porosity (specific surface area, periodic spacing, radius of gyration, s parameter and d parameter) as a function of deposition time for the ice depositions (Figs. 9.25-9.28) and as a function of temperature for ice heating (Figs. 9.30-9.33). Values extracted from averaged scans are shown for specific surface area and d parameter throughout as the uncertainties on the values obtained from the single scans were very large. Averaged scans were also used for the values of R_g and s for the 50 K deposition for the same reason. Elsewhere, the parameters shown are those extracted from single files.

9.4.1 Pore changes during deposition

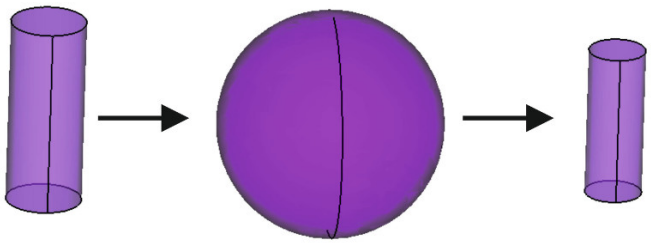

Figure 9.23: Pore expansion during deposition at 50 K. The pores start off as cylinders and transform to spheres, before collapsing back to cylinders smaller than the originals.

During the 50 K deposition, specific surface area increases from the start. Periodic spacing remains constant within uncertainties at around 60 Å, showing that the pores do not cluster as they grow. R_g and s begin to change around 3.5 hours with R_g increasing from 10 Å to 17 Å. s decreases from 1.1 to 0. This suggests that the pores are originally cylinders but expand to spheres as the ice grows. The growth of R_g and decrease of s stop abruptly after 21 hours of deposition, with R_g falling to around 7 Å and s rising to around 1.6. This suggests a rapid collapse back to cylinders which

are smaller than the original cylinders. This process is illustrated in Fig. 9.23. The specific surface area does not decrease when this collapse takes place, but continues to increase. This suggests that its increase during deposition is unrelated to the pore expansion and may instead be due to an increase in the specific surface area of the surface of the ice as it grows. The lower specific surface area of this ice compared to the 52 K and 17 K (A) ices remains a mystery but could be related to the growth of larger pores. In any case, it shows that ASW is a very complex material, with properties that depend on many factors, not all of which are currently known. d increases between 1 and 5.5 hours of deposition, from a value of 3.1 to 3.35, indicating a pore smoothing within the first few hours of growth. It then remains constant within uncertainties for the remainder of deposition.

This is the first time spherical pores have been seen (although they have often been assumed) in amorphous solid water and before collapse at 21 hours, this ice is significantly more porous than the ice grown at 77 K that is described in Chapter 8. As the temperature increased during deposition, it is not possible to tell whether the changes occurring happen as a function of time, temperature or both. However, the temperature at the start of pore expansion was 51.2 K and the temperature just before pore collapse was 56.6 K. This is within the ∼30 K-∼70 K range found by Jenniskens & Blake (1994), Horimoto et al. (2002) and Collings et al. (2003b) for the phase change from p-ASW to c-ASW. Therefore, this expansion and subsequent collapse may be taken as tentative evidence of this phase change. Using the growth rate in Table 9.5, the thickness of the ice at the start of this expansion was 9.3 μm. At the end of expansion, the thickness was 56.1 μm.

The sudden reduction in pore size could also be explained if the ice forms in "tree"-like structures as depicted in Fig. 9.24. As the ice grows thicker, the "trees" will grow taller and form larger pores (Fig. 9.24**a.** and **b.**). Eventually, the ice structures become too large and collapse under gravity (Fig. 9.24**c.**). This would lead to a reduction in pore size.

During the 52 K deposition, all parameters are fairly constant throughout deposi-

tion. Specific surface area is higher than for the 50 K deposition (around 300 m^2 cm^{-3} compared to 100-200 m^2 cm^{-3}). Periodic spacing is very similar to the 50 K deposition within uncertainties. R_g is around 7.5 Å and s is around 1.6, values which are very similar to those of the 50 K deposition after pore collapse. The uncertainties on d are rather large, but d is constant within uncertainties throughout deposition and the same within uncertainties to the values of d for the 50 K deposition. The lack of data points between 4.5 and 9.5 hours is due to the neutron beam going off between those times. The temperature at the start of deposition was 52.8 K and the temperature at the end of deposition was 60.6 K. If the pore expansion seen in the 50 K deposition was a temperature effect alone, it would be expected to occur here, so the fact that it does not suggests that the effect is not solely caused by temperature. It is possible that it requires a minimum thickness of ice to support the network of larger pores. The growth rate of the 52 K deposition was slower than the 50 K deposition (see Table 9.5) so a thickness of 9.3 μm was not reached until 5.3 hours, by which time the temperature was over 57 K. This is higher than the temperature at which the pore collapse occurred during the 50 K deposition and so this is possibly the reason the pore expansion did not occur during the 52 K deposition. However, it should be noted that this theory is extremely speculative and further work is needed to determine whether this phenomenon is reproducible.

During the first two hours of the first (AC) deposition at 17 K, R_g and s both change, decreasing from 8 Å to 4 Å and increasing from 1.6 to 2.5 respectively. This indicates a collapse from cylinders to platelets. After this, R_g and s remain constant. The periodic spacing increases slightly in this time which, taken with the changes in R_g and s suggests that a small number of pores have collapsed entirely, leaving fewer pores which are therefore spaced slightly further apart. The specific surface area is greater than for the 50 K and 52 K depositions at between 300 m^2 cm^{-3} and 400 m^2 cm^{-3} although the pores are significantly smaller after collapse. Therefore, the specific surface area cannot be simply related to the pores but must also be related to the area at the surface of the ice. d is greater than for the 50 K and 52 K ices at around 3.7, suggesting

that the pore surfaces are smoother here.

The second 17 K deposition (A) shows similar trends to the first 17 K deposition (AC). R_g and s undergo similar increases and decreases, this time around 4.5 hours. In contrast to the first 17 K deposition (AC), the periodic spacings decrease slightly at first (between 3 and 4 hours). After 4.5 hours, R_g, s and periodic spacing undergo slight fluctuations but remain broadly constant until the end of deposition. Specific surface area also remains fairly constant throughout deposition at between 300 m^2 cm^{-3} and 400 m^2 cm^{-3}. d increases from 3.0 to 3.8 between 2 and 5.5 hours, showing pore smoothing as the pores collapse. It then decreases slightly to 3.7 between 5.5 and 8 hours, showing a slight pore surface roughening. It remains at 3.7 for the remainder of deposition.

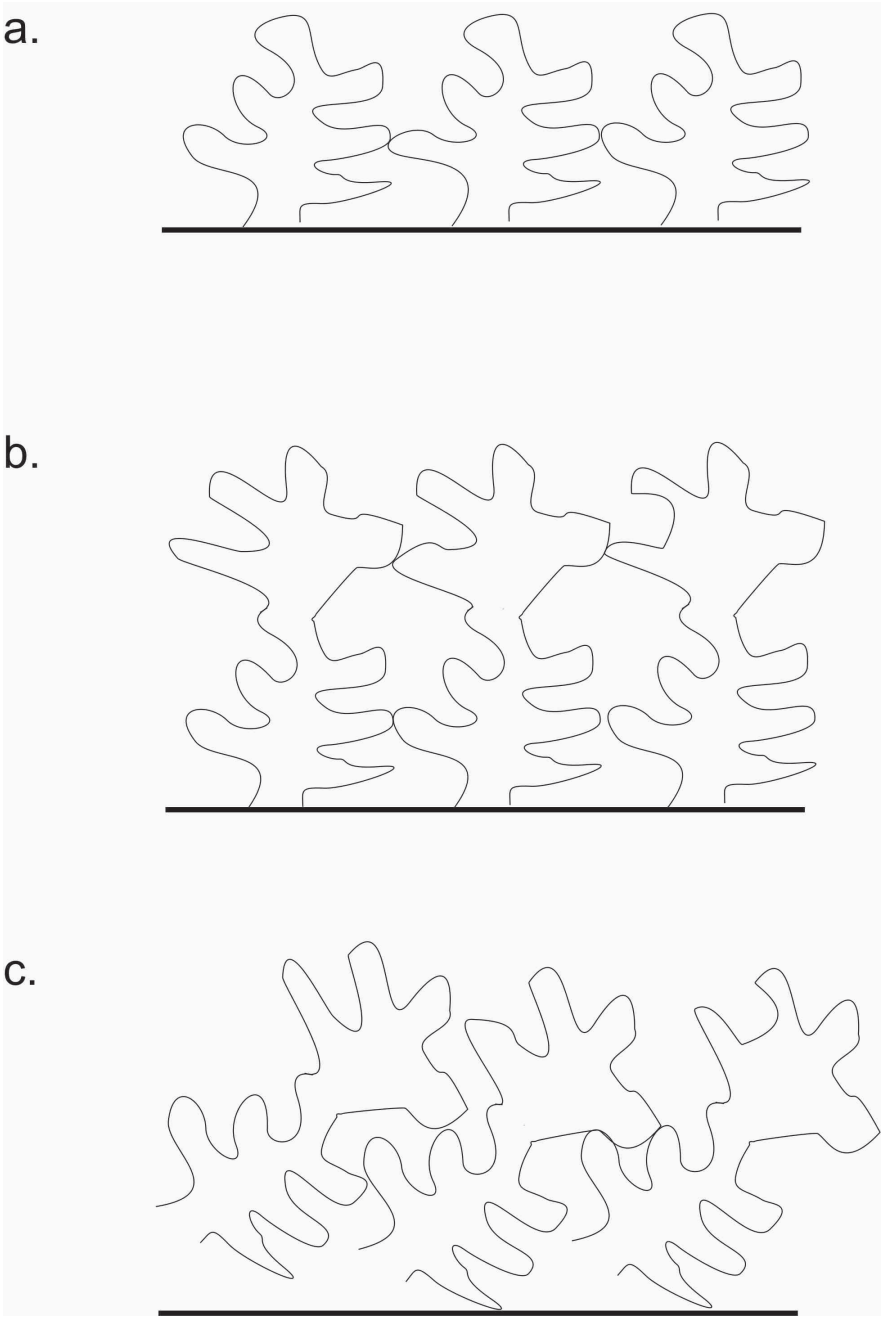

Figure 9.24: Possible ice structure during deposition leading to increase in pore size with thickness (**a.** and **b.**) and then a reduction in pore size as the structure collapses **c.**).

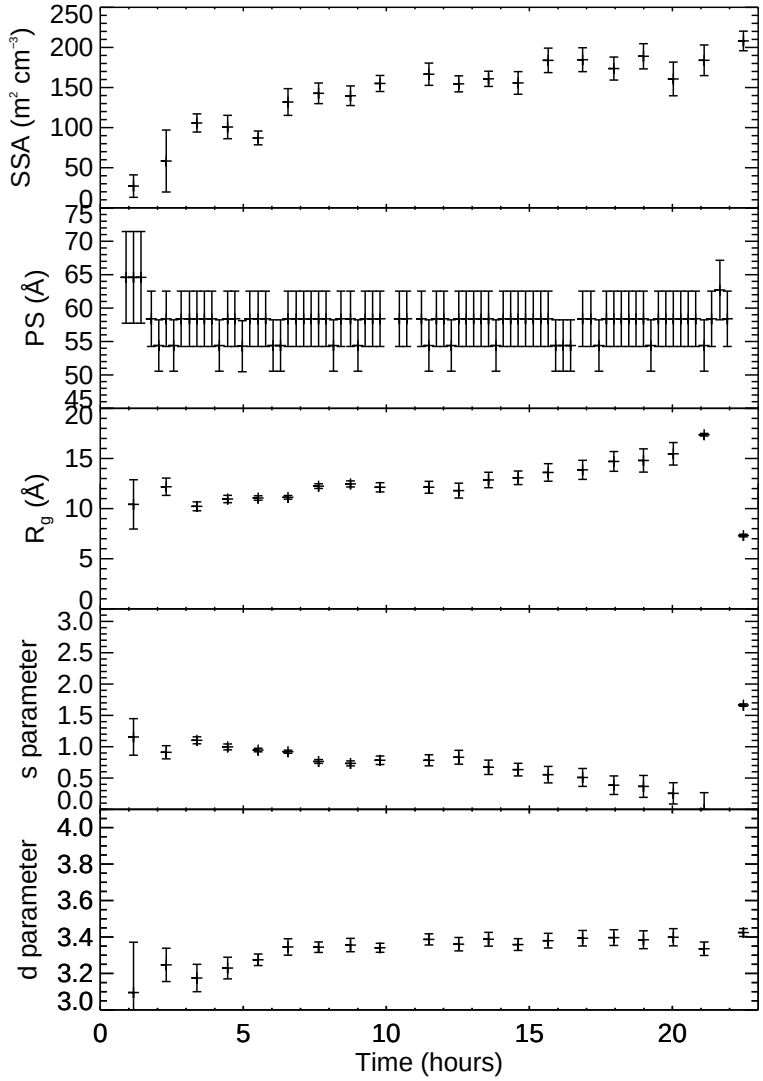

Figure 9.25: Specific surface area (SSA), periodic spacing (PS), radius of gyration (R_g), s parameter and d parameter as a function of deposition time for deposition at 50 K.

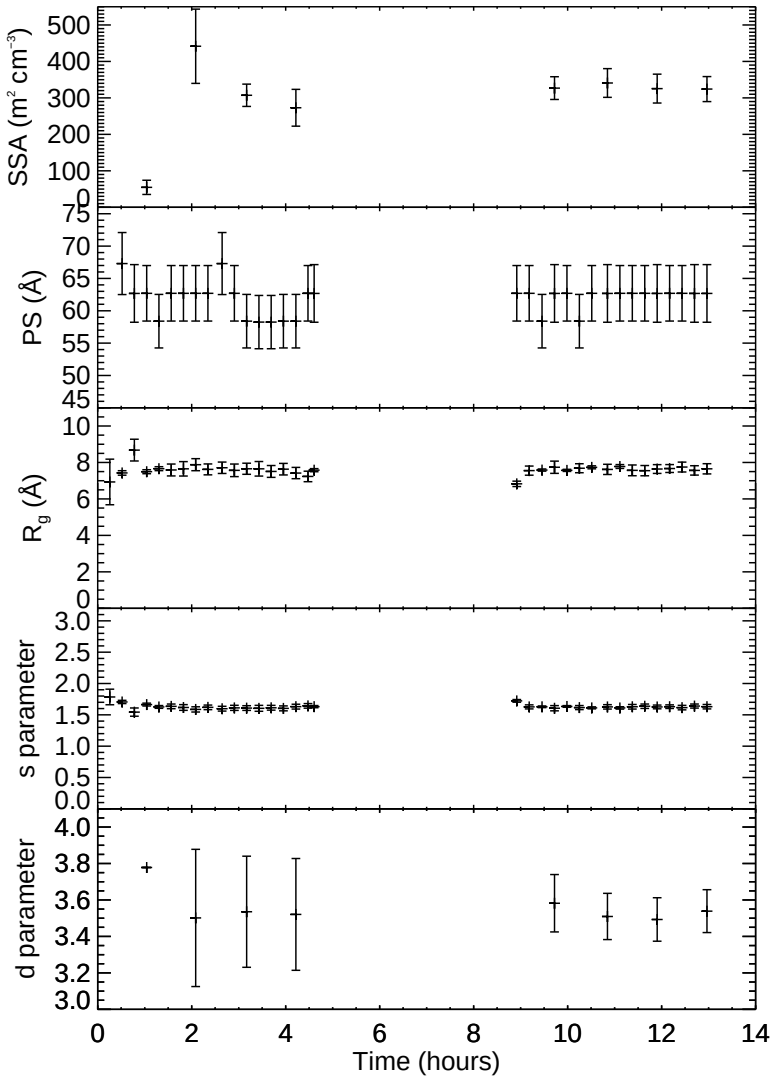

Figure 9.26: Specific surface area (SSA), periodic spacing (PS), radius of gyration (R_g), s parameter and d parameter as a function of deposition time for deposition at 52 K. The discontinuity is due to the beam going off between 4.5 and 9.5 hours of deposition.

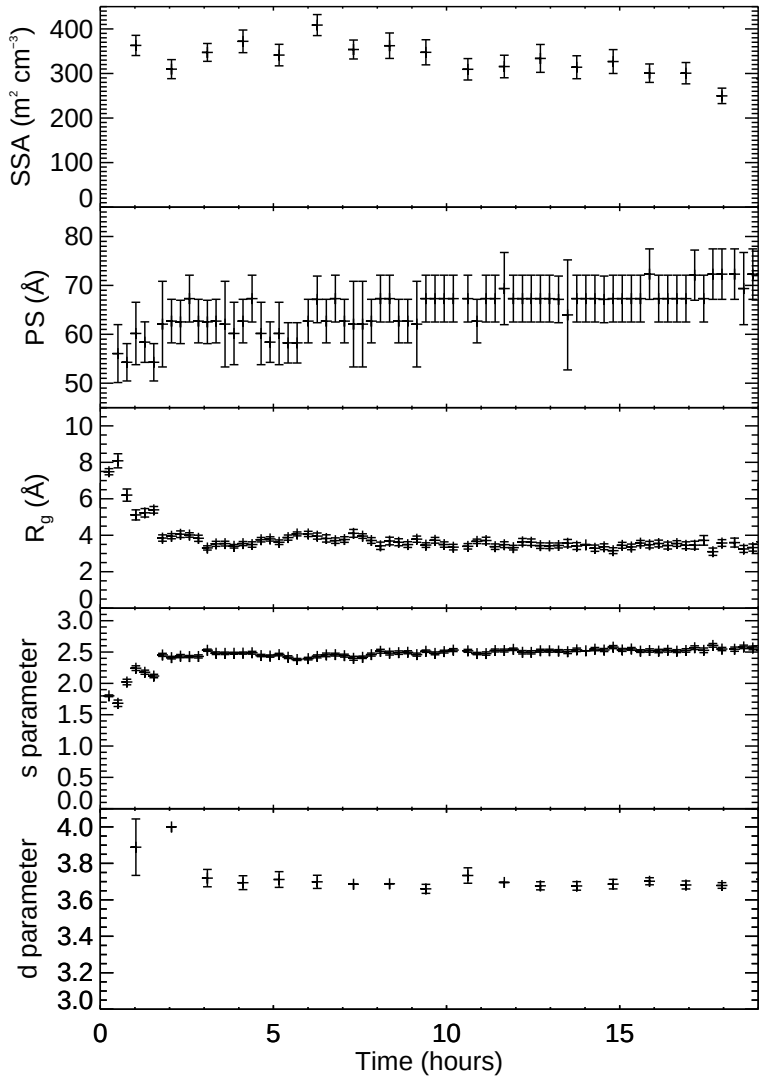

Figure 9.27: Specific surface area (SSA), periodic spacing (PS), radius of gyration (R_g), s parameter and d parameter as a function of deposition time for deposition at 17 K (AC).

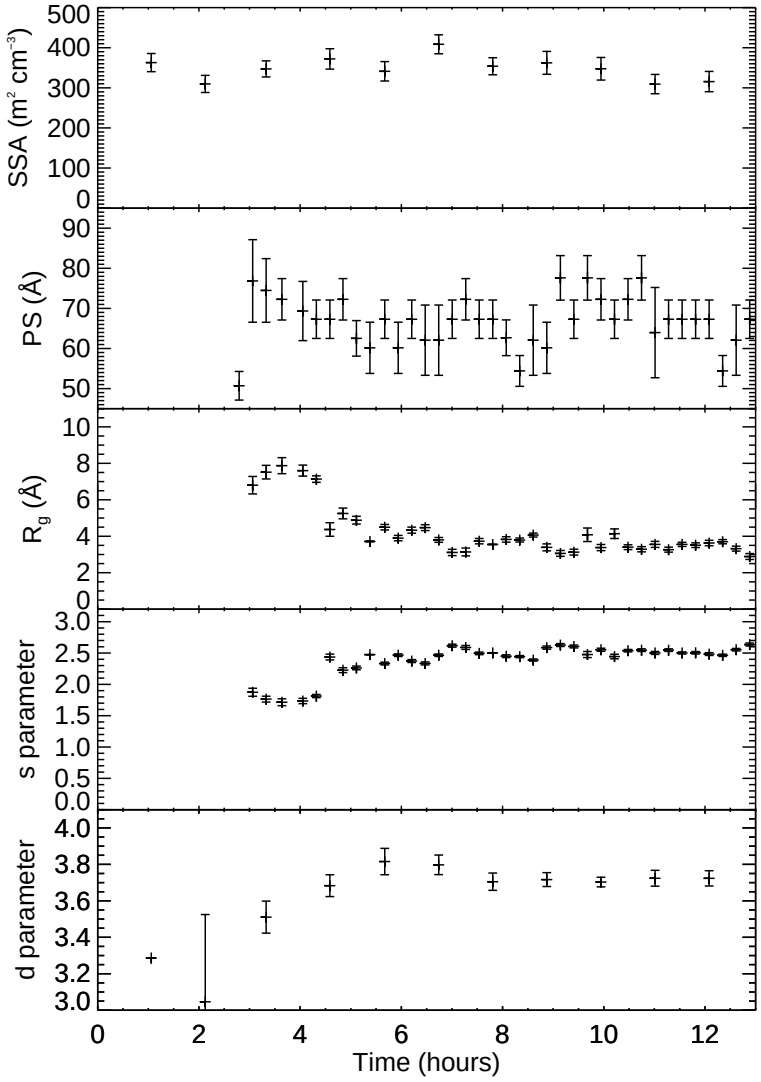

Figure 9.28: Specific surface area (SSA), periodic spacing (PS), radius of gyration (R_g), *s* parameter and *d* parameter as a function of deposition time for deposition at 17 K (A).

9.4.2 Pore changes during heating

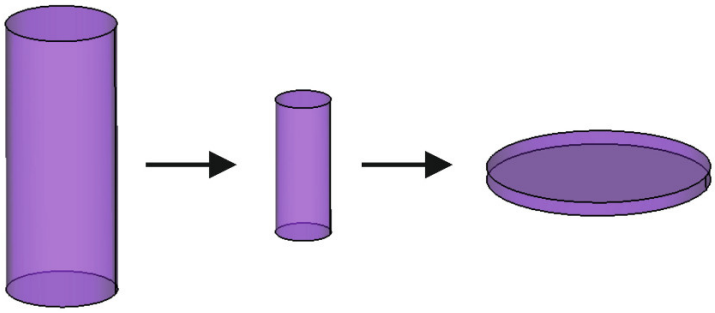

Figure 9.29: Pore collapse and pore clustering for 50 K and 52 K ices. R_g decreases at first and then increases when pore clustering starts.

When the 50 K ice is heated, the specific surface area begins to decrease from 70 K onwards. The decrease is fastest between 70 K and 120 K; after 120 K the specific surface area continues to decrease but at a much slower rate. Periodic spacing remains constant until around 100 K when it begins to increase, indicating the onset of pore clustering. There is a slight discontinuity in periodic spacing at 100 K as pore clustering continues to happen slowly while the temperature is held constant at 100 K. There is a much larger discontinuity at 110 K for the same reason. R_g decreases slightly from 7.5 Å to 7 Å between 60 K and 90 K and then increases after that, reaching 11 Å by 120 K. It also exhibits a slight discontinuity at 110 K. s increases from 1.7 at 60 K to 2.5 at 120 K. Taking these parameters together, the pores collapse from cylinders to platelets as the temperature is increased. Between 60 K and 90 K, this is accompanied by a decrease in R_g. Above 90 K, R_g begins to increase, with pore clustering becoming apparent at 100 K. As the (platelet shaped) pores begin to cluster, the radius of gyration increases. This is illustrated in Fig. 9.29.

The 52 K ice displays similar trends when heated but with a number of differences. The specific surface area begins to decrease immediately at 70 K. Periodic spacing again remains constant until 100 K when it starts to increase, showing pore clustering.

There is a small discontinuity at 110 K and a larger discontinuity at 120 K as pore clustering continues while the ice is held at these temperatures. R_g remains constant around 8 Å until 100 K when it begins to increase, reaching 20 Å by 130 K. However, a consideration of Fig. 9.18**b.** suggests that R_g does decrease slightly before 100 K. s increases slowly from 1.6 at 60 K to 2.4 at 130 K. This suggests a collapse from cylinders to platelets, beginning at 60 K. This is not accompanied by a decrease in R_g but is accompanied by pore clustering after 100 K. Both R_g and s show discontinuities at 110 K, as these parameters continue to change during the isothermal step. R_g has a large discontinuity at 120 K but this is not matched by a discontinuity in s. This suggests that pores do not continue to flatten at 120 K but they do continue to cluster and so increase in size. After 120 K, R_g is constant within uncertainties until the "hump" disappears at 130 K. The rate of increase of periodic spacing also seems to slow down after this point, suggesting that pore clustering may be almost complete, although the "hump" shifts to such low Q values after 130 K that it cannot be seen, so it is not possible to make concrete statements about the pore clustering beyond that point. d increases from around 3.5 at 70 K to around 3.8 at 120 K, suggesting smoothing of pore surfaces.

The first 17 K ice (AC) shows subtler changes than the previous two ices as it is heated. The specific surface area begins to decrease around 50 K. At this temperature, periodic spacing begins to increase, although the increase is much more modest than for the 50 K and 52 K ices. R_g and s are constant within uncertainties from 20 K to 100 K at values of 4 Å and 2.5 respectively, suggesting that the pores do not change size or shape as they are heated. This can be reconciled with the small increase in periodic spacings if the increase in periodic spacing represents a small amount of pore clustering (which does not significantly raise the average pore size) or if it represents a small number of pores collapsing entirely, leaving fewer pores overall and hence a larger spacing between them. The "hump" disappears at 100 K which suggests complete pore collapse, and R_g, s and periodic spacing can no longer be extracted. d remains around 3.6-3.7 until 80 K, where it begins to increase to 3.8 - a pore smoothing process.

The second 17 K ice (A) displays similar trends to the first 17 K ice (AC). The specific surface area decreases as the ice as heated, with the decrease starting at the higher temperature of 90 K. Periodic spacing increases a little, starting around 70 K but the increase is minimal, suggesting only very minimal amounts of pore clustering or total collapse of some pores. R_g and s again remain constant at values of around 4 Å and 2.5 respectively. d again starts around 3.6-3.7 and increases to 3.8, starting at 70 K.

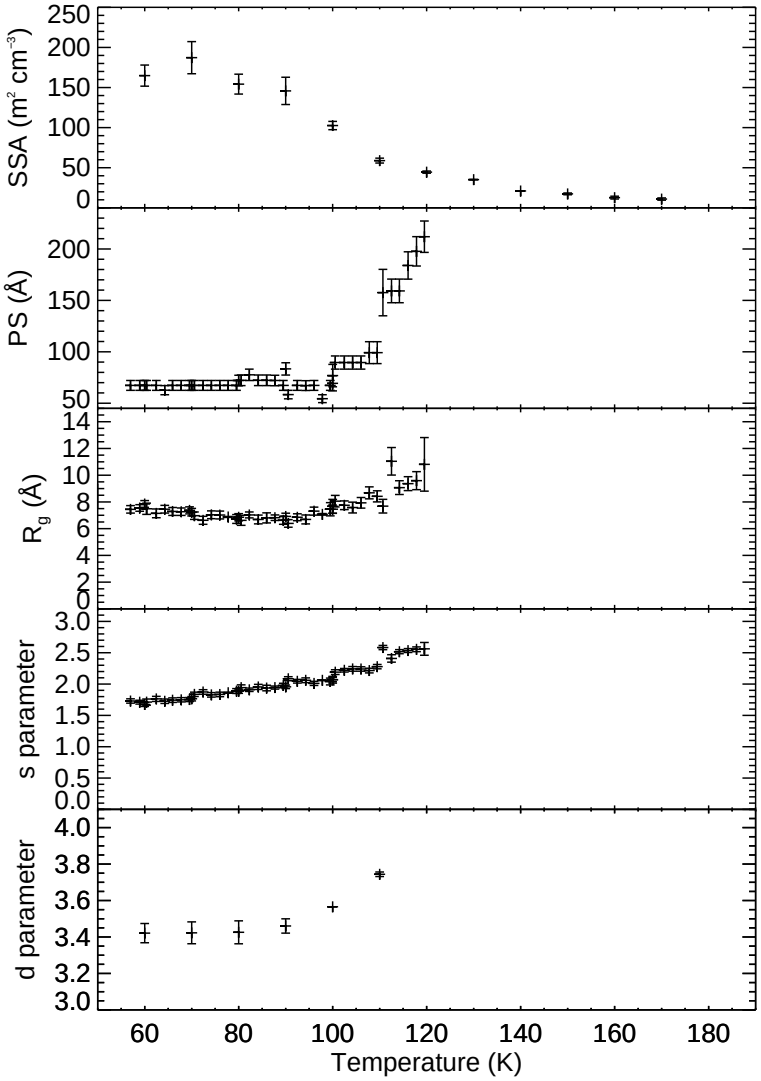

Figure 9.30: Specific surface area (SSA), periodic spacing (PS), radius of gyration (R_g), *s* parameter and *d* parameter as a function of temperature for ice deposited at 50 K.

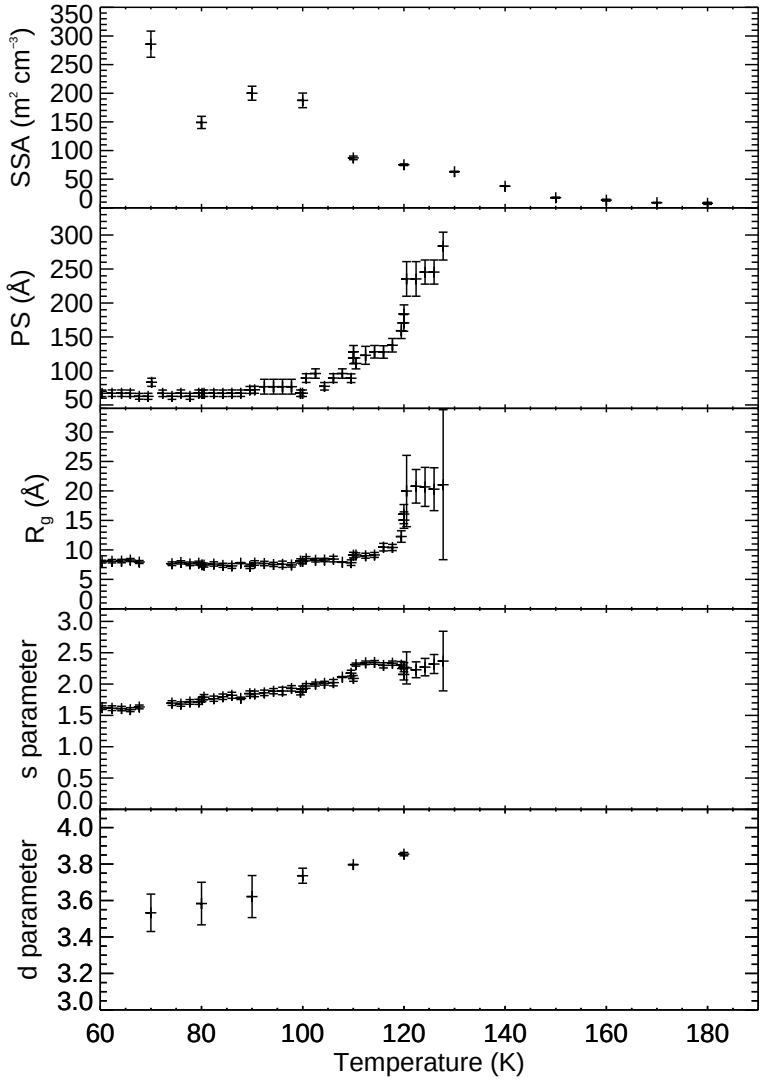

Figure 9.31: Specific surface area (SSA), periodic spacing (PS), radius of gyration (R_g), *s* parameter and *d* parameter as a function of temperature for ice deposited at 52 K.

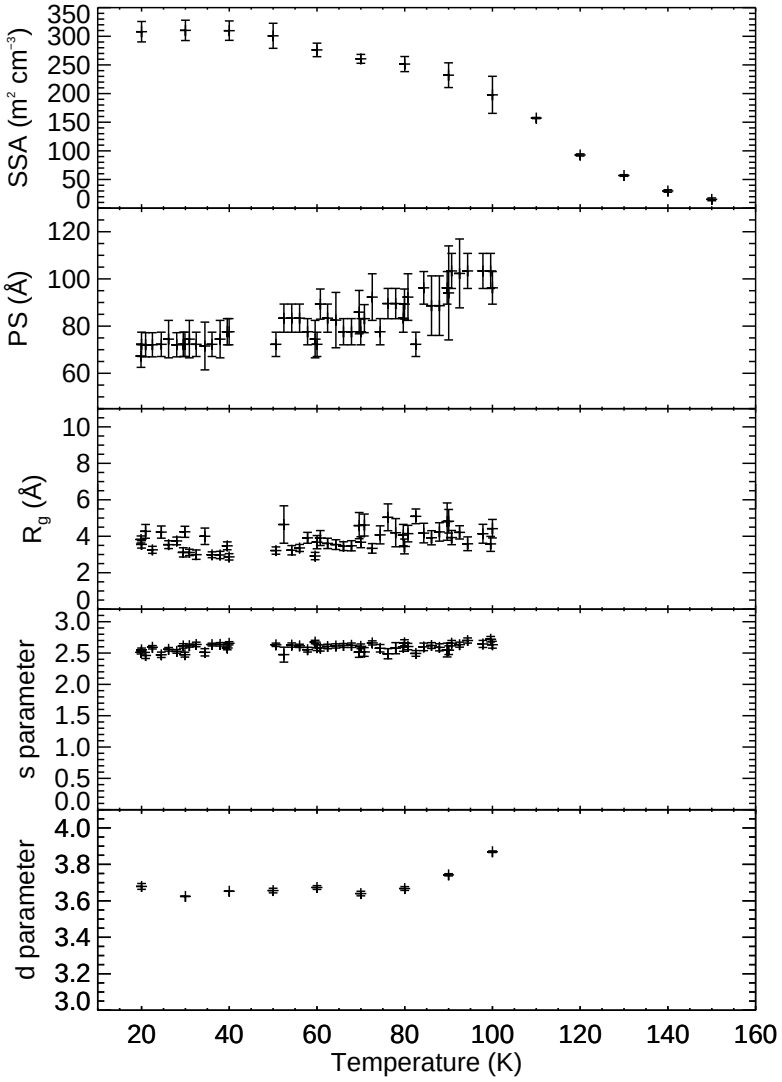

Figure 9.32: Specific surface area (SSA), periodic spacing (PS), radius of gyration (R_g), *s* parameter and *d* parameter as a function of temperature for ice deposited at 17 K (AC).

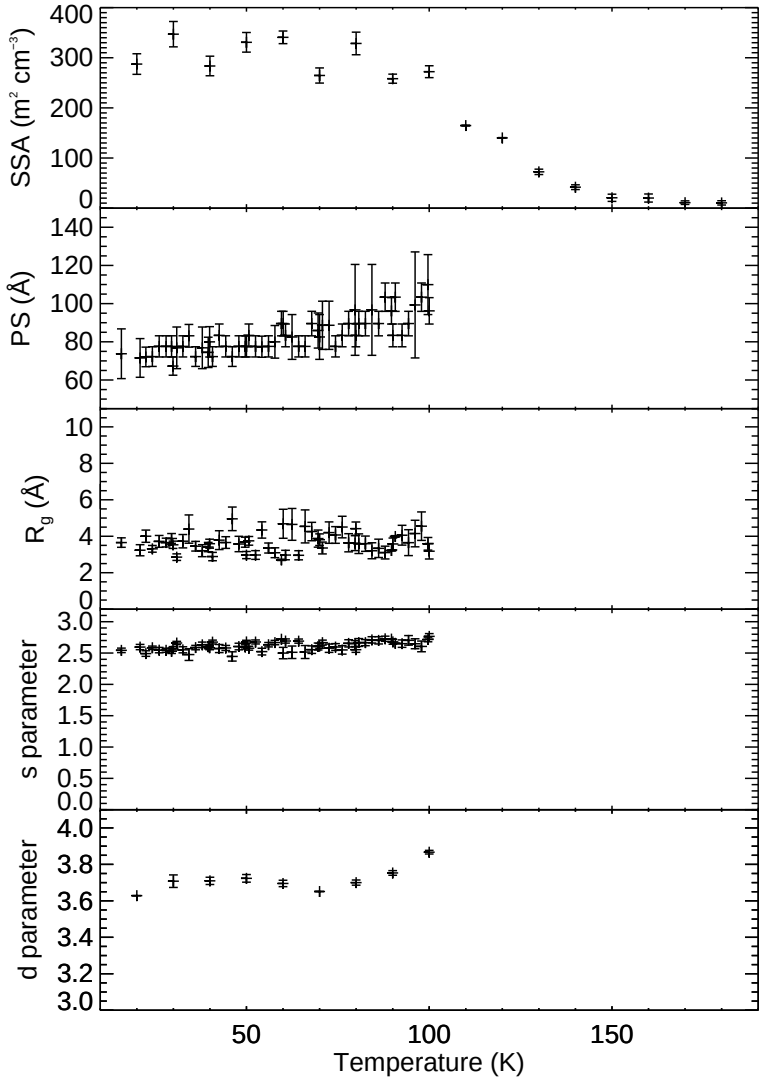

Figure 9.33: Specific surface area (SSA), periodic spacing (PS), radius of gyration (R_g), s parameter and d parameter as a function of temperature for ice deposited at 17 K (A).

9.4.3 Comparison of ices

The ices grown at 50 K and 52 K appear to be more porous than those grown at 17 K as the pores are larger (7.5-8 Å compared to 4 Å). The pores in the 17 K ices appear to undergo collapse while growing but even before this collapse, the pores are a similar size to those of the 50 K and 52 K ices. This is in contrast to previous research which suggests that ices grown at lower temperatures are likely to be more porous (Stevenson et al., 1999; Kimmel et al., 2001; Collings et al., 2003b). However, the set up used to grow the 17 K ices is likely to have had a high partial pressure of D_2O vapour surrounding the plate as the ice was grown (so high that the first ice had a crystalline component to it) and so it is likely that this is responsible for the lower porosity seen in the 17 K ices.

The specific surface areas for the 17 K ices are larger than those for the 50 K and 52 K ices. The specific surface areas do not appear to be commensurate with the pores (as the specific surface area of the 77 K ice was) and so it is likely that the ices have a large surface area on the surface of the ice (not within the pores) which completely dominates the specific surface area. The ices grown at 17 K appear to be "fluffier" than those grown at 50 K and 52 K (as shown by their higher specific surface areas). This could result in a number of "open" pores (accessible to gases that may become trapped within the pores as the ice is heated and they close). If this is correct, the 17 K ices contain more open pores than the 50 K and 52 K ices, which is in good agreement with the results of Collings et al. (2003b).

The slow pore collapse of the 50 K and 52 K ices as soon as heating begins is in contrast to the results of the previous chapter where pore collapse was sudden, rapid, and did not occur until 121 K. The reasons for the difference are not entirely clear but it is possible that ices grown below 77 K are less thermodynamically stable compared to those grown above 77 K and hence they are more prone to restructuring.

The 50 K and 52 K ices both show discontinuities in R_g, s and periodic spacing beyond 100 K. This demonstrates that pore collapse and pore clustering are auto-catalytic

when the temperature is high enough. Pore clustering begins around 100 K. Therefore, it is likely that the glass transition begins around 100 K as long range translational motion of water molecules would be necessary for pore clustering to take place. This is significantly lower than the onset of the glass transition for the 77 K ice (see Chapter 8), despite very similar heating rates for the two ices. It therefore appears that the glass transition begins at lower temperatures for ices grown below 77 K. This difference could also be due to the different experimental set up used to grow the 77 K ice; the mode of deposition has already been shown to affect the temperature of pore collapse (Mitterdorfer et al., 2014), although the reasons for this remain unclear. The 17 K ices show only subtle changes to porosity before the disappearance of the "hump" and it is likely that these can be achieved by rotational motion alone as the glass transition temperature has not yet been reached.

The first 17 K ice (AC) has a crystalline component to it. The Bragg peaks seen in Fig. 9.10 are small before the ice is heated so it is likely that the crystalline component is fairly small compared to the amorphous component. Comparing the two 17 K ices, it appears the crystalline component to the first ice does not have much effect. The periodic spacing, radius of gyration and s parameter are all very similar. However, the specific surface area is less for the 17 K (AC) ice, and the d parameter starts increasing at a higher temperature. This suggests that the crystalline component of the first ice suppresses the "fluffy" nature of the ice, reducing its specific surface area. It also suppresses the onset of rotational motion (needed for pore smoothing).

9.5 Conclusions

Four ices were grown in situ on the NIMROD beam line by depositing D_2O vapour on a cold vanadium plate at deposition temperatures of 50 K, 52 K, 17 K and 17 K. The porosity of the ices was studied as the D_2O vapour was deposited (for times ranging from 12 hours to 22.5 hours) and as it was heated between its deposition temperature and 150 K/180 K. The main conclusions of this work are as follows:

1. It is possible to grow ASW in situ on the NIMROD beam line using the experimental apparatus detailed in Chapter 6. This apparatus can be used to study both the growth and the heating of the ice.

2. Specific surface area is greater for all of the current ices than for the 77 K ice discussed in Chapter 8. The specific surface area of the 17 K ices is greater than the specific surface area of the 50 K and 52 K ices. Specific surface area increases with decreasing deposition temperature.

3. Specific surface area is not commensurate with changes to the pores. This suggests a large surface area at the surface of the ice which dominates the specific surface area measurement. This large area at the surface may indicate open pores in the ice.

4. While the 50 K ice was growing, the pores increased in size and changed shape from cylinders to platelets, collapsing to smaller cylinders after 21 hours when the surface temperature had reached 56.6 K. This is tentative evidence for the phase change from p-ASW to c-ASW seen by Jenniskens & Blake (1994), Horimoto et al. (2002) and Collings et al. (2003b). This does not occur for the 52 K ice. It is postulated that a certain thickness of ice (around 9.3 μm) is required to support the larger network of pores; this thickness was not reached for the 52 K ice until the surface temperature was above 57 K.

5. Periodic spacings were slightly smaller for the current ices than for the 77 K ice ($\sim$60Å compared to $\sim$70Å). It is not clear whether this is due to the lower deposition temperatures in the current study or the different experimental set ups.

6. Evidence for pore clustering was seen for the 50 K and 52 K ices, shown by an increase in periodic spacing and R_g beginning around 100 K. This pore clustering occurred alongside collapse from cylinders to platelets.

7. Slow pore collapse starts as soon as heating begins for the 50 K and 52 K ices. In both cases, this is indicated by an increase in s (suggesting collapse from

cylinders to platelets) and a slight decrease in R_g. This is in contrast to the 77 K ice which showed a sudden and rapid pore collapse at 121 K. It is possible that ices grown at temperatures below 77 K are less thermodynamically stable and more prone to restructuring than ices grown above 77 K.

8. d increases in all cases when the temperature is heated, showing that pore smoothing with heating is likely to be a universal process.

9. Both 17 K ices undergo pore collapse a few hours into deposition, leading to smaller pores by the end of deposition than for the 50 K and 52 K ices. This is likely to be due to the high partial pressure of D_2O vapour surrounding the plate for the set up used to grow the 17 K ices.

10. The crystalline component of the 17 K (AC) ice did not affect pore size and shape. It did reduce the specific surface area and increase the onset temperature for rotational motion.

The ices show both similarities in porosity with the 77 K ice (cylindrical pores which collapse to platelets, pore smoothing accompanying pore collapse) as well as some important differences (larger specific surface areas, slightly smaller periodic spacings, smaller pores, pore clustering and lower temperatures for the onset of pore collapse). There is tentative evidence of the p-ASW to c-ASW phase change seen by Jenniskens & Blake (1994), Horimoto et al. (2002) and Collings et al. (2003b). Porosity can change while the ice is growing, although it can also be fairly constant.

At a first glance, this data does not appear to support the theory that ices grown at lower temperatures are more porous than those grown above, as the pore sizes of all the ices studied here were smaller than those of the 77 K ice discussed in Chapter 8. However, the increasing size of the pores in the 50 K ice as it was grown (until the partial collapse after 21 hours) lends support to the theory that there is a phase change from p-ASW to c-ASW between $\sim$30 K and $\sim$70 K. This more porous form was probably not seen for the 52 K ice as the temperature was too high once sufficient ice

had been deposited. The smaller size of the pores of the 17 K ices is likely to be due to the high D_2O partial pressure surrounding the deposition plate rather than a true result, although more work is needed to confirm this, comparing the pressures surrounding the plate to those in protoplanetary disks. This is discussed in Chapter 10. The pores clustered when the ice is heated, in contrast to those of the 77 K ice of Chapter 8 which did not. It is not clear whether this is a result of the lower temperatures or the different experimental set ups used to create the ice and this is another question to be answered in further work. The specific surface areas were greater for all four ices discussed in this chapter than for the 77 K ice, which could indicate a higher number of open pores within the ice. These results, while still leaving open questions, show that porosity does change with deposition temperature and this must be taken into account when considering collisions of ASW particles.

Chapter 10

Conclusions and future work

The aim of this thesis was to answer the following questions:

How do ice particles collide in planet-forming regions, and can they help planet formation?

What is the structure and porosity of amorphous solid water in planet-forming regions and how do these properties change with time and temperature?

The work presented in this thesis demonstrates that millimetre and centimetre-sized crystalline water ice particles do not stick at relevant collision velocities and therefore cannot overcome the "bouncing barrier" and account for the early stages of planet formation. However, the energy losses seen in collision reduce the relative velocities of the ice particles, which may over time lead to higher particle concentrations in parts of the disk. This would contribute towards the high particle concentrations produced by streaming instabilities and may lead to planetisimal formation by gravitational collapse. Some of the translational energy lost is converted into rotational energy, but up to 96% of the energy lost remains unaccounted for. The mechanisms of energy loss remain a mystery and this is an important question to be answered in future work.

The work on porosity of amorphous solid water demonstrated that, contrary to what

is often assumed in astronomy, amorphous solid water grown at temperatures as high as 77 K is porous, and (under the experimental conditions described in this thesis) remains porous until 121 K. This indicates that amorphous solid water in the outer regions of protoplanetary disks is likely to be porous, which has important implications for planet formation as porosity has been linked to increased sticking in collisions. This work has shown that the structure and porosity of amorphous solid water is even more complex than previously thought, and must be fully understood in order to understand its influence in future collisional studies.

In this chapter, the detailed conclusions of this work are presented and possible extensions to this work are discussed.

10.1 Conclusions

10.1.1 Collisional properties of water ice

The work presented in this thesis provides new insights into the collisional properties of millimetre and centimetre-sized ice particles in planet-forming regions. Experiments were performed colliding together millimetre-sized pure water ice particles and centimetre-sized particles composed of pure water, water with 5% methanol and water with 5% formic acid. The collisions were carried out on board parabolic flights using a purpose-built experimental set up. The main aim was to find out if ice particles can stick together at relevant collision velocities, and hence if their collisions could aid planet formation. The main findings were:

1. Particle sticking was not observed in any case. In a few cases, particle fragmentation was observed but it was thought to be related to inherent weaknesses in these particles before collision, rather than the collision itself producing this outcome; otherwise universal bouncing was observed. The critical velocity for the onset of bouncing must be below $0.26(91)\pm0.0009$ m s^{-1} for millimetre-sized particles and below $0.01(4)\pm0.009$m s^{-1} for centimetre-sized particles. Crys-

talline ice particles cannot overcome the "bouncing barrier" in planet formation and including methanol and formic acid within the ice at a level of 5% does not change the collisional outcome from bouncing to sticking.

2. Coefficients of restitution were distributed over a broad range (0.08±0.01-0.64±0.09 for the millimetre-sized particles and 0.10(6)±0.006-0.81±0.17 for the centimetre-sized particles) but did not depend on relative impact velocity, normalised impact parameter, temperature or chemical composition. The rough, anisotropic surfaces were thought to be responsible for the ranges of coefficients of restitution.

3. The upper limits for the coefficients of restitution were 0.65 for the millimetre-sized particles and 0.81 for the centimetre-sized particles. The lower upper limit for the millimetre-sized particles was thought to be because of the higher collision velocities for these particles, although it is possible that reduced particle size and irregular particle shape could also play a role.

4. Between 0.08% and 17% of the original kinetic energy was converted into rotational kinetic energy after the collision for the millimetre-sized particles. It was not possible to extract this information for the centimetre-sized particles due to their spherical shape and lack of distinguishing marks. When combined with translational kinetic energy after the collision, this leaves between 58% and 96% of the original kinetic energy unaccounted for after the collision. It is not possible to determine where this energy goes in these experiments, but it is possible that it leads to surface fracturing or surface heating and desorption of surface material.

One of the most important results in terms of planet formation is that the collisions of millimetre and centimetre-sized crystalline water ice particles at relevant collision velocities do not result in sticking, which suggests that the presence of crystalline ice alone cannot overcome the "bouncing barrier" in planet formation. However, the loss

of energy in collisions may contribute towards particle "pile-ups" that can trigger planet formation via streaming and gravitational instabilities (Youdin & Goodman, 2005; Johansen et al., 2007; Nagel-Vega, 2010; Johansen & Klahr, 2011; Youdin, 2011). The finding of a broad range of coefficients of restitution that is independent of impact velocity, impact parameter, chemical composition and temperature, as well as the differing upper limits of coefficients of restitution and the particle rotation will be useful in modelling collisions of icy particles in both planet-forming regions and planetary ring systems.

10.1.2 Structural properties of amorphous solid water

To help interpret the results of future collision experiments of amorphous solid water particles, it is vital to have a good understanding of the structural properties of this ice, particularly its porosity and pore collapse. The work presented in this thesis has demonstrated that compact amorphous solid water is porous, and the heating and isothermal studies have led to a greater understanding of the process of pore collapse and porosity changes in amorphous solid water. The ice was studied using neutron scattering at the ISIS neutron source at RAL, taking scans both while heating the ice and while keeping the temperature constant to see how the porosity changes with both temperature and time. The aim was to investigate the process of pore collapse for an ice deposited at 77 K, and to investigate the effect of deposition temperature on porosity and pore collapse for ices grown below 77 K. The latter set of experiments also acted as a proof-of-concept for growing ASW in situ on the NIMROD beam line. The main findings were as follows:

Process of pore collapse

1. When the pore collapse occurs on heating of the ice, the pores collapse from cylinders to platelets. This mechanism of collapse occurs regardless of growth temperature and whether or not the pores cluster.

2. Pore collapse in ASW grown at 77 K occurs suddenly at 121 K when the heating rate is 0.4 K min^{-1}. Pore collapse is complete by 136 K.

3. Pore clustering is seen for ices grown at 50 K and 52 K but not for the ice grown at 77 K. It is thought that the different methods of growth are likely to be responsible for the different behaviour. This suggests that pore clustering is not a necessary process accompanying pore collapse.

4. The ice grown at 77 K is stable (i.e the specific surface area, periodic spacings, radius of gyration and *s* parameter do not change) when the ice is kept at 92 K and 117 K, indicating that pore collapse is not auto-catalytic below 117 K.

5. The glass transition of amorphous solid water involves a transition from a glassy state to an ultra cooled liquid state. For the ice grown at 77 K, it begins at 121 K and ends at 136 K. For the ices grown at 50 K and 52 K, it may start at 100 K as shown by changes to the ice in the isothermal step. These changes involve pore collapse (and pore clustering) taking place while the temperature of the ice is constant. Therefore pore collapse is auto-catalytic once the glass transition has been reached.

6. Specific surface area is not commensurate with changes to the pores. This is particularly apparent for the 50 K, 52 K and 17 K ices. As the pores are smaller for these ices than for the 77 K ice, this suggests a large surface area at the surface of the ice which dominates the specific surface area measurement. This large area at the surface may indicate open pores in the ice.

7. When pore collapse occurs, the pore surfaces get smoother. This occurs in all cases of pore collapse discussed in this thesis, suggesting that it is a universal process accompanying pore collapse.

8. Evidence of ice expansion is seen in the ice grown at 77 K when it is heated between 92 K and 117 K.

ASW grown below 77 K

1. It is possible to grow ASW in situ on the NIMROD beam line using the apparatus described in Chapter 6. Now that the concept has been proved, it will be possible to improve the set up in future.

2. The specific surface area of ASW increases with decreasing deposition temperature. This might be expected to indicate greater porosity at lower deposition temperatures, however, this is not backed up by the Guinier-Porod fits, which show smaller pores for the 50 K, 52 K and 17 K ices than for the 77 K ice. The increased specific surface area for the 50 K, 52 K and 17 K ices with respect to the 77 K ice could be due to a much greater surface area at the surface of the ice (i.e. a "fluffier" ice) which dominates the overall surface area.

3. There is tentative evidence of the p-ASW to c-ASW phase change reported by Jenniskens & Blake (1994), Horimoto et al. (2002) and Collings et al. (2003b) seen in the 50 K ice during deposition.

4. In contrast to the 77 K ice, slow pore collapse starts as soon as heating begins for the 50 K and 52 K ices. The changes are much less dramatic than for the 77 K ice. It may be that ices grown at temperatures below 77 K are less thermodynamically stable and more prone to restructuring than ices grown above 77 K.

5. The presence of a small crystalline component in the ice does not appear to affect pore size and shape, although it reduces the specific surface area and increases the onset temperature for rotational motion.

This work has answered many previously unresolved questions about the process of pore collapse in ASW. It is not auto-catalytic until the glass transition temperature is reached and the water molecules can undergo long range diffusion. Therefore, ASW in planet-forming regions is likely to remain porous for as long as the temperature remains low enough, and as discussed in Chapter 1, this may increase the sticking probability in collisions. Pore collapse in ASW can involve pore clustering but does

not necessarily involve this process. Pore clustering results in fewer, larger pores. It is likely that the size and distribution of pores will have an impact on the collisional properties of the ice; exactly how it affects collisional properties is a question to be answered in future work. The detailed understanding of porosity changes in ASW presented in this thesis provides a good basis for understanding future collision experiments of ASW.

10.2 Future work

10.2.1 Additional collision analysis

In Chapters 4 and 5, only binary collisions were considered. However, considering multiple body collisions would give a fuller understanding of collisional properties of ice, which could be used in models of ice collisions in protoplanetary disks.

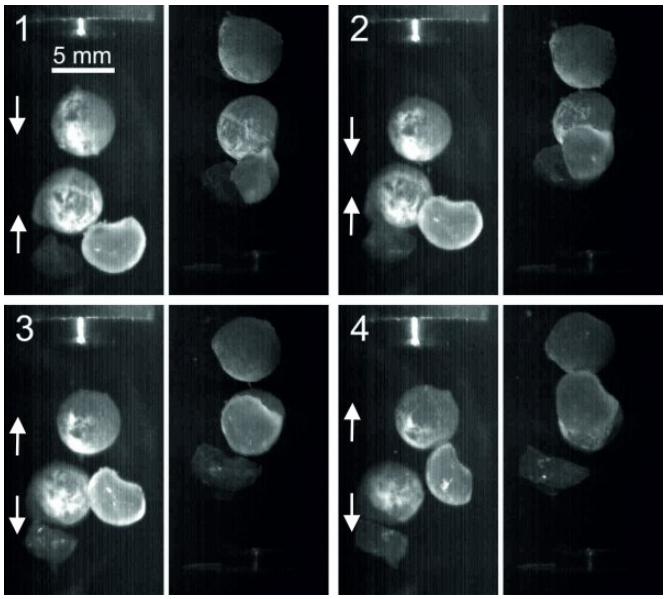

Figure 10.1: Image sequence of a collision between four ice particles. Mirror optics were used to capture two views of the collision with the view shown on the left separated from the view shown on the right by 60°. The time difference between each successively numbered image is 1/107 s. The apparent offset of the two views is due to the set up of the mirror optics. Analysing such collisions with the help of particle tracking software in future would provide additional information about ice particle collisions.

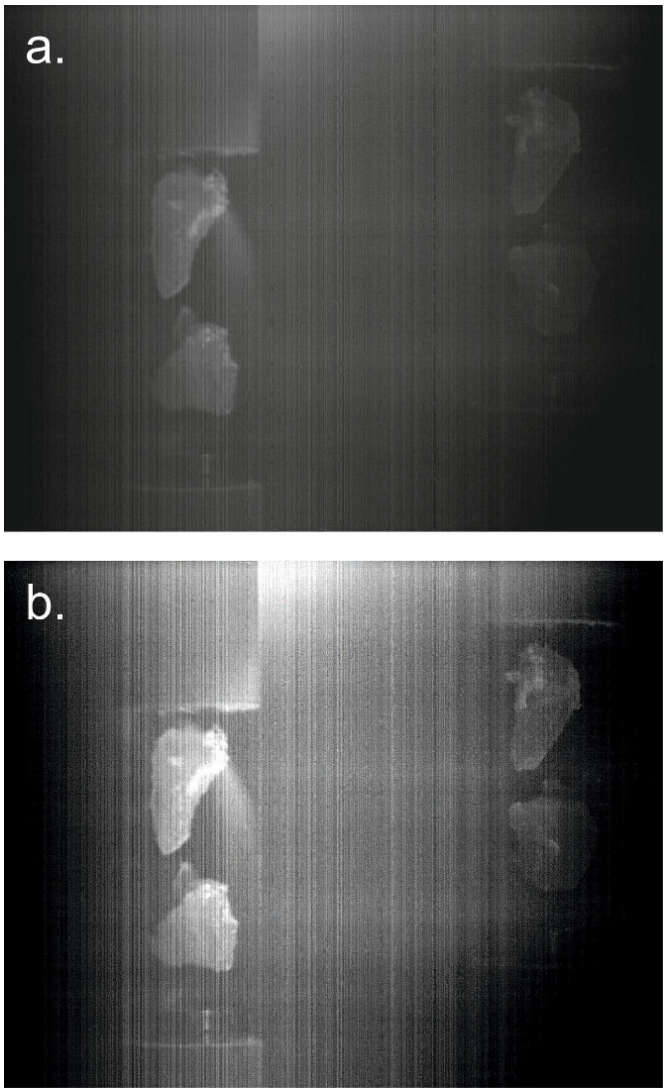

Figure 10.2: **a.** Original particle image. **b.** Image with brightness and contrast adjusted using Microsoft Office's autocorrect feature so that the particles are easier to see. Such adjustments would make it easier for particle tracking software to track the particles and could enable previously unclear collisions to be analysed.

Analysing multiple body collisions such as that shown in Fig. 10.1 requires the tracking of several different particles. The manual tracking method presented in Chapter 3 could be used but would be very time consuming. To reduce the time taken to analyse such collisions, specially developed particle tracking software could be used. Such software would need to be capable of distinguishing particles from the background of the image sequences. As the colour difference between particle and background can be very subtle in the original images, it is likely that the brightness and contrast of the images would need to be altered to increase the colour difference

between particle and background. This is illustrated in Fig. 10.2. Such image enhancement techniques might also enable the analysis of collisions previously excluded from the analysis due to poor image quality.

10.2.2 Investigating the energy loss

In Chapter 4, an investigation of the distribution of energy after the collision showed that some energy went into translation and some into rotation, but a significant proportion (as high as 96%) of the energy was unaccounted for. Possible energy dissipation mechanisms include surface fracturing, compaction of the surface and desorption of surface material. It is not possible to investigate these possibilities using the current experimental apparatus as it contains no facility for measuring desorption and it is not possible to recover the particles after collision (as they fall to the bottom of the experimental chamber when microgravity ceases and sublimate). Surface desorption could possibly be studied by incorporating a mass spectrometer into the collision volume. Surface fracturing and compaction would have to be investigated in the laboratory; this could be done by conducting collisions in the vertical plane, firing one particle up and releasing the other the fall downwards such as in the work of Blum & Munch (1993). After collision, the particle surfaces could be studied under a microscope to obtain the extent of fracturing or compaction.

10.2.3 Future collision experiments

The most obvious extension to the work presented in Chapters 4 and 5 is to carry out similar collision experiments to those detailed in those chapters but using amorphous solid water particles instead of crystalline water ice. Such experiments would utilise apparatus for growing gram quantities of ASW similar to that described in Chapter 6. This would produce millimetre-sized ASW grains that could be stored under liquid nitrogen and then loaded into the parabolic flight apparatus as described in Chapter 2. Collision experiments would be conducted on board parabolic flights. During

the course of the flight, the temperature would rise, from around 131 K to 160 K (the temperature rise from 77 K to 131 K occurs during loading of the apparatus into the aircraft, take-off and the flight to a suitable airspace to perform the parabolic manoeuvre). In this temperature range, pore collapse is likely to come to an end and crystallisation will occur, allowing the differences in collisional properties with porosity and ice phase to be ascertained. However, the results in this thesis show that pore collapse is likely to have begun well before 131 K. If collisions are to be studied below this temperature, they must either be performed in the laboratory at higher collision velocities (when the temperature can be maintained at 77 K, or higher by heating the copper block) or the parabolic flight apparatus must be modified so that the temperature rise occurs more slowly. This could possibly be achieved by increasing the size of the copper block, but care would have to be taken to ensure this does not increase the weight of the apparatus too much so that it still complies with safety and payload requirements.

All research so far (including that presented in this thesis) shows that the porosity of ASW is dependent on the method of deposition and the heating rate. Therefore, to fully understand the results of such experiments, it would be necessary to produce a sample of ASW as if for a parabolic flight but instead, perform neutron scattering scans whilst heating the ice at the same rate as the warm-up would occur in the parabolic flight apparatus. Characterising the ice in this way would enable definitive conclusions to be reached about the effects of porosity changes in the ice on its collisional properties.

10.2.4 Future studies of ice porosity

As well as characterising porosity changes in ASW to match them up with any changes in collisional properties, there are a number of other avenues to be explored in studying the porosity of amorphous solid water, including the kinetics of pore collapse, improving the in-situ growth set up, growing the ice at different pressures, and studying the porosity with a different ISIS instrument to obtain complementary information about the ice porosity.

In Chapter 8, it was mentioned that the study of the process of pore collapse could be viewed as a first step towards a kinetic model. The data presented in that chapter is insufficient to do this as pore collapse takes place in a region where both temperature and time are changing, so it is impossible to separate the effects of time and temperature. To start building a kinetic model, it would be necessary to carry out isothermal experiments at a variety of different temperatures. ASW samples would be grown at a certain temperature and then heated at a constant rate until the isothermal temperature in question was reached. The ice would be held at this temperature for several hours with scans taken every few minutes. The ice would then be destroyed and a new sample grown at the original growth temperature and heated at the same heating rate until the next isothermal temperature was reached. Performing this experiment at isothermal temperatures between 100 K and 140 K at 5 K intervals would enable the rate of decrease of parameters measuring porosity (such as R_g and s) to be measured as a function of temperature. A similar set of experiments where the ice was heated constantly at a range of heating rates would also enable the effect of heating rate on the rate of pore collapse to be measured.

It is clear from the results of Chapter 9 that the set up used to grow the 17 K ices is not suitable for growing ASW as it produced ice with a crystalline component in one case, and both ices had a lower porosity than would be expected. This is most likely due to the high D_2O partial pressure surrounding the vanadium plate. As the thermal linkage was improved between the 50 K and 17 K deposition experiments, it is possible that the enclosed heat shields are not necessary to achieve the low deposition temperature and so the obvious modification is to place "beam in" and "beam out" holes in both aluminium heat shields to reduce the partial pressure surrounding the vanadium plate. At the time of writing, experiments have been carried out with the apparatus in this configuration (shown in Fig 10.3) by other researchers at The Open University and first results suggest that it has been successful and allowed a more porous ice to be produced.

Now that the apparatus has been modified, there are numerous possible extensions

Figure 10.3: Modified in-situ ice growth set up with two aluminium heat shields with "beam in" and "beam out" holes in front of and behind the vanadium plate. *Photo credit: Tristan Youngs (ISIS)*

to this work. It was suggested in Chapter 9 that a high pressure surrounding the plate was responsible for the crystalline component and lack of porosity, and while the results that have been obtained by other researchers at The Open University since then appear to back this up, this could be confirmed by growing ice at different background pressures. Finally, the 50 K and 52 K ices showed pore clustering to such an extent that the final pore collapse could not be seen using NIMROD as the pores were more than 314 Å apart. Studying this process using another instrument at ISIS called Sans2d, which can view length scales of up to 300 nm could be a solution to this problem, however, as the smallest distance Sans2d can probe is 0.25 nm, it would not be possible to confirm that the ice was fully amorphous. Such experiments would be best left

until the conditions needed to reliably form ASW using the current apparatus are fully defined.

10.3 Concluding remarks

This thesis has produced important insights into the processes that may occur beyond the snowline in protoplanetary disks. It is apparent that crystalline water ice particles cannot overcome the "bouncing barrier" and as such, the puzzle of planet formation remains unsolved, although the loss of energy in collisions may contribute to higher particle concentrations, contributing to planet formation via streaming and gravitational instabilities. The collision experiments described in this thesis have shown that the loss of energy in collisions of crystalline ice particles is independent of the impact velocity, impact parameter, temperature and ice composition. The process of pore collapse in amorphous solid water is now far better understood; although questions still remain about the porosity of ices grown at temperatures below 77 K. The next steps will involve collisional experiments of amorphous solid water particles, which may undergo significant and complex porosity changes within the temperature regions of interest, and further studies of ice porosity, particularly below 77 K. While this thesis has shed some light on these processes, they are far from fully understood and must be the subject of further work. One thing is clear: to understand the collisional properties of ice, it is necessary to have a comprehensive understanding of its structure. This thesis represents a first and important step towards this goal.

Appendix A

Ice particle collisions: worked example

This appendix contains a worked example of tracking and extracting collisional information from video images of two millimetre-sized ice particles colliding, using the equations presented in Chapter 3.

A.1 Coefficient of restitution

Fig. A.1 shows a particle-particle collision between 2 ice fragments. The images contain two views of the collision with the view on the left separated from the view on the right by 60°. The collision occurs between frames 6 and 7. Where a particle is fully visible, the centre of mass position is marked with a yellow dot. The centre of mass positions in pixels are given in Tables A.1 and A.2. Two pixel positions are given per frame; these refer to the left and right views of the particle respectively.

To convert the pixel positions to positions in metres, the top guiding tube is measured in pixels. In the images, the top guiding tube is 256 pixels wide. The width of the guiding tube is 10 mm, therefore 1 pixel = 3.91×10^{-5} m.

The co-ordinate system chosen for the conversion of (x,y) positions in pixels to (x,y,z) positions in metres is shown in Fig. A.2. The co-ordinates are defined as x' and z' for the left view and as x'' and z'' from the right view (Fig. A.2) It should be noted that this choice of co-ordinate systems is completely arbitrary. The (x, y, z) co-

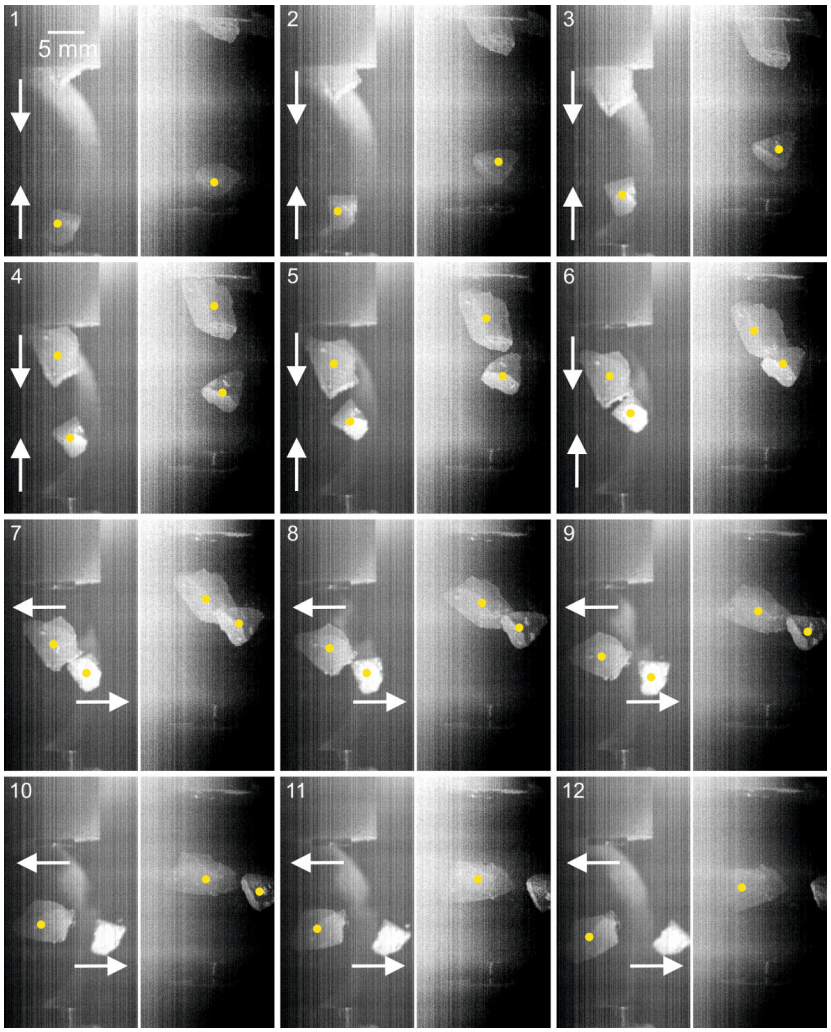

Figure A.1: Image sequence of a collision between 2 ice fragments. Beam splitter optics were used to capture two views of the collision with the view shown on the left separated from the view shown on the right by 60°. The time difference between each successively numbered image is 1/107 s. The apparent offset of the two views is due to the set up of the mirror optics. The centre of mass positions are marked by yellow dots.

ordinates were calculated from the centre of mass positions in pixels taken from the images as follows:

$$x = x'p \tag{A.1}$$

$$y = \frac{x'' - x'cos(\phi)}{sin(\phi)}p \tag{A.2}$$

$$z = \frac{z' + z''}{2}p \tag{A.3}$$

Table A.1: Centre of mass positions in pixels for the top particle. The two positions for each frame refer to the left and right views of the particle respectively. The horizontal line separates particle positions before and after the collision.

x position (pixels)	*y* position (pixels)	Frame number
349	394	4
1061	225	4
348	430	5
1056	268	5
340	475	6
1049	313	6
340	504	7
1047	345	7
322	533	8
1037	367	8
314	549	9
1037	394	9
302	579	10
1028	418	10
285	615	11
1023	439	11
288	633	12
1008	456	12

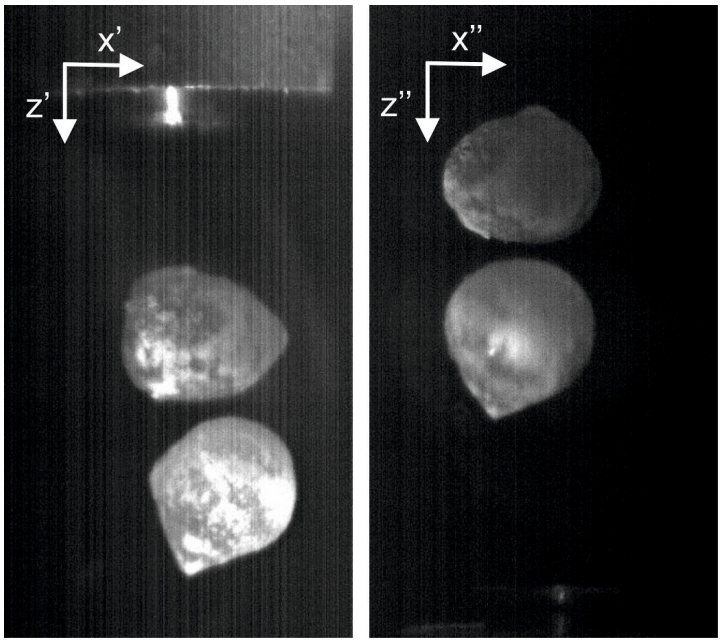

Figure A.2: Image of two ice particles just before collision as seen from two different camera views; the view on the left is separated from the view on the right by 60°. The defined co-ordinate systems are indicated.

Table A.2: Centre of mass positions in pixels for the bottom particle. The two positions for each frame refer to the left and right views of the particle respectively. The horizontal line separates particle positions before and after the collision.

x position (pixels)	y position (pixels)	Frame number
371	848	1
1088	675	1
365	801	2
1097	628	2
393	741	3
1104	586	3
400	682	4
1111	529	4
413	623	5
1122	459	5
427	600	6
1138	430	6
450	603	7
1159	441	7
473	616	8
1181	453	8
497	624	9
1211	465	9
518	637	10
1231	468	10

where p is the pixel size in metres and ϕ is the angle separating the two views of the collision (in this case, $\phi = 60°$).

Applying these conversions to the pixel positions in Tables A.1 and A.2 gives the (x, y, z) positions in metres shown in Tables A.3 and A.4.

Linear fits ($i = mt + c$ where $i = x, y, z$ and t is the frame number) to these particle positions are shown in Figs A.3 and A.4. The fit parameters are shown in Tables A.5 and A.6. These linear fits define the particle trajectories before and after the collision. As each frame is 1/107 s apart, multiplying the gradient by 107 gives the velocity component of the particle. The relative velocity is defined as the difference between the velocity of the top particle and the velocity of the bottom particle. The components and overall relative velocities are given in Table A.7.

The ratio of the relative velocities of the colliding particles after ($v_{rel,a}$) and before

Table A.3: Centre of mass positions in metres for the top particle. The large number of significant figures in this table is simply a reflection of the significant figures output by the calculation program.

x position (m)	y position (m)	z position (m)	Frame number
0.01363	0.04786	0.01209	4
0.01359	0.04763	0.01363	5
0.01328	0.04732	0.01539	6
0.01328	0.04723	0.01658	7
0.01258	0.04677	0.01758	8
0.01227	0.04677	0.01842	9
0.01180	0.04637	0.01947	10
0.01113	0.04614	0.02059	11
0.01125	0.04547	0.02127	12

Table A.4: Centre of mass positions in metres for the bottom particle. The large number of significant figures in this table is simply a reflection of the significant figures output by the calculation program.

x position (m)	y position (m)	z position (m)	Frame number
0.01449	0.04907	0.02975	1
0.01426	0.04948	0.02791	2
0.01535	0.04980	0.02592	3
0.01563	0.05011	0.02365	4
0.01613	0.05061	0.02113	5
0.01668	0.05133	0.02012	6
0.01758	0.05228	0.02039	7
0.01848	0.05327	0.02088	8
0.01941	0.05462	0.02127	9
0.02023	0.05552	0.02158	10

($v_{rel,b}$) is:

$$\varepsilon = \frac{v_{rel,a}}{v_{rel,b}} \tag{A.4}$$

Hence, the coefficient of restitution is 0.53.

Table A.5: Fit parameters for linear fits to the top particle positions in each dimension. The large number of significant figures in this table is simply a reflection of the significant figures output by the calculation program.

Dimension	m	c
x before collision	-0.00017500	0.01367500
y before collision	-0.00027000	0.04787333
z before collision	0.00165000	0.01205333
x after collision	-0.00042771	0.01440409
y after collision	-0.00031686	0.04820105
z after collision	0.00095800	0.01371600

Table A.6: Fit parameters for linear fits to the bottom particle positions in each dimension. The large number of significant figures in this table is simply a reflection of the significant figures output by the calculation program.

Dimension	m	c
x before collision	0.00048114	0.01422048
y before collision	0.00042857	0.04899524
z before collision	-0.00202171	0.02980095
x after collision	0.00088800	0.01226500
y after collision	0.00110700	0.04562000
z after collision	0.00039600	0.01806000

Table A.7: Relative velocities before and after the collision. The large number of significant figures in this table is simply a reflection of the significant figures output by the calculation program.

Parameter	Value (m s^{-1})
$v_{rel,x}$ before collision	-0.07020717
$v_{rel,y}$ before collision	-0.07474713
$v_{rel,z}$ before collision	0.39287339
v_{rel} before collision	0.40603655
$v_{rel,x}$ after collision	-0.14078139
$v_{rel,y}$ after collision	-0.15235274
$v_{rel,z}$ after collision	0.06013399
v_{rel} after collision	0.21597883

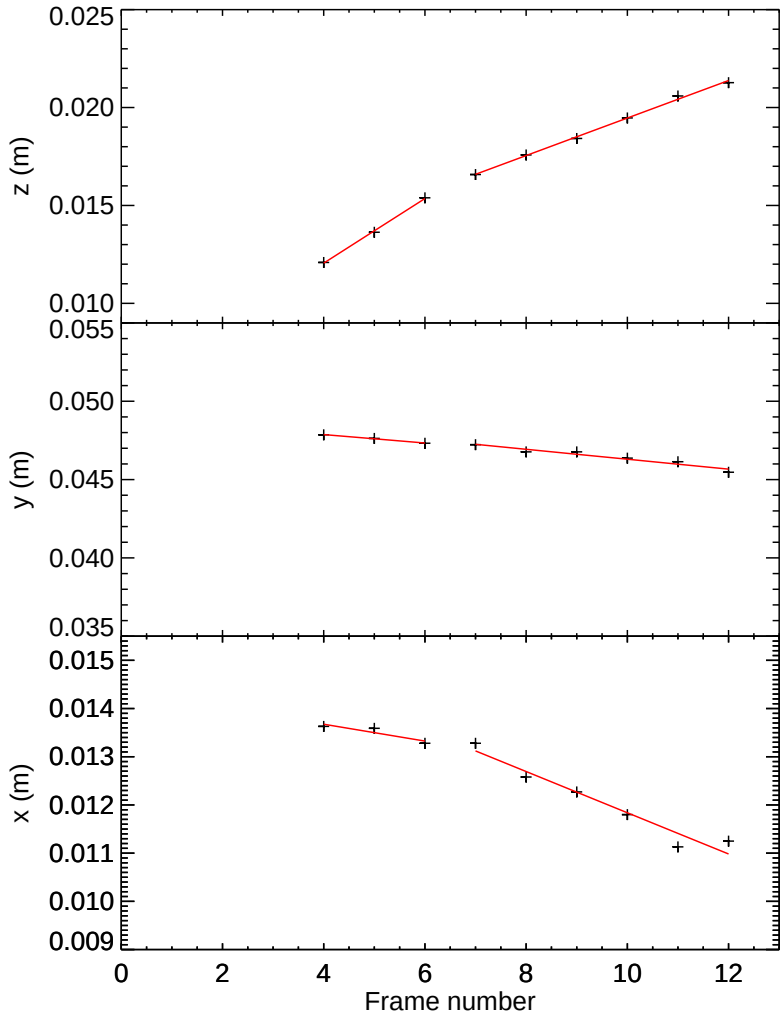

Figure A.3: Linear fits to the x, y and z positions before and after the collision for the top particle.

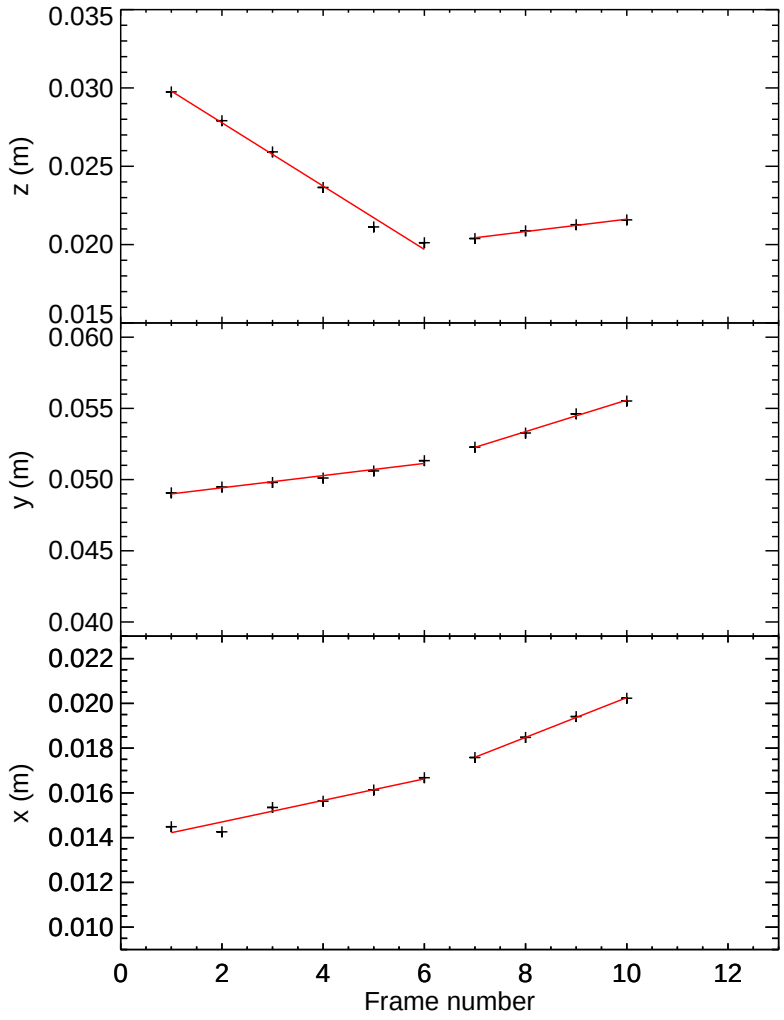

Figure A.4: Linear fits to the x, y and z positions before and after the collision for the bottom particle.

A.2 Normalised impact parameter

The first step in calculating b/R is to calculate the positions of the particles at the point of collision. This is done by solving the simultaneous equations of the particle trajectories:

$$i_{col,j} = \frac{m_b c_a - m_a c_b}{m_b - m_a} \tag{A.5}$$

where $i = x, y, z$, $j = 1, 2$ and refers to each particle, $i_{col,j}$ refers to the position of the particle's centre of mass when the collision takes place, m and c are the gradient and intercept of the straight lines respectively and a and b refer to after and before the collision.

The positions of the particles at the time of collision are given in Tables A.8 and A.9.

Table A.8: Position of the top particle at the time of collision. The large number of significant figures in this table is simply a reflection of the significant figures output by the calculation program.

$x_{col,1}$	$y_{col,1}$	$z_{col,1}$
0.01317	0.04599	0.01602

Table A.9: Position of the bottom particle at the time of collision. The large number of significant figures in this table is simply a reflection of the significant figures output by the calculation program.

$x_{col,2}$	$y_{col,2}$	$z_{col,2}$
0.01653	0.05113	0.01998

R is then calculated:

$$R = \sqrt{(x_{col,1} - x_{col,2})^2 + (y_{col,1} - y_{col,2})^2 + (z_{col,1} - z_{col,2})^2} \tag{A.6}$$

The components and overall value of R is shown in Table A.10.

Table A.10: x, y and z components of R and overall value of R. The large number of significant figures in this table is simply a reflection of the significant figures output by the calculation program.

Parameter	Value (m)
R_x	0.00336
R_y	0.00514
R_z	0.00396
R	0.00731

Obtaining b requires the vector projection of R onto $v_{rel,b}$ ($\vec{R}_{v_{rel,b}}$):

$$\vec{R}_{v_{rel,b}} = \frac{\vec{v_{rel,b}}.\vec{R}}{v_{rel,b}^2}\vec{v_{rel,b}} = \frac{v_{b,x}R_x + v_{b,y}R_y + v_{b,z}R_z}{v_{b,x}^2 + v_{b,y}^2 + v_{b,z}^2}(v_{b,x}\vec{x} + v_{b,y}\vec{y} + v_{b,z}\vec{z}) \tag{A.7}$$

Using the values in Tables A.7 and A.10, $\vec{R}_{v_{rel,b}} = 0.0023$. b is then given by:

$$b = \sqrt{R^2 - R_{v_{rel,b}}^2} \tag{A.8}$$

therefore $b = 0.0069$. Hence the normalised impact parameter, b/R is 0.95.

A.3 Normal and tangential coefficients of restitution

The normal and tangential coefficients of restitution ($\varepsilon_\perp$ and $\varepsilon_\parallel$) are calculated from the normal and tangential components of the velocities before and after the collision. The normal component of the relative velocity is calculated by taking a vector projection of v_{rel} onto R ($\vec{v_{relR}}$):

$$v_\perp = \vec{v_{relR}} = \frac{\vec{R}.\vec{v_{rel}}}{R^2}\vec{R} = \frac{R_x v_{rel,x} + R_y v_{rel,y} + R_z v_{rel,z}}{R_x^2 + R_y^2 + R_z^2}(R_x\vec{x} + R_y\vec{y} + R_z\vec{z}) \tag{A.9}$$

Using the values in Tables A.7 and A.10, $v_{\perp,b}$ is 0.13 m s^{-1} and $v_{\perp,a}$ is 0.14 m s^{-1} where a and b refer to after and before the collision respectively. The tangential component is then calculated by trigonometry:

$$v_\parallel = \sqrt{v^2 - v_\perp^2} \tag{A.10}$$

Hence $v_{\parallel,b}$ is 0.39 m s^{-1} and $v_{\parallel,a}$ is 0.16 m s^{-1} where a and b refer to after and before the collision respectively. Using Equation A.4, $\varepsilon_{\perp}$ is then 1.09 and $\varepsilon_{\parallel}$ is 0.42.

A.4 Rotation

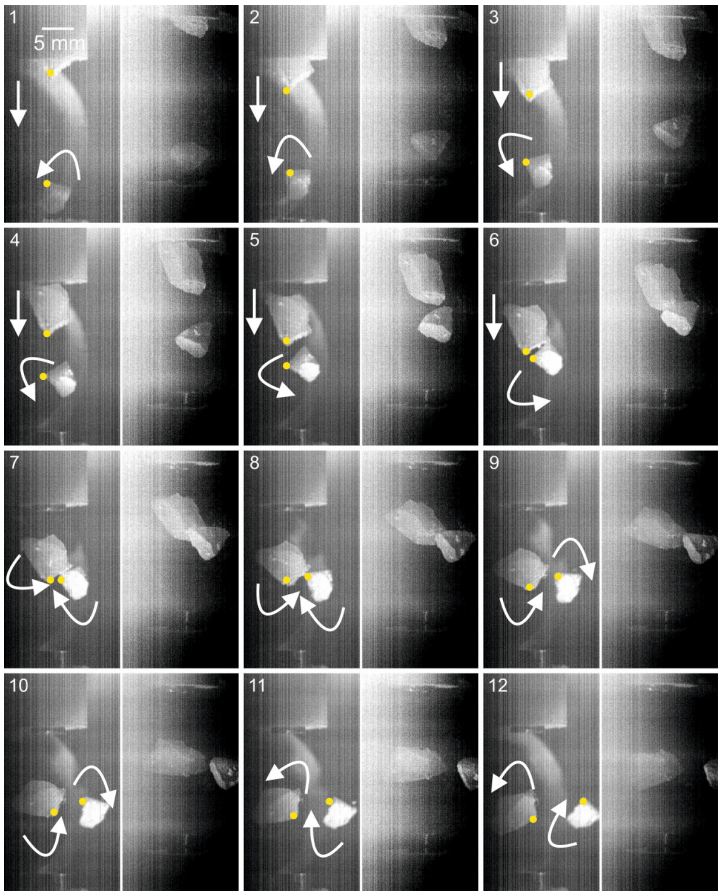

Figure A.5: Image sequence of a collision between 2 ice fragments. Beam splitter optics were used to capture two views of the collision with the view shown on the left separated from the view shown on the right by 60°. The time difference between each successively numbered image is 1/107 s. The apparent offset of the two views is due to the set up of the mirror optics. The points used to track the rotation of the particles are marked by yellow dots.

Fig. A.5 shows a particle-particle collision between 2 ice fragments. The images contain two views of the collision with the view on the left separated from the view on the right by 60°. The collision occurs between frames 6 and 7. Arrows indicate the direction of rotation of the particles. Before the collision, the bottom particle rotates but the top particle does not. After the collision, both particles rotate. The degree of

rotation (estimated to the nearest 30° from the image sequence) is given in Table A.11. Clockwise rotation is defined as positive.

Table A.11: Degree of rotation of the particles from the first given frame to the last given frame. Clockwise rotation is defined as positive.

Particle	Rotation (°)	Frames
Top before	0	1-6
Bottom before	-60	3-6
Top after	-90	7-11
Bottom after	30	7-9

These values give the angular velocities shown in Table A.12.

Table A.12: Angular velocities of the particles before and after collision. Clockwise rotation is defined as positive.

Particle	Angular velocity (rad s^{-1})
Top before	0
Bottom before	-28.0
Top after	-33.6
Bottom after	18.7

The relative angular velocities are shown with the relative velocities in Table A.13.

Table A.13: Relative velocities and relative angular velocities before and after the collision.

Time period	Relative velocity (m s^{-1})	Relative angular velocity (rad s^{-1})
Before collision	0.41	28.0
After collision	0.22	-52.3

The fraction of the total kinetic energy before the collision ($E_{tot,b}$) (translational and rotational) that is transferred into translational kinetic energy after the collision ($E_{trans,a}$) is:

$$\frac{E_{trans,a}}{E_{tot,b}} = \frac{v_{rel,a}^2}{v_{rel,b}^2 + r^2\omega_{rel,b}^2} \tag{A.11}$$

where a and b denote after and before the collision respectively. The fraction that is converted into rotational energy after the collision ($E_{rot,a}$) is:

$$\frac{E_{rot,a}}{E_{tot,b}} = \frac{r^2\omega_a^2}{v_b^2 + r^2\omega_b^2} \tag{A.12}$$

The fraction of energy unaccounted (E_{unacc}) for is:

$$\frac{E_{unacc}}{E_{tot,b}} = 1 - \frac{E_{trans,a} + E_{rot,a}}{E_{tot,b}} \tag{A.13}$$

Using the values in Table A.12, $\frac{E_{trans,a}}{E_{tot,b}} = 27\%$, $\frac{E_{rot,a}}{E_{tot,b}} = 1.7\%$ and $\frac{E_{unacc}}{E_{tot,b}} = 72\%$.

A.5 Uncertainty analysis

The equations for calculating uncertainties on the particle relative velocities and coefficients of restitution are derived in Chapter 3. Only the final equations are given here.

The squared uncertainty on the particle position is given by:

$$\sigma_i^2 = t^2\sigma_m^2 + \sigma_c^2 + e_p \tag{A.14}$$

where $i = x, y, z$, t is time in seconds, m and c are the gradient and intercept of the particle trajectory and e_p is the uncertainty on estimating the particle centre of mass. Here, e_p is estimated to be 5 pixels. The uncertainties on the particle positions are given in Tables A.14 and A.15.

Table A.14: Uncertainties on the particle position for the top particle. a and b refer to after and before the collision respectively. The large number of significant figures in this table is simply a reflection of the significant figures output by the calculation program.

Uncertainty	Value (m)
$\sigma_{x,b}$	0.00019677
$\sigma_{y,b}$	0.00019574
$\sigma_{z,b}$	0.00019650
$\sigma_{x,a}$	0.00019774
$\sigma_{y,a}$	0.00019724
$\sigma_{z,a}$	0.00019655

Table A.15: Uncertainties on the particle position for the bottom particle. a and b refer to after and before the collision respectively. The large number of significant figures in this table is simply a reflection of the significant figures output by the calculation program.

Uncertainty	Value (m)
$\sigma_{x,b}$	0.00019837
$\sigma_{y,b}$	0.00019696
$\sigma_{z,b}$	0.00019956
$\sigma_{x,a}$	0.00019576
$\sigma_{y,a}$	0.00019697
$\sigma_{z,a}$	0.00019611

The squared uncertainty on each velocity component ($\sigma_{v_i}^2$) is:

$$\sigma_{v_i}^2 = \frac{\sigma_i^2}{t^2} \tag{A.15}$$

Using the values in Tables A.14 and A.15, the uncertainties on each velocity components can be calculated according to Equation A.15. These are given in Tables A.16 and A.17.

Table A.16: Uncertainties on the velocity components for the top particle. a and b refer to after and before the collision respectively. The large number of significant figures in this table is simply a reflection of the significant figures output by the calculation program.

Uncertainty	Value (m s^{-1})
$\sigma_{v_{x,b}}$	0.01052716
$\sigma_{v_{y,b}}$	0.01047231
$\sigma_{v_{z,b}}$	0.01051273
$\sigma_{v_{x,a}}$	0.00423174
$\sigma_{v_{y,a}}$	0.00422087
$\sigma_{v_{z,a}}$	0.00420612

Uncertainties on the components of relative velocity are given by:

$$v_{i,rel} = v_{i1} - v_{i2} \tag{A.16}$$

where $i = x, y, z$ and 1 and 2 refer to each particle. The uncertainties on the relative velocity components are given in Table A.18.

Table A.17: Uncertainties on the velocity components for the bottom particle. a and b refer to after and before the collision respectively. The large number of significant figures in this table is simply a reflection of the significant figures output by the calculation program.

Uncertainty	Value (m s^{-1})
$\sigma_{v_{x,b}}$	0.00424515
$\sigma_{v_{y,b}}$	0.00421503
$\sigma_{v_{z,b}}$	0.00427052
$\sigma_{v_{x,a}}$	0.00418932
$\sigma_{v_{y,a}}$	0.00421510
$\sigma_{v_{z,a}}$	0.00419679

Table A.18: Uncertainties on the relative velocity components. a and b refer to after and before the collision respectively. The large number of significant figures in this table is simply a reflection of the significant figures output by the calculation program.

Uncertainty	Value (m s^{-1})
$\sigma_{v_{rel,x,b}}$	0.01135087
$\sigma_{v_{rel,y,b}}$	0.01128874
$\sigma_{v_{rel,z,b}}$	0.01134702
$\sigma_{v_{rel,x,a}}$	0.00595466
$\sigma_{v_{rel,y,a}}$	0.00596513
$\sigma_{v_{rel,z,a}}$	0.00594175

The uncertainty on the overall relative velocity is given by:

$$\sigma^2_{v_{rel}} = \frac{v^2_{rel,x}\sigma^2_{v_{rel,x}} + v^2_{rel,y}\sigma^2_{v_{rel,y}} + v^2_{rel,z}\sigma^2_{v_{rel,z}}}{v^2_{rel,x} + v^2_{rel,y} + v^2_{rel,z}} \tag{A.17}$$

Using the values in Table A.18, the uncertainty on the relative velocity before the collision is 0.011 m s^{-1} and the uncertainty on the relative velocity after the collision is 0.006 m s^{-1}.

The uncertainty on the coefficient of restitution is given by:

$$\sigma^2_{\varepsilon} = \frac{\sigma^2_{v_{rel,a}}}{v^2_{rel,b}} + \frac{v^2_{rel,a}\sigma^2_{v_{rel,b}}}{v^4_{rel,b}} \tag{A.18}$$

Therefore the uncertainty on the coefficient of restitution is 0.02.

Appendix B

Python and IDL programs for neutron scattering data analysis

This appendix contains the Python and IDL programs discussed in Chapter 7 that were used to reduce and analyse the neutron scattering data presented in Chapters 8 and 9.

B.1 Running Gudrun

The programs in this section are those described in Section 7.2.4 of Chapter 7. run_gudrun_single.py reduces sample files singly using Gudrun and run_gudrun_average.py averages sample files using Gudrun.

B.1.1 Single sample files: run_gudrun_single.py

```
#This script runs Gudrun for a number of specified files in
    the filenames.txt file.
#The thickness is changed each time until the DCS level is +/-
     0.3% of expected level.
#This script processes single files.
#It was made to run on a gudrun_dcs.dat file created by "
    tristans version with low q.txt" (to be tested on other
    versions.
#Before starting:
#    1) Create the gudrun_dcs.dat file from the Gudrun gui.
#    2) Make sure that gudrun_dcs.dat is in the bin directory
    of Gudrun (along with gudrun_dcs.exe).
#    3) Create the filenames.txt file with all the files and
    densities (separated by a tab) you want to process.
    Densities must be to 2 decimal places.
#    4) Set directory to the Gudrun bin directory.
#    5) Set file_start and density to the file and density
    currently in gudrun_dcs.dat.
#Files will be outputted in the bin directory.
#If Gudrun fails to run, the script will continue on the next
    file.
#If Gudrun fails to run on all files, check gudrun_dcs.dat as
    it may not be set up correctly.

import subprocess
import os
import time

#Starting parameters.
```

```
directory="/Users/crh236/Documents/Gudrun 2014/bin"
file_start='NIMROD00030675.raw'
density='0.87'

#Navigate to Gudrun folder.
os.chdir(directory)

#Get list of files to process.
f=open('filenames1.txt', 'r')
filename=f.readlines()
f.close()



#Start file loop.
print("Starting at "+time.asctime( time.localtime(time.time())
    )+".\n")

for file in filename:
    #Read gudrun dat file.
    f=open('gudrun_dcs.dat', 'r')
    stuff = f.read()
    f.close()

    #Change file name.
    stuff1=stuff.replace(file_start,file[0:18])

    #Change density.
    stuff1=stuff1.replace(density, file[19:23])

    density=file[19:23]
```

```
f=open('gudrun_dcs.dat', 'w')
f.write(stuff1)
f.close()



#Get thickness.
a=stuff.find('Force calculation of sample corrections?')

t_start=a+219
t_end=t_start+14

thickness = stuff[t_start:t_end]
#thickness = float(thickness)
dcs_ch = 0.005

print("Running for file "+file[0:18]+".")

#Start Gudrun loop.
while abs(dcs_ch) > 0.003:

    print("Thickness = "+thickness+"\n")

    #Write dat file
    f=open('gudrun_dcs.dat', 'w')
    f.write(stuff1)
    f.close()

    #Run Gudrun
```

```
print("Starting Gudrun at "+ time.asctime( time.
    localtime(time.time()) )+".")

cmd = "gudrun_dcs.exe"
process=subprocess.Popen(cmd,  creationflags=0
    x08000000)
process.wait()

print("Finished Gudrun at "+ time.asctime( time.
    localtime(time.time()) )+".")

#Check if gud file exists
test=os.path.isfile(directory+"/"+file[0:14]+".gud")
if test==False:
    break

#Read gud file
f=open(file[0:14]+'.gud', 'r')
stuff = f.readlines()
f.close()

#Reads dcs level.
dcs_line=stuff[51]
if dcs_line[1:8]=='WARNING':
    number=dcs_line[29:34]
    sign=dcs_line[36:41]
    print(dcs_line[1:])
    if sign == 'ABOVE':
        dcs=float(number)
        dcs_ch=dcs*0.01
```

```
            else:
                dcs=float(number)*-1.0
                dcs_ch=dcs*0.01

        else:
            dcs_line=dcs_line.rstrip('\n')
            print(dcs_line[1:]+".\n")
            dcs=float(dcs_line[20:25])
            dcs_ch=(dcs-100.0)*0.01

        if dcs_ch <= -1.0:
            break

        #Changes thickness.
        thickness1=thickness

        thickness=float(thickness)+dcs_ch*float(thickness)
        thickness=str(thickness)
        thickness=thickness[0:14]

        stuff1=stuff1.replace(thickness1,thickness)

    if test==True and dcs_ch > -1.0:
        print("Satisfactory DCS level achieved.\n")
    elif test==False:
        print("File error for "+file[0:18]+".\n")
    else:
        print("Satisfactory DCS level will not be achieved.\n"
            )
```

```
    if test==True:
        f=open(file[0:14]+'_thickness.txt', 'w')
        f.write(thickness1)
        f.close()

    file_start=file[0:18]

print("All files completed.\n")
print("Finished at "+time.asctime( time.localtime(time.time()))
    )+".\n")
```

B.1.2 Averaged sample files: run_gudrun_average.py

```
#This script runs Gudrun for a number of specified files in
    the filenames.txt file.
#The thickness is changed each time until the DCS level is +/-
     0.3% of expected level.
#This script processes averaged files.
#It was made to run on a gudrun_dcs.dat file created by "
    tristans version with low q.txt" (to be tested on other
    versions.
#Before starting:
#    1) Create the gudrun_dcs.dat file from the Gudrun gui.
#    2) Make sure that gudrun_dcs.dat is in the bin directory
    of Gudrun (along with gudrun_dcs.exe).
#    3) Create the filenames.txt file with the number of files
    to be averaged, density and list of files (separated by a
    tab) you want to process. Densities must be to 2 decimal
    places.
#    4) Set directory to the Gudrun bin directory.
#    5) Set file_start and density to the file and density
    currently in gudrun_dcs.dat.
#Files will be outputted in the bin directory.
#If Gudrun fails to run, the script will continue on the next
    file.
#If Gudrun fails to run on all files, check gudrun_dcs.dat as
    it may not be set up correctly.
#Number of files must be a two digit number, both in the input
     file and in gudrun_dcs.dat i.e. 04 not 4.

import subprocess
import os
```

```
import time

#Starting parameters.
directory="/Users/crh236/Documents/Gudrun 2014/bin"
file_start='NIMROD00030468.raw          SAMPLE Ice data files\
   nNIMROD00030469.raw          SAMPLE Ice data files\
   nNIMROD00030470.raw          SAMPLE Ice data files\
   nNIMROD00030471.raw          SAMPLE Ice data files\n'
density='0.59'

#Navigate to Gudrun folder.
os.chdir(directory)

#Get list of files to process.
f=open('filenames.txt', 'r')
filename=f.readlines()
f.close()


#Start file loop.
print("Starting at "+time.asctime( time.localtime(time.time())
    )+".\n")

for file in filename:
    #Get number of files to be averaged.
    fn=(file[0:2])

    #Create file list for Gudrun.
    sample_string=file[8:26]+"          SAMPLE Ice data files\
       n"
```

```
for a in range(1, int(fn)):
        sample_string=sample_string+file[8+19*a:26+19*a]+"
                    SAMPLE Ice data files\n"


#Read gudrun dat file.
f=open('gudrun_dcs.dat', 'r')
stuff = f.read()
f.close()

#Change file name.
stuff1=stuff.replace(file_start ,sample_string)

#Change density.
stuff1=stuff1.replace(density, file[3:7])

density=file[3:7]

#Change number of files.
a=stuff1.find('SAMPLE Ice          {')
stuff1=stuff1[:a+23]+fn+stuff1[a+25:]

#Write new gudrun dat file.
f=open('gudrun_dcs.dat', 'w')
f.write(stuff1)
f.close()

#Change starting file.
file_start=sample_string
```

```
#Get thickness.
a=stuff.find('Force calculation of sample corrections?')

t_start=a+219
t_end=t_start+14

thickness = stuff[t_start:t_end]
#thickness = float(thickness)
dcs_ch = 0.005

print("Running for file "+file[8:26]+" + "+fn+".")

#Start Gudrun loop.
while abs(dcs_ch) > 0.003:

    print("Thickness = "+thickness+"\n")


    #Write dat file
    f=open('gudrun_dcs.dat', 'w')
    f.write(stuff1)
    f.close()

    #Run Gudrun
    print("Starting Gudrun at "+ time.asctime( time.
        localtime(time.time()) )+".")

    cmd = "gudrun_dcs.exe"
    process=subprocess.Popen(cmd, creationflags=0
        x08000000)
```

```
process.wait()

print("Finished Gudrun at "+ time.asctime( time.
    localtime(time.time()) )+".")

#Check if gud file exists
test=os.path.isfile(directory+"/"+file[8:22]+".gud")
if test==False:
    break

#Read gud file
f=open(file[8:22]+'.gud', 'r')
stuff = f.readlines()
f.close()

#Reads dcs level.
dcs_line=stuff[51]
if dcs_line[1:8]=='WARNING':
    number=dcs_line[29:34]
    sign=dcs_line[36:41]
    print(dcs_line[1:])
    if sign == 'ABOVE':
        dcs=float(number)
        dcs_ch=dcs*0.01
    else:
        dcs=float(number)*-1.0
        dcs_ch=dcs*0.01

else:
    dcs_line=dcs_line.rstrip('\n')
```

```
            print(dcs_line[1:]+".\n")
            dcs=float(dcs_line[20:25])
            dcs_ch=(dcs-100.0)*0.01

        if dcs_ch <= -1.0:
            break

        #Changes thickness.
        thickness1=thickness

        thickness=float(thickness)+dcs_ch*float(thickness)
        thickness=str(thickness)
        thickness=thickness[0:14]

        stuff1=stuff1.replace(thickness1,thickness)

    if test==True and dcs_ch > -1.0:
        print("Satisfactory DCS level achieved.\n")
    elif test==False:
        print("File error for "+file[8:26]+".\n")
    else:
        print("Satisfactory DCS level will not be achieved.\n"
            )

    if test==True:
        f=open(file[8:22]+'_thickness.txt', 'w')
        f.write(thickness1)
        f.close()

    file_start=sample_string
```

```
print("All files completed.\n")
print("Finished at "+time.asctime( time.localtime(time.time())
    )+".\n")
```

B.2 Extracting parameters relating to porosity

The programs in this section extract parameters relating to porosity as detailed in Section 7.3 of Chapter 7. porod_constant.py extracts the Porod constant from the quasi-plateau in a $I(Q)*Q^4$ plot and uses it to calculate the specific surface area as detailed in Section 7.3.1 of Chapter 7. periodic_spacings.py extracts the periodic spacings of the pores from pseudopeaks as detailed in Section 7.3.2 of Chapter 7. gp_fits.pro performs a Guinier-Porod fit to the "hump" relating to the pores to extract the radius of gyration, s parameter relating to pore shape and d parameter relating to pore surface roughness as detailed in Section 7.3.3 of Chapter 7.

B.3 Specific surface area: porod_constant.py

```
#porod_constant.py

import os
import glob
import numpy
import matplotlib.pyplot as plt

#Navigate to correct directory.
directory="/Users/crh236/Documents/ISIS August 2014/Data/
    Averaged/2nd ice (good)/Isothermal"
os.chdir(directory)

f=open('code.txt', 'r')
code=f.read()
f.close()

code=code.rstrip('\n')

#Get files and labels.
result=glob.glob('*.mdcs01')
n=len(result)
sliceObj=slice(9,14)
label=[]
for i in range(n):
    label.append(result[i][sliceObj])

label2=code[0]
label3=code[1:4]
label4=code[0:2]
```

```
label5=code[2:4]
if len(code) == 5:
    label6 = code[4]


if label2=='i':
    x='Time = '
    y= ' s'
    x1='Time (minutes)'
    z='Isothermal at '+label3+' K'

if label2=='h':
    x='Temperature = '
    y=' K'
    x1='Temperature (K)'
    z='Heating to '+label3+' K'

if label4=='hi':
    z='Heating ('+label5+' K deposition)'

if len(code) == 5:
    if label6 == 'g':
        z= 'Heating ('+label5+' K deposition, good ice)'
    if label6 == 'b':
        z= 'Heating ('+label5+' K deposition, bad ice)'

#Get temperature/time file.
result2=glob.glob('t*txt')
f=open(result2[0], 'r')
t=f.readlines()
```

```
f.close()

t=[line.rstrip('\n') for line in t]

#Get density file.
density=numpy.loadtxt('density.txt')

#Create list of legend labels.
legend_label = []
for line in t:
    legend_label.append(x+line+y)

#Convert t to float.
#t=[float(line) for line in t]
t=numpy.array(t)

#Change time to minutes.
if label2=='i':
    t=t/60.0

#Create arrays for Porod constant and error.
K=numpy.zeros(n)
K_err=numpy.zeros(n)

#Do for all files in directory.
for i in range(n):
    #Get values and select part.
    q,intensity,yerr=numpy.loadtxt(result[i], unpack=True)
    r = numpy.where((q >= 0.07) & (q <= 0.4))
    m = numpy.size(r)
```

```
#Convert DCS to I(Q).
y = (intensity*density[i]*3.01E22*1.0E-24*3.0)*(q
    *10.0**(8))**4
yerr = (yerr*intensity*density[i]*3.01E22*3.0)

#Slice arrays.
q = q[r]
y = y[r]
yerr = yerr[r]

#Compute rate of change.
p = numpy.size(y)
roc = numpy.zeros(p)

for j in range(p):
    roc[j] = y[j] - y[j-1]
    if roc[j] < 0.0:
        roc[j]=roc[j]*(-1.0)

numpy.savetxt('roc_'+label[i]+'.txt', roc, fmt='%1.4e',
    newline=os.linesep)

a = numpy.amin(roc)
b = numpy.argmin(roc)

#Select linear region.
c = numpy.where(roc <= 0.2E28)
```

```
    e = numpy.size(c)
    d = numpy.zeros(e)
    d = d.astype(int)
    for j in range(e-1):
        d[j] = c[0][j] - c[0][j-1]
    f = numpy.where(d != 1)
    f = numpy.asarray(f)
    f = numpy.append(f, e-1)
    g = numpy.size(f)


    #1 linear region.
    if g == 2:
        K[i] = (y[c[0][f[1]-1]]-y[c[0][f[0]]+1])/2.0+y[c[0][f
            [0]]+1]
        K_err[i] = (y[c[0][f[1]]-1]-y[c[0][f[0]]+1])/2.0

    #2 linear regions.
    if g == 3:
        u = f[1]-f[0]
        v = f[2]-f[1]

        if v > u:
            K[i] = (y[c[0][f[2]-1]]-y[c[0][f[1]]+1])/2.0+y[c
                [0][f[1]]+1]
            K_err[i] = (y[c[0][f[2]-1]]-y[c[0][f[1]]+1])/2.0


        if u > v:
```

```
            K[i] = (y[c[0][f[1]-1]]-y[c[0][f[0]]+1])/2.0+y[c
                [0][f[0]]+1]
            K_err[i] = (y[c[0][f[1]-1]]-y[c[0][f[0]]-1])/2.0


    #3 linear regions.
    if g == 4:
        l = f[1]-f[0]
        u = f[2]-f[1]
        v = f[3]-f[2]
        arr1 = numpy.array([l, u, v])
        sub = numpy.argmax(arr1)
        K[i] = (y[c[0][f[sub+1]-1]]-y[c[0][f[sub]]+1])/2.0+y[c
            [0][f[sub]]+1]
        K_err[i] = (y[c[0][f[sub+1]-1]]-y[c[0][f[sub]]+1])/2.0

    #4 linear regions.
    if g == 5:
        l = f[1]-f[0]
        u = f[2]-f[1]
        v = f[3]-f[2]
        w = f[4]-f[3]
        arr1 = numpy.array([l, u, v, w])
        sub = numpy.argmax(arr1)
        K[i] = (y[c[0][f[sub+1]-1]]-y[c[0][f[sub]]+1])/2.0+y[c
            [0][f[sub]]+1]
        K_err[i] = (y[c[0][f[sub+1]-1]]-y[c[0][f[sub]]+1])/2.0

    #5 Linear regions.
    if g == 6:
```

```
        l = f[1]-f[0]
        u = f[2]-f[1]
        v = f[3]-f[2]
        w = f[4]-f[3]
        x = f[5] - f[4]
        arr1 = numpy.array([l, u, v, w])
        sub = numpy.argmax(arr1)
        K[i] = (y[c[0][f[sub+1]-1]]-y[c[0][f[sub]]+1])/2.0+y[c
            [0][f[sub]]+1]
        K_err[i] = (y[c[0][f[sub+1]-1]]-y[c[0][f[sub]]+1])/2.0

    if g > 6:
        print('More than 5 linear regions for '+label[i])

    K_line =numpy.zeros(m)+ K[i]

    #Plot roc.
    plt.errorbar(q, roc, yerr=yerr)
    plt.plot(q[b], roc[b], 'ro')
    plt.axis([0.07,0.4,0.0,1.0E28])
    plt.savefig(label[i]+'_roc.png')
    plt.close()

    #Plot Porod constant.
    plt.plot(q, y, 'k')
    plt.plot(q, K_line, 'k-')
    plt.plot(q, K_line+K_err[i],'k--')
    plt.plot(q, K_line-K_err[i], 'k--')
    plt.savefig(label[i]+'_Porod_constant.png')
    plt.close()
```

```
#Save Porod constant values.
numpy.savetxt('Porod_constant_'+code+'.txt', numpy.transpose([
    K, K_err]), fmt=['%1.4e','%1.4e'], newline=os.linesep)


#Plot all Porod constants.
colormap = plt.cm.gist_ncar
plt.gca().set_color_cycle([colormap(i) for i in numpy.linspace
    (0, 0.9, n)])
for i in range (n):
    #Get values and select part.
    q,intensity ,yerr=numpy.loadtxt(result[i], unpack=True)
    r = numpy.where((q >= 0.07) & (q <= 0.4))
    m = numpy.size(r)

    #Convert DCS to I(Q).
    y = (intensity*density[i]*3.01E22*1.0E-24*3.0)*(q
        *10.0**(8))**4
    yerr = (yerr*intensity*density[i]*3.01E22*3.0)

    #Slice arrays.
    q = q[r]
    y = y[r]
    yerr = yerr[r]

    #Compute K_line.
    K_line=numpy.zeros(2)+K[i]

    plt.plot(q, y, label=legend_label[i])
```

```
plt.gca().set_color_cycle([colormap(i) for i in numpy.linspace
    (0, 0.9, n)])
for i in range (n):
    #Compute K_line.
    K_line=numpy.zeros(2)+K[i]

    plt.plot([0.07,0.4],K_line, '--')

plt.title(z)
plt.xlabel('Q ($\AA^{-1}$)')
plt.ylabel('I(Q)*Q$^4$')
plt.legend(loc='upper left', fontsize='xx-small')
plt.savefig(code+'Porod_constant.eps')

plt.close()

#Compute SSA.
SSA = K/(2.0*numpy.pi*(5.414E10)**2.0)/10000.0
SSA_err = K_err/(2.0*numpy.pi*(5.414E10)**2.0)/10000.0

#Save SSA to file.
numpy.savetxt('SSA_'+code+'.txt', numpy.transpose([SSA,
    SSA_err]), fmt=['%12.8f','%12.8f'], newline=os.linesep)

#Plot SSA.
plt.errorbar(t, SSA, yerr=SSA_err)
plt.axis([10.0,190.0,0.0,360.0])
plt.title(z)
```

```
plt.xlabel(x1)
plt.ylabel('Specific surface area (m$^2$ cm$^{-3}$)')
plt.savefig(code+'_SSA.eps')
plt.savefig(code+'_SSA.png')
plt.close()
```

B.4 Periodic spacings: periodic_spacings.py

```
#periodic_spacings.py

import os
import glob
import numpy
import matplotlib.pyplot as plt

#Navigate to correct directory.
directory="/Users/crh236/Documents/ISIS August 2014/Data/
    Averaged/2nd ice (good)/Isothermal"
os.chdir(directory)

f=open('code.txt', 'r')
code=f.read()
f.close()

code=code.rstrip('\n')

#Get files and labels.
result=glob.glob('*.mdcs01')
n=len(result)
sliceObj=slice(9,14)
label=[]
for i in range(n):
    label.append(result[i][sliceObj])

label2=code[0]
label3=code[1:4]
label4=code[0:2]
```

```
label5=code[2:4]
if len(code) == 5:
    label6 = code[4]


if label2=='i':
    x='Time = '
    y= ' s'
    x1='Time (minutes)'
    z='Isothermal at '+label3+' K'

if label2=='h':
    x='Temperature = '
    y=' K'
    x1='Temperature (K)'
    z='Heating to '+label3+' K'

if label4=='hi':
    z='Heating ('+label5+' K deposition)'

if len(code) == 5:
    if label6 == 'g':
        z= 'Heating ('+label5+' K deposition, good ice)'
    if label6 == 'b':
        z= 'Heating ('+label5+' K deposition, bad ice)'

#Get temperature/time file.
result2=glob.glob('t*txt')
f=open(result2[0], 'r')
t=f.readlines()
```

```
f.close()

t=[line.rstrip('\n') for line in t]

#Get density file.
density=numpy.loadtxt('density.txt')

#Create list of legend labels.
legend_label = []
for line in t:
    legend_label.append(x+line+y)

#Convert t to float.
#t=[float(line) for line in t]
t=numpy.array(t)

#Change time to minutes.
if label2=='i':
    t=t/60.0

#Create arrays.
peak1 = numpy.zeros(n)
peak2 = numpy.zeros(n)

peak1_err = numpy.zeros(n)
peak2_err = numpy.zeros(n)

intensity1 = numpy.zeros(n)
intensity2 = numpy.zeros(n)
```

```
intensity1_err = numpy.zeros(n)
intensity2_err = numpy.zeros(n)

d = numpy.array([2.5,3.0])
dn = numpy.size(d)

#Do for all files in directory.
for i in range(n):
    #Get values and select part.
    q,y,yerr=numpy.loadtxt(result[i], unpack=True)
    r = numpy.where((q >= 0.02) & (q <= 0.15))
    m = numpy.size(r)

    ###d=2.5

    #Convert DCS to I(Q).
    y1 = (y*density[i]*3.01E22*1.0E-24*3.0)*(q*10.0**(8))**2.5
    yerr = (yerr*y*density[i]*3.01E22*3.0)

    #Slice arrays.
    q = q[r]
    y = y[r]
    y1 = y1[r]
    yerr = yerr[r]

    #Compute rate of change.
    p = numpy.size(y)
    roc = numpy.zeros(p)

    for j in range(p):
```

```
        roc[j] = y1[j] - y1[j-1]

    numpy.savetxt('roc_pseudo_2.5'+label[i]+'.txt', roc, fmt='
        %1.4e', newline=os.linesep)

    #Find pseudopeak position.
    a = numpy.where(roc <= 0.0)
    a = a[0]
    p = numpy.size(a)
    roc_a = numpy.zeros(p)
    roc_a = roc_a.astype(int)

    for j in range(p):
        roc_a[j] = a[j] - a[j-1]

    b = numpy.where(roc_a != 1)
    b = b[0]
    peak_sub = a[b[numpy.size(b)-1]]-1

    #Put pseudopeak positions in arrays.
    peak1[i] = q[peak_sub]
    peak1_err[i] = (q[peak_sub +1] - q[peak_sub -1])/2.0
    intensity1[i] = y[peak_sub]
    intensity1_err[i] = (y[peak_sub +1] - y[peak_sub -1])/2.0

    #Plot pseudopeak.
    plt.plot(q, y1, 'k')
    plt.errorbar(q[peak_sub], y1[peak_sub], yerr=peak1_err[i],
        fmt='ro')
    plt.savefig(label[i]+'_pseudopeak_2.5.png')
```

```
plt.close()


###d=3


#Convert DCS to I(Q).
y1 = (y*density[i]*3.01E22*1.0E-24*3.0)*(q*10.0**(8))**3.0
yerr = (yerr*y*density[i]*3.01E22*3.0)


##Slice arrays.
#q = q[r]
#y = y[r]
#y1 = y1[r]
#yerr = yerr[r]


#Compute rate of change.
p = numpy.size(y)
roc = numpy.zeros(p)


for j in range(p):
    roc[j] = y1[j] - y1[j-1]


numpy.savetxt('roc_pseudo_3'+label[i]+'.txt', roc, fmt='
   %1.4e', newline=os.linesep)


#Find pseudopeak position.
a = numpy.where(roc <= 0.0)
a = a[0]
p = numpy.size(a)
roc_a = numpy.zeros(p)
roc_a = roc_a.astype(int)
```

```
        for j in range(p):
            roc_a[j] = a[j] - a[j-1]

        b = numpy.where(roc_a != 1)
        b = b[0]
        peak_sub = a[b[numpy.size(b)-1]]-1

        #Put pseudopeak positions in arrays.
        peak2[i] = q[peak_sub]
        peak2_err[i] = (q[peak_sub +1] - q[peak_sub -1])/2.0
        intensity2[i] = y[peak_sub]
        intensity2_err[i] = (y[peak_sub +1] - y[peak_sub -1])/2.0

        #Plot pseudopeak.
        plt.plot(q, y1, 'k')
        plt.errorbar(q[peak_sub], y1[peak_sub], yerr=peak1_err[i],
            fmt='ro')
        plt.savefig(label[i]+'_pseudopeak_3.png')
        plt.close()

#Save pseudopeak values.
numpy.savetxt('pseudopeak_2.5_'+code+'.txt', numpy.transpose([
    peak1, peak1_err]), fmt=['%1.4e','%1.4e'], newline=os.
    linesep)
numpy.savetxt('pseudopeak_3_'+code+'.txt', numpy.transpose([
    peak2, peak2_err]), fmt=['%1.4e','%1.4e'], newline=os.
    linesep)
numpy.savetxt('intensity_2.5_'+code+'.txt', numpy.transpose([
    intensity1, intensity1_err]), fmt=['%1.4e','%1.4e'],
```

```
    newline=os.linesep)
numpy.savetxt('intensity_3_'+code+'.txt', numpy.transpose([
    intensity2, intensity2_err]), fmt=['%1.4e','%1.4e'],
    newline=os.linesep)

#Plot all pseudopeaks.
colormap = plt.cm.gist_ncar
plt.gca().set_color_cycle([colormap(i) for i in numpy.linspace
    (0, 0.9, n)])
for i in range (n):
    #Get values and select part.
    q,intensity,yerr=numpy.loadtxt(result[i], unpack=True)
    r = numpy.where((q >= 0.03) & (q <= 0.15))
    m = numpy.size(r)

    #Convert DCS to I(Q).
    y = (intensity*density[i]*3.01E22*1.0E-24*3.0)*(q
        *10.0**(8))**2.5
    yerr = (yerr*intensity*density[i]*3.01E22*3.0)

    #Slice arrays.
    q = q[r]
    y = y[r]
    yerr = yerr[r]

    plt.plot(q, y, label=legend_label[i])

plt.xlabel('Q ($\AA^{-1}$)')
plt.ylabel('I(Q)*Q$^{2.5}$')
plt.legend(loc='upper right', fontsize='xx-small')
```

```
plt.savefig(code+'_pseudopeak_2.5.eps')
plt.savefig(code+'_pseudopeak_2.5.png')
plt.close()

for i in range (n):
    #Get values and select part.
    q,intensity,yerr=numpy.loadtxt(result[i], unpack=True)
    r = numpy.where((q >= 0.02) & (q <= 0.15))
    m = numpy.size(r)

    #Convert DCS to I(Q).
    y = (intensity*density[i]*3.01E22*1.0E-24*3.0)*(q
        *10.0**(8))**3.0
    yerr = (yerr*intensity*density[i]*3.01E22*3.0)

    #Slice arrays.
    q = q[r]
    y = y[r]
    yerr = yerr[r]

    plt.plot(q, y, label=legend_label[i])

plt.xlabel('Q ($\AA^{-1}$)')
plt.ylabel('I(Q)*Q$^{3.0}$')
plt.legend(loc='upper right', fontsize='xx-small')
plt.savefig(code+'_pseudopeak_3.0.eps')
plt.savefig(code+'_pseudopeak_3.0.png')
plt.close()

#Compute periodic spacings.
```

```
ps1 = (2.0*numpy.pi)/peak1
ps1_err = ((2.0*numpy.pi)/peak1**2.0)*peak1_err
ps2 = (2.0*numpy.pi)/peak2
ps2_err = ((2.0*numpy.pi)/peak2**2.0)*peak2_err

#Save periodic spacings.
numpy.savetxt('ps_2.5_'+code+'.txt', numpy.transpose([ps1,
    ps1_err]), fmt=['%1.4e','%1.4e'], newline=os.linesep)
numpy.savetxt('ps_3_'+code+'.txt', numpy.transpose([ps2,
    ps2_err]), fmt=['%1.4e','%1.4e'], newline=os.linesep)

#Plot periodic spacings
plt.errorbar(t, ps1, yerr=ps1_err, fmt='k+', label='d=2.5')
plt.errorbar(t, ps2, yerr=ps2_err, fmt='r+', label='d=3.0')
plt.xlabel(x1)
plt.ylabel('Periodic spacings ($\AA$)')
plt.title(z)
plt.axis([float(t[0])-10.0, float(t[n-1])+10.0, 0.0,250.0])
plt.legend(loc='upper left', fontsize='small')
plt.savefig(code+'_periodic_spacings_both.eps')
plt.savefig(code+'_periodic_spacings_both.png')
plt.close()
```

B.5 Guinier-Porod fits: gp_fits.pro

```
PRO GP_FIT

;This procedure performs a Guinier Porod fit on the data.
;This procedure calls the guinier_porod1.pro function.
;It requires a 'code.txt' file to be present in the current
    directory.

READCOL, 'code.txt', code, FORMAT='a' ;Gets folder label.
result = FILE_SEARCH('*mdcs01') ;Gets mdcs01 files.
label = STRMID(result, 9, 5) ;Gets data label.
n = N_ELEMENTS(result)
Rg = FLTARR(n)
s = FLTARR(n)
d = FLTARR(n)
G = FLTARR(n)
A_arr = FLTARR(n)

Rgerror = FLTARR(n)
serror = FLTARR(n)
derror = FLTARR(n)
status=FLTARR(n) ;Creates arrays for fit status values.
;status=FLTARR(n) ;Creates arrays for fit status values.
chisq_arr=FLTARR(n)

t_f = FILE_SEARCH('t*txt')
READCOL, t_f, t

;READCOL, 'gp_parameters_av_d050.txt', Ga, sa, Rga, Aa, da
;av = N_ELEMENTS(Ga)
```

```
;j = INDGEN(av)


FOR i = 0, n-1 DO BEGIN

  READCOL, result[i], X, Y, Yerr ;Read in data.
  q = WHERE(X GE 0.05 AND X LE 0.2)
  m = N_ELEMENTS(q)

  A = [0.27, 2.45, 4.5, 0.021, 3.42]

  parinfo = replicate({value:0.D, fixed:0, limited:[0,0], $
                                   limits:[0.D,0]}, 5)

            parinfo(1).limited(0) = 1
            parinfo(1).limited(1) = 1
            parinfo(1).limits(0)  = 0.0
            parinfo(1).limits(1)  = 3.0
            parinfo(2).limited(0) = 1
            parinfo(2).limits(0)  = 0.0
            parinfo(4).limited(0) = 1
            parinfo(4).limited(1) = 1
            parinfo(4).limits(0)  = 3.0
            parinfo(4).limits(1)  = 4.0
            parinfo(*).value = [0.99, 1.66, 7.6, 0.013, 3.45]


  weights = 1.0/Yerr^2.0
```

```
P = MPFITFUN('guinier_porod1', X[q[0]:q[m-1]], Y[q[0]:q[m
    -1]], Yerr[q[0]:q[m-1]], A, PERROR=sigma,  WEIGHTS=
    weights[q[0]:q[m-1]], PARINFO=parinfo, MAXITER=1000,
    STATUS=st, YFIT=yfit, DOF=dof, BESTNORM=bestnorm)

CHISQ = TOTAL( (Y[q[0]:q[m-1]]-GUINIER_POROD1(X[q[0]:q[m
    -1]],P))^2.0 * ABS(WEIGHTS[q[0]:q[m-1]]) )
Q1 = (1.0/P[2])*SQRT((P[4]-P[1])*(3.0-P[1])/2.0)

filename = label[i]+'_GP_fit.txt' ;Prints fit parameters to
    file.
OPENW, ounit, filename, /GET_LUN
PRINTF, ounit, P, SIGMA, chisq, Q1, FORMAT = "(F12.8)"
FREE_LUN, ounit

filename = label[i]+'_GP_yfit.txt' ;Prints yfit values to
    file.
OPENW, ounit, filename, /GET_LUN
PRINTF, ounit, yfit, FORMAT = "(F12.8)"
FREE_LUN, ounit

cgPLOT, X[q[0]:q[m-1]], Y[q[0]:q[m-1]], psym = 1, XRANGE
    =[0.01, 0.21], /XLOG, /YLOG  ;Plots graph of fit.

cgOPLOT, X[q[0]:q[m-1]], yfit, linestyle=1

image = tvrd(true=1)
WRITE_PNG, label[i]+'_GP_fit.png', image ;Prints graph to
    file for 'sanity check'.
```

```
   s[i] = P[1] ;Fills s array.
   Rg[i] = P[2] ;Fills Rg array.
   d[i] = P[4] ;Fills d array.
   G[i] = P[0]
   A_arr[i] = P[3]

   serror[i] = sigma[1] * SQRT(BESTNORM / DOF) ;Fills s error
      array.
   Rgerror[i] = SIGMA[2] * SQRT(BESTNORM / DOF) ;Fills Rg error
       array.
   derror[i] = SIGMA[4] * SQRT(BESTNORM / DOF) ;Fills d error
      array.

   status[i] = st ;Fills status array.
   chisq_arr[i] = chisq

ENDFOR

filename = 's_'+code+'.txt' ;Prints b values to file.
OPENW, ounit, filename, /GET_LUN
FOR i = 0, n-1 DO BEGIN
PRINTF, ounit, t[i], s[i], serror[i], FORMAT = "(3F13.8)"
ENDFOR
FREE_LUN, ounit

filename = 'Rg_'+code+'.txt' ;Prints b values to file.
OPENW, ounit, filename, /GET_LUN
FOR i = 0, n-1 DO BEGIN
PRINTF, ounit, t[i], Rg[i], Rgerror[i], FORMAT = "(3F13.8)"
ENDFOR
```

```
FREE_LUN, ounit

filename = 'd_'+code+'.txt' ;Prints b values to file.
OPENW, ounit, filename, /GET_LUN
FOR i = 0, n-1 DO BEGIN
PRINTF, ounit, t[i], d[i], derror[i], FORMAT = "(3F13.8)"
ENDFOR
FREE_LUN, ounit

filename = 'status_gp_'+code+'.txt' ;Prints status value to
    file.
OPENW, ounit, filename, /GET_LUN
PRINTF, ounit, status, FORMAT = "(F12.8)"
FREE_LUN, ounit

filename = 'chisq_gp_'+code+'.txt' ;Prints status value to
    file.
OPENW, ounit, filename, /GET_LUN
PRINTF, ounit, chisq_arr, FORMAT = "(F12.8)"
FREE_LUN, ounit

filename = 'gp_parameters_'+code+'.txt' ;Prints b values to
    file.
OPENW, ounit, filename, /GET_LUN
FOR i = 0, n-1 DO BEGIN
PRINTF, ounit, G[i],s[i], Rg[i], A_arr[i],d[i], FORMAT = "(5
    F13.8)"
ENDFOR
FREE_LUN, ounit
```

```
END
```

Bibliography

Aikawa, Y., Kamuro, D., Sakon, I., Itoh, Y., Terada, H., Noble, J. A., Pontoppidan, K. M., Fraser, H. J., Tamura, M., Kandori, R., Kawamura, A., & Ueno, M. (2012). Akari observations of ice absorption bands towards edge-on young stellar objects. *Astronomy & Astrophysics*, 538.

Al-Halabi, A., Fraser, H. J., Kroes, G. J., & van Dishoeck, E. F. (2004). Adsorption of co on amorphous water-ice surfaces. *Astronomy & Astrophysics*, 422(3), 777–791.

Angell, C. A. (2004). Amorphous water. *Annual Review of Physical Chemistry*, 55, 559–583.

Aumatell, G. & Wurm, G. (2011). Breaking the ice: planetesimal formation at the snowline. *Monthly Notices of the Royal Astronomical Society*, 418(1).

Ayotte, P., Smith, R. S., Stevenson, K. P., Dohnalek, Z., Kimmel, G. A., & Kay, B. D. (2001). Effect of porosity on the adsorption, desorption, trapping, and release of volatile gases by amorphous solid water. *Journal of Geophysical Research-Planets*, 106(E12), 33387–33392.

Beitz, E., Güttler, C., Blum, J., Meisner, T., Teiser, J., & Wurm, G. (2011). Low-velocity collisions of centimeter-sized dust aggregates. *The Astrophysical Journal*, 736, 34.

Bellissentfunel, M. C., Bosio, L., Hallbrucker, A., Mayer, E., & Sridiborbez, R. (1992). X-ray and neutron-scattering studies of the structure of hyperquenched glassy water. *Journal of Chemical Physics*, 97(2), 1282–1286.

Besson, J. M., Pruzan, P., Klotz, S., Hamel, G., Silvi, B., Nelmes, R. J., Loveday, J. S., Wilson, R. M., & Hull, S. (1994). Variation of interatomic distances in ice-viii to 10 gpa. *Physical Review B*, 49(18), 12540–12550.

Blum, J. (2000). Laboratory experiments on preplanetary dust aggregation. *Space Science Reviews*, 92(1-2), 265–278.

Blum, J. (2010). Dust growth in protoplanetary disks - a comprehensive experimental/theoretical approach. *Research in Astronomy & Astrophysics*, 10(12), 1199–1214.

Blum, J. & Munch, M. (1993). Experimental investigations on aggregate aggregate collisions in the early solar nebula. *Icarus*, 106(1), 151–167.

Blum, J. & Wurm, G. (2000). Experiments on sticking, restructuring, and fragmentation of preplanetary dust aggregates. *Icarus*, 143(1), 138–146.

Blum, J. & Wurm, G. (2001). Drop tower experiments on sticking, restructuring, and fragmentation of preplanetary dust aggregates. *Microgravity Science and Technology*, 13(1), 29–34.

Blum, J. & Wurm, G. (2008). The growth mechanisms of macroscopic bodies in protoplanetary disks. *Annual Review of Astronomy & Astrophysics*, 46, 21–56.

Blum, J., Wurm, G., Kempf, S., Poppe, T., Klahr, H., Kozasa, T., Rott, M., Henning, T., Dorschner, J., Schrapler, R., Keller, H. U., Markiewicz, W. J., Mann, I., Gustafson, B. A. S., Giovane, F., Neuhaus, D., Fechtig, H., Grun, E., Feuerbacher, B., Kochan, H., Ratke, L., El Goresy, A., Morfill, G., Weidenschilling, S. J., Schwehm, G., Metzler, K., & Ip, W. H. (2000). Growth and form of planetary seedlings: Results from a microgravity aggregation experiment. *Physical Review Letters*, 85(12), 2426–2429.

Boogert, A. C. A., Pontoppidan, K. M., Knez, C., Lahuis, F., Kessler-Silacci, J., van Dishoeck, E. F., Blake, G. A., Augereau, J. C., Bisschop, S. E., Bottinelli, S., Brooke, T. Y., Brown, J., Crapsi, A., Evans, N. J., Fraser, H. J., Geers, V., Huard, T. L., Jorgensen, J. K., Oberg, K. I., Allen, L. E., Harvey, P. M., Koerner, D. W., Mundy, L. G., Padgett, D. L., Sargent, A. I., & Stapelfeldt, K. R. (2008). The c2d spitzer spectroscopic survey of ices around low-mass young stellar objects. i. h2o and the 5-8 mu m bands. *The Astrophysical Journal*, 678(2), 985–1004.

Bossa, J. B., Isokoski, K., de Valois, M. S., & Linnartz, H. (2012). Thermal collapse of porous interstellar ice. *Astronomy & Astrophysics*, 545.

Bowron, D. T., Soper, A. K., Jones, K., Ansell, S., Birch, S., Norris, J., Perrott, L., Riedel, D., Rhodes, N. J., Wakefield, S. R., Botti, A., Ricci, M. A., Grazzi, F., & Zoppi, M. (2010). Nimrod: The near and intermediate range order diffractometer of the isis second target station. *Review of Scientific Instruments*, 81(3).

Boxe, C. S., Bodsgard, B. R., Smythe, W., & Leu, M. T. (2007). Grain sizes, surface areas, and porosities of vapor-deposited h2o ices used to simulate planetary icy surfaces. *Journal of Colloid and Interface Science*, 309(2), 412–418.

Braga-Ribas, F., Sicardy, B., Ortiz, J. L., Snodgrass, C., Roques, F., Vieira-Martins, R., Camargo, J. I. B., Assafin, M., Duffard, R., Jehin, E., Pollock, J., Leiva, R., Emilio, M., Machado, D. I., Colazo, C., Lellouch, E., Skottfelt, J., Gillon, M., Ligier, N., Maquet, L., Benedetti-Rossi, G., Gomes, A. R., Kervella, P., Monteiro, H., Sfair, R., El Moutamid, M., Tancredi, G., Spagnotto, J., Maury, A., Morales, N., Gil-Hutton, R., Roland, S., Ceretta, A., Gu, S.-H., Wang, X.-B., Harpsøe, K., Rabus, M., Manfroid, J., Opitom, C., Vanzi, L., Mehret, L., Lorenzini, L., Schneiter, E. M., Melia, R., Lecacheux, J., Colas, F., Vachier, F., Widemann, T., Almenares, L., Sandness, R. G., Char, F., Perez, V., Lemos, P., Martinez, N., Jørgensen, U. G., Dominik, M., Roig, F., Reichart, D. E., Lacluyze, A. P., Haislip, J. B., Ivarsen, K. M., Moore, J. P., Frank, N. R., & Lambas, D. G. (2014). A ring system detected around the centaur (10199) chariklo. *Nature*, 508, 72–75.

Bridges, F. G., Hatzes, A., & Lin, D. N. C. (1984). Structure, stability and evolution of saturn's rings. *Nature*, 309(5966), 333–335.

Bridges, F. G., Supulver, K. D., Lin, D. N. C., Knight, R., & Zafra, M. (1996). Energy loss and sticking mechanisms in particle aggregation in planetesimal formation. *Icarus*, 123(2), 422–435.

Brown, D. E., George, S. M., Huang, C., Wong, E. K. L., Rider, K. B., Smith, R. S., & Kay, B. D. (1996). H2o condensation coefficient and refractive index for vapor-deposited ice from molecular beam and optical interference measurements. *Journal of Physical Chemistry*, 100(12), 4988–4995.

Buch, V. & Devlin, J. P. (1991). Spectra of dangling oh bonds in amorphous ice - assignment to 2-coordinated and 3-coordinated surface molecules. *Journal of Chemical Physics*, 94(5), 4091–4092.

Carmona, A., Ancker, M. E. v. d., Henning, T., Pavlyuchenkov, Y., Dullemond, C. P., Goto, M., Thi, W. F., Bouwman, J., & Waters, L. B. F. M. (2008). A search for mid-infrared molecular hydrogen emission from protoplanetary disks. *ASTRONOMY & ASTROPHYSICS*, 477(3), 839–852.

Cazaux, S., Bossa, J. B., Linnartz, H., & Tielens, A. (2015). Pore evolution in interstellar ice analogues simulating the effects of temperature increase. *Astronomy & Astrophysics*, 573.

Chokshi, A., Tielens, A., & Hollenbach, D. (1993). Dust coagulation. *The Astrophysical Journal*, 407(2), 806–819.

Cleeves, L. I., Bergin, E. A., Alexander, C. M. O., Du, F. J., Graninger, D., Oberg, K. I., & Harries, T. J. (2014). The ancient heritage of water ice in the solar system. *Science*, 345(6204), 1590–1593.

Collings, M. P., Dever, J. W., Fraser, H. J., & McCoustra, M. R. S. (2003a). Laboratory studies of the interaction of carbon monoxide with water ice. *Astrophysics and Space Science*, 285(3-4), 633–659.

Collings, M. P., Dever, J. W., Fraser, H. J., McCoustra, M. R. S., & Williams, D. A. (2003b). Carbon monoxide entrapment in interstellar ice analogs. *The Astrophysical Journal*, 583(2), 1058–1062.

Colwell, J. E., Esposito, L. W., & Sremcevic, M. (2006). Self-gravity wakes in saturn's a ring measured by stellar occultations from cassini. *Geophysical Research Letters*, 33(7).

Colwell, J. E., Esposito, L. W., Sremcevic, M., Stewart, G. R., & McClintock, W. E. (2007). Self-gravity wakes and radial structure of saturn's b ring. *Icarus*, 190(1), 127–144.

Colwell, J. E., Nicholson, P. D., Tiscareno, M. S., Murray, C. D., French, R. G., & Marouf, E. A. (2009). *The Structure of Saturn's Rings*, (pp. 375). Springer.

Cuppen, H. M., Ioppolo, S., Romanzin, C., & Linnartz, H. (2010). Water formation at low temperatures by surface o-2 hydrogenation ii: the reaction network. *PHYSICAL CHEMISTRY CHEMICAL PHYSICS*, 12(38), 12077–12088.

Cuzzi, J., Clark, R., Filacchione, G., French, R., Johnson, R., Marouf, E., & Spilker, L. (2009). *Ring Particle Composition and Size Distribution*. Saturn from Cassini-Huygens. Dordrecht: Springer.

Cuzzi, J. N., Burns, J. A., Charnoz, S., Clark, R. N., Colwell, J. E., Dones, L., Esposito, L. W., Filacchione, G., French, R. G., Hedman, M. M., Kempf, S., Marouf, E. A., Murray, C. D., Nicholson, P. D., Porco, C. C., Schmidt, J., Showalter, M. R., Spilker, L. J., Spitale, J. N., Srama, R., Sremčević, M., Tiscareno, M. S., & Weiss, J. (2010). An evolving view of saturn's dynamic rings. *Science*, 327, 1470.

Cuzzi, J. N. & Pollack, J. B. (1978). Saturns rings - particle composition and size distribution as constrained by microwave observations .1. radar observations. *Icarus*, 33(2), 233–262.

Cuzzi, J. N., Pollack, J. B., & Summers, A. L. (1980). Saturn rings - particle composition and size distribution as constrained by observations at microwave wavelengths .2. radio interferometric observations. *Icarus*, 44(3), 683–705.

Delsemme, A. H. (1983). Ice in comets. *Journal of Physical Chemistry*, 87(21), 4214–4218.

Deschamps, F., Mousis, O., Sanchez-Valle, C., & Lunine, J. I. (2010). The role of methanol in the crystallization of titan's primordial ocean. *The Astrophysical Journal*, 724(2), 887–894.

Dohnalek, Z., Kimmel, G. A., Ciolli, R. L., Stevenson, K. P., Smith, R. S., & Kay, B. D. (2000). The effect of the underlying substrate on the crystallization kinetics of dense amorphous solid water films. *Journal of Chemical Physics*, 112(13), 5932–5941.

Duffard, R., Pinilla-Alonso, N., Ortiz, J. L., Alvarez-Candal, A., Sicardy, B., Santos-Sanz, P., Morales, N., Colazo, C., Fernandez-Valenzuela, E., & Braga-Ribas, F. (2014). Photometric and spectroscopic evidence for a dense ring system around centaur chariklo. *Astronomy & Astrophysics*, 568.

Ehrenfreund, P., Fraser, H. J., Blum, J., Cartwright, J. H. E., Garcia-Ruiz, J. M., Hadamcik, E., Levasseur-Regourd, A. C., Price, S., Prodi, F., & Sarkissian, A. (2003). Physics and chemistry of icy particles in the universe: answers from microgravity. *Planetary and Space Science*, 51(7-8), 473–494.

Elliott, S. R. (1995). Interpretation of the principal diffraction peak of liquid and amorphous water. *Journal of Chemical Physics*, 103(7), 2758–2761.

Elsaesser, M. S., Winkel, K., Mayer, E., & Loerting, T. (2010). Reversibility and isotope effect of the calorimetric glass ->liquid transition of low-density amorphous ice. *Physical Chemistry Chemical Physics*, 12(3), 708–712.

Esposito, L. W. (2002). Planetary rings. *Reports on Progress in Physics*, 65(12), 1741–1783.

Fillion, J. H., Dulieu, F., Romanzin, C., & Cazaux, S. (2011). *Gas-surface interactions and heterogeneous chemistry on interstellar grains analogues*, volume 18 of *EPJ Web of Conferences*. EPJ Web of Conferences.

Fisher, M. & Devlin, J. P. (1995). Defect activity in amorphous ice from isotopic exchange data - insight into the glass-transition. *Journal of Physical Chemistry*, 99(29), 11584–11590.

Fraser, H. J., Collings, M. P., & McCoustra, M. R. S. (2002). Laboratory surface astrophysics experiment. *Review of Scientific Instruments*, 73(5), 2161–2170.

Gálvez, O., Maté, B., Herrero, V. J., & Escribano, R. (2008). Trapping and adsorption of co2 in amorphous ice: A ftir study. *Icarus*, 197(2), 599–605.

Garaud, P., Meru, F., Galvagni, M., & Olczak, C. (2013). From dust to planetesimals: An improved model for collisional growth in protoplanetary disks. *The Astrophysical Journal*, 764, 146.

Glatter, O. & Kratky, O. (1982). *Small Angle X-ray Scattering*. Academic Press.

Gundlach, B. & Blum, J. (2015). The stickiness of micrometer-sized water-ice particles. *The Astrophysical Journal*, 798(1).

Gundlach, B., Kilias, S., Beitz, E., & Blum, J. (2011). Micrometer-sized ice particles for planetary-science experiments - i. preparation, critical rolling friction force, and specific surface energy. *Icarus*, 214(2), 717–723.

Güttler, C., Blum, J., Zsom, A., Ormel, C. W., & Dullemond, C. P. (2010). The outcome of protoplanetary dust growth: pebbles, boulders, or planetesimals? i. mapping the zoo of laboratory collision experiments. *Astronomy & Astrophysics*, 513.

Güttler, C., Heißelmann, D., Blum, J., & Krijt, S. (2012). Normal collisions of spheres: A literature survey on available experiments. *ArXiv*, 1204, 1.

Hallbrucker, A., Mayer, E., & Johari, G. P. (1989a). Glass-liquid transition and the enthalpy of devitrification of annealed vapor-deposited amorphous solid water - a comparison with hyperquenched glassy water. *Journal of Physical Chemistry*, 93(12), 4986–4990.

Hallbrucker, A., Mayer, E., & Johari, G. P. (1989b). The heat capacity and glass transition of hyperquenched glassy water. *Philosophical Magazine Part B*, 60(2), 179–187.

Hallbrucker, A., Mayer, E., & Johari, G. P. (1989c). The heat capacity and glass transition of hyperquenched glassy water. *Philosophical Magazine Part B*, 60(2), 179–187.

Hallbrucker, A., Mayer, E., Omard, L. P., Dore, J. C., & Chieux, P. (1991). Structural characterization of hyperquenched glassy water and vapor-deposited amorphous ice. *Physics Letters A*, 159(8-9), 406–410.

Hammouda, B. (2010). A new guinier-porod model. *Journal of Applied Crystallography*, 43, 716–719.

Handa, Y. P. & Klug, D. D. (1988). Heat-capacity and glass-transition behavior of amorphous ice. *Journal of Physical Chemistry*, 92(12), 3323–3325.

Hass, D. D., Zhao, H., Dobbins, T., Allen, A. J., Slifka, A. J., & Wadley, H. N. G. (2010). Multi-scale pore morphology in directed vapor deposited yttria-stabilized zirconia coatings. *Materials Science and Engineering: A*, 527(23), 6270–6282.

Hatzes, A. P., Bridges, F. G., & Lin, D. N. C. (1988). Collisional properties of ice spheres at low impact velocities. *MONTHLY NOTICES OF THE ROYAL ASTRONOMICAL SOCIETY*, 231(4), 1091–1115.

Hedman, M. M., Nicholson, P. D., Salo, H., Wallis, B. D., Buratti, B. J., Baines, K. H., Brown, R. H., & Clark, R. N. (2007). Self-gravity wake structures in saturn's a ring revealed by cassini vims. *Astronomical Journal*, 133(6), 2624–2629.

Heißelmann, D., Blum, J., Fraser, H. J., & Wolling, K. (2010). Microgravity experiments on the collisional behavior of saturnian ring particles. *Icarus*, 206(2), 424–430.

Hertzsch, J. M. (2002). A model for surface effects in slow collisions of icy grains. *Planetary and Space Science*, 50(7-8), 745–755.

Higa, M., Arakawa, M., & Maeno, N. (1996). Measurements of restitution coefficients of ice at low temperatures. *Planetary and Space Science*, 44(9), 917.

Higa, M., Arakawa, M., & Maeno, N. (1998). Size dependence of restitution coefficients of ice in relation to collision strength. *Icarus*, 133(2), 310–320.

Hill, C. R., Heißelmann, D., Blum, J., & Fraser, H. J. (2015a). Collisions of small ice particles under microgravity conditions. *Astronomy & Astrophysics*, 573, A49.

Hill, C. R., Heißelmann, D., Blum, J., & Fraser, H. J. (2015b). Collisions of small ice particles under microgravity conditions (ii): Does the chemical composition of the ice change the collisional properties? *Astronomy & Astrophysics*, 575, A6.

Hobbs, P. V. (1965). Aggregation of ice particles in clouds and fogg at low temperatures. *Journal of the Atmospheric Sciences*, 22(3), 296–300.

Hobbs, P. V., Chang, S., & Locatell.Jd (1974). Dimensions and aggregation of ice crystals in natural clouds. *Journal of Geophysical Research*, 79(15), 2199–2206.

Horimoto, N., Kato, H. S., & Kawai, M. (2002). Stepwise morphological change of porous amorphous ice films observed through adsorption of methane. *Journal of Chemical Physics*, 116(11), 4375–4378.

Hornekaer, L., Baurichter, A., Petrunin, V. V., Luntz, A. C., Kay, B. D., & Al-Halabi, A. (2005). Influence of surface morphology on d-2 desorption kinetics from amorphous solid water. *Journal of Chemical Physics*, 122(12).

Ioppolo, S., Cuppen, H. M., Romanzin, C., van Dishoeck, E. F., & Linnartz, H. (2008). Laboratory evidence for efficient water formation in interstellar ices. *The Astrophysical Journal*, 686(2), 1474–1479.

Isokoski, K., Bossa, J. B., Triemstra, T., & Linnartz, H. (2014). Porosity and thermal collapse measurements of h2o, ch3oh, co2, and h2o:co2 ices. *Physical Chemistry Chemical Physics*, 16(8), 3456–3465.

Jenniskens, P. & Blake, D. F. (1994). Structural transitions in amorphous water ice and astrophysical implications. *Science*, 265(5173), 753–756.

Johansen, A. & Klahr, H. (2011). Planetesimal formation through streaming and gravitational instabilities. *Earth Moon and Planets*, 108(1), 39–43.

Johansen, A., Oishi, J. S., Mac Low, M.-M., Klahr, H., & Henning, T. (2007). Rapid planetesimal formation in turbulent circumstellar disks. *Nature*, 448(7157), 1022–1025.

Johari, G. P., Hallbrucker, A., & Mayer, E. (1987). The glass liquid transition of hyperquenched water. *Nature*, 330(6148), 552–553.

Kataoka, A., Tanaka, H., Okuzumi, S., & Wada, K. (2013). Fluffy dust forms icy planetesimals by static compression. *Astronomy & Astrophysics*, 557, L4.

Kimmel, G. A., Stevenson, K. P., Dohnalek, Z., Smith, R. S., & Kay, B. D. (2001). Control of amorphous solid water morphology using molecular beams. i. experimental results. *Journal of Chemical Physics*, 114(12), 5284–5294.

Klinger, J. (1981). Some consequences of a phase-transition of water ice on the heat-balance of comet nuclei. *Icarus*, 47(3), 320–324.

Kothe, S., Blum, J., Weidling, R., & Güttler, C. (2013). Free collisions in a microgravity many-particle experiment. iii. the collision behavior of sub-millimeter-sized dust aggregates. *Icarus*, 225, 75–85.

Kothe, S., Güttler, C., & Blum, J. (2010). The physics of protoplanetesimal dust agglomerates. v. multiple impacts of dusty agglomerates at velocities above the fragmentation threshold. *The Astrophysical Journal*, 725(1), 1242–1251.

Krijt, S., Güttler, C., Heißelmann, D., Dominik, C., & Tielens, A. G. G. M. (2013). Energy dissipation in head-on collisions of spheres. *Journal of Physics D: Applied Physics*, 46(43), 435303.

Langkowski, D., Teiser, J., & Blum, J. (2008). The physics of protoplanetesimal dust agglomerates. ii. low-velocity collision properties. *The Astrophysical Journal*, 675(1), 764–776.

Lauretta, D. & McSween, H. (2006). *Meteorites and the Early Solar System II*. University of Arizona Press.

Leger, A., Klein, J., Cheveigne, S. D., Guinet, C., Defourneau, D., & Belin, M. (1979). 3.1 mu-m absorption in molecular clouds is probably due to amorphous h2o ice. *ASTRONOMY & ASTROPHYSICS*, 79(1-2), 256–259.

Li, J. C., Bennington, S. M., & Ross, D. K. (1994). Further evidence for the existence of 2 kinds of h-bonds in ice ih. *Physics Letters A*, 192(2-4), 295–300.

Love, S. G., Pettit, D. R., & Messenger, S. R. (2014). Particle aggregation in microgravity: Informal experiments on the international space station. *Meteoritics & Planetary Science*, 49(5), 732–739.

Manico, G., Raguni, G., Pirronello, V., Roser, J. E., & Vidali, G. (2001). Laboratory measurements of molecular hydrogen formation on amorphous water ice. *The Astrophysical Journal*, 548(2), L253–L256.

Marboeuf, U., Thiabaud, A., Alibert, Y., Cabral, N., & Benz, W. (2014). From planetesimals to planets: volatile molecules. *Astronomy & Astrophysics*, 570.

Mayer, E. & Brüggeller, P. (1982). Vitrification of pure liquid water by high-pressure jet freezing. *Nature*, 298(5876), 715–718.

Mayer, E. & Pletzer, R. (1984). Polymorphism in vapor-deposited amorphous solid water. *Journal of Chemical Physics*, 80(6), 2939–2952.

Mayor, M. & Queloz, D. (1995). A jupiter-mass companion to a solar-type star. *Nature*, 378(6555), 355–359.

McCartney, S. A. & Sadtchenko, V. (2013). Fast scanning calorimetry studies of the glass transition in doped amorphous solid water: Evidence for the existence of a unique vicinal phase. *Journal of Chemical Physics*, 138(8).

McMillan, J. A. & Los, S. C. (1965). Vitreous ice - irreversible transformations during warm-up. *Nature*, 206(4986), 806.

Meisner, T., Wurm, G., Teiser, J., & Schywek, M. (2013). Preplanetary scavengers: Growing tall in dust collisions. *Astronomy & Astrophysics*, 559, 123.

Mitterdorfer, C., Bauer, M., Youngs, T. G. A., Bowron, D. T., Hill, C. R., Fraser, H. J., Finney, J. L., & Loerting, T. (2014). Small-angle neutron scattering study of micropore collapse in amorphous solid water. *Physical Chemistry Chemical Physics*, 16(30), 16013–16020.

Nagel-Vega, E. (2010). Planet formation in a disk around a star: The two dense-ring model. *Revista Mexicana De Ciencias Geologicas*, 27(2), 323–332.

Nield, V. M. & Whitworth, R. W. (1995). The structure of ice ih from analysis of single-crystal neutron diffuse-scattering. *Journal of Physics-Condensed Matter*, 7(43), 8259–8271.

Noble, J. A., Fraser, H. J., Aikawa, Y., Pontoppidan, K. M., & Sakon, I. (2013). A survey of h2o, co2, and co ice features toward background stars and low-mass young stellar objects using akari. *The Astrophysical Journal*, 775(2).

Oba, Y., Miyauchi, N., Hidaka, H., Chigai, T., Watanabe, N., & Kouchi, A. (2009). Formation of compact amorphous h2o ice by codeposition of hydrogen atoms with oxygen molecules on grain surfaces. *The Astrophysical Journal*, 701(1), 464–470.

Oberg, K. I., Boogert, A. C. A., Pontoppidan, K. M., van den Broek, S., van Dishoeck, E. F., Bottinelli, S., Blake, G. A., & Evans, N. J. (2011a). *Ices in Starless and Starforming Cores*, (pp. 65–78). IAU Symposium Proceedings Series. Cambridge Journals.

Oberg, K. I., Boogert, A. C. A., Pontoppidan, K. M., van den Broek, S., van Dishoeck, E. F., Bottinelli, S., Blake, G. A., & Evans, N. J. (2011b). The spitzer ice legacy: Ice evolution from cores to protostars. *The Astrophysical Journal*, 740(2).

Ollivier, M., Encrenaz, T., Roques, F., Selsis, F., & Casoli, F. (2009). *Planetary Systems: Detection, Formation, and Habitability of Extrasolar Planets*. Astronomy and Astrophysics Library. Springer.

Paglia, G., Buckley, C. E., Udovic, T. J., Rohl, A. L., Jones, F., Maitland, C. F., & Connolly, J. (2004). Boehmite-derived gamma-alumina system. 2. consideration of hydrogen and surface effects. *Chemistry of Materials*, 16(10), 1914–1923.

Palumbo, M. E. (2006). Formation of compact solid water after ion irradiation at 15 k. *Astronomy & Astrophysics*, 453(3), 903–909.

Papaloizou, J. C. B. & Terquem, C. (1999). Critical protoplanetary core masses in protoplanetary disks and the formation of short-period giant planets. *The Astrophysical Journal*, 521(2), 823–838.

Papoular, R. (2005). On water ice formation in interstellar clouds. *MONTHLY NOTICES OF THE ROYAL ASTRONOMICAL SOCIETY*, 362(2), 489–497.

Paraskov, G. B., Wurm, G., & Krauss, O. (2007). Impacts into weak dust targets under microgravity and the formation of planetesimals. *Icarus*, 191(2), 779–789.

Patashni, H., Rupprech, G., & Schuerma, D. W. (1974). Energy-source for comet outbursts. *Nature*, 250(5464), 313–314.

Pletzer, R. & Mayer, E. (1989). Type-i isotherms for n-2 adsorption on vapor-deposited amorphous solid water. *Journal of Chemical Physics*, 90(9), 5207–5208.

Podio, L., Kamp, I., Codella, C., Cabrit, S., Nisini, B., Dougados, C., Sandell, G., Williams, J. P., Testi, L., Thi, W.-F., Woitke, P., Meijerink, R., Spaans, M., Aresu, G., Ménard, F., & Pinte, C. (2013). Water Vapor in the Protoplanetary Disk of DG Tau. *The Astrophysical Journal*, 766, L5.

Pontoppidan, K. M., van Dishoeck, E. F., & Dartois, E. (2004). Mapping ices in protostellar environments on 1000 au scales - methanol-rich ice in the envelope of serpens smm 4. *Astronomy & Astrophysics*, 426(3), 925–940.

Poppe, T. & Blum, J. (1997). Experiments on pre-planetary grain growth. *Hypervelocity Impacts in Space and Planetology*, 20, 1595–1604.

Poppe, T., Blum, J., & Henning, T. (2000a). Analogous experiments on the stickiness of micron-sized preplanetary dust. *The Astrophysical Journal*, 533(1), 454–471.

Poppe, T., Blum, J., & Henning, T. (2000b). Experiments on collisional grain charging of micron-sized preplanetary dust. *The Astrophysical Journal*, 533(1), 472–480.

Poulet, F., Cruikshank, D. P., Cuzzi, J. N., Roush, T. L., & French, R. G. (2003). Compositions of saturn's rings a, b, and c from high resolution near-infrared spectroscopic observations. *Astronomy & Astrophysics*, 412(1), 305–316.

Raunier, S., Chiavassa, T., Allouche, A., Marinelli, F., & Aycard, J. (2003). Thermal reactivity of hnco with water ice: an infrared and theoretical study. *Chemical Physics*, 288(2), 197–210.

Raut, U., Famá, M., Teolis, B. D., & Baragiola, R. A. (2007). Characterization of porosity in vapor-deposited amorphous solid water from methane adsorption. *Journal of Chemical Physics*, 127(20).

Ros, K. & Johansen, A. (2013). Ice condensation as a planet formation mechanism. *Astronomy & Astrophysics*, 552, A137.

Saito, E. & Sirono, S.-i. (2011). Planetesimal formation by sublimation. *The Astrophysical Journal*, 728, 20.

Salo, H., Schmidt, J., & Spahn, F. (2001). Viscous overstability in saturn's b ring - 1. direct simulations and measurement of transport coefficients. *Icarus*, 153(2), 295–315.

Salter, D. M., Heißelmann, D., Chaparro, G., van der Wolk, G., Reissaus, P., Borst, A. G., Dawson, R. W., de Kuyper, E., Drinkwater, G., Gebauer, K., Hutcheon, M., Linnartz, H., Molster, F. J., Stoll, B., van der Tuijn, P. C., Fraser, H. J., & Blum, J. (2009). A zero-gravity instrument to study low velocity collisions of fragile particles at low temperatures. *Rev. Sci. Ins.*, 80(7), 074501.

Salzmann, C. G., Radaelli, P. G., Hallbrucker, A., Mayer, E., & Finney, J. L. (2006). The preparation and structures of hydrogen ordered phases of ice. *Science*, 311(5768), 1758–1761.

Schäfer, C., Speith, R., & Kley, W. (2007). Collisions between equal-sized ice grain agglomerates. *Astronomy & Astrophysics*, 470(2), 733–739.

Schegerer, A. A. & Wolf, S. (2010). Spatially resolved detection of crystallized water ice in a t tauri object. *Astronomy & Astrophysics*, 517, 87.

Schmidt, J., Salo, H., Spahn, F., & Petzschmann, O. (2001). Viscous overstability in saturn's b-ring - ii. hydrodynamic theory and comparison to simulations. *Icarus*, 153(2), 316–331.

Schräpler, R. & Blum, J. (2011). The physics of protoplanetesimal dust agglomerates. vi. erosion of large aggregates as a source of micrometer-sized particles. *The Astrophysical Journal*, 734, 108.

Schräpler, R., Blum, J., Seizinger, A., & Kley, W. (2012). The physics of protoplanetesimal dust agglomerates. vii. the low-velocity collision behavior of large dust agglomerates. *The Astrophysical Journal*, 758, 35.

Schriver-Mazzuoli, L., Schriver, A., & Hallou, A. (2000). Ir reflection-absorption spectra of thin water ice films between 10 and 160 k at low pressure. *Journal of Molecular Structure*, 554(2-3), 289–300.

Schutte, W. A., Boogert, A. C. A., Tielens, A., Whittet, D. C. B., Gerakines, P. A., Chiar, J. E., Ehrenfreund, P., Greenberg, J. M., van Dishoeck, E. F., & de Graauw, T. (1999). Weak ice absorption features at 7.24 and 7.41 mu m in the spectrum of the obscured young stellar object w 33a. *Astronomy & Astrophysics*, 343(3), 966–976.

Seizinger, A., Krijt, S., & Kley, W. (2013). Erosion of dust aggregates. *Astronomy & Astrophysics*, 560, 45.

Sepulveda, A., Leon-Gutierrez, E., Gonzalez-Silveira, M., Rodriguez-Tinoco, C., Clavaguera-Mora, M. T., & Rodriguez-Viejo, J. (2012). Glass transition in ultra-thin films of amorphous solid water. *Journal of Chemical Physics*, 137(24).

Shimaki, Y. & Arakawa, M. (2012). Low-velocity collisions between centimeter-sized snowballs: Porosity dependence of coefficient of restitution for ice aggregates analogues in the solar system. *Icarus*, 221(1), 310–319.

Smith, R. G. & Wright, C. M. (2011). The librational band of water ice in afgl 961: revisited. *MONTHLY NOTICES OF THE ROYAL ASTRONOMICAL SOCIETY*, 414(4), 3764–3768.

Smith, R. S. & Kay, B. D. (1999). The existence of supercooled liquid water at 150 k. *Nature*, 398(6730), 788–791.

Smoluchowski, R. (1978). Amorphous ice on saturnian rings and on icy satellites - its formation, stability, and observability. *Science*, 201(4358), 809–811.

Smoluchowski, R. (1981). Amorphous ice and the behavior of cometary nuclei. *The Astrophysical Journal*, 244(1), L31–L34.

Soper, A. K. (1983). Multiple-scattering from an infinite-plane slab. *Nuclear Instruments & Methods in Physics Research*, 212(1-3), 337–347.

Soper, A. K. & Egelstaff, P. A. (1980). Multiple-scattering and attenuation of neutrons in concentric cylinders .1. isotropic first scattering. *Nuclear Instruments & Methods*, 178(2-3), 415–425.

Stevenson, K. P., Kimmel, G. A., Dohnalek, Z., Smith, R. S., & Kay, B. D. (1999). Controlling the morphology of amorphous solid water. *Science*, 283(5407), 1505–1507.

Strauss, H. L., Chen, Z., & Loong, C. K. (1994). The diffusion of h-2 in hexagonal ice at low-temperatures. *Journal of Chemical Physics*, 101(8), 7177–7180.

Supulver, K. D., Bridges, F. G., & Lin, D. N. C. (1995). The coefficient of restitution of ice particles in glancing collisions - experimental results for unfrosted surfaces. *Icarus*, 113(1), 188–199.

Supulver, K. D., Bridges, F. G., Tiscareno, S., Lievore, J., & Lin, D. N. C. (1997). The sticking properties of water frost produced under various ambient conditions. *Icarus*, 129(2), 539–554.

Takahashi, J. (1999). Md simulation for h 2 formation on amorphous ice. *EARTH PLANETS AND SPACE*, 51(11), 1215–1222.

Takaizumi, K. & Wakabayashi, T. (1997). The freezing process in methanol-, ethanol-, and propanol-water systems as revealed by differential scanning calorimetry. *Journal of Solution Chemistry*, 26(10), 927–939.

Teiser, J., Kupper, M., & Wurm, G. (2011). Impact angle influence in high velocity dust collisions during planetesimal formation. *Icarus*, 215(2), 596–598.

Teiser, J. & Wurm, G. (2009a). Decimetre dust aggregates in protoplanetary discs. *Astronomy & Astrophysics*, 505(1), 351–359.

Teiser, J. & Wurm, G. (2009b). High-velocity dust collisions: forming planetesimals in a fragmentation cascade with final accretion. *MONTHLY NOTICES OF THE ROYAL ASTRONOMICAL SOCIETY*, 393(4), 1584–1594.

Thomson, F. S., Marouf, E. A., Tyler, G. L., French, R. G., & Rappoport, N. J. (2007). Periodic microstructure in saturn's rings a and b. *Geophysical Research Letters*, 34(24).

Townrow, S. & Coleman, P. G. (2015). Structural changes in amorphous solid water films on heating to 120Ű140ăk and 150Ű160ăk seen by positronium annihilation spectroscopy. *Journal of Physics: Condensed Matter*, 27(22), 225401.

van Dishoeck, E. F., Kristensen, L. E., Benz, A. O., Bergin, E. A., Caselli, P., Cernicharo, J., Herpin, F., Hogerheijde, M. R., Johnstone, D., Liseau, R., Nisini, B., Shipman, R., Tafalla, M., van der Tak, F., Wyrowski, F., Aikawa, Y., Bachiller, R., Baudry, A., Benedettini, M., Bjerkeli, P., Blake, G. A., Bontemps, S., Braine, J., Brinch, C., Bruderer, S., Chavarría, L., Codella, C., Daniel, F., de Graauw, T., Deul, E., di Giorgio, A. M., Dominik, C., Doty, S. D., Dubernet, M. L., Encrenaz, P., Feuchtgruber, H., Fich, M., Frieswijk, W., Fuente, A., Giannini, T., Goicoechea, J. R., Helmich, F. P., Herczeg, G. J., Jacq, T., Jørgensen, J. K., Karska, A., Kaufman, M. J., Keto, E., Larsson, B., Lefloch, B., Lis, D., Marseille, M., McCoey, C., Melnick, G., Neufeld, D., Olberg, M., Pagani, L., Panić, O., Parise, B., Pearson, J. C., Plume, R., Risacher, C., Salter, D., Santiago-García, J., Saraceno, P., Stäuber, P., van Kempen, T. A., Visser, R., Viti, S., Walmsley, M., Wampfler, S. F., & Yıldız, U. A. (2011). Water in Star-forming Regions with the Herschel Space Observatory (WISH). I. Overview of Key Program and First Results. PASP, 123, 138–170.

Vidali, G., Roser, J. E., Ling, L., Congiu, E., Manico, G., & Pirronello, V. (2006). The formation of interstellar molecules via reactions on dust grain surfaces. *Faraday Discussions*, 133, 125–135.

Wang, H., Bell, R. C., Iedema, M. J., Tsekouras, A. A., & Cowin, J. P. (2005). Sticky ice grains aid planet formation: Unusual properties of cryogenic water ice. *The Astrophysical Journal*, 620(2), 1027–1032.

Wang, Z., Chakrabarty, D., & Kaplan, D. L. (2006). A debris disk around an isolated young neutron star. *Nature*, 440(7085), 772–775.

Weidenschilling, S. J. (1977). Aerodynamics of solid bodies in the solar nebula. *MONTHLY NOTICES OF THE ROYAL ASTRONOMICAL SOCIETY*, 180, 57–70.

Weidenschilling, S. J. (1980). Dust to planetesimals - settling and coagulation in the solar nebula. *Icarus*, 44, 172–189.

Weidenschilling, S. J. (1997). The origin of comets in the solar nebula: A unified model. *Icarus*, 127(2), 290–306.

Weidenschilling, S. J. & Cuzzi, J. N. (1993). Formation of planetesimals in the solar nebula.

Weidenschilling, S. J., Cuzzi, J. N., & Lunine, J. I. (1993). Formation of planetesimals in the solar nebula.

Weidling, R., Güttler, C., & Blum, J. (2012). Free collisions in a microgravity many-particle experiment. i. dust aggregate sticking at low velocities. *Icarus*, 218, 688–700.

Wenzel, J., Linderstromlang, C. U., & Rice, S. A. (1975). Amorphous solid water - neutron-diffraction study. *Science*, 187(4175), 428–430.

Williams, D. A., Hartquist, T. W., & Whittet, D. C. B. (1992). The ice threshold in molecular clouds - a diagnostic of the infrared radiation-field. *MONTHLY NOTICES OF THE ROYAL ASTRONOMICAL SOCIETY*, 258(3), 599–601.

Windmark, F., Birnstiel, T., Güttler, C., Blum, J., Dullemond, C. P., & Henning, T. (2012a). Planetesimal formation by sweep-up: how the bouncing barrier can be beneficial to growth. *Astronomy & Astrophysics*, 540, C1.

Windmark, F., Birnstiel, T., Ormel, C. W., & Dullemond, C. P. (2012b). Breaking through: The effects of a velocity distribution on barriers to dust growth. *Astronomy & Astrophysics*, 544, A73.

Wolszczan, A. & Frail, D. A. (1992). A planetary system around the millisecond pulsar psr1257 + 12. *Nature*, 355, 145–147.

Wu, Y. C., Jiang, J., Wang, S. J., Kallis, A., & Coleman, P. G. (2011). Porosity and crystallization of water ice films studied by positron and positronium annihilation. *Physical Review B*, 84(6).

Wu, Y. C., Kallis, A., Jiang, J., & Coleman, P. G. (2010). Structural and phase changes in amorphous solid water films revealed by positron beam spectroscopy. *Physical Review Letters*, 105(6).

Wurm, G., Blum, J., & Colwell, J. E. (2001). Aerodynamical sticking of dust aggregates. *Physical Review E*, 64(4).

Wurm, G., Paraskov, G., & Krauss, O. (2005). Growth of planetesimals by impacts at similar to 25 m/s. *Icarus*, 178(1), 253–263.

Yen, H.-W., Takakuwa, S., Ohashi, N., Aikawa, Y., Aso, Y., Koyamatsu, S., Machida, M. N., Saigo, K., Saito, M., Tomida, K., & Tomisaka, K. (2014). Alma observations of infalling flows toward the keplerian disk around the class i protostar l1489 irs. *The Astrophysical Journal*, 793(1).

Youdin, A. N. (2011). On the formation of planetesimals via secular gravitational instabilities with turbulent stirring. *The Astrophysical Journal*, 731(2).

Youdin, A. N. & Goodman, J. (2005). Streaming instabilities in protoplanetary disks. *The Astrophysical Journal*, 620(1), 459–469.

Zamankhan, P. (2010). Simulations of collision of ice particles. *Communications in Nonlinear Science and Numerical Simulation*, 15(6), 1538–1552.

Zasowski, G., Kemper, F., Watson, D. M., Furlan, E., Bohac, C. J., Hull, C., & Green, J. D. (2009). Spitzer infrared spectrograph observations of class i/ii objects in taurus: Composition and thermal history of the circumstellar ices. *The Astrophysical Journal*, 694(1), 459–478.

Zebker, H. A., Marouf, E. A., & Tyler, G. L. (1985). Saturn's rings - particle size distributions for thin layer model. *Icarus*, 64, 531–548.

Zhou, J. L., Xie, J. W., Liu, H. G., Zhang, H., & Sun, Y. S. (2012). Forming different planetary systems. *Research in Astronomy and Astrophysics*, 12(8), 1081–1106.

Zondlo, M. A., Onasch, T. B., Warshawsky, M. S., Tolbert, M. A., Mallick, G., Arentz, P., & Robinson, M. S. (1997). Experimental studies of vapor-deposited water-ice firms using grazing-angle ftir-reflection absorption spectroscopy. *Journal of Physical Chemistry B*, 101(50), 10887–10895.

Zsom, A., Ormel, C. W., Güttler, C., Blum, J., & Dullemond, C. P. (2010). The outcome of protoplanetary dust growth: pebbles, boulders, or planetesimals? ii. introducing the bouncing barrier. *Astronomy & Astrophysics*, 513.

Publications

C. Mitterdorfer, M. Bauer, T. G. A. Youngs, D. T. Bowron, **C. R. Hill**, H. J. Fraser, J. L. Finney, T. Loerting (2014), "Small-angle neutron scattering study of micropore collapse in amorphous solid water", PCCP, 16, 16013

C. R. Hill, D. Heißelmann, J. Blum, H. J. Fraser (2015), "Collisions of small ice particles under microgravity conditions" A&A, 573, A49

C. R. Hill, D. Heißelmann, J. Blum, H. J. Fraser (2015), "Collisions of small ice particles under microgravity conditions (II): Does the chemical composition of the ice change the collisional properties?" A&A, 575, A6

C. R. Hill, C. Mitterdorfer, T. G. A. Youngs, D. T. Bowron, H. J. Fraser, T. Loerting, "Neutron scattering analysis of water's glass transition and micropore collapse in amorphous solid water", *submitted to PRL*